UNIVERSITÀ DEGLI STUDI DI TRIESTE
e
UNIVERSITÀ CA' FOSCARI DI VENEZIA

XXXI CICLO DEL DOTTORATO DI RICERCA IN

CHIMICA

SELF-ASSEMBLY INTO HYDROGELS OF D,L-HETEROCHIRAL TRIPEPTIDES

Settore scientifico-disciplinare: CHIM/06

DOTTORANDA
EVELINA PARISI

COORDINATORE
PROF. BARBARA MILANI

SUPERVISORE DI TESI
PROF. SILVIA MARCHESAN

ANNO ACCADEMICO 2017/2018

A Pulla e Nevio

"La colpa di Eva è stata quella di voler conoscere, sperimentare, indagare con le proprie forze le leggi che regolano l'universo, la terra, il proprio corpo, di rifiutare l'insegnamento calato dall'alto, in una parola Eva rappresenta la curiosità della scienza contro la passiva accettazione della fede."

Margherita Hack

Table of Contents

List of abbreviations VII
Abstract IX
Riassunto X

1. INTRODUCTION 12
1.1 Introduction 13
1.1.1. Gels and hydrogels 13
1.1.2. Low-molecular-weight gelators (LMWGs) 14
1.1.2.1. LMWGs based on peptides 15
1.2. Peptides 15
1.2.1. Peptide primary structure 15
1.2.2. Peptide secondary structure 16
1.2.2.1. α-helices 17
1.2.2.2. β-sheets 18
1.2.3. Tertiary and quaternary structure 19
1.3. Peptide self-assembly 19
1.3.1. Introduction 19
1.3.2. Self-assembly driving forces 20
1.4. Type of self-assembling peptides 21
1.4.1. Systems based on α-helical structure and coiled coil 23
1.4.2. Ionic complimentary peptides 23
1.4.4. Surfactant like-peptides 25
1.4.5. Systems based on aromatic interactions 26
1.5. Factors affecting self-assembly 28
1.5.1. Peptide sequence 28
1.5.2. Concentration 28
1.5.3. pH 29
1.5.4. Salts 29
1.5.5. Enzymes 30
1.5.6. Temperature 30
1.5.7. Light-activation 31
1.6. Applications of self-assembling peptides 31
1.6.1. Tissue engineering 31
1.6.2. Drug delivery 32

2. AIM OF THE PROJECT 34
2.1 Aim of the project 35

3. RESULTS AND DISCUSSION 38
3.1. Peptide preparation 39
3.1.1. Peptide synthesis 39
3.1.2. Peptide characterisation 43
3.1.3. Synthesised peptides 44
3.2. MGC (Minimum Gelation Concentration) and hydrogel preparation 44
3.2.1. MGC definition 44
3.2.2. Peptide hydrogel preparation 45
3.3. Peptide hydrogel characterisation 47
3.3.1. Oscillatory Rheometry 47
3.3.2. Nanostructure morphology assessed by TEM 52
3.3.2. Circular Dichroism Spectroscopy (CD) 59
3.3.2.1. Circular dichroism spectra at 1 mM 61
3.3.2.2. Circular dichroism spectra at MGC 65
3.3.2.3. Determination of Tm (melting temperature) of self-assembled peptide hydrogels 70
3.3.3. Fourier-Transformed Infrared Spectroscopy (FT-IR) 76
3.3.4. X-Ray Diffraction (XRD) single crystal structures 77
3.3.4.1. XRD structures of xFF group sequences 78
3.3.4.2. XRD structures of xFW group sequences 98
3.3.4.3. XRD structures of xXX group sequences 104

4.PEPTIDE-HYDROGEL APPLICATION 109
4.1. Peptide hydrogel potential bio-application 110
4.2. Preparation of the hydrogels for cell assays 111
4.4. Cytotoxicity assays 113
4.4.1. LIVE/DEAD® viability/cytotoxicity assay 113
4.4.2. MTS Cell Proliferation Assay 120

5.CONCLUSIONS 123
5.1. Conclusions 124
5.2. Future perspective 125

6.MATERIALS AND METHODS 126
6.1. Peptide synthesis 127

6.1.1. Peptide synthesis 127
6.1.2. Loading of the first amino acid on the resin 127
6.1.3. Calculation of the first amino acid loading on the resin 127
6.1.4. Colorimetric tests 128
6.1.4.1. Chloranil test 128
6.1.4.2. Bromophenol Blue test 128
6.1.5. Cleavage of peptide from the resin 128
6.1.6. Peptide purification 129
6.1.7. Peptide characterisation 129
6.2. Peptide hydrogel preparation 129
6.3. Hydrogel characterisation 130
6.3.1. Oscillatory Rheometry 130
6.3.2. Transmission Electron Microscopy (TEM) 130
6.3.3. Circular Dichroism (CD) Spectroscopy 130
6.3.4. Fourier-Transformed Infrared Spectroscopy (FT-IR) 131
6.3.5.1. Crystallographic details 131
6.3.6. Trypan blue exclusion test of cell viability 138
6.3.7. Fibroblast cell culture live/dead assay 139
6.3.8. MTS assay 139

7.SUPPLEMENTARY 140

References 208

A passage from "Twenty thousand leagues under the sea" by Jules Verne 216

List of abbreviations

	List of abbreviations
A, a	Alanine (Upper case L-series, Lowercase D-series)
AP	Aggregation Propensity
ATR-IR	Attenuated Total Reflectance Infrared Spectroscopy
B1	Buffer 1
B2	Buffer 2
Boc	*tert*-butoxycarbonyl
C,c	Cysteine (Upper case L-series, Lowercase D-series)
CD	Circular Dichroism
CG	Coarse-grain
D,d	Aspartic Acid (Upper case L-series, Lowercase D-series)
DCM	Dichloromethane
DIPEA	*N*,*N*-Diisopropyl ethylamine
DMSO-d_6	Deutereted dimethyl sulfoxide
E,e	Glutamic Acid (Upper case L-series, Lowercase D-series)
EDTA	Ethylenediaminetetraacetic acid
ESI-MS	ElectroSpray Ionisation Mass Spectroscopy
F,f	Phenylalanine (Upper case L-series, Lowercase D-series)
Fmoc	9-Fluorenylmethoxycarbonyl
FT-IR	Fourier Transform Infrared Spectroscopy
G,g	Glicine (Upper case L-series, Lowercase D-series)
G’	Elastic or storage modulus
G’’	Viscous or loss modulus
HBTU	(*O*-benzotriazol-1-yl)-1,1,3,3-tetramethyluronium hexafluorophoshate
HOAt	1-Hydroxy-7-azabenzotriazole
HPLC	High Performance Liquid Chromatography
I,i	Isoleucine (Upper case L-series, Lowercase D-series)
IR	Infrared
K,k	Lysine (Upper case L-series, Lowercase D-series)
L,l	Leucine (Upper case L-series, Lowercase D-series)

LC-MS	Liquid Chromatography- Mass Spectrometry
L-HDGA	*N,N'*-hexadecanedioyldi-L-glutamic acid
LMWG	Low Molecular Weight Gelators
LPPS	Liquid-Phase Peptide Synthesis
LVR	Linear Viscoelastic Regime
M,m	Methionine (Upper case L-series, Lowercase D-series)
MGC	Minimum Gelation Concentration
NMR	Nuclear Magnetic Resonance
PBS	Phosphate Buffered Saline
P,p	Proline (Upper case L-series, Lowercase D-series)
R,r	Arginine (Upper case L-series, Lowercase D-series)
RP-HPLC	Reversed Phase High Performance Liquid Chromatography
R_t	Retention Time
RT	Room Temperature
S,s	Serine (Upper case L-series, Lowercase D-series)
$SOCl_2$	Thionyl chloride
SPPS	Solid-phase peptide synthesis
T,t	Threonine (Upper case L-series, Lowercase D-series)
TEM	Transmission Electron Microscopy
TFA	Trifluoroacetic acid
ThT	Thioflavin T
TIPS	Triisopropylsilane
T_m	Melting Temperature
TMS	Tetramethylsilane
UV	Ultraviolet irradiation
UV-Vis	Ultraviolet-Visible irradiation
V,v	Valine (Upper case L-series, Lowercase D-series)
W,w	Tryptophan (Upper case L-series, Lowercase D-series)
XRD	X-ray Diffraction
Y,y	Tyrosine (Upper case L-series, Lowercase D-series)
β_a	Anti-parallel β-sheets
β_p	Parallel β-sheets

Abstract

In the last two decades, peptide-based biomaterials have become very popular in different research areas such as diagnostics, therapeutics and regenerative medicine. In particular, ultrashort (2-3 amino acids) peptides are particularly attractive for their ease of preparation and low-cost. Their self-assembly can yield supramolecular hydrogels that are inherently biocompatible and biodegradable. Unfortunately, prediction of self-assembly and hydrogelation of unprotected tripeptides is remarkably difficult, as shown in recent studies.

Interestingly, it was reported that substitution of the N-terminal amino acid with its D-enantiomer can yield self-assembling tripeptides that gel, from hydrophobic L-analogues that do not. For this reason, a series of 16 tripeptides of stereoconfiguration D-L-L was chosen as a subject of study for self-assembly and hydrogelation and is described in this thesis. The tripeptides were synthesised by solid-phase, purified by RP-HPLC, characterised at the molecular level by ^{1}H-NMR, ^{13}C-NMR, ESI-MS, and CD. The tripeptides were probed for self-assembly and gelation at physiological conditions (*i.e.*, phosphate buffer, pH 7.3). Their supramolecular behaviour was then investigated by means of CD, FT-IR, transmission electron microscopy (TEM), and single-crystal X-ray diffraction analyses.

12 new hydrogelators were identified and their minimum gelling concentration (MGC) was determined. The systems were investigated by means of oscillatory rheometry. Finally, selected sequences were evaluated for cytotoxicity *in vitro* on fibroblast cell culture, revealing a promising performance for future applications as biomaterials.

Riassunto

Negli ultimi due decenni, i biomateriali a base di peptidi sono diventati molto popolari in diverse aree della ricerca come la diagnostica, la terapia e la medicina rigenerativa. In particolare, peptidi molto brevi (2-3 amminoacidi) sono molto interessanti per la loro semplicità di preparazione e basso costo. La loro auto-organizzazione può portare alla formazione di idrogel che sono per la loro natura tendenzialmente biocompatibili e biodegradabili. Purtroppo però predire quali sequenze di tripeptidi (privi di gruppi protettori) siano in grado di formare gel è estremamente difficile, come riportato in recenti studi.

Tuttavia, un aspetto interessante è che recentemente si è visto che la sostituzione dell'amminoacido N-terminale con il suo D-enantiomero può risultare in tripeptidi che gelificano, a partire da L-analoghi idrofobici che non formano gel. Per questo motivo, una serie di 16 tripeptidi con stereoconfigurazione D-L-L è stata scelta come soggetto di studio per l'auto-organizzazione e gelificazione ed è descritta in questa tesi. I tripeptide sono stati sintetizzati in fase solida, purificati tramite RP-HPLC, caratterizzati a livello molecolare tramite ^{1}H-NMR, ^{13}C-NMR, ESI-MS e CD. I tripeptidi sono stati quindi testati per l'auto-organizzazione in idrogel in condizioni fisiologiche (tampone fosfato, pH 7.3). Il loro comportamento supramolecolare è stato quindi studiato tramite CD, FT-IR, microscopia a trasmissione elettronica (TEM), e diffrazione di raggi-X su singolo cristallo.

12 nuove sequenze in grado di formare idrogel sono state identificate e la loro concentrazione minima di gelificazione (MGC) è stata determinata. I sistemi sono stati studiati tramite reometria oscillatoria. Infine, sono state selezionate delle sequenze per effettuare delle prove di citotossicità *in vitro* su cultura cellular di fibroblasti. Questi esperimenti hanno rivelato una promettente performance per lo sviluppo futuro di biomateriali.

1. INTRODUCTION

1.1 Introduction

1.1.1. Gels and hydrogels

Gels are ubiquitous systems of polymeric materials composed of a 3D-network that holds high amounts of solvent [1]. These soft materials, with a behaviour recognisable as a compromise between typical solid-like and liquid-like systems, feature gelator molecules (*elastic component*) and an entrapped liquid (*fluid component*) to form a final interconnected complex system held together through intra- and intermolecular of forces. When the fluid component contained in a gel is water at high percentage (typically 95% or more by weight or volume), and the elastic component prevails over the viscous component, the viscoelastic material is defined as a *hydrogel*.

Considering the forces directly involved during the gelation process, hydrogels can be distinguished in two classes: chemical hydrogels, in which polymers are covalently interconnected through cross-linking molecules; physical hydrogels, where the interactions between gelator chains are weak and reversible (*e.g.*, hydrogen bonds, van der Waals forces, ionic and hydrophobic interactions). Control over the cross-linking density is a useful strategy for both classes, to obtain a final hydrogel with well-defined properties (*e.g.*, stability or stimuli-responsive controlled degradation, *Figure 1.1*). In contrast to the majority of chemical hydrogels, physical hydrogels are formed reversibly, and they can be dissolved simply by changing the environmental conditions.

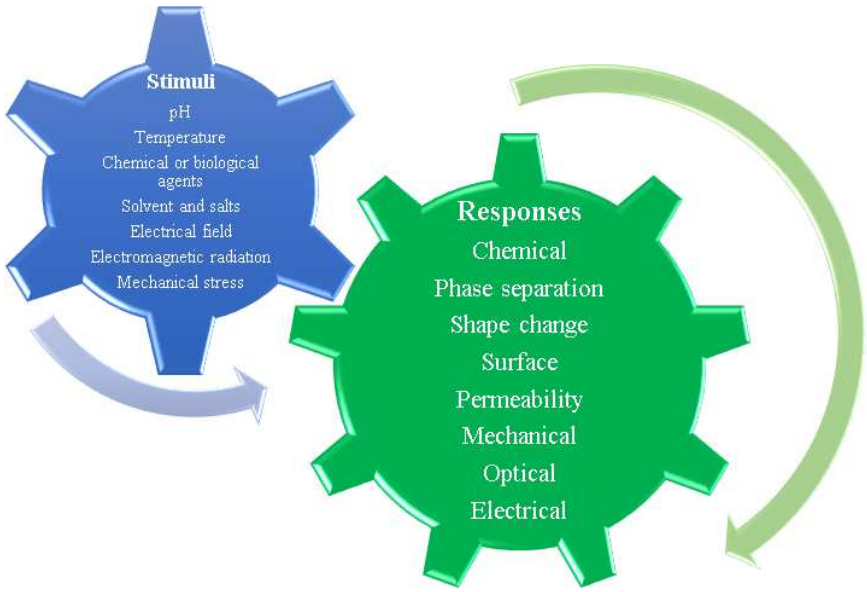

Figure 1.1: Common stimuli and relative-responses in hydrogels.

An interesting group of physical hydrogels includes supramolecular systems, which are formed by low-molecular-weight gelators (LMWG) that reversibly organise into *superstructures*, *i.e.,* structures of a scale size that is notably bigger than the individual components. These hydrogels are often preferred for biomedical applications (*e.g.*, disease diagnosis, bioimaging, drug delivery, wound

dressing, tissue engineering) [2]. Over the last years, short peptides have attracted great research interest, thanks to the simple and low-cost synthesis of potentially unlimited building blocks, and to their biocompatibility and biodegradability [3].

1.1.2. Low-molecular-weight gelators (LMWGs)

The main difference between supramolecular and polymeric hydrogels is related to the molecular weight of the gelators, which is typically low in the former case, hence the wording "low-molecular-weight gelators". One advantage of LMWGs is a higher level of a molecular order that spans to the nano- and often micro-scale, thus providing unique properties to the gels. The ordering (*i.e.*, assembly) and disassembly can be controlled by means of an external stimulus or trigger, while to obtain polymeric hydrogels a simple swelling is often sufficient. Two examples of physical stimuli-controlled (*e.g.*, temperature, ultrasound, ionic strength, etc.) LMWGs are shown in *Figure 1.2* [4]. Another common approach is the use of chemical triggers (*e.g.*, pH, photochemical reactions, catalysis).

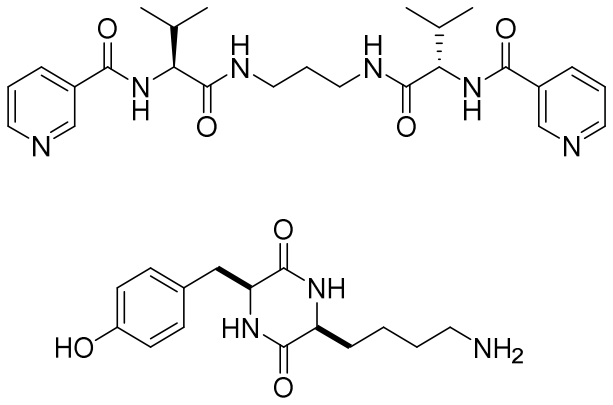

Figure 1.2.: Molecular structures of two LMWGs controlled by temperature (top) and ultrasound (bottom) stimuli [4].

An example of catalytic supramolecular hydrogel was obtained by Liu's group [5] introducing Cu^{2+} into a glutamic acid-based bolaamphiphilic lipid (*N,N'*-hexadecanedioyldi-L-glutamic acid, L-HDGA, *Figure 1.3*.). Thanks to the high density of catalytic sites (Cu^{2+}), it is possible to observe nanotube formation with multilayer walls showing enhanced catalytic behaviour.

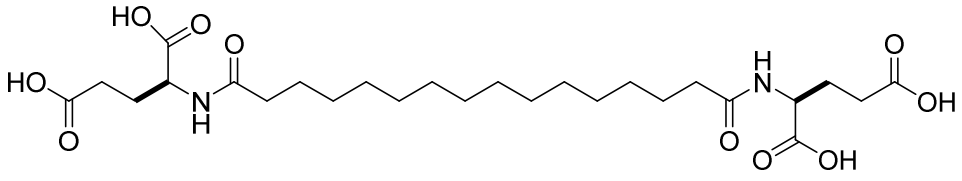

Figure 1.3.: N,N'-hexadecanedioyldi-L-glutamic acid, L-HDGA molecular structure as hydrogelator [4].

1.1.2.1. LMWGs based on peptides

LMWGs are very interesting systems that are drawing attention within the scientific community for their great potential for diverse material applications. LMWGs can be amphiphilic peptides or peptide derivatives that self-organize into nanometric fibrils to yield a 3D-network that gels (*Figure 1.4*) [6].

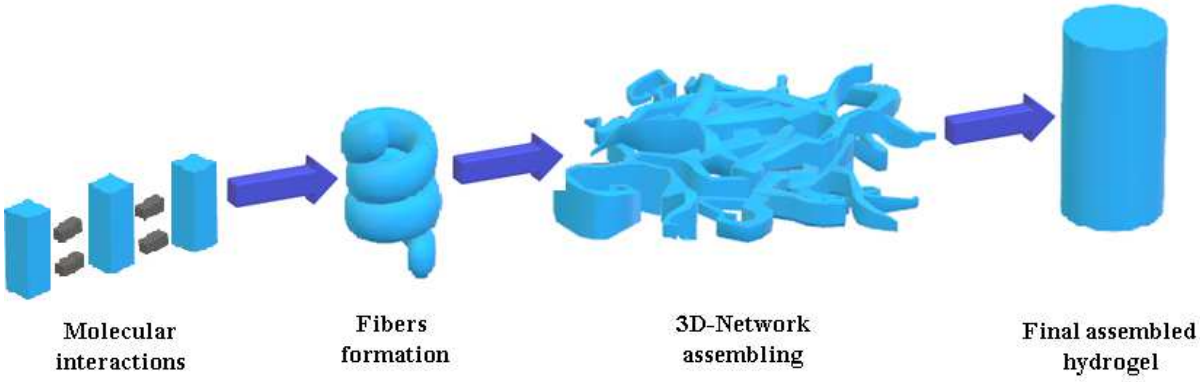

Figure 1.4: Evolution of the steps from small molecules to final hydrogel.

The prediction of self-assembly for uncapped peptide sequences as short as three amino acids is remarkably difficult and until today, there is still a need for general self-assembly rules that can be universally applied. For example, all possible combinations of the 20 natural L-amino acids into triplets correspond to 20^3 = 8,000 tripeptides, but experiments guided by an *in silico* screening of the 8,000 led to the identification of just 4, remarkably similar, LMWGs (KYF, KYY, KFF and KYW) [7]. In this context, fast, coarse-grain computation tools can come to help to select appropriate parameters, such as hydrophobicity and aggregation propensity, in large sets.

1.2. Peptides

1.2.1. Peptide primary structure

Peptides and proteins are biological polymers formed by different α-amino acids (2-amino carboxylic acids) as constituent monomers. Besides the 20 amino acids already present in nature, several of them can be easily synthetically prepared. Except for proline, which has the amine taking part in the five-membered pyrrolidine ring, all the others amino acids present a primary amino group, a carboxylic group, a hydrogen and a side chain (R) bonded to the same carbon centre (α-carbon, C_α) (*Figure 1.5*). Every amino acid, except glycine (where R = H), are chiral molecules. They can exist in two enantiomers (L- or D-forms), of which L-amino acids compose the vast majority of protein building blocks. Exceptions include, for instance, D-Ser and D-Asp found in humans, typically due to aging, and D-Ala in microorganisms, such as in the cell walls of bacteria, but not in bacterial proteins.

The behaviour and relative classification (aliphatic, aromatic, sulfur-containing, neutral, acidic and basic) of the amino acids is directly correlated to the side chain (R) chemical structure.

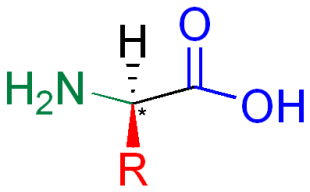

Figure 1.5: General structure of an amino acid: in green the amino group, in blue the carboxylic group, in red the side chain typical for each amino acid. All groups are bonded to the same carbon atom.

Two amino acids can be linked together via a condensation reaction that leads to a dipeptide and a water molecule as products, thanks to the formation of a new amide bond (peptide bond) between the carboxylic group of one amino acid and the amine group of the other one. Except in the case of proline, the peptide bond is planar due to the electron delocalisation between the amide nitrogen and the carbonyl oxygen (*Figure 1.6*) and present in more stable and energetically favoured *trans* configuration, compared to the *cis,* in which the steric repulsion between the groups bonded to the C_α is higher (*Figure 1.7*).

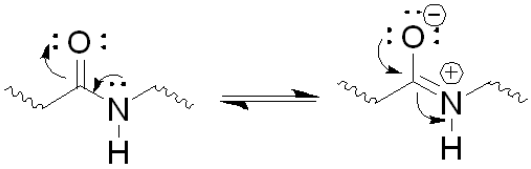

Figure 1.6: Resonance structures of peptide bond.

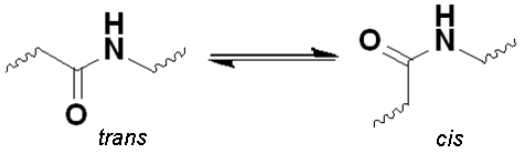

Figure 1.7: Peptide bond cis/trans isomers.

1.2.2. Peptide secondary structure

The peptide chain can have different spatial conformations since rotation around C_α-N and C_α-C bonds is allowed, considering the two torsion angles φ and ψ respectively generated (*Figure 1.8*). These angles can theoretically assume values between -180° and 180° but in practice only some combinations, corresponding to specific regions shown in Ramachandran plots [8], are energetically allowed.

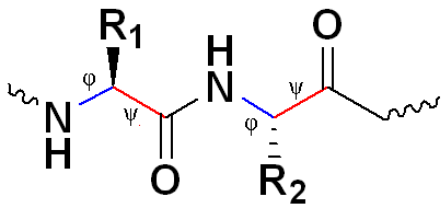

Figure 1.8: Peptide backbone: in blue C_α-C bond (and relative torsion angle φ), in red C_α-N bond (and relative torsion angle ψ).

The *secondary structure* of a peptide implies its regular conformation stabilised *via* intramolecular or intermolecular non-covalent interactions. Amongst these, hydrogen bonds between hydrogen bond donors (*e.g.*, R_2N-H groups) and acceptors (*e.g.,* R_2-C=O groups) and hydrophobic interactions play an elected role. There are different kinds of secondary structures, mainly α-helices, coiled coils, β-sheets, β-hairpins, β-turns and random coils. In this section only α-helices and β-sheets will be described[9].

1.2.2.1. α-helices

The most predominant *α-helix* structure in nature is right-handed and it is characterised by the presence of units (turns) of 5.2 Å containing 3.6 amino acid residues. The formation of the helices is spontaneous and stabilised by the hydrogen bonds between the carbonyl oxygen of the backbone and the amide hydrogen of the fourth amino acid nearer to the C-terminus of the peptide chain. Typical values are -57° and -47° for φ and ψ angles respectively in α-helices. *Coiled coils* are formed when more α-helices can interlock in more stable structures, and this is a useful feature for supramolecular assembly[10] [11].

Woolfson *et al.* showed that 28-mer peptides can be combined to obtain unilamellar spheres (~100 nm of diameter) starting from two non-covalent heterodimeric and homotrimeric coiled-coil bundles to final hexagonal systems able to close themselves into cages [10] (*Figure 1.9.*).

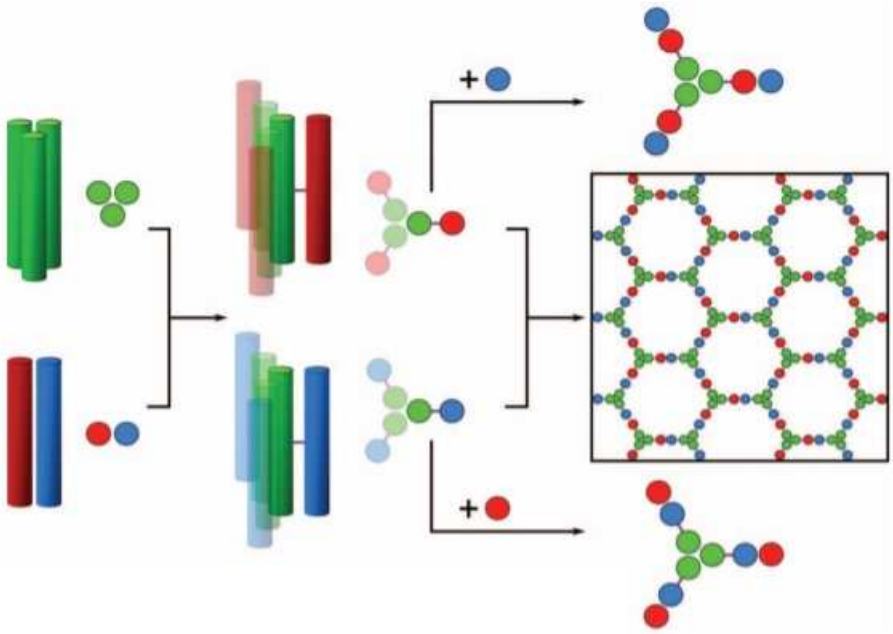

Figure 1.9.: Schematics for the design and self-assembly of peptide-based cages, the cylinders on the left are coiled-coil structures, reprinted from [10] *© 2013 American Association for the Advancement of Science.*

One disadvantage is that stable coiled-coils are obtained from relatively long sequences of at least 28 amino acids, even though 5-mers obtained from non-natural peptides with residues prone to helix-formation were shown to assemble into helices [12].

1.2.2.2. β-sheets

A *β-sheet* (or β-pleated sheet) is another common secondary structure present in nature in which β-sheets consists of β-strands kept together thanks to hydrogen bonds formation through neighbouring peptide backbones. Two arrangements of β-sheets are possible: parallel and antiparallel. In the first case, the peptide strands and all the C-termini of the peptide are in the same direction (βp), whereas in the second case, the adjacent chains are aligned in opposite directions and the N-termini and C-termini are alternate (βa). βa structure is more stable and energetically favoured due to the presence of linear hydrogen bonds, compared to the more distorted hydrogen bonds present in the parallel arrangement. When β-strands present some twist, the resulting β-sheets consequently become twisted, curled or backfolded. For these structures, torsion angles occupy a wide region in the Ramachandran plot, corresponding to the relative different structures, but typical values for an anti-parallel β-sheet are -139° and 135° for φ and ψ angles respectively. β-sheet forming peptides are common amongst LMWGs and typically form long stacks that give rise to fibrils, but one disadvantage is poor control over a defined length of the stack and its directionality.

1.2.3. Tertiary and quaternary structure

The tertiary structure is obtained when the peptide chain is able to fold trough loops and turns *via* intramolecular interactions (*e.g.*, hydrogen bonding, hydrophobic and electrostatic interactions, disulphide bonds) to reach a final three-dimensional arrangement. A quaternary structure is obtained when such forces and folds are stablished intermolecularly between different peptide chains. These concepts have been applied only limitedly in self-assembly, for instance to achieve coiled-coils that give rise to geometric structures [13] or to design planar β-propeller recombinant proteins, such as Pizza6, designed by Noguchi *et al.* [14]. β-propeller proteins are symmetric proteins, formed by six repetitive motifs of four β-sheet antiparallel organized around a central axis. Noguchi's group studied four W-containing Pizza derivative proteins whose crystals confirm the conservation of the structures and, in particular, Pizza6-AYW was identified as a perfect symmetrical β-propeller model (*Figure 1.10*, [15]).

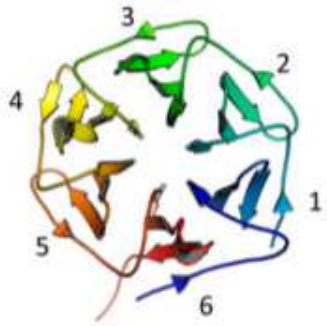

Figure 1.10.: Example of Pizza6 structure, adapted from [15] *© 2014, published on PNAS.*

1.3. Peptide self-assembly

1.3.1. Introduction

Molecular self-assembly is defined as the spontaneous and reversible process resulting from the self-organisation of simple building blocks into complex structures with a higher level of supramolecular order, and with well-defined properties. This phenomenon is widely applied by nature and it has been a source of inspiration for nanotechnologists to allow the construction of reversible structures [16].

Self-assembled systems are formed through the natural organisation of a high number of simple components linked together *via* weak non-covalent interactions. Self-assembled materials often are characterised by amphiphilic character due to the presence of both hydrophobic and hydrophilic regions, with examples in nature ranging from lipids, to peptides and proteins assembled together into extracellular matrix, membranes, cytoskeleton.

In peptide-based materials, amino acids are the building blocks combined to obtain the desired final self-assembled superstructures. Although the infinite possibilities for short peptide sequences

could be stimulating for the scientists on one side, they present a great challenge on the other side. For these reasons, a rational design is needed and begins with the accurate choice of the amino acids for the sequences to test. Indeed, in a short peptide sequence, the R side chain of each amino acid plays an active role that can dramatically affect the possibility to achieve a self-supporting system. Aliphatic hydrophobic residues furnish common hydrophobic surrounding conditions whereas aromatic ones can take an active role *via* π-π stacking, in which p-orbitals in π-conjugate systems generate basic interactions involved in peptide and protein folding. Hydrophilic residues, such as the hydroxide group or the amide of the peptide bond, are fundamental to form hydrogen bonds. The use of charged residues can also be used to favour (opposite charge) or to avoid (same-charge) ionic interactions and, consequently, self-assembly.

About 15 years ago, supramolecular peptide-based materials based on weak interactions raised doubts over their applicability due to limited stability and chemical resistance [17]. By contrast, over the last years, research started to focus on these systems as powerful biomaterials for several applications (*e.g.*, drug delivery systems, injectable matrices, cell culture scaffolds) [18].

1.3.2. Self-assembly driving forces

Self-assembly is a thermodynamically process managed to ensure to the final system a maximum degree of entropy due to the attenuation of the interactions between polar (*i.e.* water molecules) and non-polar molecules (*i.e.*, hydrophobic peptides molecules). Initially, water molecules in aqueous solution can transiently form hydrogen bonds with surrounding water or other polar molecules until a non-polar molecule is introduced into the system that acts as an ordering driver into the neighbourhood. When an amphipathic molecule is immersed in an aqueous solution its polar groups can establish dynamic hydrogen bonds with water molecules, disfavouring an order status achievement, while its non-polar part promotes its attainment. A final enhancement of the entropy of the whole system can be reached following the self-assembly of the amphipathic molecules involved, due to the reduction of the interactions between the water molecules and its non-polar portions.

Although the hydrophobic ensemble can furnish stability to the system, the presence of different stabilising factors to maintain the self-assembled structure is needed. In some conditions, simply energy given by heat (also at room temperature) is sufficient to disrupt the architecture of the superstructure in absence of other stabilising factors. In these cases, assembly and disassembly phases can be considered as a unique dynamic event.

Besides the hydrophobic interactions among the stabilising factors it is worthwhile to mention: *hydrogen bonds*, *electrostatic interactions*, *van der Waals forces*, *π-π interactions, halogen bonds*. *Hydrogen bonds* are characterised by a well-precise geometry resulted by the alignment of the

atoms of the hydrogen donors and acceptors involved, commonly nitrogen and oxygen atoms in peptides. *Electrostatic interactions* are observed between polar charged groups through connecting axes from positive to negative charge. A reduction of interactions number is easily understandable after the addition of salts in solution, because the ions from the salt can act as competitive counter-ions. *Van der Waals* forces can be noticed between two atoms close to each other and are oriented in a non-directional way. The two nuclei involved are attracting each other due to the transient electric dipoles originated by the surrounding electron cloud, only until the distance between them is higher compared to the sum of their Van der Waals radii. *π-π interactions* arise from the stacking of aromatic groups in the hydrophobic portion of the peptides due to the attraction between the π-electron clouds present on their surfaces. They can be classified based on typology as we consider the aromatic rings relative orientation (*e.g.*, parallel, parallel-displaced, edge-to-face orientations), which is influenced also by substituents, as described also by Hunter and Sanders [19].

Finally, *halogen bonds* have been only very recently exploited for peptide self-assembly, by exploiting iodine-substituted phenylalanine residues, which can interact with oxygen atoms or other halogen atoms or the aromatic ring, with specific orientations, as shown in *Figure 1.11* [20].

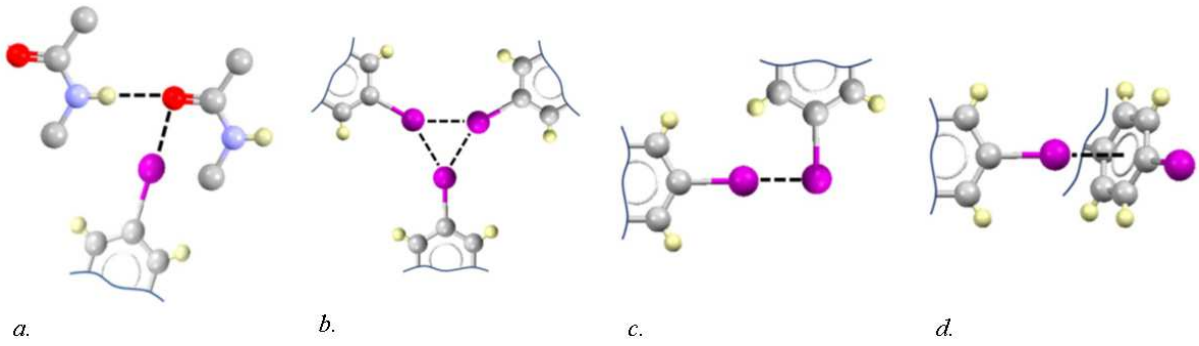

Figure 1.11: Halogen bonds in p-iodo-phenylalanine: orthogonal hydrogen and halogen bonds involving the carbonyl oxygen atom of the peptide bond (a.), type II iodine- iodine contacts (b.), iodine-π interactions (c.), triangular iodine synthon (d., adapted from [20] *© 2015 Creative Commons Attribution 4.0 International License.*

.

1.4. Type of self-assembling peptides

One of the early research groups to work on self-assembled short peptide sequences was Zhang's group [21] who for the first time proposed a classification of self-assembling peptides in four categories [22]. *Type I* peptides are self-assembling ionic complementary peptides characterised by their ability to form well-defined structures, such as β-sheets, in aqueous solution due the presence of both charged and neutral hydrophilic and hydrophobic residues, respectively. *Type II* peptides are able to self-assemble and disassemble in response to external change in the surrounding environment. An example is the dipolar DAR16-IV (ADADADADARARARAR) peptide that has a secondary

structure composed of β-sheets at room temperature and by α-helices at high temperature [23] and able to come back to β-sheet conformation only after weeks at room temperature. *Type III* peptides start to self-assemble in monolayers in the presence of an initial supporting surface that can be used to favour interaction with several molecules; they present a high potential for biomedical purposes. *Type IV* peptides or surfactant-like peptides have a hydrophilic head and a hydrophobic tail, which can have different levels of hydrophobicity (*Figure 1.12*). Another classification of peptides based on the structure of the monomeric units that allow the self-assembly is possible and it considers the amphiphilic peptides able to organise in different secondary structures.

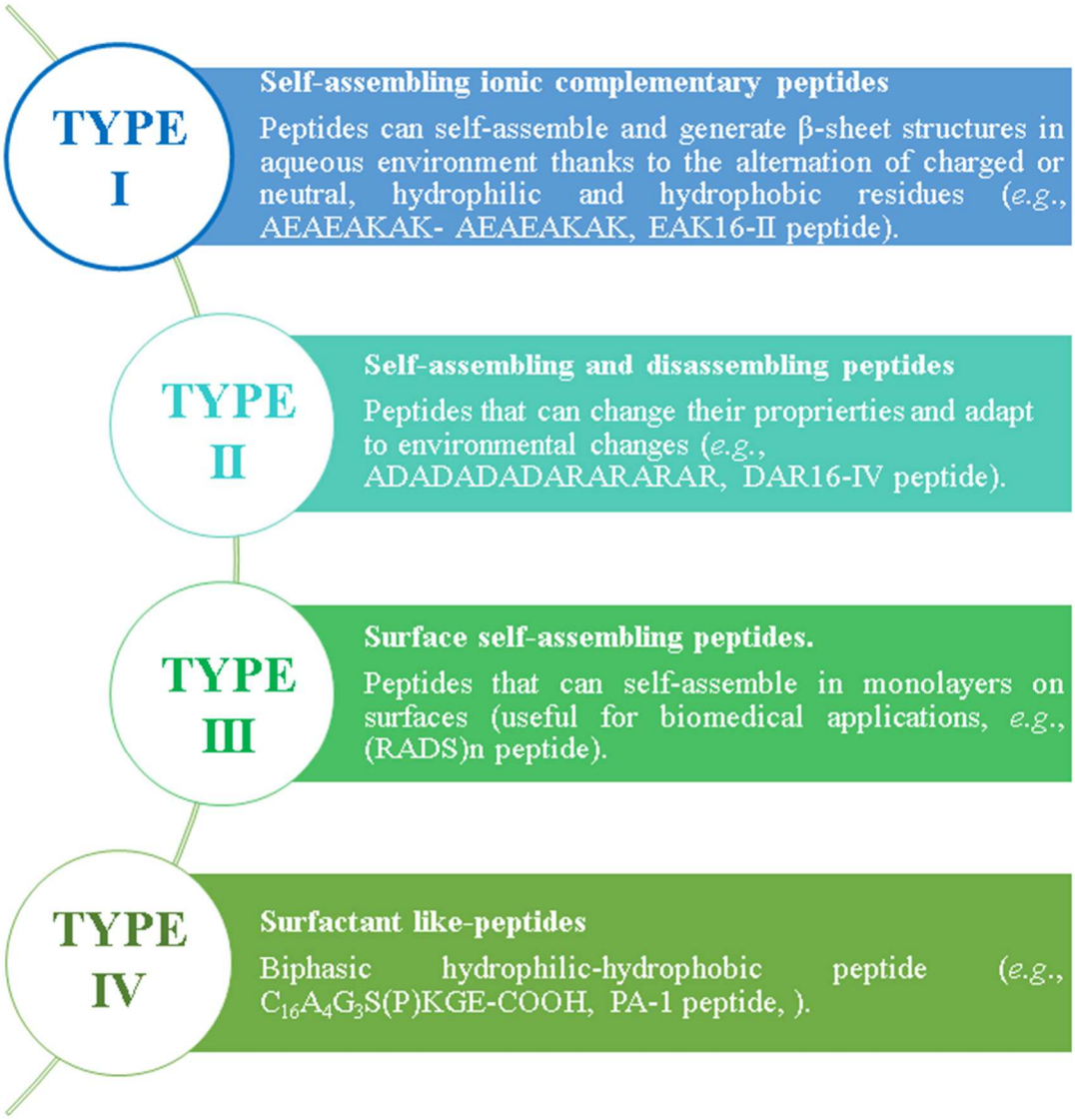

Figure 1.12: Zhang's Self-assembling peptide classification [21] .

1.4.1. Systems based on α-helical structure and coiled coil

As mentioned in section 1.2.2.1, α-helix is one of the most diffused secondary structure of peptides and proteins in nature. Woolfson's group largely studied the coiled-coil systems focusing on heptad (*i.e.*, 7 amino-acid repeating unit) *abcdef*, where *a* and *d* are hydrophobic residues, while the other residues are polar [24] (*Figure 1.13*). In a common α-helix, a turn is completed after 3.6 residues, hence the hydrophobic residues at 1st and 4th positions form a hydrophobic seam along the peptide chain. A coiled-coil oligomer is a quaternary structure achieved when two or more amphipathic helices assemble through their hydrophobic portions. Since the usual amino acids involved in inter-helix hydrophobic interactions are leucine repeated residues, these portions were called *leucine zippers*.

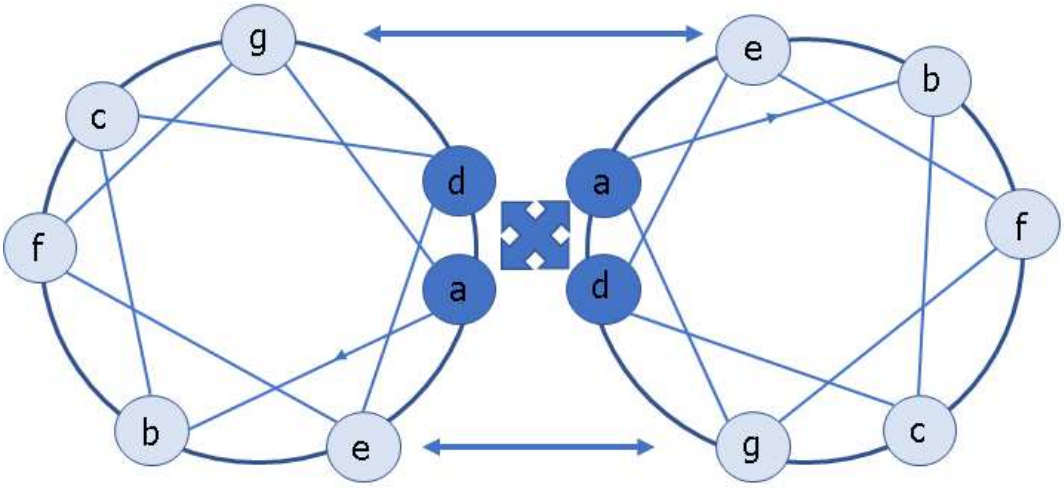

Figure 1.13: Formation of a heptad dimer due hydrophobic interactions between a and d residues [24].

Woolfson *et al.* designed a system of a linear peptide made by 28 amino acids in which the *a* and *d* hydrophobic residues in each heptad were able to interact each other and create a hydrophobic core, whereas the two polar residues in *e* and *g* positions were coupled *via* electrostatic interactions. The amino acidic sequence of the peptide was chosen to let charged sticky ends free to accept more coiled coils and to extend the length of the fibril. The charged outer portion of fibrils surface favoured lateral fibril association.

1.4.2. Ionic complementary peptides

In these peptides, the self-assembly mechanism is possible thanks not only to hydrogen bonding and hydrophobic interactions, but also to electrostatic ones generated by the alternation of positively or negatively charged, and neutral, amino acids. These systems are very attractive because they also allow the addition of different functionalised motifs at the peptide termini with consequent modifications of the system final properties. The self-assembly process can be affected by several

factors, such as the peptide sequence, concentration, pH and salts, but mostly their amphiphilic character is the direct cause that drives the formation of β-sheet secondary structures. Boden et al. classified the hierarchical assembly of β-sheet peptides into tapes, ribbons, fibrils, and fibres [25] (*Figure 1.14*).

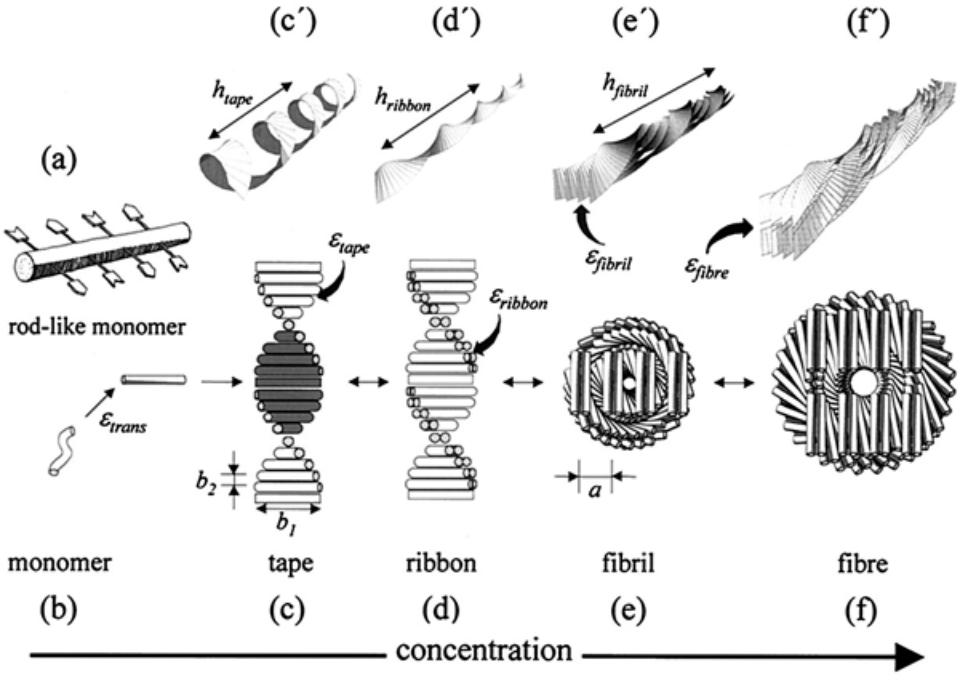

Figure 1.14: Hierarchical formation of peptide fibres, adapted from [25]*, © 2001 National Academy of Sciences..*

1.4.3. Systems based on β-hairpin structure

β-hairpin structure is composed by two β-strands connected *via* a short turn, as described by Pochan and Scheineder's groups [26]. They designed a series of peptides (*e.g.*, MAX series) able to fold into β-hairpin structures only after a trigger by an external source (i.e. pH, temperature, ionic strength, light, enzymes). The 20-residue peptide featured a short turn composed by 4 residues (VpPT, where V is valine, p is D-proline, P is proline, T is threonine). Proline is often involved in β-turns because its ring structure introduces a kink in the peptide chain. The addition of D-proline further promotes the formation of hairpin-like structures. Importantly, it was noticed that the presence of alternate valine (hydrophobic) and lysine (hydrophilic) residues led to the formation of respectively a hydrophobic and a hydrophilic face after the folding. Successively, the β-hairpins self-assembled into larger fibrillar aggregates *via* hydrogen bonding and hydrophobic interactions due to the interactions between neighbouring β-hairpins. It was possible to create a well-organised nanostructure that corresponds to hydrogel formation at the macroscale (*Figure 1.15*). Moreover, the authors were able to control the pH responsiveness of the self-assembly by modifying the global charge of the molecules by substituting specific residues.

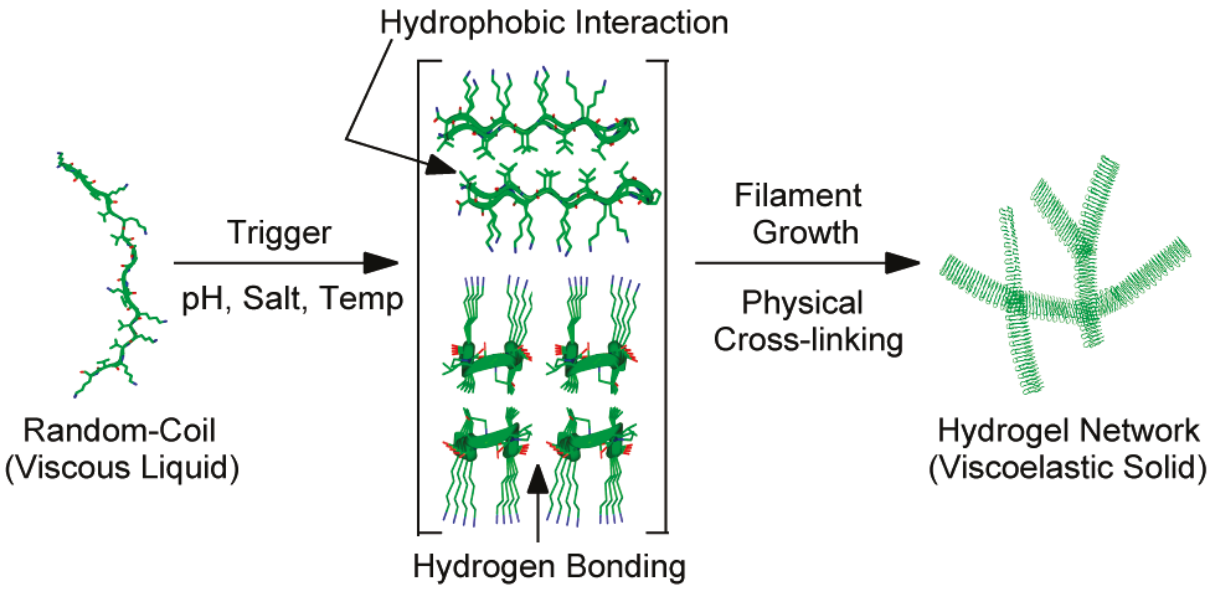

Figure 1.15: Peptide folding and self-assembly mechanism through formation of β-hairpin structure, adapted with permission from [27], *© 2009 American Chemical Society.*

1.4.4. Surfactant like-peptides

Surfactant molecules are formed by two portions, a polar head and a hydrophobic tail. Surfactant like-peptides present a hydrophilic peptide sequence attached to a hydrophobic aliphatic chain, as designed in Stupp's group [28]. Thanks to a pH triggered self-assembly, the selected peptide amphiphile (PA-1) containing four cysteine residues, three glycine residues, a phosphorylated serine residue and a final promoting cell adhesion RGD sequence (Arg-Gly-Asp) was able to self-organise into a cylindric shape structure in which peptide segments were on the surface and alkyl tails inside. Several studies about the influence of the peptide sequence and the alkyl chain length were performed by the group (*Figure 1.16*).

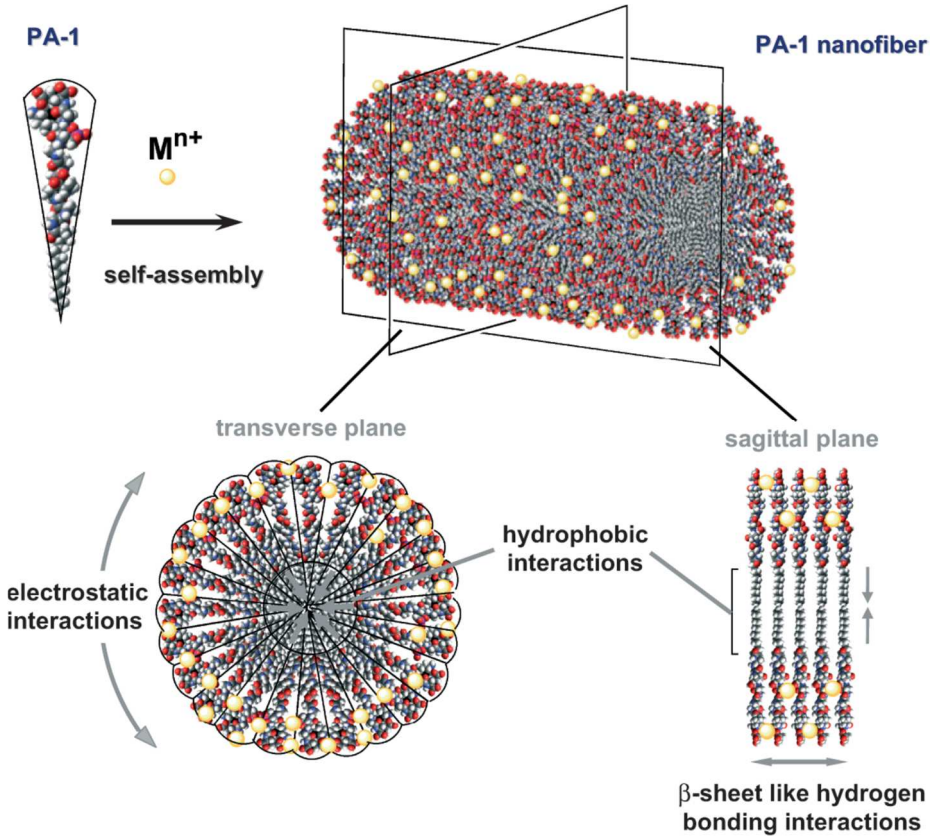

Figure 1.16 Scheme of surfactant-like peptide assembly (PA-1), adapted from [28]*, © 2006 John Wiley and Sons.*

Zhang's group synthesised peptides (hepta- or octa-peptides) composed of a charged head and a neutral tail that were able to operate as a surfactant, forming nanotubes and nanovesicles with diameters between 30 and 50 nm (*Figure 1.17*) [29].

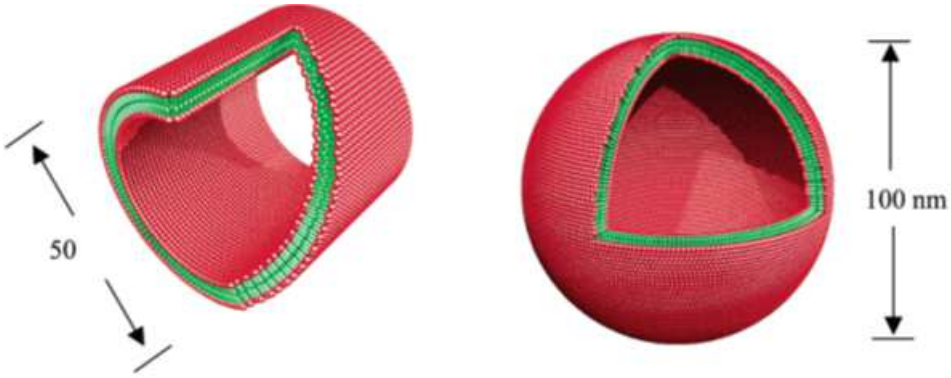

Figure 1.17: Nanotubes (left) and nanovesicles (right) molecular models formed by surfactant-like peptides (in green glycine tails, in red negative charged heads), adapted with permission from [29]*, © 2002 American Chemical Society.*

1.4.5. Systems based on aromatic interactions

The use of short aromatic peptides was studied with the final aim to obtain organised self-assembled structures. In a peptide system, the aromatic moieties can be included either by aromatic amino acid side chains or by adding selected groups to the peptide chain. These groups interact

through π-π interactions that provide order and increases stability to direct the self-assembly process. Gazit's group focused their studies on short aromatic dipeptide, a diphenylalanine (FF, present in Alzheimer's β-amyloid peptide sequence) able to self-assemble into nanotubes [30] after the dissolution of the peptide in organic solvent and successive solvent evaporation. Moreover, after the addition of fluorenylmethoxycarbonyl (Fmoc) group at N-terminus it was noticed the formation of anti-parallel β-sheets thanks to π-π interactions of the Fmoc groups [31][32]. Nanospherical structures were obtained *via* self-assembly also for other aromatic dipeptides, such as for diphenylglycine, or the tripeptide CFF (where C is cysteine), for this latter the hypothesis was that the formation of disulfide bridges drove the closure of the 2D-layers into tightly packed spherical structure [33] (*Figure 1.18*).

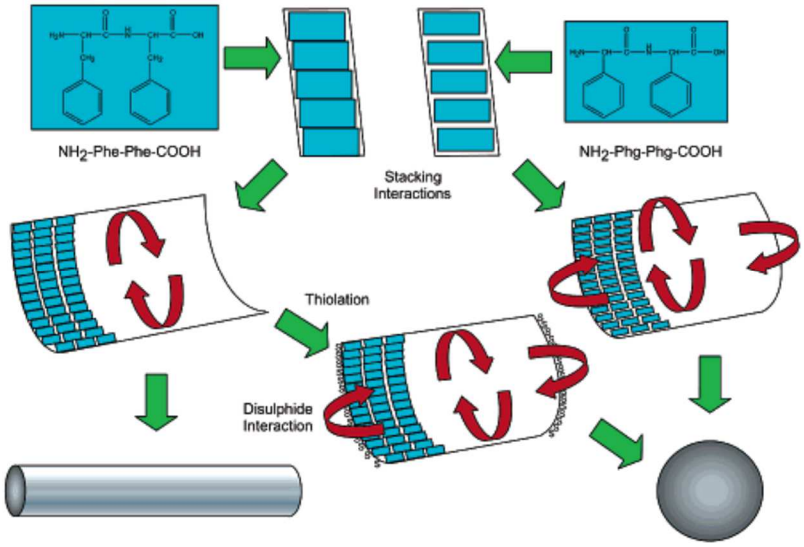

Figure 1.18: A model of tubular and spherical peptide nanostructure self-assembly: in the first case, the closure of the extended sheet occurs along one axis of the two-dimensional layer whereas in the second case the closure of the sheet happens along two axes, the latter could be assisted thanks to the introduction of a thiol group, reprinted with permission from [33]*, © 2004 American Chemical Society.*

Ulijn's group extended the investigation on short aromatic dipeptides and tripeptides, considering the introduction at the N-terminus of naphthalene or benzyloxycarbonyl groups [34][35]. Later, further studies showed that the Fmoc groups operated as zipper between the anti-parallel β-sheets, giving a twist to the structure. Ulijn *et al.* noticed also how the pH can affect the self-assembly process for Fmoc-FF: the gelation process at high pH was due to the entanglement of flexible fibrils whereas at lower pH the gel formation did not occur because rigid ribbon structures were observed. Gels derived from Fmoc-FF were tested for different applications, such as cell culture [36] and drug delivery [37].

1.5. Factors affecting self-assembly

1.5.1. Peptide sequence

The amino acid sequence of a peptide can play an active role to determine its final secondary structure and properties, whereby the chemical nature (*e.g.*, hydrophilic or hydrophobic) of each side chain plays a role. The charge distribution can directly affect the self-assembly process for an ionic complementary peptide. Hong's group reported that, for pH values between 4 and 11, EAK16-II peptide (*i.e.*, AEAEAKAKAEAEAKAK) self-assembled in fibrillar structures, whereas, at near neutral pH condition (6.5-7.5), the EAK16-IV peptide (*i.e.*, AEAEAEAEAKAKAKAK) formed globular structures [38]. When the pH presented values lower than 6.5 or higher than 7.5, EAK16-IV was able to switch from the globular to a fibrillar structure (stacked β-sheet). To rationalise EAK16-IV behaviour, it was hypothesised that at neutral pH electrostatic interactions were established between E (glutamic acid) and K (lysine), with the consequent formation of a hydrophilic core and a hydrophobic surface exposed to the solvent, leading the peptide to self-assemble in a globular structure. Since the peptide chains were straightened at non-neutral pH due to the absence of electrostatic interactions, then, fibre formation was observed.

Dobson's group reported that KTVIIE peptide formed β-sheet structures at pH 2.6, whereas KTV**L**IE and KTVI**Y**E formed random coils (where T is threonine, V is valine, I is isoleucine, Y is tyrosine) [39]. The ionic-complementarity between K and E and the hydrophobic interactions of the middle residues led to the formation of antiparallel β-sheets in the former case. Considering that leucine was less hydrophobic compared to isoleucine, in the case of KTVLIE peptide, the interactions were weaker and random coil structure formation was observed, instead of β-sheets. Furthermore, the aromatic interactions between tyrosine residues of different KTVIYE peptide molecules could not favour the formation of β-sheet structures.

1.5.2. Concentration

Concentration of the peptide plays a direct role affecting how the self-assembly can occur. The peptide molecules are dispersed in solvents below a critical aggregation concentration (CAC), whereas when CAC is reached, they start to organise in aggregates. Chen's group focussed their studies on the concentration effect on self-assembly of EAK16-II peptides using several techniques [40], such as light scattering and atomic force microscopy (AFM). They started from an analogy between the CAC and the critical micelle concentration (CMC), that is directly correlated to surfactant molecules properties and their ability to assemble in micelles excluding hydrophobic tails from direct contact with polar solvents. They built a two-phase model: in a first phase, the peptide monomers can self-assemble forming globular or filamentous protofibrils of β-sheet structures depending from

peptide concentration, in a second phase, for concentration values above the CAC, the protofibril can associate into fibrils or bigger globules. Studies on EAK16-II showed that high peptide concentration can affect the length and not the width of the fibrils.

1.5.3. pH

The ionisation state of peptides and protein in a certain environment is directly correlated to its pH, which is a fundamental parameter to take into account in experimental procedures. Indeed, charged amino acids play an active role through hydrogen bonding and electrostatic interactions to stabilise the peptide final conformation. In addition to the Hong's group research previously reported, another study about the effect of pH was conducted by Boden's group [41] on QQRFQWQFEQQ (P_{11}-II) peptide assembly (where Q is glutamine, R is arginine, W is tryptophan). Below pH 5, only arginine was positively charged and the formation of stable nematic gels (*i.e.*, a liquid-crystal gel arranged in linear parallel lines) was possible thanks to the stabilisation of the fibrillar dispersion. Above pH 5, when also the γ-carbonyl group of glutamic acid was negatively charged, the peptide was globally neutral, and flocculation occurred. Thanks to other experiments conducted on another peptide QQRFQWQFQQQ (P_{11}-III), it was noticed that the stabilisation of dispersed fibrils happened when a positive or negative charge of one unit per peptide molecule was present.

1.5.4. Salts

The presence of salts, their concentration and valency, can have direct effects on the solubility, stability, conformation, activity and self-assembly of several biological molecules. When salt ions are present in a peptide solution, they screen charges with a consequent reduction of the interactions between peptide molecules. This renders the peptide more hydrophobic/less hydrophilic and acts directly on the modes of self-assembly. According to the DLVO (Derjaguin-Landau-Verwey-Overbeck) theory [42][43] (which elucidates the aggregation of aqueous dispersions and delineates the role of the forces between charged surfaces that interact via a liquid medium), the combination of the electrostatic repulsions and the van der Waals attractions between amino acids of the same and opposite charge, respectively, are fundamental to understand how salts can favour self-assembly. When the kinetic barrier created by the electrostatic repulsion forces is reduced thanks to the screening of electrostatic repulsive charges, the non-covalent attractive forces can act and start to drive the self-assembly process.

Studies on the salt effect on peptide self-assembly were performed by Chen's group [44], who investigated the effect of the presence of sodium chloride (NaCl) on the self-assembly of EAK16-I peptide (*i.e.*, AEAKAEAKAEAKAEAK). It was noticed that salt addition promoted the formation

of peptide fibrils at low peptide concentrations, thanks to a screening effect of the peptide charges. However, it also increased the peptide concentration required for a transition from fibrils to fibres. In the case of EAK16-II (*i.e.*, AEAEAKAKAEAEAKAK), Zhang *et al.* reported that different cations can influence differently the self-assembly [45]. In this study, it was noticed that the monovalent cations promoted self-assembly and the related nanostructure formation decreased with the reduction of hydrated radii $Li^+ > Na^+ > K^+ > Cs^+$. Also Carrick, Aggeli *et al.* studied the responses to different pH triggers for P_{11} peptides series [46] and how the salt concentrations can be exploited to manipulate the self-assembly process in physiological conditions and potential *in-vivo* applications.

1.5.5. Enzymes

It is possible to take advantage of enzymes and their ability to drive assembly or disassembly of peptide-based hydrogels thanks to their high selectivity and possibility to work in mild conditions (37°C, pH between 5 and 8). Guilbald *et al.* were able to self-assemble FEFK peptide through reverse-hydrolysis mechanism reaction [47]. Initially, partial hydrolysis of the peptide into FE and FK dipeptides occurred. Over time, reverse hydrolysis was observed with the formation of tetra-, hexa-, octa- and decapeptides. Thanks to their ability to self-assemble in fibrils, the octapeptides (FEFKFEFK and FEFEFKFK) were the thermodynamically favoured products.

Laromaine *et al.* developed a Fmoc-protected peptide functionalised nanoparticle using thermolysin enzyme [48]. In the self-assembled Fmoc-GFC-NH_2 peptide, the cysteine could anchor gold nanoparticles and after the enzymatic cleavage of the G-F portion, the hydrolysis caused the disassembly of the system. The disassembly occurred because of the removal of hydrophobic interactions between Fmoc groups and the electrostatic repulsions between the particles bound NH_3^+ groups. The dispersion of the gold nanoparticles can be evaluated *via* UV-Vis absorbance measurements.

1.5.6. Temperature

Temperature can have different effects on peptide self-assembly: the process can be favoured or disfavoured at high temperature, and heating may lead to conformational modification. Pochan *et al.* synthesised a peptides series (MAX series) able to reversibly assemble and disassemble at different temperatures. Heating led to dehydration of non-polar residues and triggered the peptide to fold after a hydrophobic collapse. Self-assembly temperature-control can be operated simply through modifications of hydrophobic amino acidic residues in the peptide sequences. This approach opens the door to self-assembly thermo-control in several applications.

1.5.7. Light-activation

The use of light can be employed to trigger self-assembly for biomedical applications. Haines *et al*. investigated in detail a peptide of the MAX series able to self-assemble into a hydrogel after UV irradiation [30]. Two peptides were synthesised: MAX7 (VKVKVKVKVDPPTKVKCKVKV) and MAX7CNB. In the latter, the cysteine residue present in the sequence was protected by a photoactive group (*α-carboxy-2-nitrobenzyl*, CNB) that had a negative charge at pH 9 and located in the hydrophobic face of the peptide. The UV irradiation, and the subsequent photoactive group removal, left the peptide without charge on the hydrophobic side, thus promoting hydrophobic interactions and triggering the self-assembly. CD analysis showed that MAX7CNB presented random coil structure at pH 9, while after the CNB removal the peptide was able to self-assemble in β-sheets.

1.6. Applications of self-assembling peptides

1.6.1. Tissue engineering

Tissue engineering is defined as a discipline in which science and engineering are combined to replace, repair or generate tissues or organs [49]. One of the possible approaches of tissue engineering involves the isolation of specific cells from the body, the succeeding tissue growth *in vitro* or *in vivo* to replace a damaged tissue [50][51]. Another tissue engineering strategy contemplates the use of artificial scaffolds able to mimic the natural environment (*i.e.*, the extracellular matrix) to favour the tissue growth directly *in situ*. The efficiency of this second approach is directly correlated to the chemical and mechanical properties of the scaffold and to the cell-scaffold and surrounding-environment interactions. A novel potential use of tissue engineering concerns the direct injection of healthy cells or of a mixture of cells and viscous solution of a hydrogel into defect sites *in vivo*. Tissue engineering can also be applied for non-clinical purposes. In this latter case, cells are cultured to obtain multicellular structures useful for drug development and testing [52].

The ability of peptides to self-assemble into hydrogels places them in a prominent position within the potential materials for tissue engineering applications. Many studies were conducted to confirm that self-assembling peptide gels can be used for cell culture for different cell lines (*e.g.*, neuronal [53], osteoblast [28], endothelial cells [54]). The success of peptide-base hydrogels as scaffold is due to their biocompatibility, biodegradability and several biological functionalities that can be introduced for specific applications. The self-assembled systems formed by EAK16-II and RAD16-II were shown as potential scaffolds for growing mammalian cells such as mouse fibroblast, bovine aortic endothelial cells, human foreskin fibroblast due to the fine cell attachment and proliferation compared to tissue culture dishes [55].

An example of a sequence already present in nature combined with another motif to form a mixed system concerned the case of the incorporation of ALK peptide motif (ALKRQGRTLYGFGG) attached to RADA16 peptide to enhance cell growth and proliferation [56].

Xie *et al.* [57] mixing RADA16 and RGDA16 peptides were able to build a new scaffold system to earmark to the attachment, spreading and proliferation of pre-osteoblasts. RGDA16 was not able to form a gel at the required concentration, but it did so only after mixing with RADA16. The new mixture system showed promising results in terms of initial attachment and proliferation of cells compared to RADA16 scaffold alone, thanks to the recognition of RGD sequence by the cell integrin receptors and the consequent improved proliferation [58]. Recently, Marchesan's group developed a heterochiral short peptides series (FxF series, in which x is a D-aliphatic hydrophobic amino acid) able to form hydrogels that present high cell viability and do not show evident signs of cytotoxicity *in vitro* on mouse fibroblasts as potential scaffolds [59].

1.6.2. Drug delivery

Drug delivery systems (DDS) are devices able to entrap and to release specific drug molecules in appropriate conditions. These carriers act by protecting the drug molecule from degradation and enzymatic modifications, and by maintaining the drug physical and chemical properties unaltered until the target is reached for drug release. However, problems such as poor solubility of the drug or the transportation through biological barriers need to be overcome. A good cell penetration is observed for viral based drug delivery systems, although the problems relative to the safety limited their use. For non-viral systems such as liposomes or polymeric carriers the safety issue is not present, but cell penetration ability is considerably reduced.

It was noticed that amphiphilic peptides can assemble and incorporate hydrophobic molecules increasing their solubility in aqueous environments, leaving the hydrophilic face on the outside portion of the final system. The ability of peptide-based hydrogels to load and release the drug can be manipulated by adjusting the amino acidic sequence and the chain length properly.

Scheneider's group demonstrated that MAX1 and MAX8 peptide hydrogels were able to encapsulate and to release biomolecules [60]. The release of the model drugs tested (*i.e.* lactoferrin and dextran molecules) was influenced by the hydrogel network size and electrostatic interactions between the hydrogel and the drug molecules. The mesh size of the hydrogel, monitored by peptide concentration and peptide sequences, was used as a tool to control the diffusion of the drug. Also, the electrostatic interactions between the hydrogel network and molecules can affect the releasing rate, indeed negatively charged dextrans can interact more with more electropositive MAX1 ($^{+9}$) than with

MAX 8 ($^{+7}$) and their diffusion were limited. In the case of lactoferrin (positively charged) the electrostatic repulsions between the protein and the peptide network led to a faster release.

Sutton *et al.* conducted their studies on Fmoc gels composed by just one aromatic amino acid [37]. Fmoc-Y formed a strongly bonded and ordered filaments system compared to lower persistence length and less stable filaments in Fmoc-F system. The hypothesised mechanism of dye molecules diffusion was based on the ability of the network to break and to reform itself. Marchesan's group proposed the use of short hydrophobic heterochiral tripeptide (lFF, where l is D-leucine) to vehiculate and to release the hydrophobic antibiotic ciprofloxacin [61] and anti-inflammatory drugs equipped with aromatic rings such as naproxene and ketoprofen [62].

2.AIM OF THE PROJECT

2.1 Aim of the project

Peptide self-assembly has attracted the attention of multi-disciplinary research groups thanks to the potential applications of the resulting biomaterials, thanks to their inherent biocompatibility, biodegradability and biofunctionality. Self-assembly is defined as the spontaneous process through which a monomer (a short heterochiral tripeptide in this project), is able to self-organise *via* non-covalent interactions into a final 3D well-ordered structure. The amphiphilicity nature of a peptide is a necessary, but not sufficient, condition to manage its self-organisation. Understanding the assembly mechanisms could allow the development of new tools to build a rational design for complex nanostructures (*e.g.*, physical hydrogels with multiple components in a hierarchical structure) [63].

Nevertheless, general design rules are almost missing and a large part of LMWG are discovered by serendipity or modifying established gelators [64]. The focus on extremely short peptide sequences is due to their economic and large scale potential production [65]. Previously, it was discovered that fluorenylmethyloxycarbonyl (Fmoc) dipeptides were able to form hydrogels during studies performed of D-Ala-D-Ala motif normally present in bacterial cell wall by Zhang's group [66]. One of the most studied Fmoc-dipeptide systems is based on Fmoc-FF [67]: Ulijn *et al.* selected several Fmoc-dipeptide derivatives considering various degree of hydrophobicity of the sequence and found that Fmoc-FF was able to form stable hydrogels [68], whereas Gazit *et al.* explored different capping moieties on N-terminus (Fmoc, Boc, Benzyloxycarbonyl or Z).

Lately, the research focus moved to peptide hydrogels made by natural, unmodified amino acids as building blocks without the use of organic solvents, characterised by a relevant flexibility. Already in 2003 very short sequences were tested by Gazit considering the aromatic motif D-Phe-D-Phe, but exploiting also the FW, WY, WF, WW motifs. Thanks to that study, Gazit's group noticed that nanotubular structures were obtained from ff, FF and FW peptides [30]. Moreover, Zhang *et al.* observed that WF nanoparticles were able to shift the peptide intrinsic fluorescence signal from the UV to Vis range, opening the way to their potential use in imaging and as sensing probes [69].

To find new unprotected tripeptide sequences able to self-assemble in hydrogels, computational tools such as quantum chemistry, atomist molecular mechanics, coarse-grained molecular mechanics are becoming valuable tools [70], [71]. In particular, inspiration for this project came from Frederix *et al.*'s study that involved a computational assessment of the aggregation propensity (AP) of all the 8,000 possible combination of natural tripeptides [72] (*Figure 2.1*). Coarse-grained molecular dynamics analysis showed a weak correlation between the AP and the hydrophilicity of the tested sequences, proving that only hydrophobicity does not drive organised self-assembly. Despite the great efforts, unfortunately Frederix and co-workers identified only 4 hits

out of 8,000 of unprotected L-tripeptides (KYF, KYY, KFF, KYW) able to self-assemble into hydrogels.

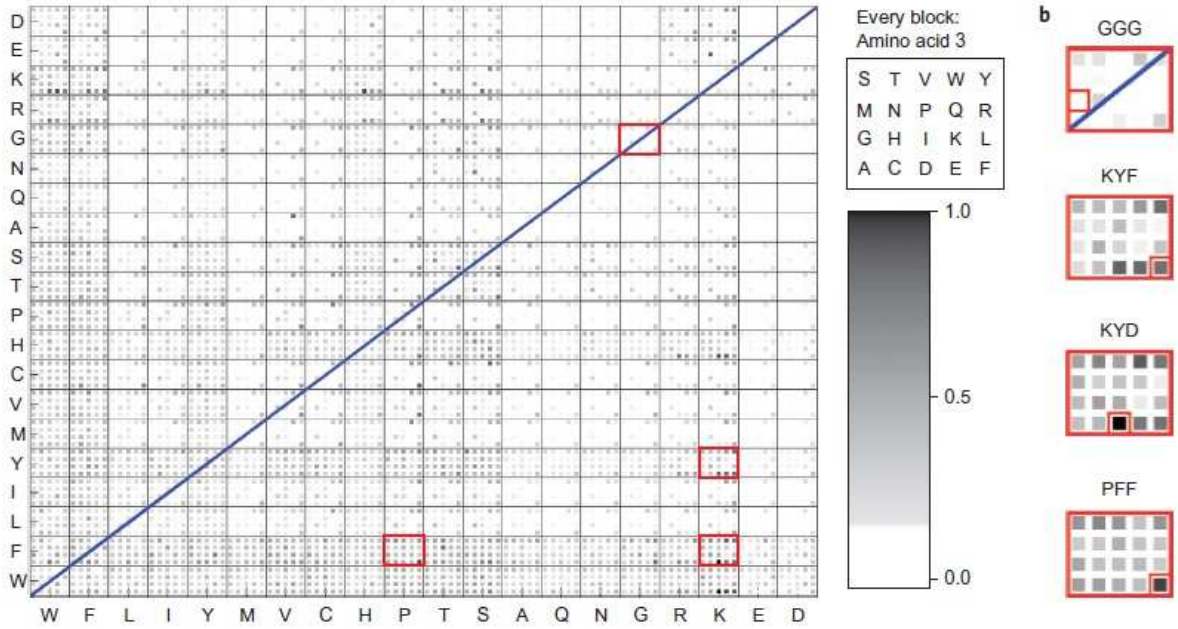

Figure 2.1: Normalized AP_H score for all 8,000 combinations of tripeptides after a 50 ns simulation. In each rectangle, the third amino acid is represented by the position of the coloured square at the locations indicated in the legend on the right, darker shade indicates a larger degree of aggregation, adapted from [7] *©2015 Springer Nature and Copyright Clearance Center.*

For this project, the first AP score top 20 sequences resulting from Frederix *et al.*'s simulations were chosen, and the N-terminus was replaced with its corresponding D- enantiomer amino acid. Sequences containing sulfur atoms were excluded, due to their particular reactivity, leaving 16 candidates for this study. The 16 heterochiral D-L-L tripeptides have been synthesised, characterised and tested with the purposes to identify self-assembling sequences and eventually the principles underlying the latter (*Table 2.1*).

No.	Selected L-L-L sequences		D-L-L analogs
1	PFF		pFF
2	WFL		wFL
3	MFF		mFF*
4	VFF		vFF
5	FFM		fFM*
6	FWF		fWF
7	FFF		fFF
8	WWF		wWF
9	FWI		fWI
10	FYI		fYI
11	VFW		vFW
12	PWF		pWF
13	IFF		iFF
14	LCF		lCF*
15	WLL		wLL
16	SFW		sFW
17	IFW		iFW
18	WFF		wFF
19	FFW		fFW
20	IMW		iMW*

*Table 2.1: Tripeptide sequences chosen for this project (*excluded sequences).*

3.RESULTS AND DISCUSSION

3.1. Peptide preparation

3.1.1. Peptide synthesis

Sequence (one-letter code)	Sequence (three-letter code)	Structure
fYI	**D-Phe-L-Tyr-L-Ile**	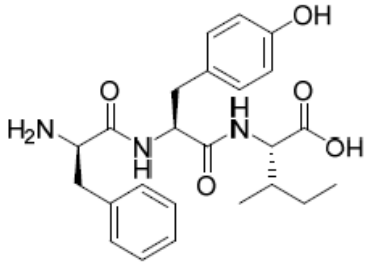
pFF	**D-Pro-L-Phe-L-Phe**	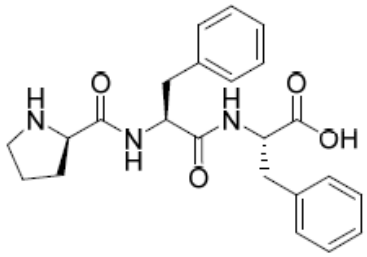
vFF	**D-Val-L-Phe-L-Phe**	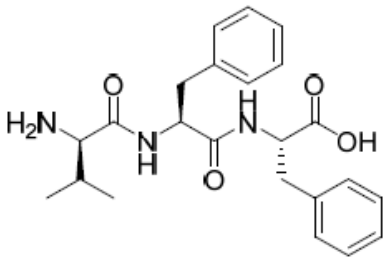
iFF	**D-Ile-L-Phe-L-Phe**	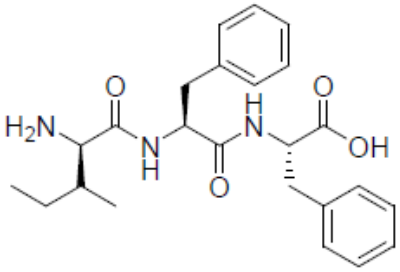
fFF	**D-Phe-L-Phe-L-Phe**	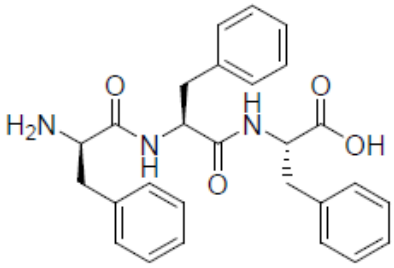

sFW	**D-Ser-L-Phe-L-Trp**	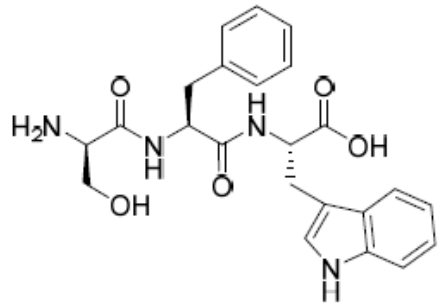
vFW	**D-Val-L-Phe-L-Trp**	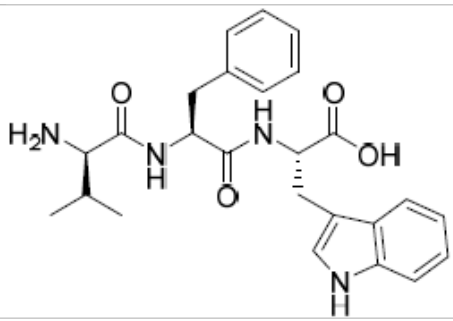
iFW	**D-Ile-L-Phe-L-Trp**	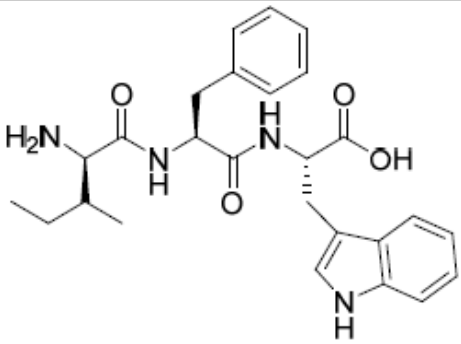
fFW	**D-Phe-L-Phe-L-Trp**	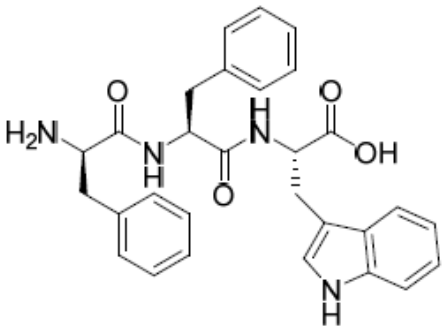
pWF	**D-Pro-L-Trp-L-Phe**	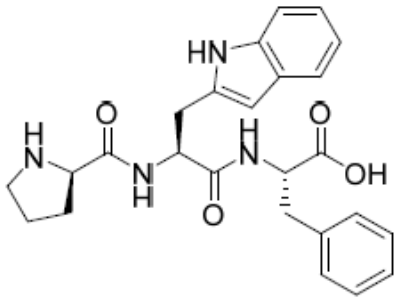

fWI	**D-Phe-L-Trp-L-Ile**	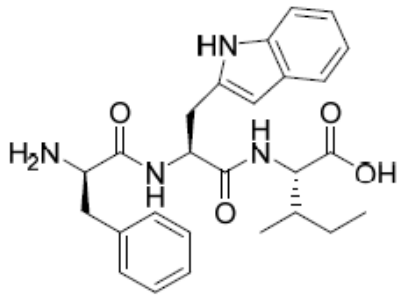
wLL	**D-Trp-L-Leu-L-Leu**	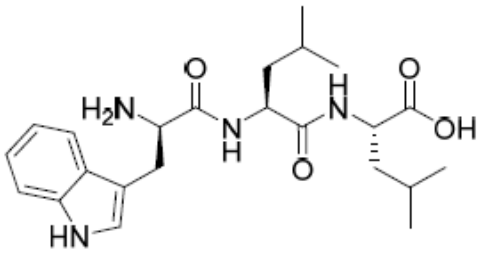
wFL	**D-Trp-L-Phe-L-Leu**	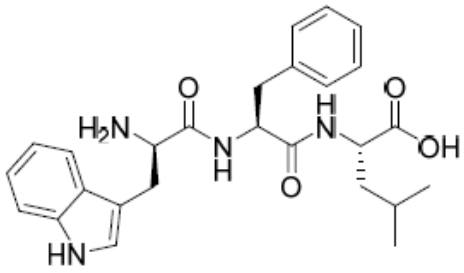
fWF	**D-Phe-L-Trp-L-Phe**	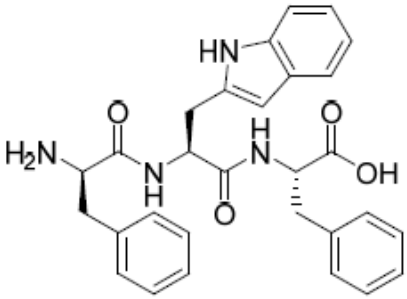
wWF	**D-Trp-L-Trp-L-Phe**	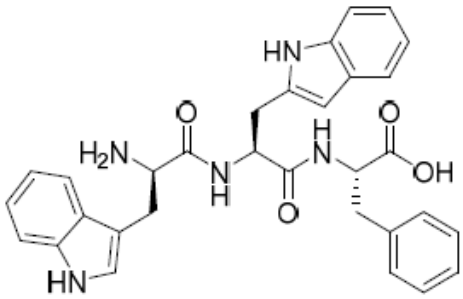
wFF	**D-Trp-L-Phe-L-Phe**	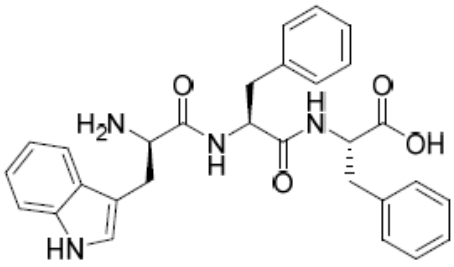

Table 3.1: Selected peptides synthesised in this project.

All the selected peptides (*Table 3.1*) were synthesised according to the Fmoc-based solid-phase peptide synthesis (SPPS) method via *O*-(Benzotriazol-1-yl)-*N,N,N′,N′*-tetramethyluronium hexafluorophosphate (HBTU) activation and with 1-Hydroxy-7-azabenzotriazole (HOAt), using 2-2-Chlorotrityl Chloride resin as solid support. Synthesis reactions were performed in specific peptide vessels so as to remove easily the exceeding compounds through filtration, since the forming-peptide is anchored to the resin (*Figure 3.1*).

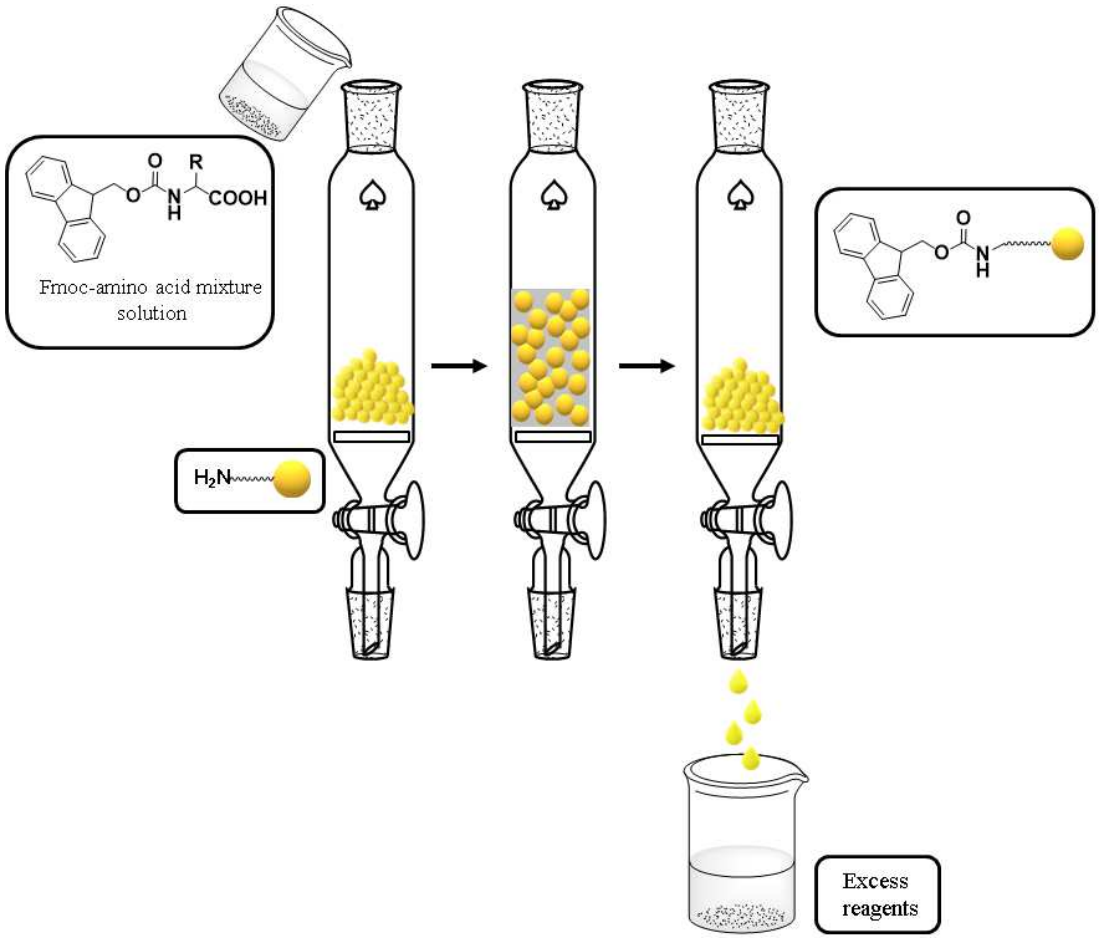

Figure 3.1: Schematic representation of coupling step during the synthesis.

It should be noted that SPPS is not at all efficient relative to Liquid Phase Peptide Synthesis (LPPS), considering the use of reagents in large excess and the vast amount of solvents required during the filtration steps. However, SPPS has a number of advantages over LPPS. Firstly, SPPS reduces the time of washing steps and side reactions (*e.g.*, diketopiperazine formation). Secondly, it can be conveniently monitored by colorimetric tests at each step. Thirdly, purification is far more convenient also for the unexperienced chemist.

After the loading of the first amino acid and the following deprotection of its Fmoc-group at N-terminus position, *coupling* reactions of two more amino acids were performed, each of them followed by protecting group removal. The completion of each synthesis step was monitored by two colorimetric tests: acetaldehyde/chloranil and bromophenol blue tests, able to detect primary amines

(and also secondary amines in the case of acetaldehyde/chloranil test) due to the intense colour formation of few beads of resins after the reaction with specific reagents.

At the end of the synthesis, the cleavage of the tripeptide from the resin was performed, according to the characteristic of the resin (*i.e.*, 2-chlorotritylchloride resin), with a mixture of trifluoroacetic acid and dichloromethane (TFA-DCM, 49.5-49.5%) and very low quantity of water and triisopropylsilane (H_2O and TIPS, 0.5%-0.5%) acting as scavengers (*Figure 3.2*).

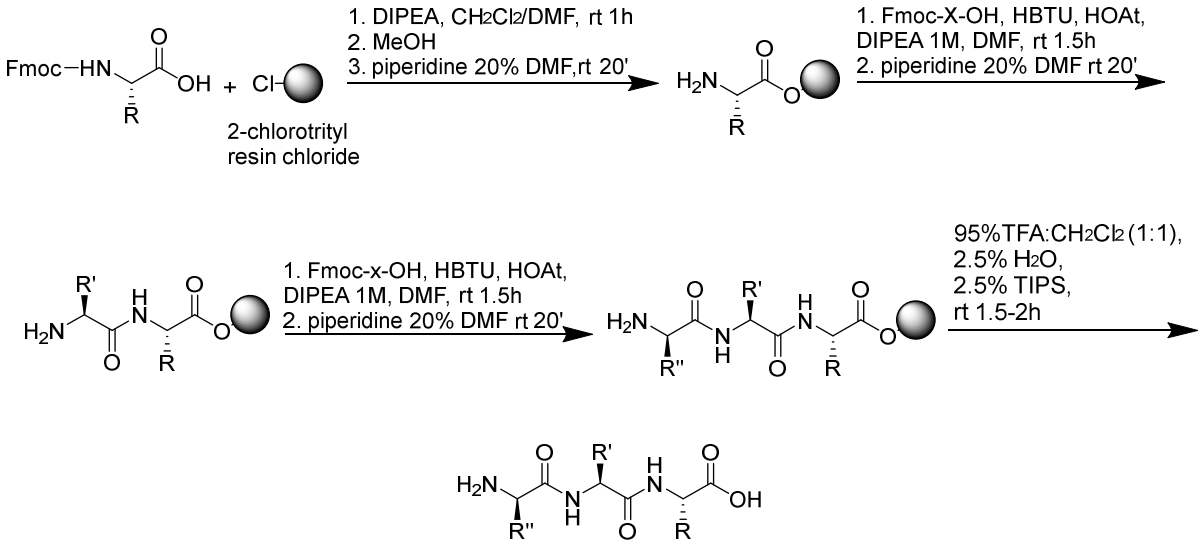

Figure 3.2.: Solid phase peptide synthesis scheme for heterochiral tripeptides (DLL).

Synthesis products were carried out using reverse-phase High Performance Liquid Chromatography (HPLC), considering a gradient of Acetonitrile/Water (MeCN/ H_2O) with 0.05% of TFA. All the peptides were then freeze-dried, and fluffy dry powders were obtained.

3.1.2. Peptide characterisation

All the synthesised peptides were characterised using ^{1}H- and ^{13}C-NMR, and ESI-MS analyses, confirming their identity and purity. A typical ^{1}H-NMR peptide spectrum presented specific regions of interest at different ppm values. At low fields, it was possible to identify the signals of amine protons of N-terminus and amide bonds (~8-9 ppm) and aromatic protons (~7-7.5 ppm), followed by the signals of the hydrogen atoms bound to α-carbon atoms (3-5 ppm), while at higher fields, the signals of hydrogen atoms bound to β, γ, and δ carbon atoms were detected. ESI-MS spectra showed for all the peptides the molecular ion peak (all spectra and details are provided in Supplementary section).

3.1.3. Synthesised peptides

The synthesised peptides were 16, excluding the sulfur-containing ones, of the AP score top-20 sequences resulting from the simulations of Frederix's project, with a D-amino acid at N-terminus of the sequence. Considering the structures of the amino acids present in the tripeptides, they were divided into three groups based on the aromatic amino acids, for ease of further investigation: xFF group (without W or w), xFW group, and xXX group as a third miscellaneous group containing all the remaining tripeptides (where x is a D-amino acid at N-terminus position and X is a generic L-amino acid). All the sequences are shown in *Table 3.2*, according to their retention time (R_t) at HPLC and logPs (*i.e.*, the logarithm of the partition coefficient, defined as the compound concentration ratio between the aqueous phase and the organic phase such as octanol, that gives a measure of the lipophilicity of a molecule) calculated using ChemDraw® software.

Seq.	Retention time (Rt, min)	LogP
fYI	13.3	2.4
pFF	14.0	1.9
vFF	14.7	2.3
iFF	15.2	2.7
fFF	15.5	3.1
sFW	13.6	0.1
vFW	14.7	1.8
iFW	15.2	2.2
fFW	15.5	2.6
pWF	14.3	1.3
fWI	14.9	2.1
wLL	15.0	1.6
wFL	15.3	2.1
fWF	15.5	2.5
wWF	15.7	1.9
wFF	15.7	2.6

Table 3.2: Retention time (experimental determined by reverse-phase HPLC) and LogP (average of LogP values calculated).

3.2. MGC (Minimum Gelation Concentration) and hydrogel preparation

3.2.1. MGC definition

The minimum gelation concentration (MGC) is usually defined as the lowest concentration of the gelator (the tripeptide) which leads to a stable gel. However, the MGC depends also on the time considered for self-assembly, *e.g.*, a peptide may self-assemble over a month at a given concentration. For this project, all the experiments have been performed considering a peptide

concentration able to reach a stable and homogenous gel in a period of time shorter than 1 hour, approximately around 30-45 minutes, to allow convenient use of time for further investigation and analyses.

3.2.2. Peptide hydrogel preparation

The peptide hydrogel protocol formation is based on an already published procedure [73] and it includes a two-step process: the first step involves the dissolution of each peptide in an alkaline buffer (0.1 M sodium phosphate buffer, pH 11.8-12.0, *i.e.* buffer 1, B1) with the help of sonication (for different time intervals, as required for each sequence), whereas the second step consists in the addition of the same volume of a mild acidic buffer (0.1 M sodium phosphate buffer, pH~5.8, *i.e.* buffer 2, B2) that triggers the gelation process and the achievement of final hydrogel at neutral pH 7.3 ± 0.1 (*Figure 3.3*), as verified by using a pH-meter.

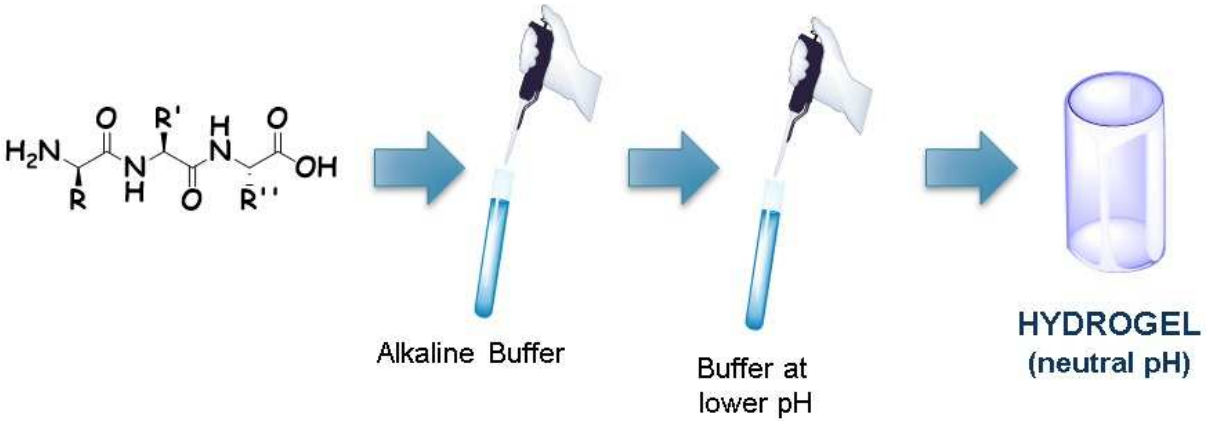

Figure 3.3: Schematic procedure of hydrogel preparation starting from a generic DLL heterochiral tripeptide.

The "inversion test" was chosen for a first, rapid visual evaluation and screening at macroscopic level of sequences able to form hydrogels. This test consists in the preparation of several samples at different concentrations for all the peptides. Each sample was prepared according the protocol procedures and the formation of the gel was determined after turning the vials upside down and observing if the hydrogel remained permanently attached to the vial bottom or started to flow down along the glass vial or broke itself in pieces (*Figure 3.4*).

Out of the 16 tripeptides, 12 passed the inversion test, and rheological studies were then performed to assess the viscoelastic properties of the materials, as described further below. The MGC were quite in good agreement with the hydrophobicity, showing an inverse relation between the HPLC Rt and MGC (*Table 3.3*). Exceptions to the trend were ascribed to differences in the peptide sequence, since self-assembly is a complex phenomenon that is influenced by a number of factors including steric hindrance, geometry of the side chain, and ability to engage in non-covalent interactions.

Sequences	Rt (min)	MGC (mM)
pFF	14.0	24
vFF	14.7	21
iFF	15.2	11
fFF	15.5	2
vFW	14.7	20
iFW	15.2	7
fFW	15.6	11
fWI	14.9	22
wLL	15.0	17
wFL	15.3	8
fWF	15.5	11
wWF	15.7	12

Table 3.3: Retention time (experimentally determined by reversal-phase HPLC) and MGC.

The 4 non-gelling tripeptides were: fYI, sFW, pWF and wFF. The ones containing serine (sFW) and tyrosine (fYI) were the most hydrophilic of the series, as shown by their HPLC R_t (*Table 3.1*). They were the only ones to display a hydroxyl group of the amino acid side chain that may be in an unfavourable position for the hydrophobicity-driven self-organisation. Proline is a known β-breaker to disfavour self-assembly, and this effect may be more evident for pWF relative to pFF, due to the stronger propensity for self-assembly of the FF motif relative to WF [30]. Finally, wFF appeared to pack so well that crystallisation, as opposed to hydrogelation, was favoured, as noted in several samples and described further below in the relevant section.

Figure 3.4: Example of "inversion test".

3.3. Peptide hydrogel characterisation

3.3.1. Oscillatory Rheometry

Oscillatory Rheometry was used to confirm the hydrogel nature of the self-assembled heterochiral tripeptides synthesised. Rheology is defined as the study of deformation and flow of the matter and the relationship between stress and deformation is a specific character of the material investigated. In particular, if an external force is exerted on a material, its particles will be displaced relative to each other and this displacement of particles is defined as *strain*. Type and extent of strain are specific properties of a material. In oscillatory rheometry an oscillatory (sinusoidal) deformation (*stress* or *strain*) is applied to a sample, the material response (*strain* or *stress*) is measured and the *phase angle* δ, or phase shift, between the deformation and response is measured (*Figure 3.5*). When $0° < \delta < 90°$, the response is viscoelastic [74].

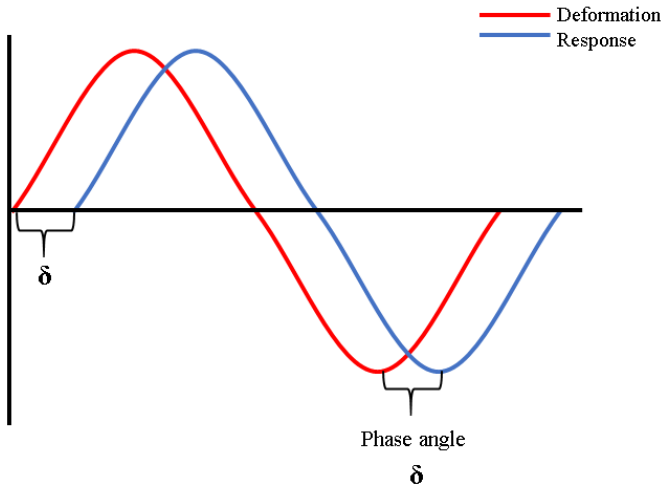

Figure 3.5: A deformation (stress) applied on a material produce a characteristic response (strain).

Viscoelastic materials exhibit both viscous and elastic properties. Because of physical differences, a distinction is made between viscoelastic liquids and viscoelastic solids, indeed the elastic portion of viscoelastic liquids is described by Hooke's law, which is also known as the spring model, whereas the viscous portion is described by Newton's damper model [75].

For an elastic (solid) material, stress and strain are in phase while for a viscous (fluid) material stress and strain are out of phase. Linear viscoelastic regime LVR represents the range of *stress* (or *strain*) in which all the rheological parameters measured are characteristic of the system regardless of the conditions of analysis. Typical materials such as hydrogels present elastic modulus G' higher in value (Pa) than viscous modulus G'', where the elastic (*storage*) modulus G' measures the elasticity of material and the ability of material to store energy, while the viscous (*loss*) modulus G'' measures the ability of material to dissipate energy that is lost as heat[76].

Oscillation analysis can be conducted modifying the applied frequency of the stimulus (*frequency sweep*), the application time of the stimulus (*time sweep*), the maximum applied force intensity (*stress* or *strain sweep*) and the temperature (*sweep temperature*). All these analytical procedures allow to analyse the viscoelastic phenomenon from different prospects to reach a complete characterisation of the investigated material. Usually the tests are not performed all together, but the choice falls on some of them for specific purposes. In particular, during the studies of the hydrogels obtained from the heterochiral peptides, the sequence of the oscillatory rheological analysis included:

- *time sweep*, the stimulus is applied, and its maximum intensity, frequency and analysis temperature remain constant within the LVR,
- *frequency sweep*, the rate of deformation, which is the material response to increasing frequency, is monitored at a constant stress and temperature, the test runs inside of LVR;
- *stress sweep*, the material response to increasing deformation stress is monitored at a constant frequency and temperature.

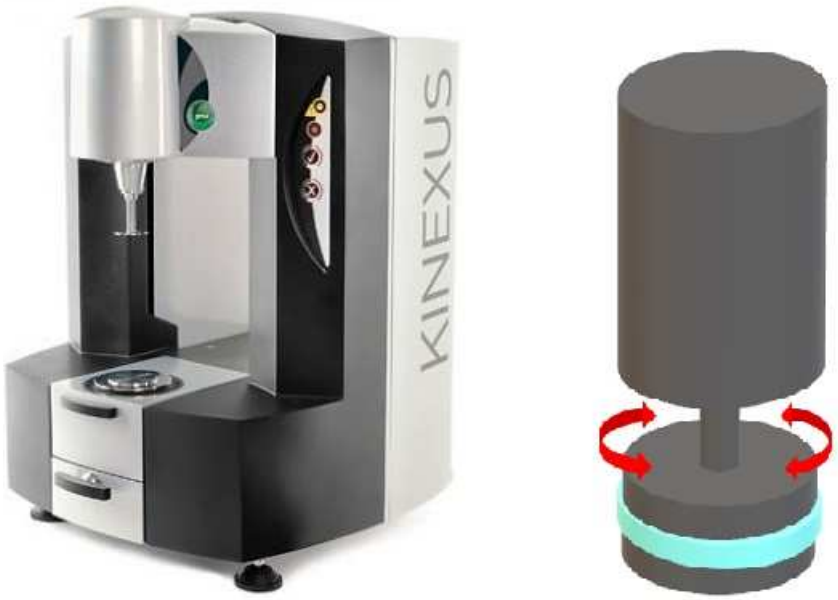

Figure 3.6. Oscillatory rheometer used for this project (left) and schematic representation of the parallel geometry used for hydrogel studies, where the red arrow represents the direction of the oscillation during the application of the stress on the sample (right).

The hydrogel-nature found by the inversion test was confirmed by frequency sweep analysis (*Figure 3.7*), performed after 1 hour of *in situ* preparation of each sample (time sweeps analyses are reported in Supplementary section). To compare different systems properly it would be necessary to have the same operational conditions (same constant stress and frequency applied during the experiments) and sample preparation (same MGC) for all of them. However, considering the wide range of solubility and MGC for all the peptides, and their different behaviours that led us to choose the most appropriately experimental condition for each of them, an absolute comparison could not be carried

out between all the samples. For this reason, data were reported according to the group classification described above in *Table 3.1* (*Figure 3.7,* frequency sweeps, where G'>G'' in peptide hydrogels prepared at their specific MGC). Each analysis was repeated at least three times on independent samples. A representative seta of data is reported [77].

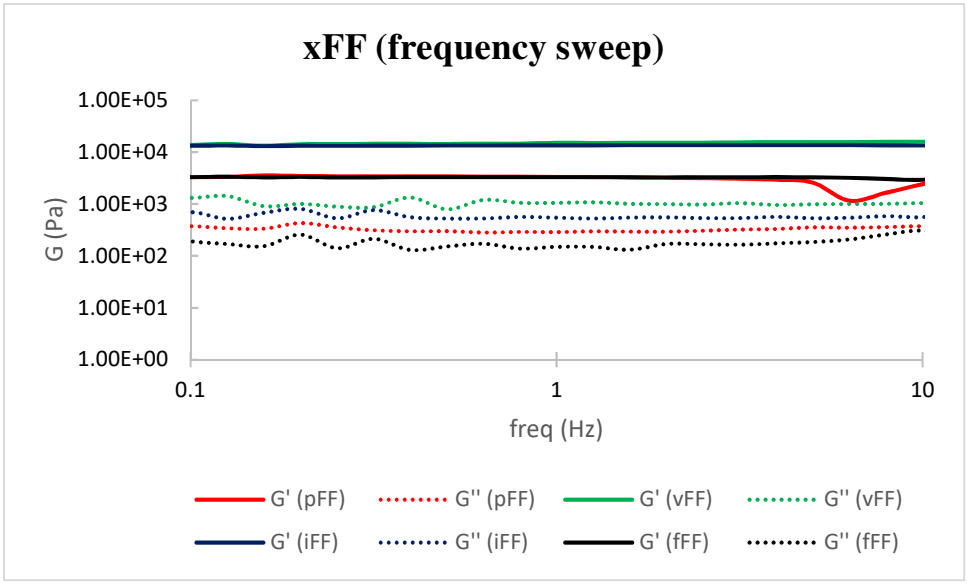

a.

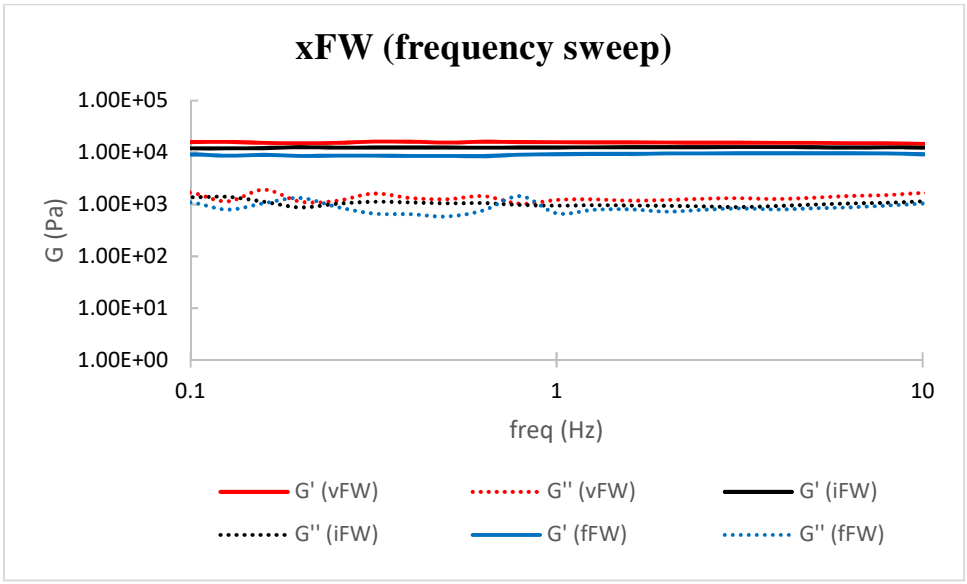

b.

c.

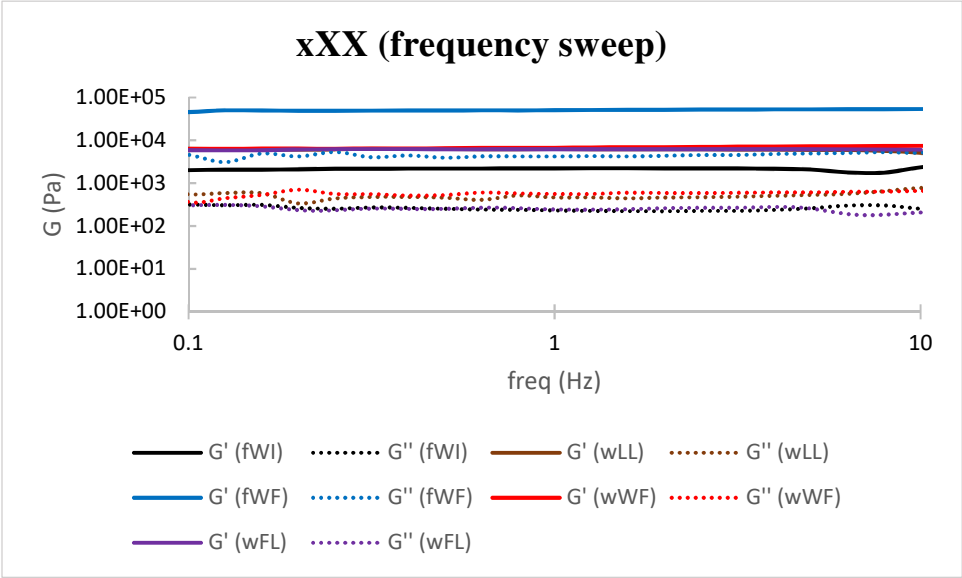

Figure 3.7.: Frequency sweeps of all the heterochiral tripeptides synthesised.

It can be seen that the first xFF group displayed two sets of materials based on G' values; at MGC, vFF and iFF had almost equal G' of 14.0 kPa, while the G' for pFF and fFF was significantly lower (4.1 kPa and 3.5 kPa, respectively), possibly due to a negative effect of having proline as a β-breaker, and three adjacent sterically-demanding phenylalanine residues, respectively. The second group xFW was more homogeneous, with all tripeptides at MGC with a modulus within the same scale range (9.1-16.0 kPa), regardless of the presence of three or two aromatic residues. The third group, which was more diverse in terms of peptide sequences, was also quite heterogeneous in terms of G' moduli, although all tripeptides with w at the N-terminus (wLL, wFL, wWF) had similar G' (*i.e.*, 7.1, 9.9, and 6.6 kPa, respectively), regardless of the number of aromatic residues present.

Each hydrogel presented a typical value of resistance to the increasing force applied during the stress sweep analysis that represented a robustness index of each material following the external perturbance (*breaking point* of the hydrogel, *Figure 3.8*). At the end of the stress sweep analysis, it was possible to observe an inversion of trend curves of G' and G'', with G''>G' and a state-system out of the LVR (*Figure 3.9*).

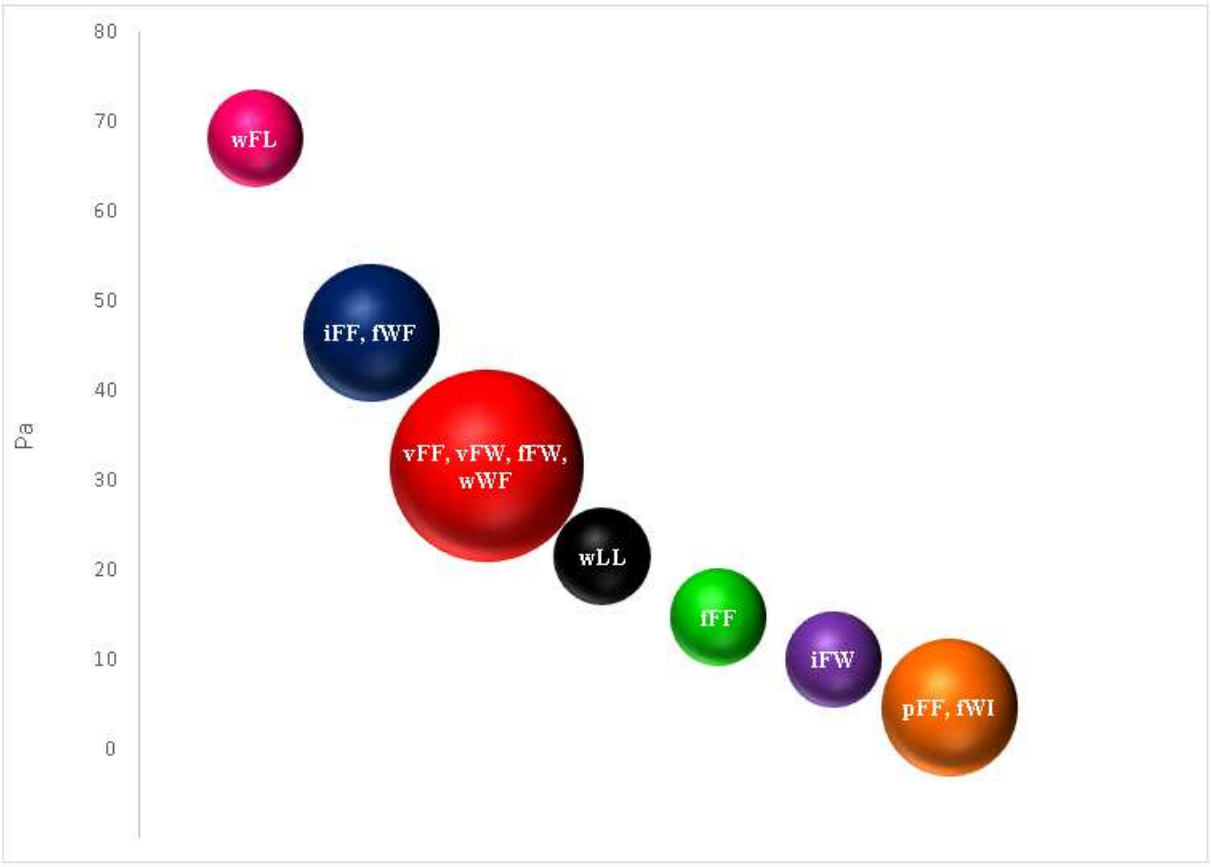

Figure 3.8.: Distribution of breaking point of hydrogels through all the sequences tested.

a.

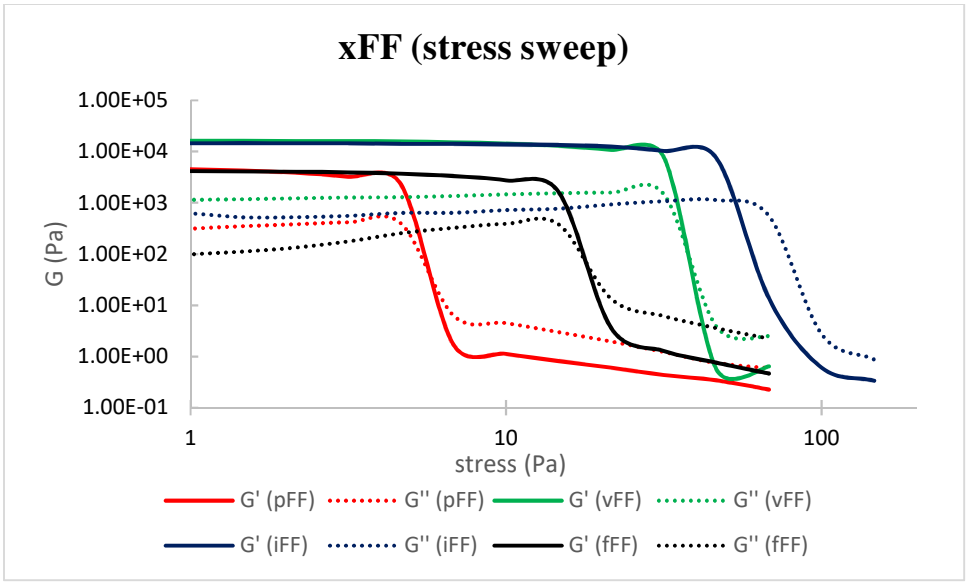

b.

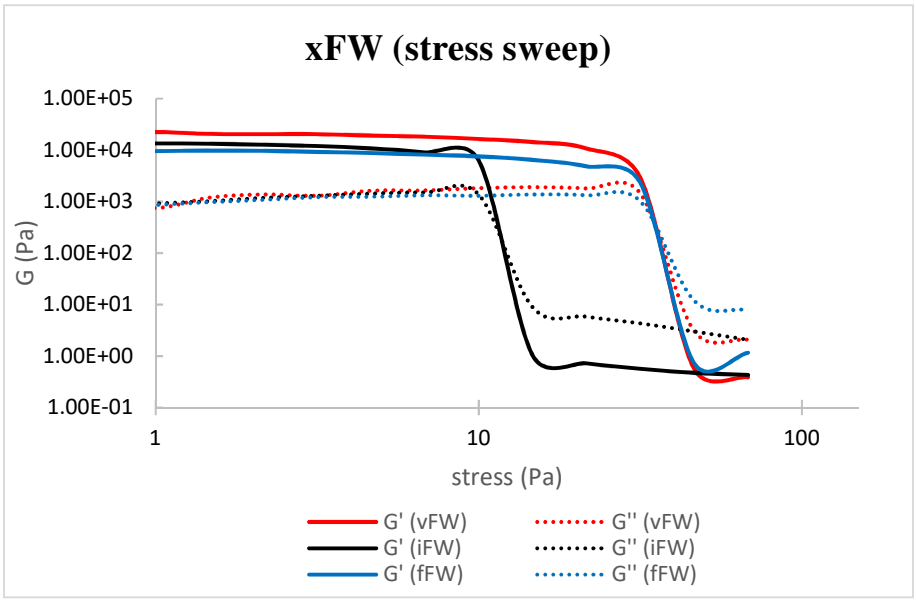

c.

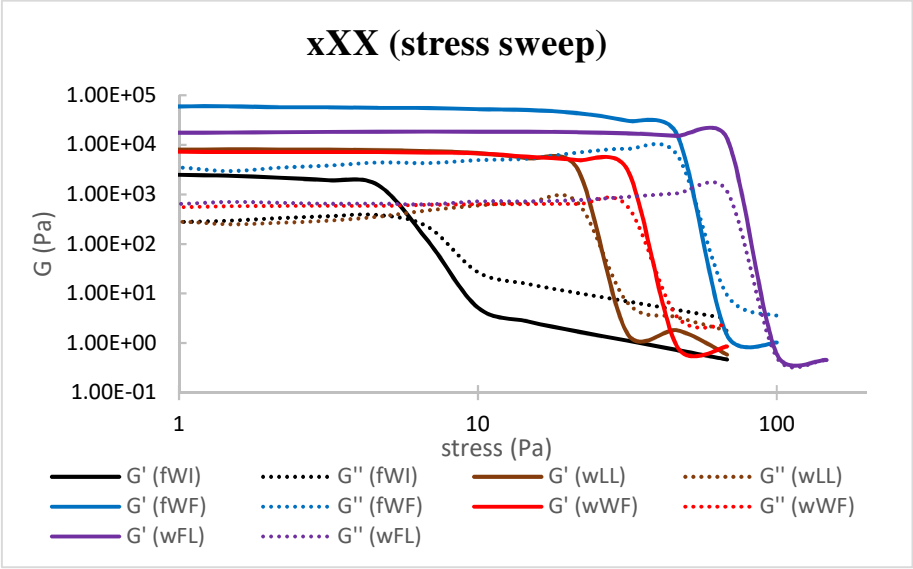

Figure 3.9.: Stress sweeps of all the heterochiral tripeptides synthesised.

3.3.2. Nanostructure morphology assessed by TEM

Nanomorphology of the superstructures obtained through the self-assembly of the heterochiral tripeptides synthesised were studied and investigated by TEM analysis (images were collected by Dr. Daniel Iglesias and Dr. Slavko Kralj). With this technique, a beam of electrons was transmitted through the sample, placed on an appropriate grid to obtain a final image thanks to a camera and apposite software. TEM imaging of nanostructures made by organic matter such as small peptide molecules are very challenging, because the sample could quickly be decomposed during the electron beam action. The ideal technique for this kind of samples reported in the past was cryo-TEM [78], in which the samples were cooled to cryogenic temperature embedded in an environment of vitreous water. Indeed, for vFF, which was previously published, vFF cryo-TEM images revealed a nanotape morphology, which could not be discerned from our TEM images.

The images of the dried hydrogels samples are reported according to the classification in xFF, xFW and xXX groups. For xFF and xFW groups (except for pFF, featuring proline as a β-sheet breaker [79]) it was possible to observe a relation between the value of *storage modulus* G' of each hydrogel and the nanofibre size, in terms of diameter (nm) measured from TEM images (reported in *Table 3.4*), whereas for xXX group, due to the poor similarities between the sequences, a similar relation was not found. In addition, also the bundling ability and the size distribution width of the individual fibrils were very different amongst samples, as shown below. Interestingly, iFW, and possible vFW, appeared to form large and hollow nanotubes, although further investigation will be needed to confirm this hypothesis.

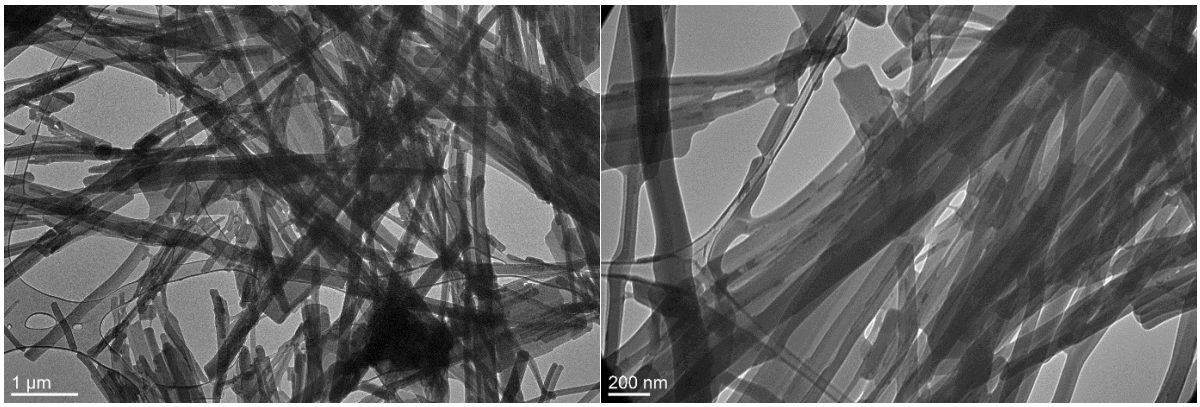

Figure 3.10.: pFF

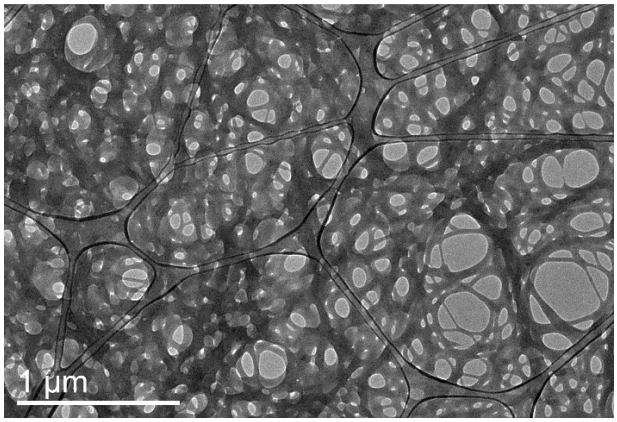

Figure 3.11.: vFF

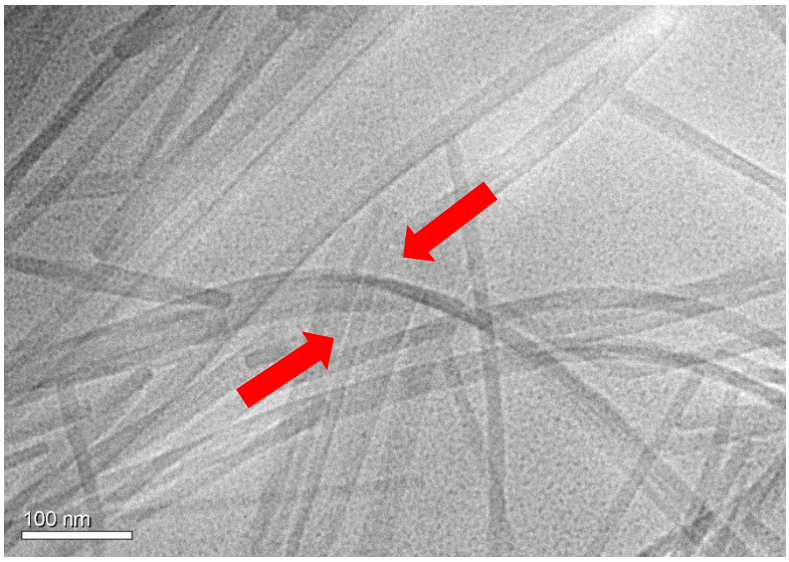

Figure 3.12: vFF (image collected using Cryo-TEM technique, courtesy of Lynne Waddington) shows nanotapes.

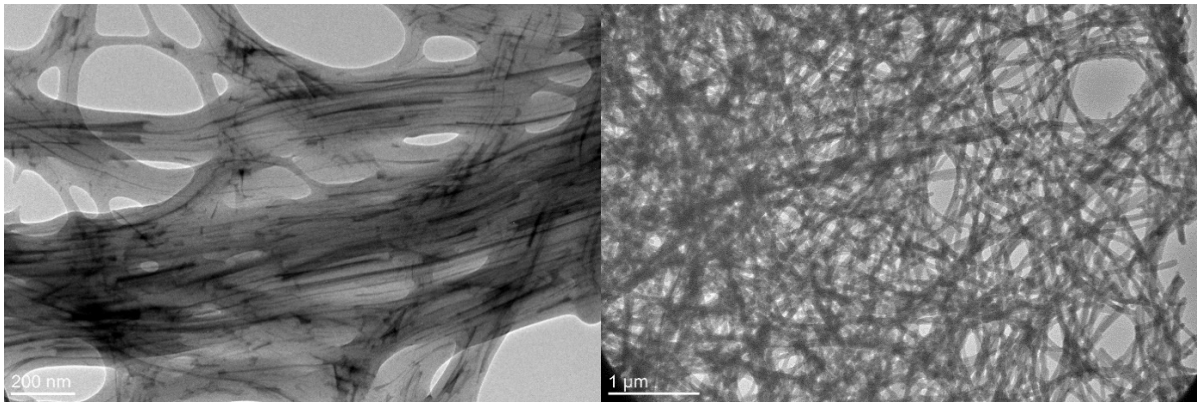

Figure 3.13: iFF

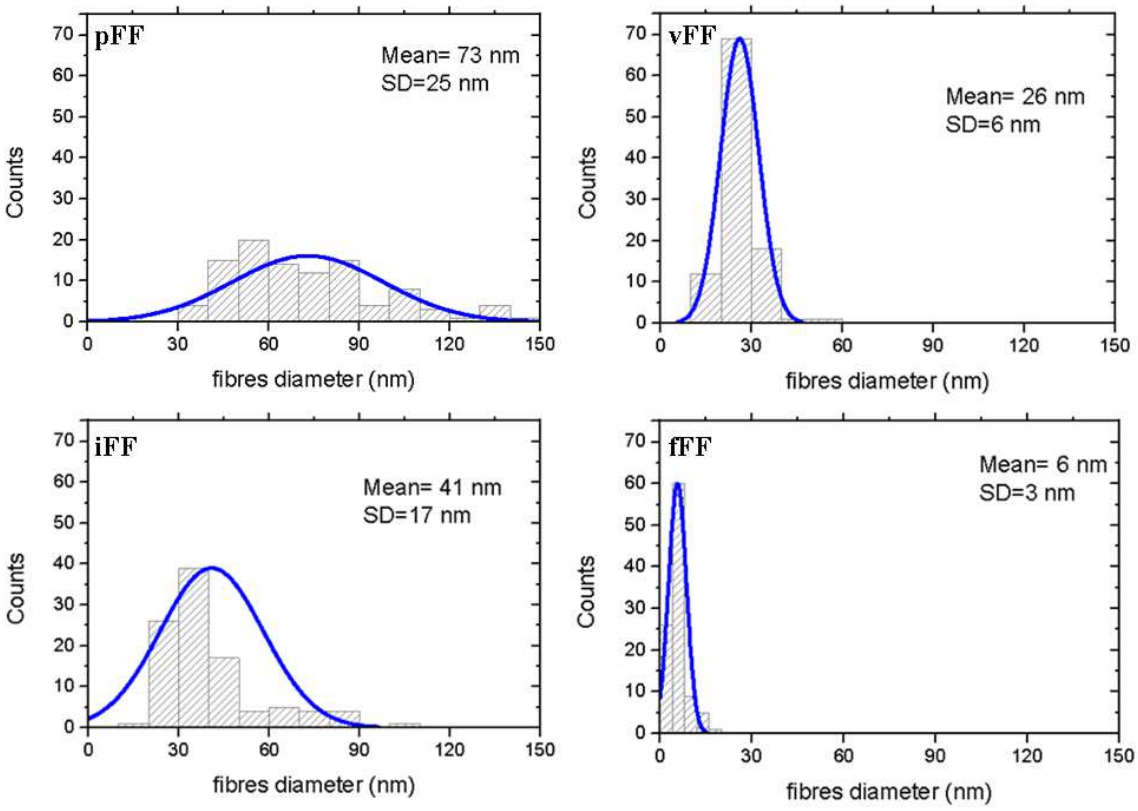

Figure 3.14: Gaussian distribution for xFF peptides fibres diameter (nm).

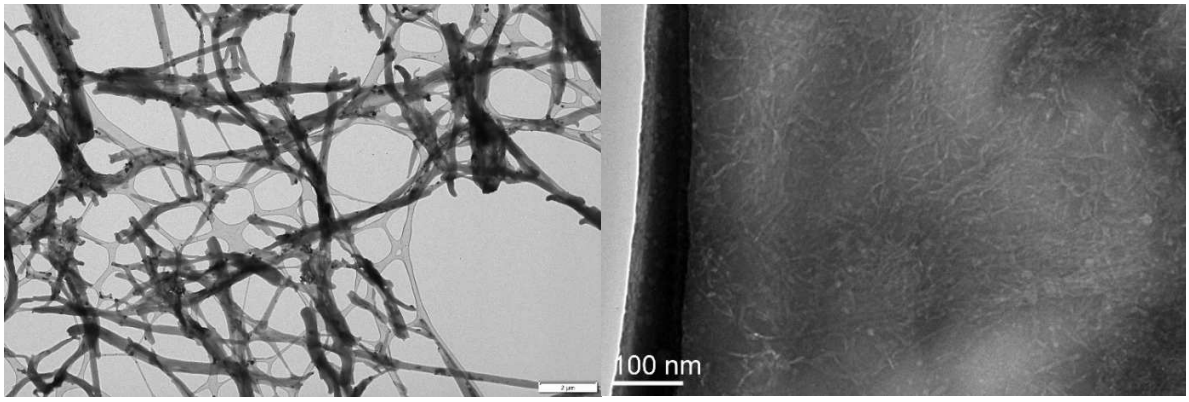

Figure 3.15: fFF (scale bar= 2µm for image on the left).

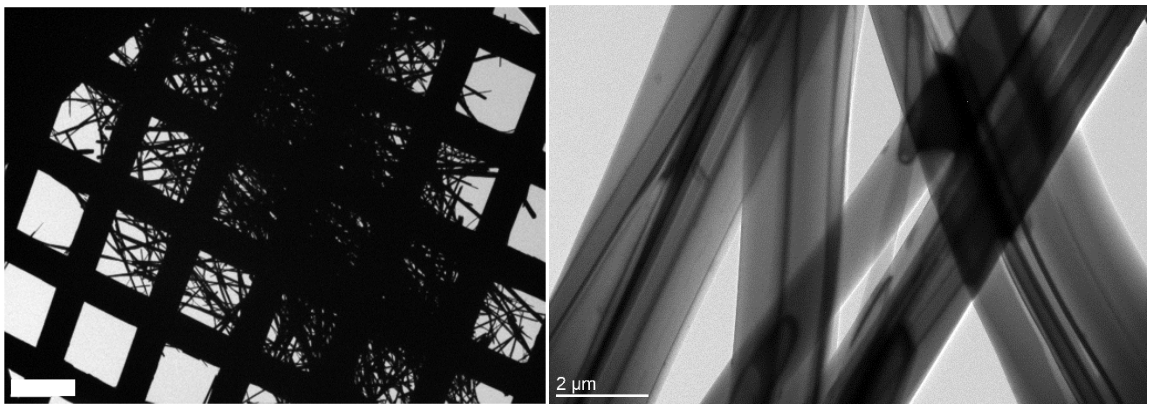

Figure 3.16: vFW (scale bar = 58µm, size of each grid box, left image)

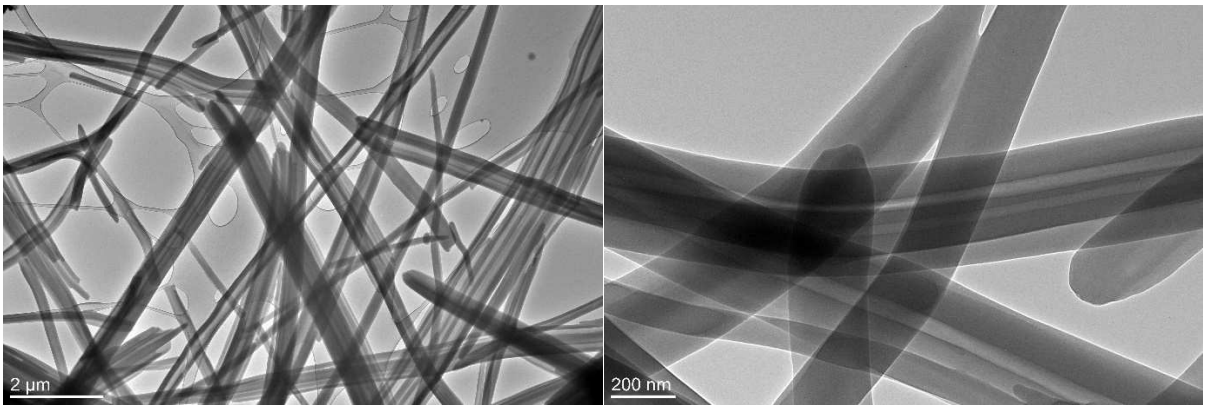

Figure 3.17: iFW

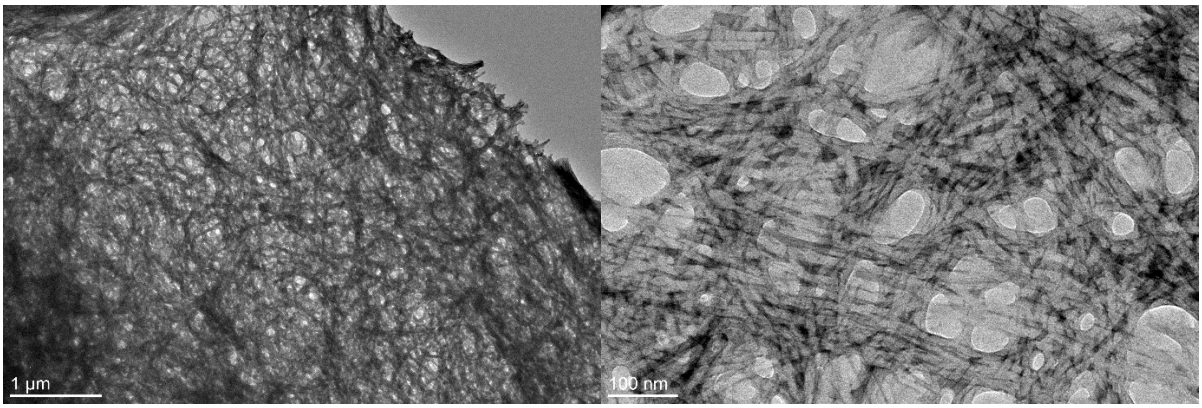

Figure 3.18: fFW

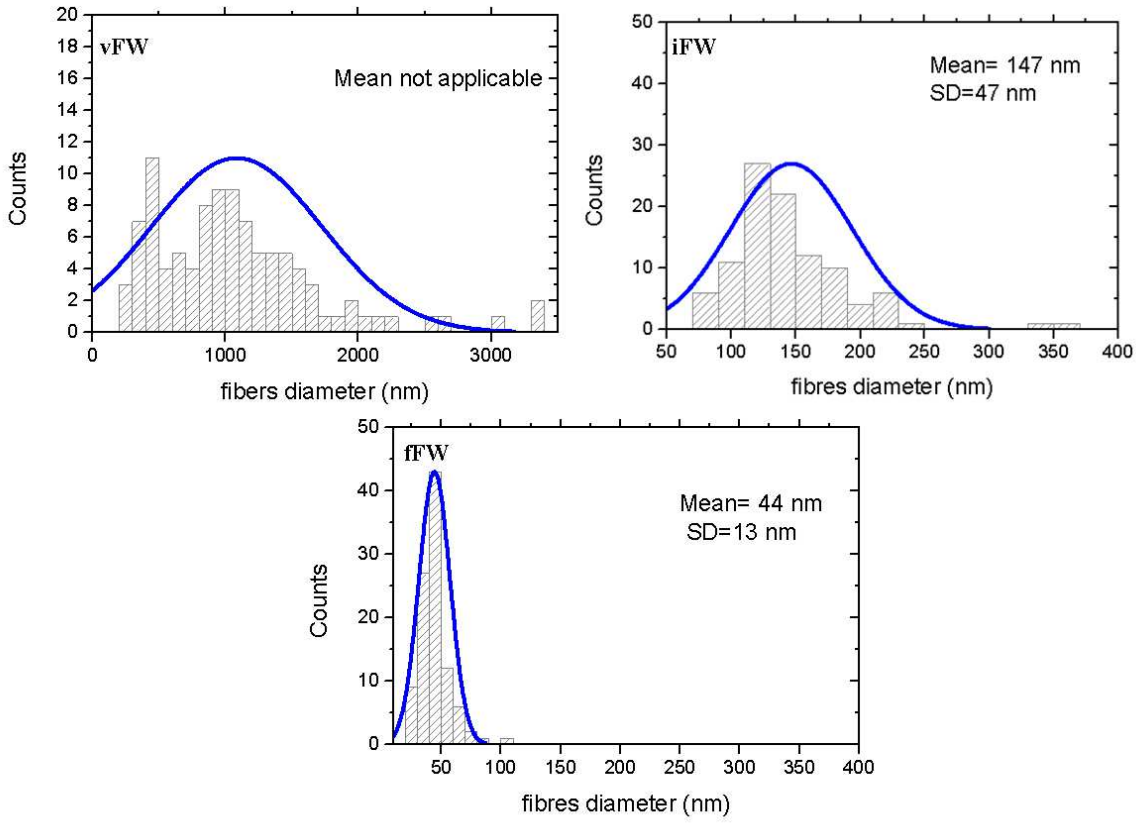

Figure 3.19: Gaussian distribution for xFW peptides fibres diameter (nm).

xFF	G' (kPa)	size (nm)	xFW	G' (kPa)	size (nm)
iFF	14.7	41±17	vFW	16	Not meas.
fFF	14.1	26±6	iFW	13.3	147±47
pFF	4.1	73±25	fFW	9.1	44±13
vFF	3.5	6±3			

Table 3.4: Correlation between storage modulus G' (kPa) and nanofibres size, in terms of diameter (nm).

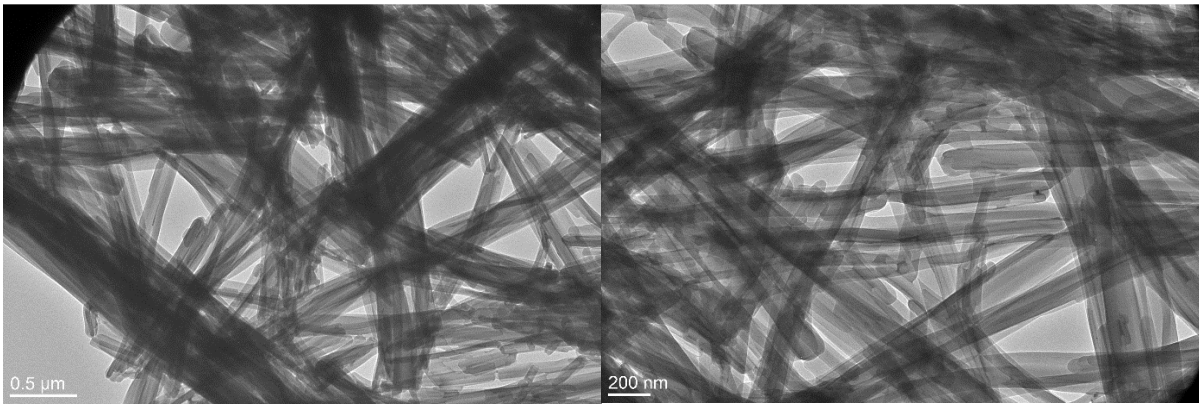

Figure 3.20: fWI

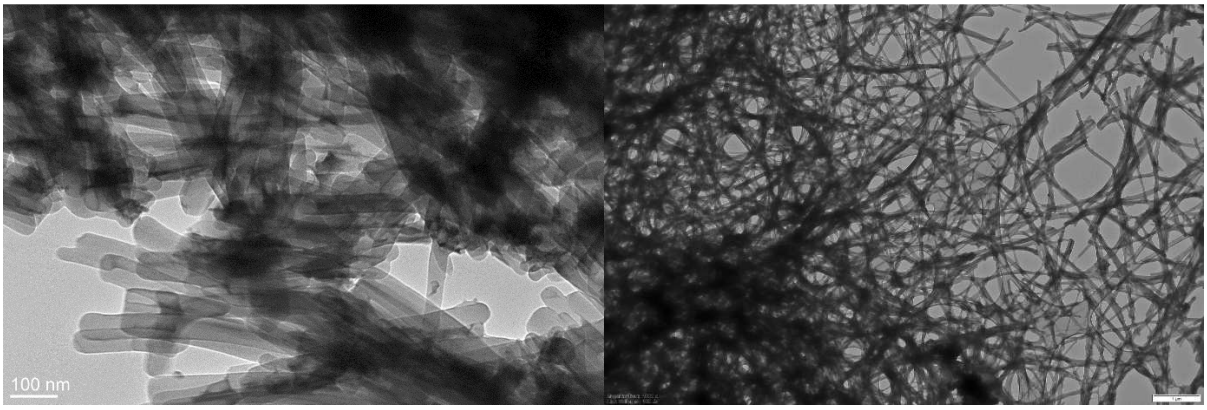

Figure 3.21: wLL (scale bar = 1µm for image on the right).

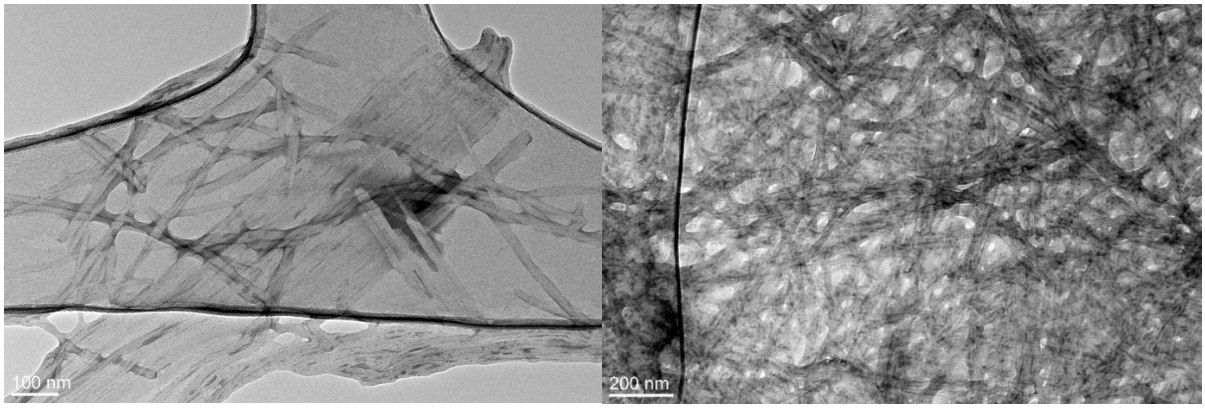

Figure 3.22: wFL

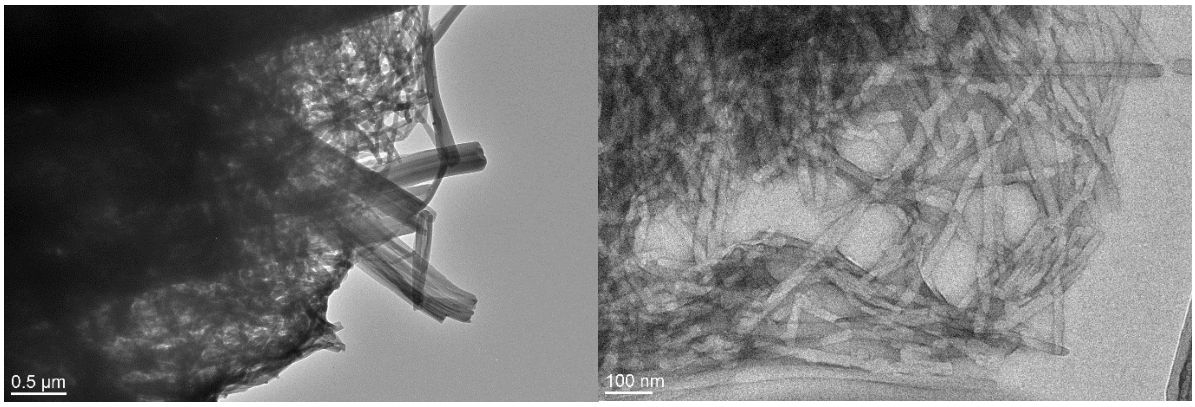

Figure 3.23: fWF

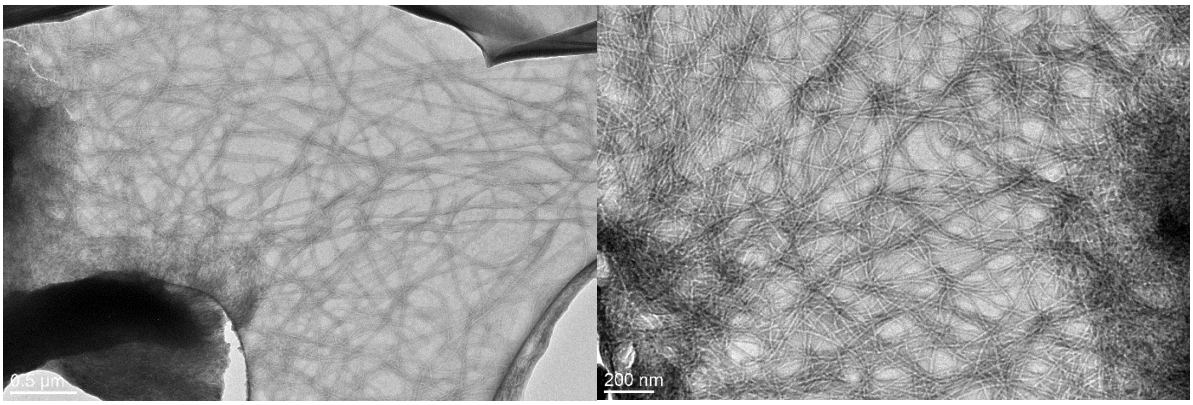

Figure 3.24: wWF

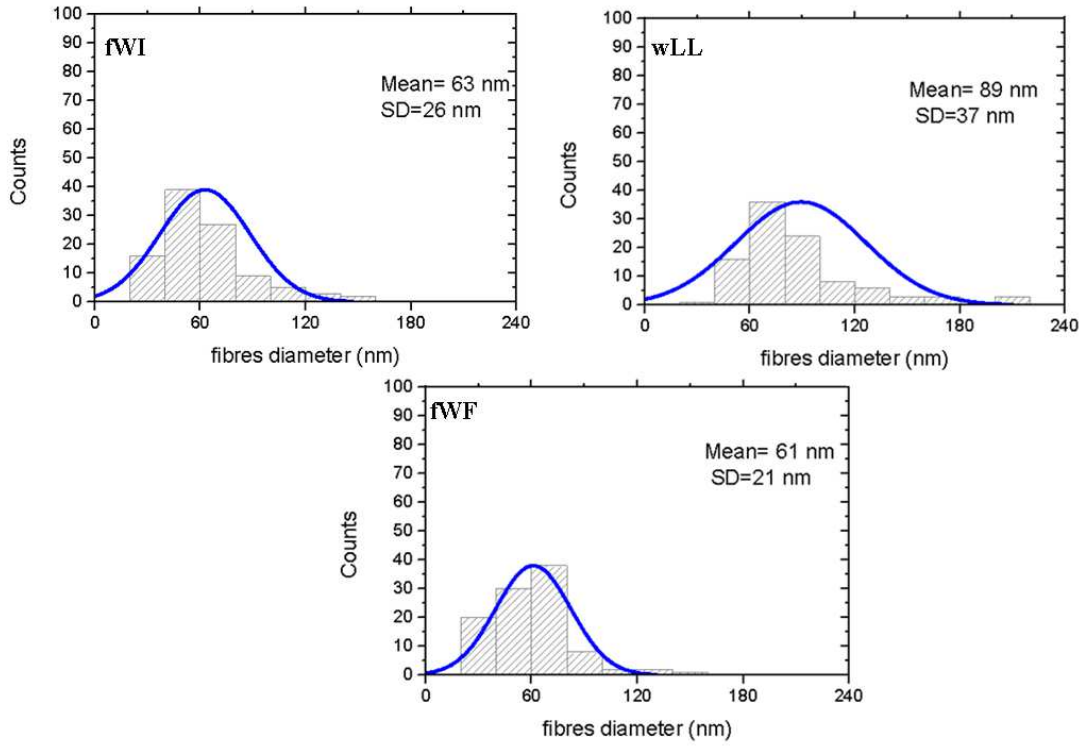

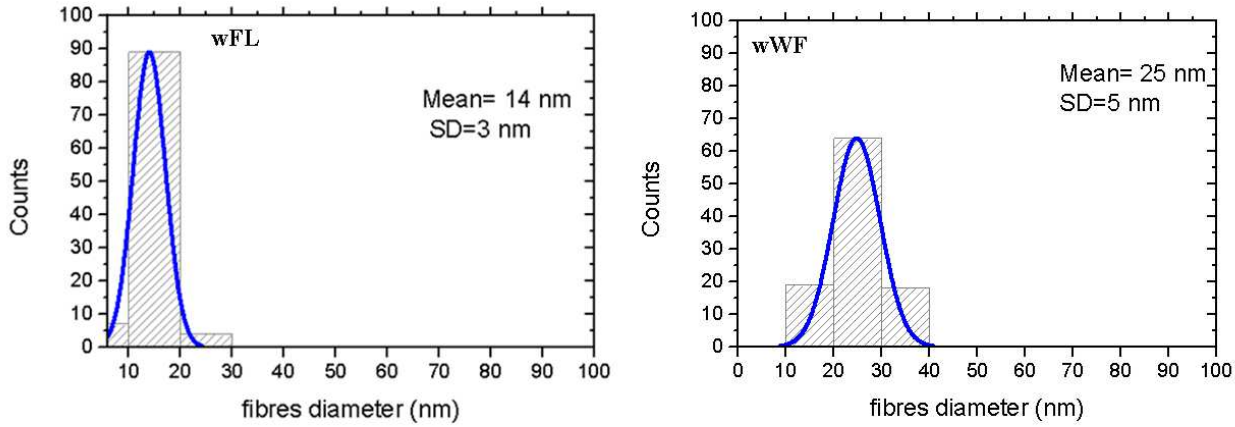

Figure 3.25: Gaussian distribution for xXX peptides fibres diameter (nm).

3.3.2. Circular Dichroism Spectroscopy (CD)

Circular Dichroism (CD) Spectroscopy was used to study the secondary structure of the heterochiral tripeptides synthesised. CD is a valid technique and an excellent tool usually used to investigate rapidly the conformation of protein folding [80], [81]. Circular dichroism (CD) spectroscopy is a light unequal absorption spectroscopy that measures the difference in absorbance of right-handed and left-handed circularly polarised light by a substance. Every beam light is associated with time dependent electric and magnetic fields (*Figure 3.26*).

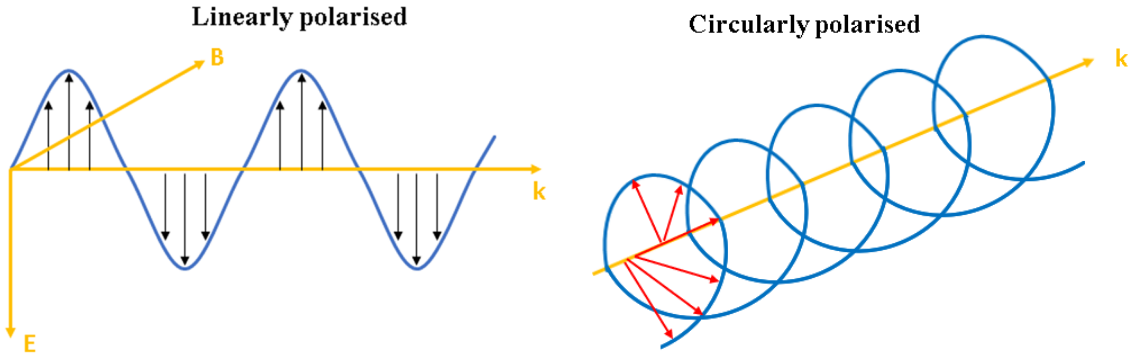

Figure 3.26.: Electric field vector, E, in linearly polarised light oscillates in one plane (left) while electric field vector in circularly polarized light rotates about its propagation direction k, where B is magnetic field (right).

The electric field (E) can oscillate sinusoidally in a single plane after the polarisation of light after its passing through prisms or filters. This sinusoidal wave is originated by two equal length vectors that are tracing out two circles: one that rotates clockwise (E_R) and one that rotates counter clockwise (E_L) (*Figure 3.27*). The two waves are 90° shifted in phase and can be divided with specific prisms or electronic devices. When an asymmetric molecule interacts with a beam of light, it can absorb right and left handed circularly polarised light to different extents and the plane of the light wave can be rotated. The sum of E_R and E_L vectors generates a vector that traces out an ellipse and the light is

defined “elliptically polarised”. The difference in absorbance of E_R and E_L (expressed in units of ΔE) for an asymmetric molecule and the angle whose tangent is the ratio of the minor to the major axis of the ellipse (expressed in degrees ellipticity, where $[\Theta]deg \cdot c^2/dmol = 3298\ \Delta E$) can be used both to report CD [80].

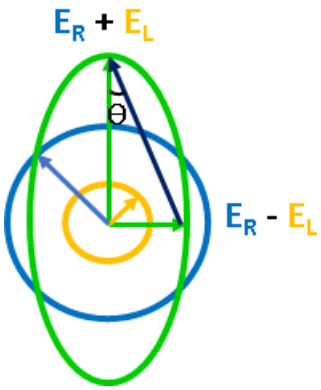

Figure 3.27: Elliptical polarized light (green) is composed of unequal contributions of right (blue) and left (yellow) circular polarized light.

Considering that amino acids are the simplest chiral biological molecules, they were studied using CD, although not presenting a secondary structure they were neglected for three decades [82] and only lately CD signal of amino acids was reported [83], [84]. In literature, there are not many examples of short peptides CD spectra, since they are not expected to fold and give an appropriate CD spectrum. However, a peculiar signal could be noticed when the peptide molecules assemble themselves in supramolecular structures, thanks to the weak interactions between the single peptide molecules involved.

Since self-assembly does not present a linear correlation with the peptide concentration, two sets of CD spectra were recorded. The first set refers to a common concentration well below the MGC (1 mM, for all the sequences) in which the peptide molecules are expected to be present at monomeric state in solution – lack of self-assembly was supported by the fact that the CD spectra did not change over time (*i.e.*, 1 hour). The second set was performed at the MGC for each peptide, present in a very wide range (2 mM < MGC < 24 mM). Self-assembly was supported by the fact that the CD spectra in this case evolved over time and upon heating. Unlike protein folding, for which it is possible to observe a linear correlation between peptide concentration and relative CD signal, in self-assembled peptides this correlation is not well identifiable.

While for the peptides in B1 buffer solution (pH = 11.8-12.0) at 1 mM concentration there were not practical problems during the sample transfer in the quartz CD cuvette for the spectrum recording, in the case of peptide hydrogel, the formation *in situ* within the CD cell is required. This implies some issues to overcome, such as the correct hydrogel formation, without bubbles or

precipitates, and the use of a very thin cuvette of 0.1 mm size to reduce the optical path to compensate the relative high concentrations of peptide hydrogels needed to be investigate in this study. A general rule about the influence of the amino acid chirality and final supramolecular structure chirality has not been identified yet. Indeed, some studies conducted on all the possible 8 combinations for N-terminus Boc- protected heterochiral self-assembled FFF reported that the first amino acid chirality drives the final supramolecular chirality [85], whereas other reported studies reported a correlation between the supramolecular tripeptide chirality with the chirality of the central amino acid [61], [78]. These suggest that further studies need to be carried out.

For monomeric state experiments, each peptide was dissolved in B1 (11.8 < pH < 12) at 1 mM concentration while for gelling peptides, each sample was dissolved in B1 and then transferred in the CD cuvette, where B2 (pH ~ 5.8) was added and spectra were recorded after 2 minutes. Spectra acquisition for gelling peptide was performed for a period of 1 hour, to evaluate the change in shape of CD spectra until the signal stabilisation, that usually occurs after 20 minutes. Each measurement was repeated at least 3 times.

3.3.2.1. Circular dichroism spectra at 1 mM

The CD signals for each peptide at 1mM of concentration in alkaline B1 buffer were recorded, analysed and are reported below. The xFF group spectra for the four peptides (pFF, vFF, iFF, fFF) able to self-assemble in more complex superstructures once the MGC is reached and for the one peptide not able to form hydrogel (crystals and then precipitate at tested increasing concentrations) are reported in *Figure 3.28*.

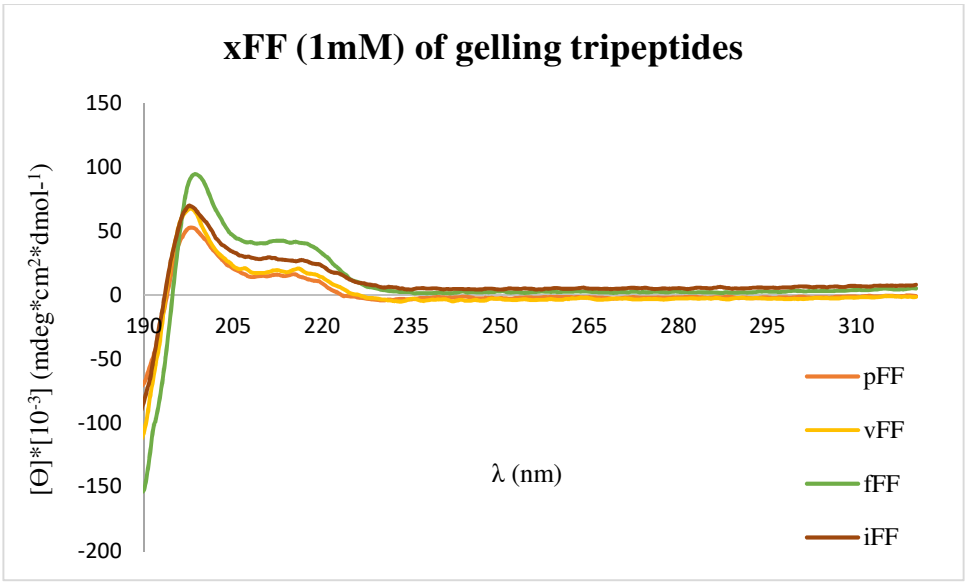

a.

b.

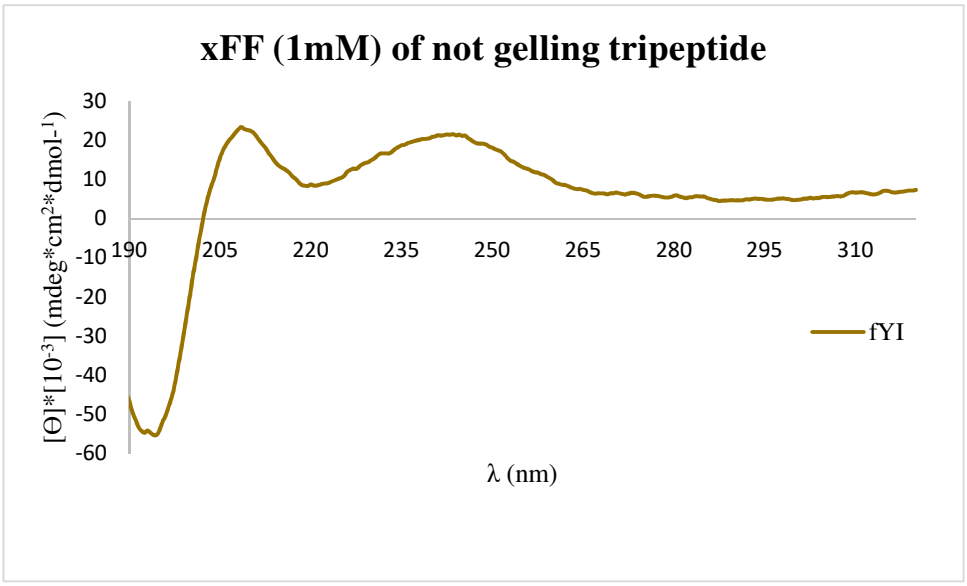

Figure 3.28: Monomeric CD spectra for xFF tripeptides (a. gelling b. not gelling) at 1mM concentration.

In the monomer state, the first four heterochiral tripeptides displayed a particular CD signature very similar to the one reported in a previous study of our group [59], different from the most common observed conformations usually present in literature (*i.e.* α-helix, β-sheet, random coils), while for fYI the self-assembly process could be disadvantaged from the presence of para-hydroxylic substituent of the tyrosine. Moreover, it was noticed that fYI organised spontaneously in crystals (*Figure 3.29*).

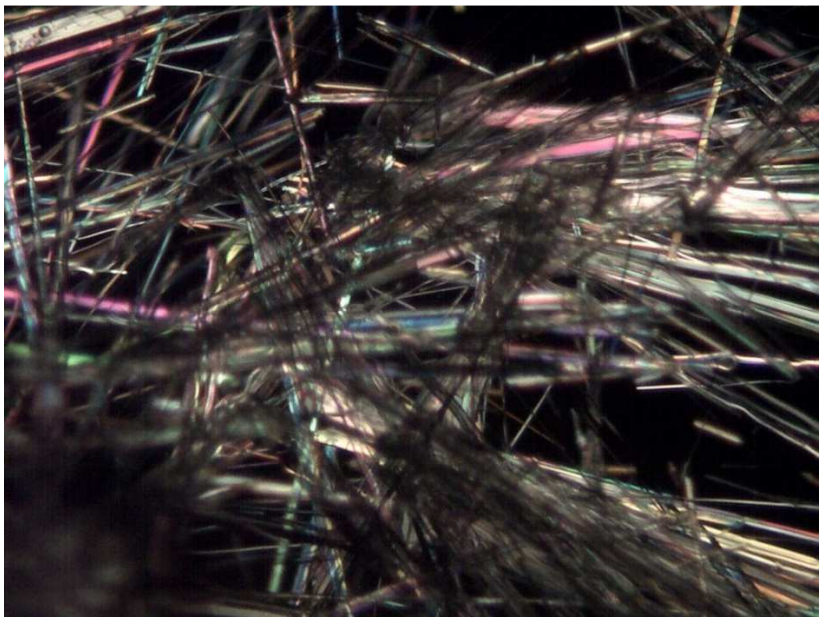

Figure 3.29: fYI crystals under a cross-polarised light filter (image acquired thanks to Dr. Rita De Zorzi).

As for FxF peptide series, it seems applicable also for xFF group the hypothesis of the presence of a statistical coil, in which unfolded peptides specific conformation states could co-exist in equilibrium. Similarly, also in this case the two positive maxima present at 200 and 220 nm could be assigned to

π-π*and n-π* transitions of peptide bonds respectively and the relative dipole orientations of the two amides could reveal an analogous statistic distribution according to CD signatures. In the case of FxF in L-D-L stereoconfiguration, this resulted in the display of all the amino acid side-chains on the same side relative to the peptide backbone, thus yielding an amphipathic spatial conformation due to the presence of exclusively hydrophobic amino acids [59].

For the xFW group, the spectra for all the peptides of the group are reported: three gelling heterochiral peptides at their specific MGC and one that forms white precipitate at different tested concentrations (*Figure 3.30*). All of the xFW heterochiral tripeptides present the same monomeric characteristic CD signature but only the more hydrophobic ones were noted to self-assemble to achieve a final hydrogel, indeed sFW was shown to be unable to form hydrogel also at high concentrations, due to the presence of the hydroxylic side chain of serine.

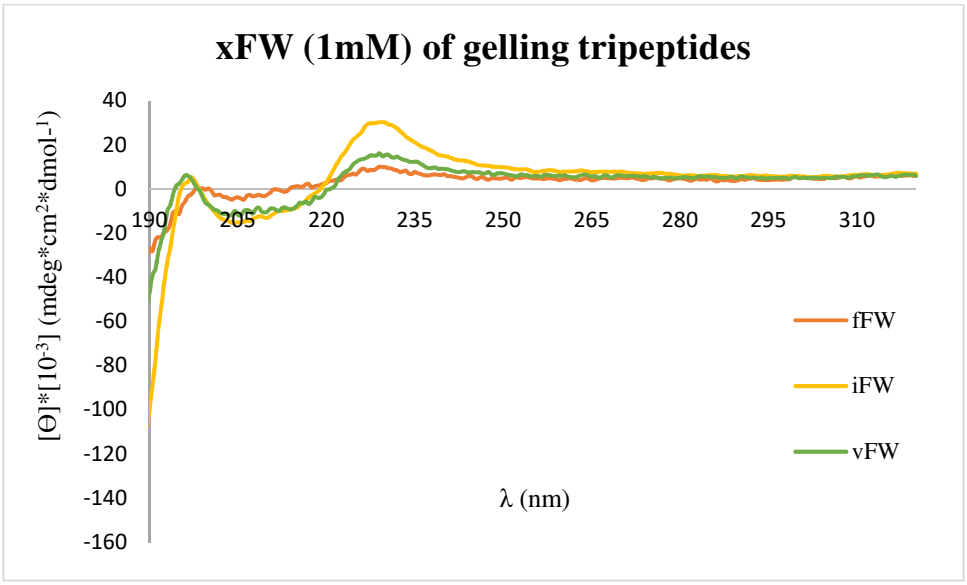

a.

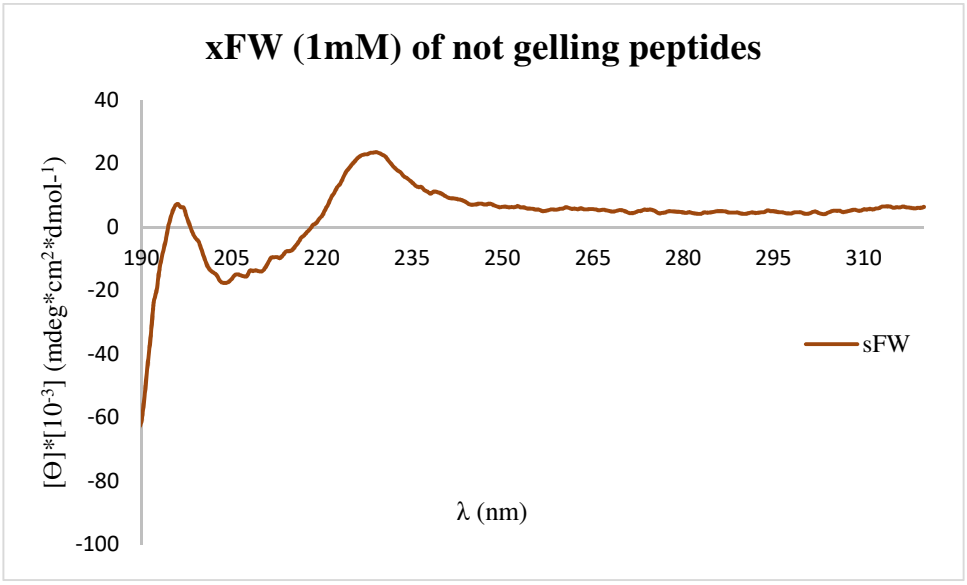

b.

Figure 3.30: Monomeric CD spectra for xFW tripeptides (a. gelling b. not gelling) at 1mM concentration

In the third group xXX, the heterochiral peptides signatures obtained were various for gelling and not gelling peptides, reflecting the diversity in their sequences. For clarity, spectra were divided in other three sub-classes considering the recurring shapes (*Figure 3.31*), in which only pWF and wFF were not able to self-assemble in superstructured hydrogels but to organised in ordered crystals instead (*Figure 3.32*).

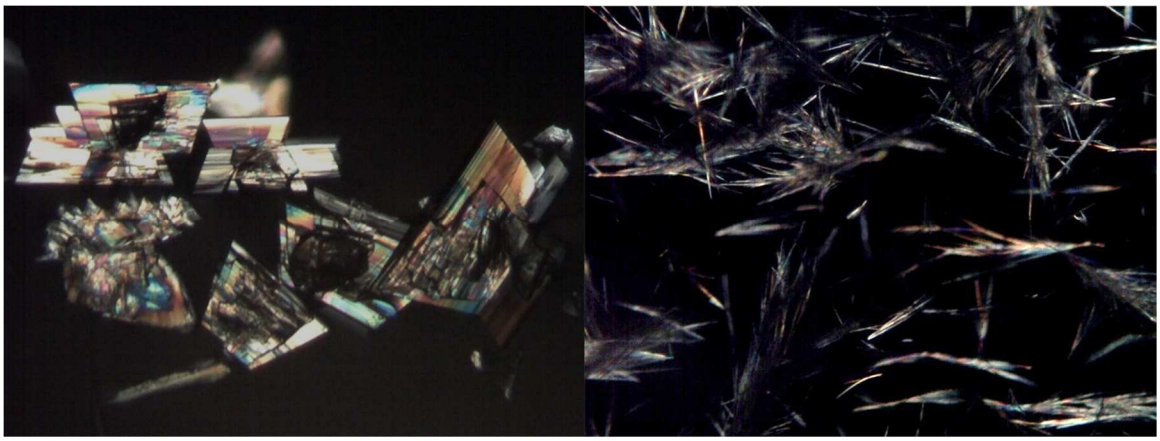

Figure 3.31: pWF (left) and wFF (right) crystals under a cross-polarised light filter (images acquired thanks to Dr. Rita De Zorzi).

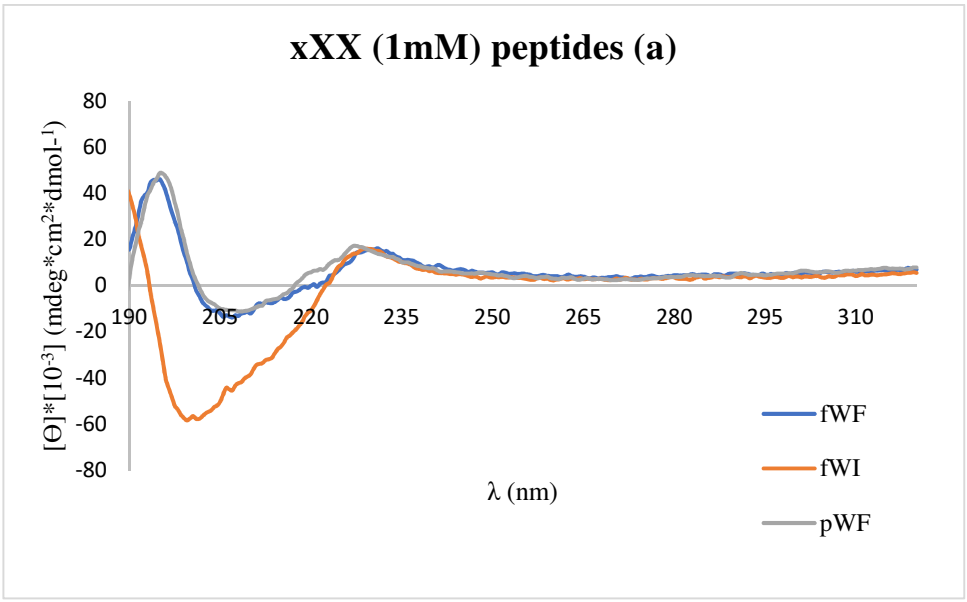

a.

b.

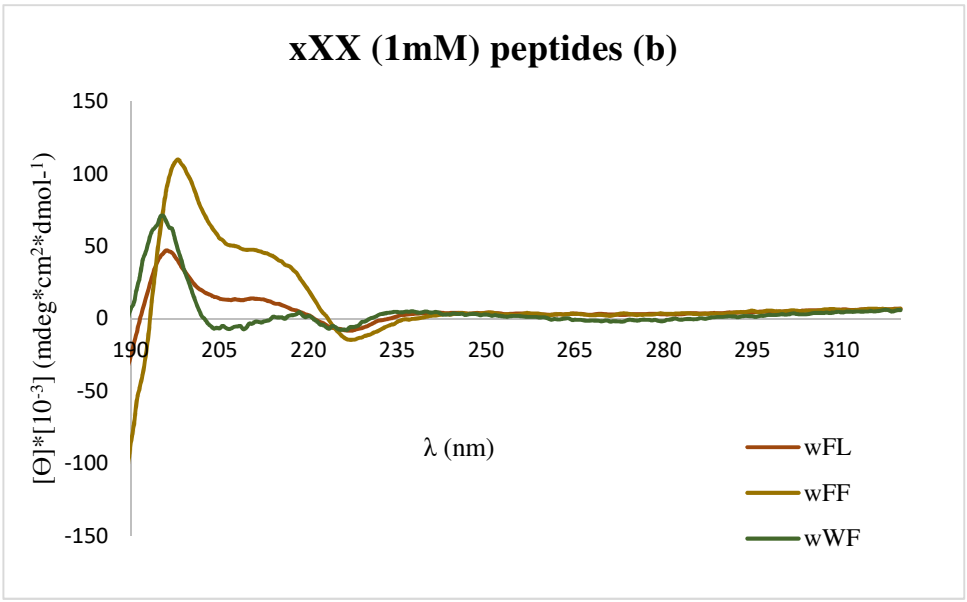

c.

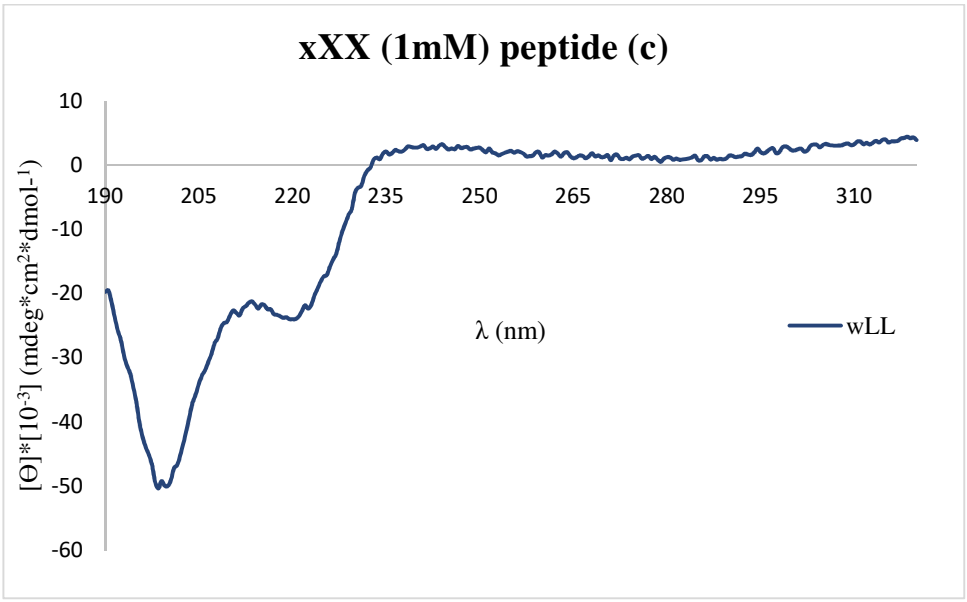

Figure 3.32: Monomeric CD spectra for xXX tripeptides (pWF and wFF do not assembly into final hydrogel) at 1mM concentration

In particular, wLL presented a characteristic spectrum in which an opposite chirality was predominant compared to the other sequences. CD spectra of fLL and lLL could be useful for a comparison to investigate whether the xLL motif has a predominant D-like CD spectrum due to a predominant effect of the N-terminus over the L-LL aliphatic motif, and whether this is valid only for aromatic or also aliphatic residues.

3.3.2.2. Circular dichroism spectra at MGC

CD spectra were collected for each peptide at MGC.

The xFF group bears two L-phenylalanine residues just like the series FxF, recently described by our group [59], so that a meaningful comparison was possible. pFF tripeptide was the only one

that did not show a significant difference compared to monomeric state CD spectra (*Figure 3.33*), similarly to what was previously reported for FiF.

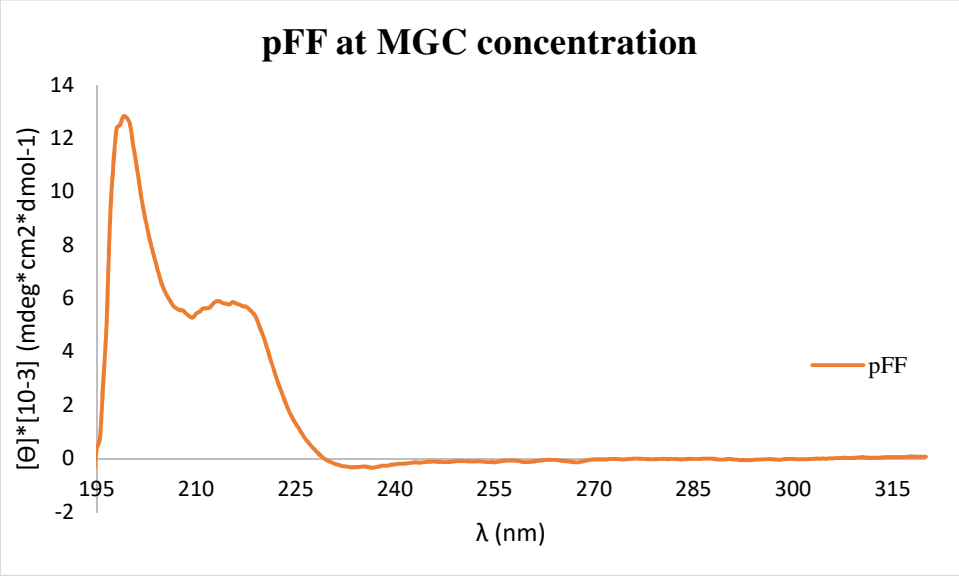

Figure 3.33: Heterochiral tripeptide pFF CD spectra at MGC concentration.

vFF tripeptide [86] hydrogel had a CD signature that was similar to the one displayed by FvF hydrogel, and it was characterised from the presence of positive maxima present at 205, 217 and 220 nm and one intense negative minimum at 195 nm (*Figure 3.34*). The remaining two gelling peptides fFF and iFF displayed CD spectra with negative minima reminiscent of FlF hydrogel spectra in 200-220 nm region (*Figure 3.35*).

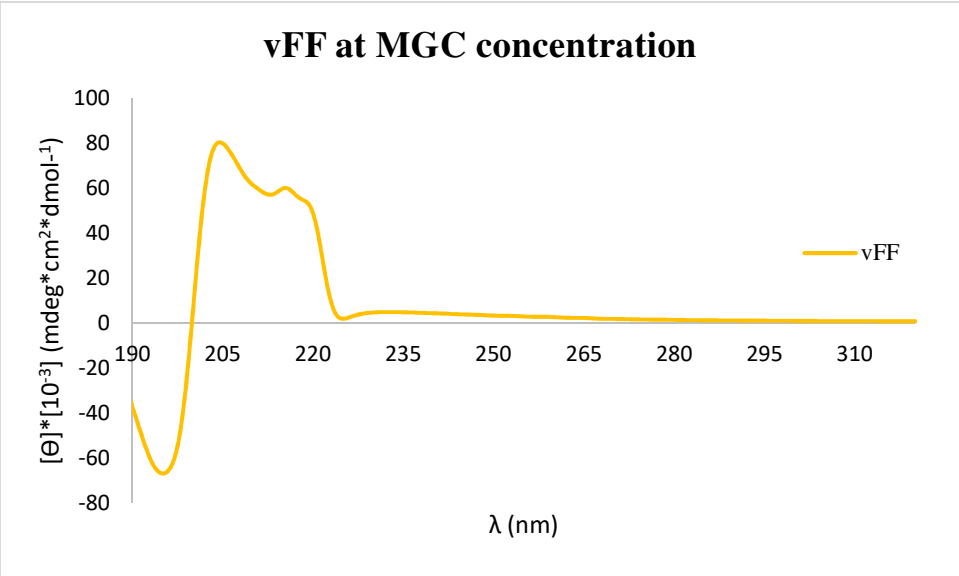

Figure 3.34: Heterochiral tripeptide vFF CD spectra at MGC concentration.

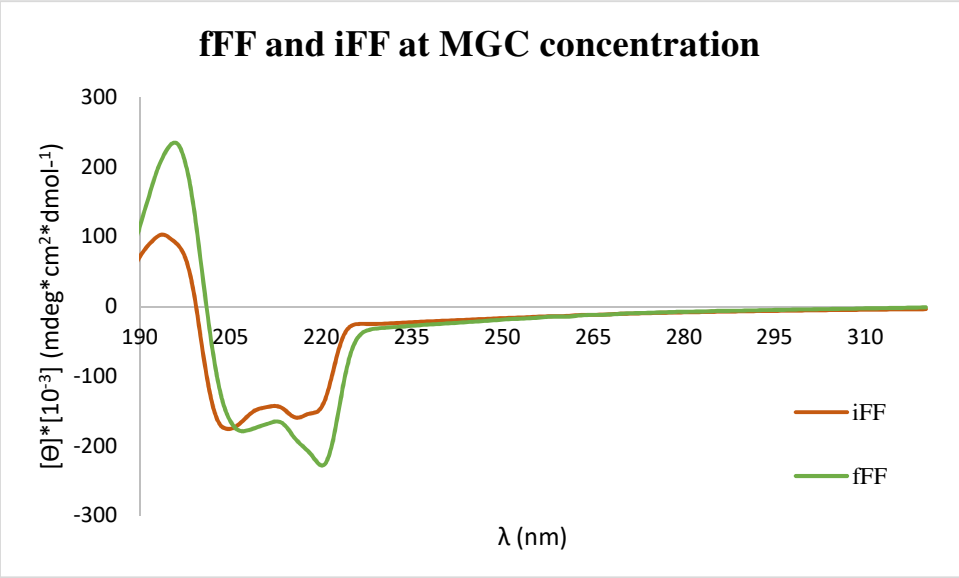

Figure 3.35: Heterochiral tripeptides fFF and iFF CD spectra at MGC concentration.

In the case of xFW group, the signal in the region 260-320 nm was directly correlated to the presence of aromatic amino acids such as W and F. The first usually presents a peak close to 290 nm and structure between 290 and 305 nm, while F shows weaker and sharper band with structure between 255 and 270 nm [87]. The structures in this range result from vibronic transitions in which different vibrational levels of the excited state are concerned. In these cases, the aromatic side chains give a strong contribution to the CD signals below 250 nm (far UV region) [88] as shown in *Figure 3.36*.

a.

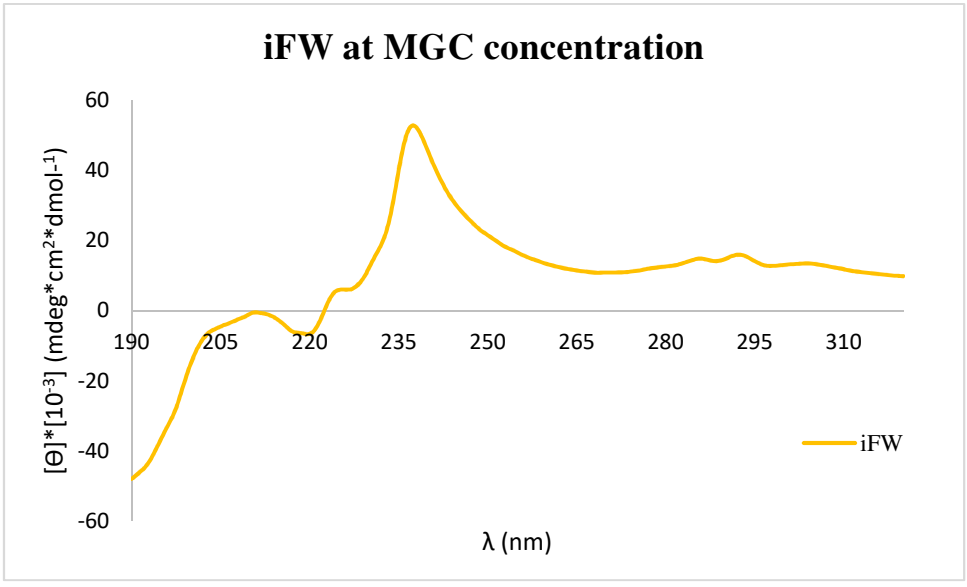

b.

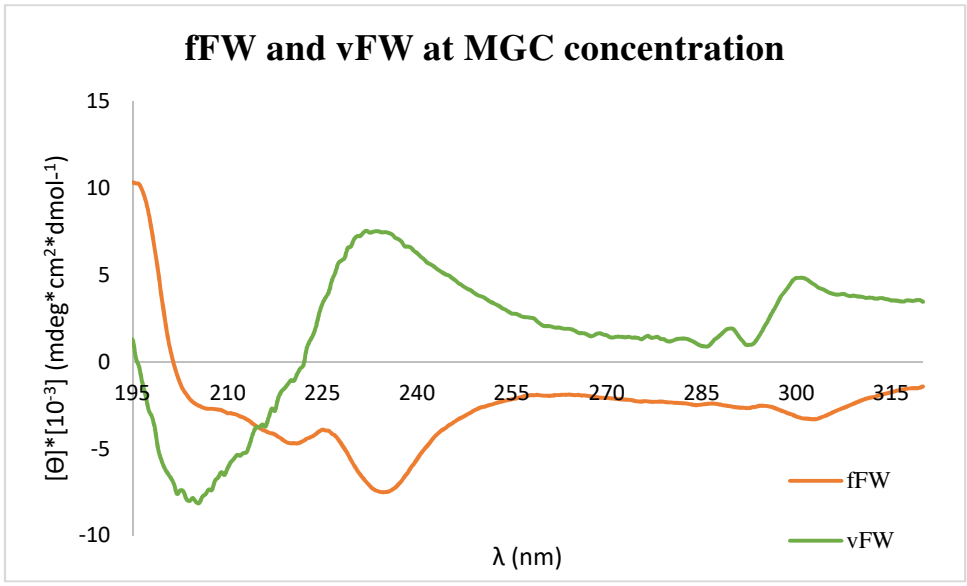

Figure 3.36: Heterochiral tripeptides iFW, fFW and vFW CD spectra at MGC concentration.

The contribution of the aromatic side chain of F and W was visible also in the amide region, thus not making it possible to estimate in a unique way the peptide secondary structure [89]. This applied also for the third group of xXX tripeptides, reported in *Figure 3.37*.

a.

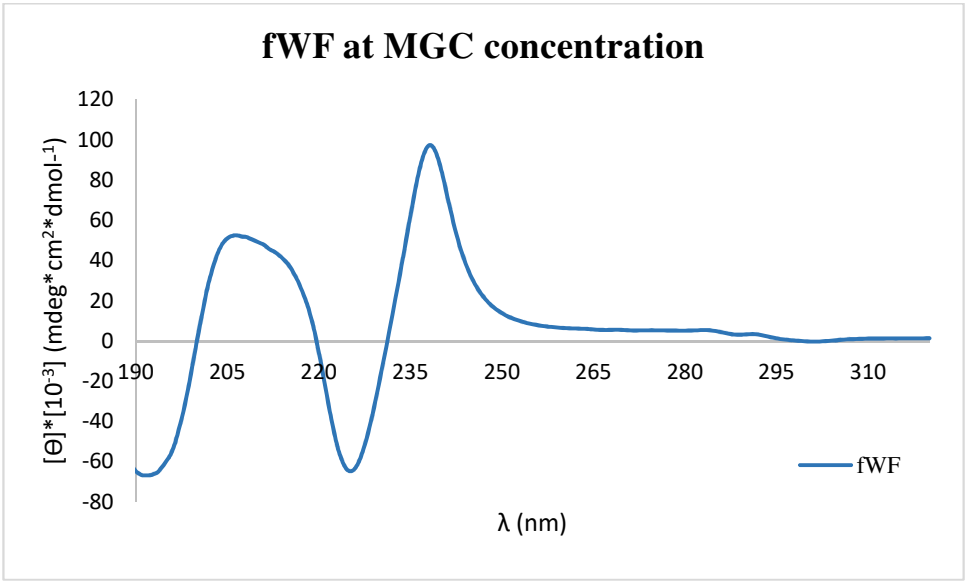

b.

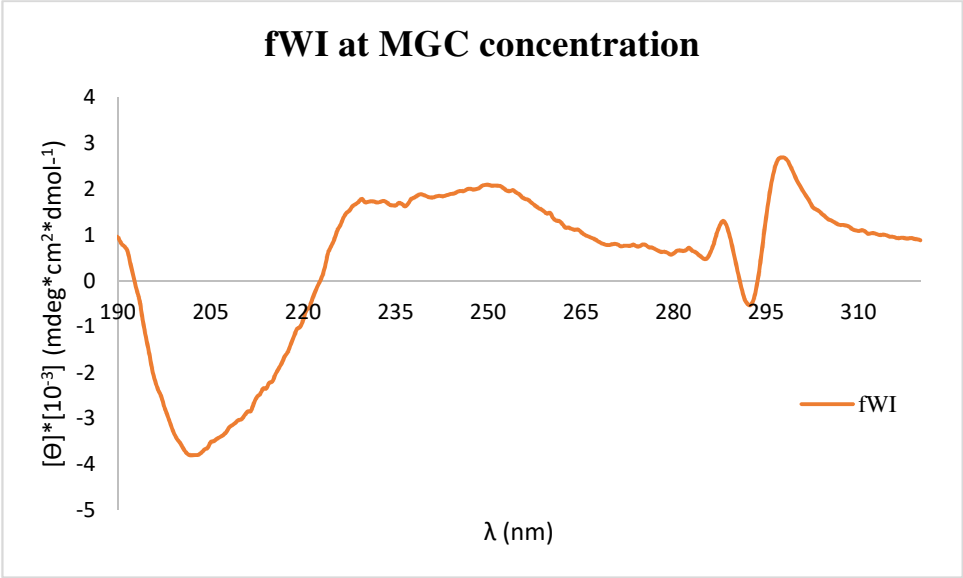

c.

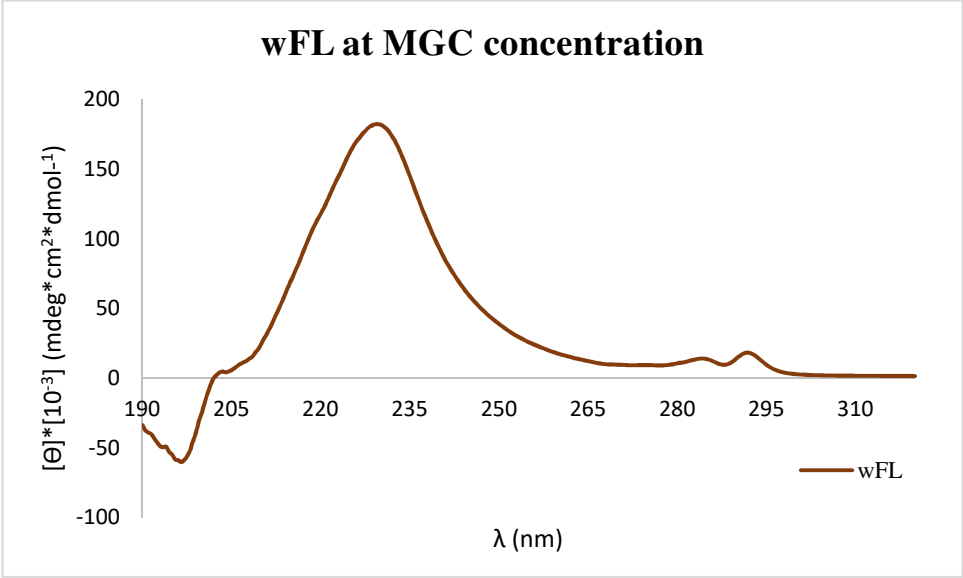

d.

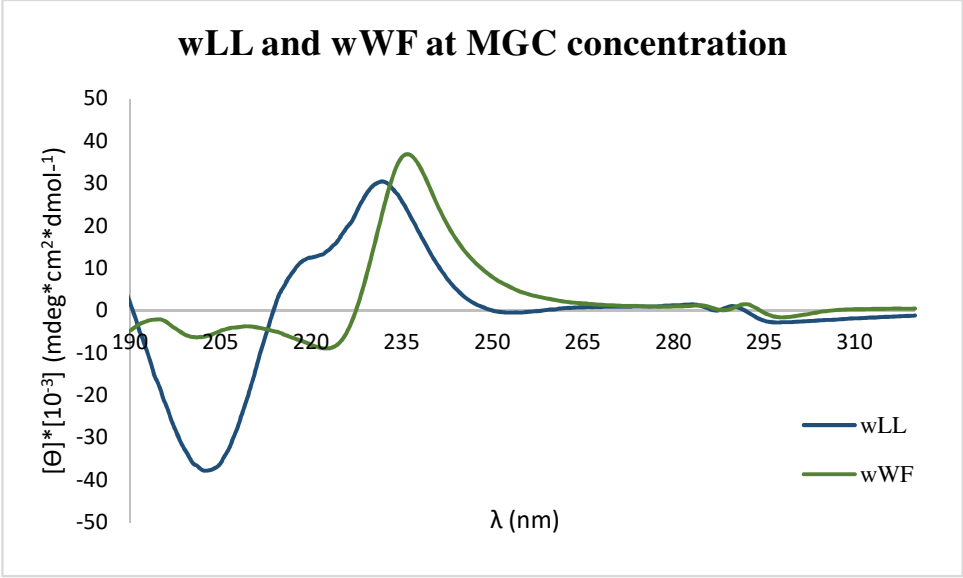

Figure 3.37: Heterochiral gelling tripeptides of xXX group CD spectra at MGC concentration.

Considering that induced CD band can be negative in presence of W and positive in presence of F but considering that in many of these sequences both the two aromatic amino acids are present, probably one of the two contributions can prevail over the other in some cases, although still a certain rule cannot be defined.

3.3.2.3. Determination of Tm (melting temperature) of self-assembled peptide hydrogels

Supramolecular structures of each self-assembled hydrogel were monitored by CD over a temperature ramp up to 85°C, after 1 hour from the gel formation inside the CD cuvette. Melting temperature (Tm) are obtained plotting molar ellipticity (ϴ) at specific wavelength for each sample as the temperature is increased (*Figure 3.38*, *3.39*, *3.40*). Thermal reversibility propensity was detected through the "hot-bath test" according to which every gel is placed in a water bath in which water temperature is increased from 25°C to 85°C with a ramp of ~ 5°C/min, mimicking the heating condition of CD. Next, each sample was removed from the water bath and it was left to cool down slowly at RT (room temperature) to observe if the hydrogel reformed. Experimental observations collected during the hot-bath test were compared with CD data and summarised in Tables below for every peptide group, showing a good agreement (*Table 3.5*, *3.6, 3.7*). Spectra recorded for each sample during the ramp up to 85°C are shown in the Supplementary section.

Seq.	MGC	Tr	After heat	Rev.	Tm
fYI*	n.a.		n.a.	n.a.	n.a.
pFF	24mM			NO	39°C
vFF	21mM			YES	70°C
iFF	11mM			YES	57°C
fFF	2mM			NO (weak gel)	45°C

Table 3.5: Sequences tested, picture of the xFF hydrogels before and after the hot-bath test, thermal reversibility and Tm (°C) calculated (not hydrogel formation observed).*

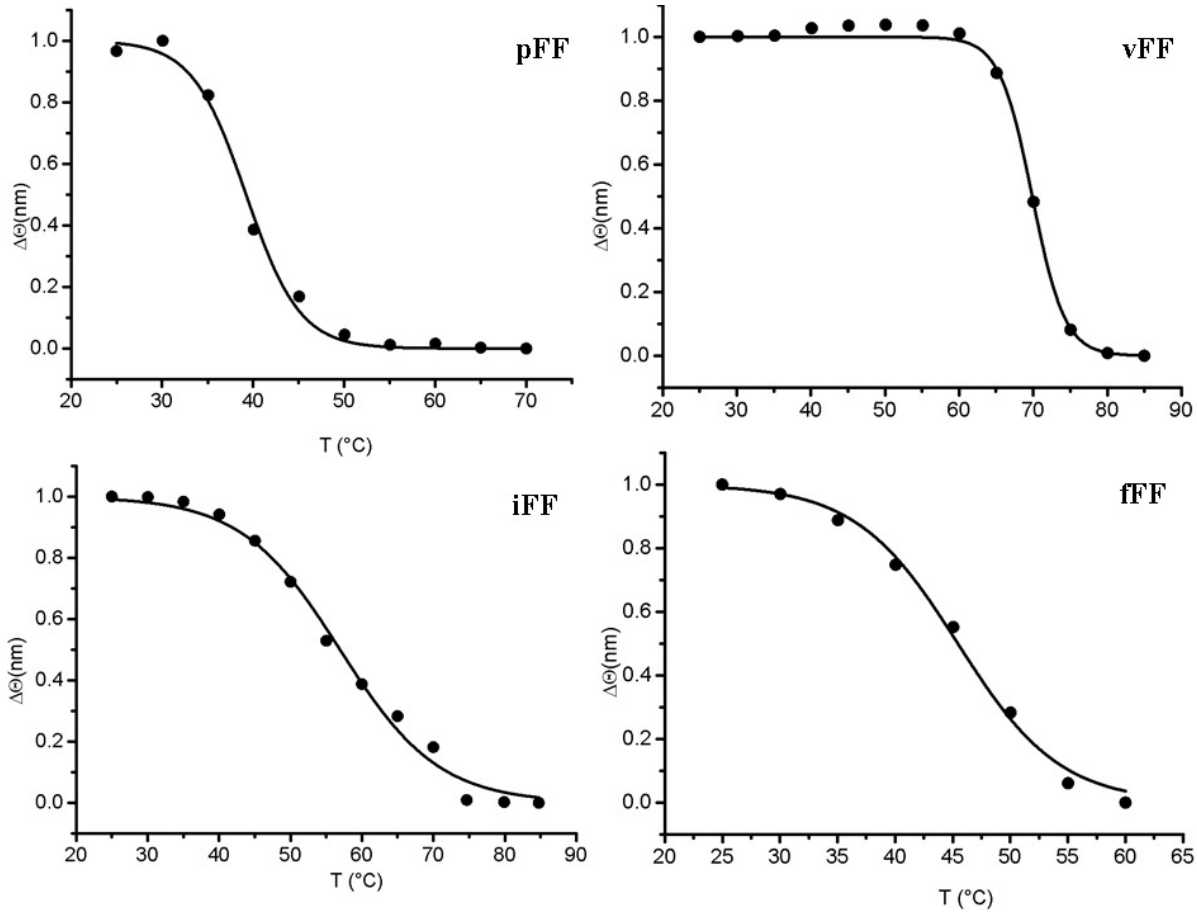

Figure 3.38: Monitoring of supramolecular structure by CD over a temperature ramp up to 85°C.
Melting temperature (Tm) can be determined by plotting molar ellipticity [Θ] at specific wavelength (nm) for each peptide, as the temperature is increased (λ=204 nm, except for pFF, for which is considered the average in 198.5-200.5 nm range).

Seq.	MGC	Tr	After heat	Rev.	Tm
sFW*	n.a.		n.a.	n.a.	n.a.
vFW	20mM			NO	55°C
iFW	7mM			YES	64°C
fFW	11mM			YES	61°C

Table 3.6: Sequences tested, picture of the xFW hydrogels before and after the hot-bath test, thermal reversibility and Tm –(°C) calculated (not hydrogel formation observed).*

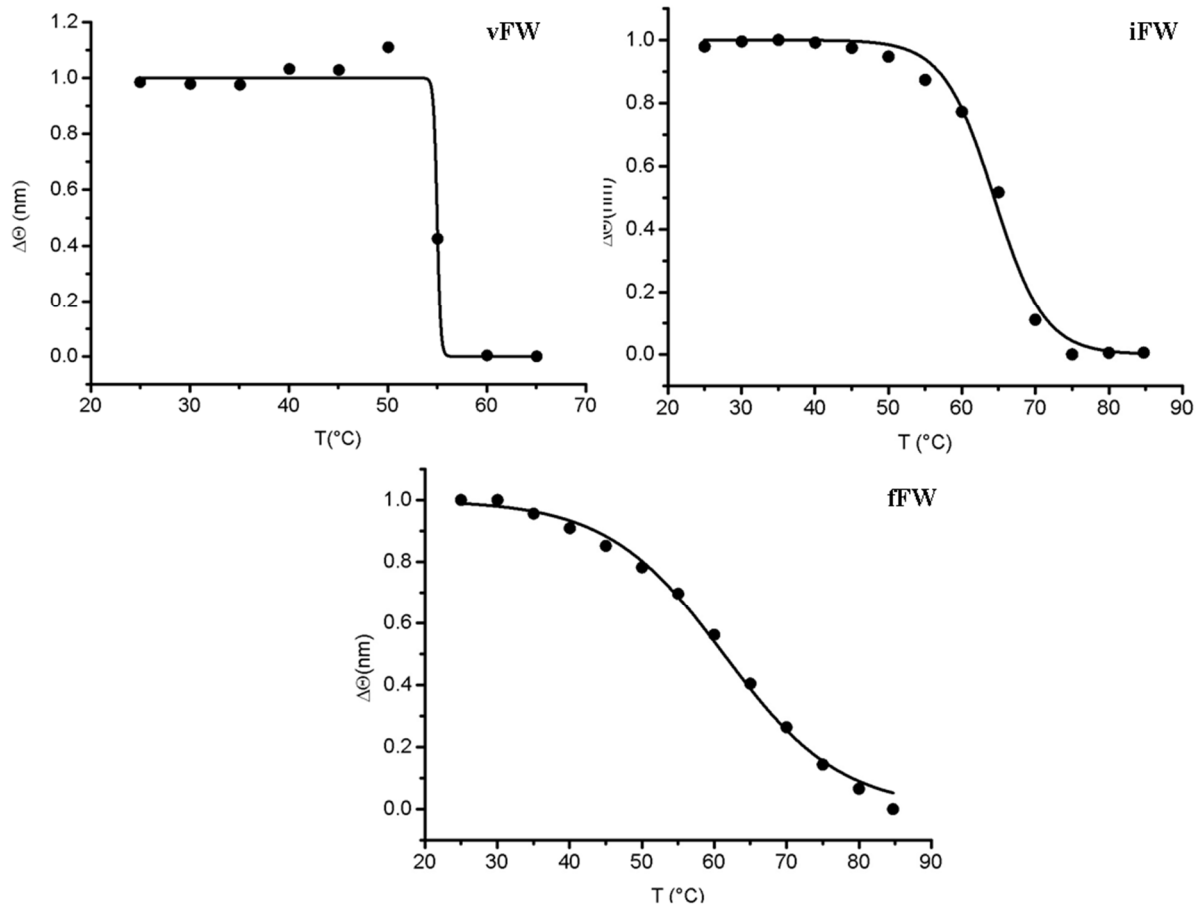

Figure 3.39: Monitoring of supramolecular structure by CD over a temperature ramp up to 85°C.
Melting temperature (Tm) can be determined by plotting molar ellipticity [Θ] at specific wavelength (nm) for each peptide, as the temperature is increased (λiFW=237.5 nm, whereas for vFW, is considered the average in 230-234 nm range, for fFW, is considered the average in 232-236 nm range).

Seq.	MGC	Tr	After heat	Rev.	Tm
pWF*	n.a.		n.a.	n.a.	n.a.
fWI	22mM			YES	61°C
wLL	17mM		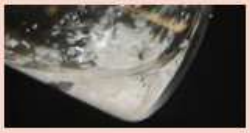	NO	60°C
wFL	8mM			YES	54°C
fWF	11mM			YES	63°C
wWF	12mM			NO	67°C
wFF*	n.a.		n.a.	n.a.	n.a.

Table 3.7: Sequences tested, picture of the xXX hydrogels before and after the hot-bath test, thermal reversibility and Tm °C) calculated (not hydrogel formation observed).*

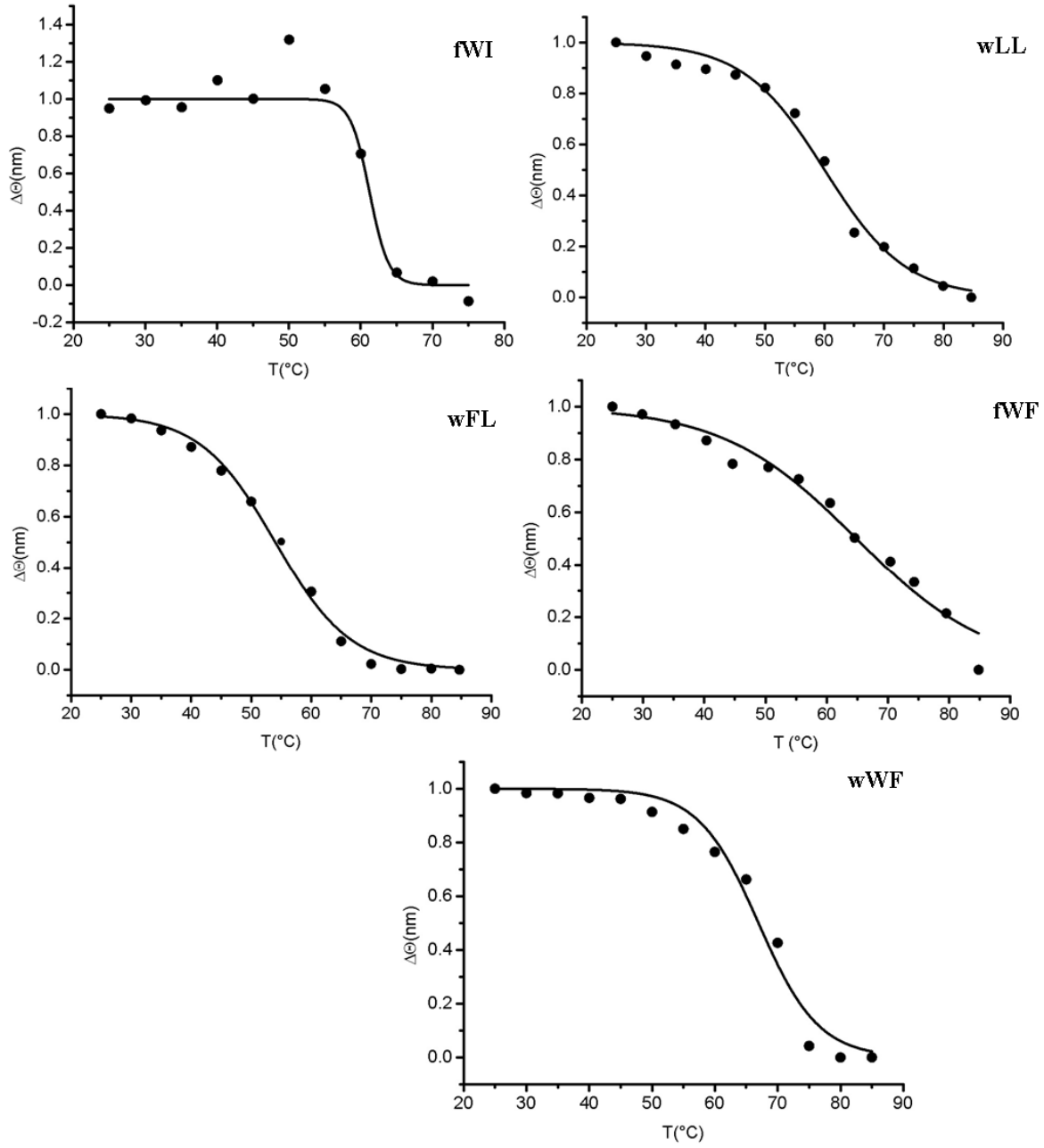

Figure 3.40: Monitoring of supramolecular structure by CD over a temperature ramp up to 85°C. Melting temperature (Tm) can be determined by plotting molar ellipticity [Θ] at specific wavelength (nm) for each peptide, as the temperature is increased (λfWF=238 nm, λfwFL=229.5 nm, λwWF=236 nm, whereas for fWI, is considered the average in 203-205 nm range, for wLL, is considered the average in 233-236 nm range).

3.3.3. Fourier-Transformed Infrared Spectroscopy (FT-IR)

Fourier Transform-Infrared Spectroscopy (FT-IR) is an analytical technique that measures the absorption of infrared radiation by the sample material versus wavelength. When the infrared radiation passes through the sample, the absorbed IR radiation excites molecules into a higher vibrational state. The energy difference between the initial state and the excited vibrational state establishes a function as the wavelength of the light absorbed by the sample molecule. The FT-IR spectrometer is composed by an interferometer, which modulate the wavelength from the source, and

a detector, which measures the intensity of transmitted light as a function of its wavelength. The resulting interferogram is then analysed applying Fourier transforms to obtain the infrared spectrum, presented as a plot of intensity (as percentage of light transmittance or absorbance) versus wavenumber, as reciprocal of wavelength (in cm^{-1}). Attempts of peptides secondary structure investigations were performed through FT-IR, using the KBr pellet method. The pellet prepared for each sample contains the dried hydrogel form obtained after storing under vacuum overnight the hydrogels. In a typical FT-IR peptide spectra, amide I (1600-1700 cm^{-1}) and amide II (1480-1575 cm^{-1}) bands are the two more important and informative vibrational bands of the protein backbone [90] [91]. FT-IR of small peptides could be very challenging and difficult to explain due to the fact that the highly flexible short peptides compared to bigger proteins can generate large deviations of amide bands associated with different secondary structures. Additional bands in the amide I region could be detected due to the peptide aggregation that could be misunderstanding and fallaciously attributed to a particular peptide structure. Moreover, the COO^- stretching vibration of the trifluoroacetate counterion that can remain with the peptide after its cleavage from the resin and HPLC purification procedure can generate an intense absorbance band at 1673 cm^{-1} [92] and the absorption of water can do the same at 1650 cm^{-1} in amide I region [93]. This latter band is typically the most intense absorbance band usually associated to the C=O stretching vibration and correlated to backbone conformation and it is unique for each peptide sample tested, whereas amide II band is associated to N-H bending vibration and C-N stretching vibration and less informative. The FT-IR collected for all the peptides were not sufficiently informative due to the incomplete adequacy of this technique for this type of samples as it could be instead the Attenuated Total Reflectance Infrared Spectroscopy (ATR-IR), which was previously successfully to collect valuable information about peptide secondary structure [78]. In ATR-IR, the samples (*e.g.*, thin films, layer of dried gels) are pressed on the top of a crystal (*e.g.*, diamond, germanium) and a beam of infrared light passing through the latter, reflects the surface in contact with the sample, extending the wave inside it. Once the beam has come out it is collected by a detector. FT-IR spectra are reported in the Supplementary section.

3.3.4. X-Ray Diffraction (XRD) single crystal structures

All the single crystal structures from the heterochiral and homochiral tripeptides were prepared in the Superstructures lab (thanks also to the other members of the team) and solved at Synchrotron Elettra in Research Area at Basovizza (Trieste) thanks to Dr. Rita De Zorzi, Dr. Sabrina Semeraro and Caterina Deganutti. The structures obtained until now (more trials are still ongoing)

are summarised in the table below, considering the challenge of crystallisation process for some sequences it was possible to solve the enantiomer structures and collect equally useful data and information, considering that in ordinary X-ray diffraction method both the enantiomers give same diffraction pattern.

Sequences	XRD
fYI	✓
pFF	
vFF	✓
VFF	✓
iFF	✓
IFF	✓
fFF	✓
FFF	✓

Sequences	XRD
sFW	
vFW	✓
iFW	✓
fFW*	

Sequences	XRD
pWF	✓
fWI	
wLL	
wFL	
fWF	
wWF	
wFF	✓

*Table 3.8: Single crystal XRD structure solved (*excluded, because not zwitterionic, with TFA as counterion).*

3.3.4.1. XRD structures of xFF group sequences

In this section are reported the XRD structures solved for peptides of xFF group, except for pFF for which crystallisation trials are still ongoing. In particular for the gelling peptides vFF, iFF and fFF, a comparison could be drawn with the homochiral peptides VFF, IFF and FFF structures (thanks to Maria Cristina Cringoli form our group, unpublished data).

fYI (crystallised from methanol and water, and from phosphate buffers)

The structures of the peptide fYI crystallised by vapour diffusion of water in a methanol solution, and from a phosphate buffer are isomorphous as shown by the unit cell parameters (see Supplementary section) and by the arrangement of the peptides in the uni cell. The information collected from both XRD structures are very important because they show same arrangements of the peptides in organic solvent and in buffer solution used for hydrogel preparation. This let us to

hypothesise that in general the structures crystallised in water/alcohol mixtures show the same supramolecular packing as in buffer.

The asymmetric unit contains two molecules of the peptide in its zwitterion form. For both structures, the additional electron densities present in the asymmetric unit were recognized as 3 molecules of water, used as precipitant in the crystallization experiment or present in the mother solution. A total of 4 molecules of peptide, related by symmetry operators of the $P2_1$ space group, are present in the unit cell. The crystal is formed by a close packing of the peptide, with water molecules filling the residual space (*Figure 3.41*).

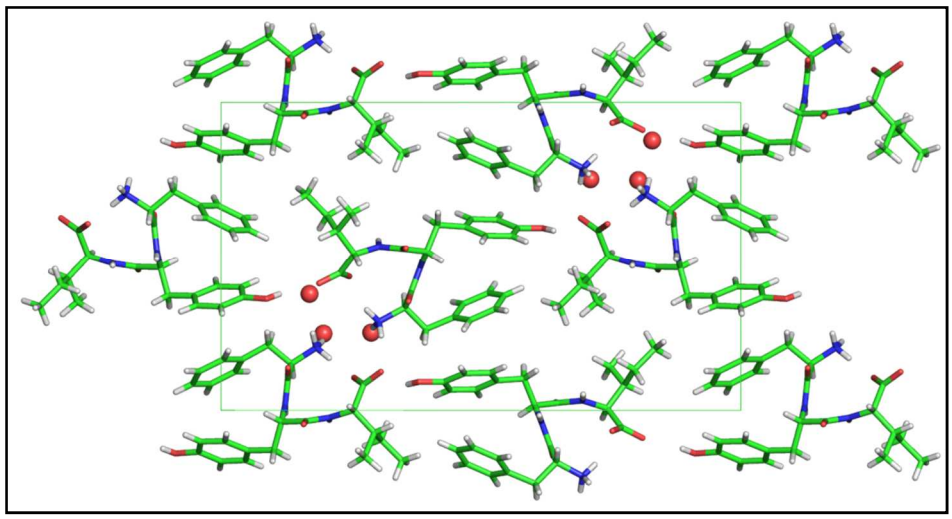

Figure 3.41: Crystal packing in the crystal of the peptide fYI, grown in methanol and water. Views along the a crystallographic axis (peptide molecules are shown as sticks, water molecules are shown as spheres, carbon atoms are shown in green, oxygen in red, nitrogen in blue and hydrogen in white).

Hydrophilic interactions are present in the regions occupied by the N- and C-termini of the peptides and involving also the solvent molecules, the hydroxyl group of the Y residue and the carboxyl and amino groups of the backbone (*Figure 3.42*). Hydrogen bond distances range from 2.7 to 3.2 Å.

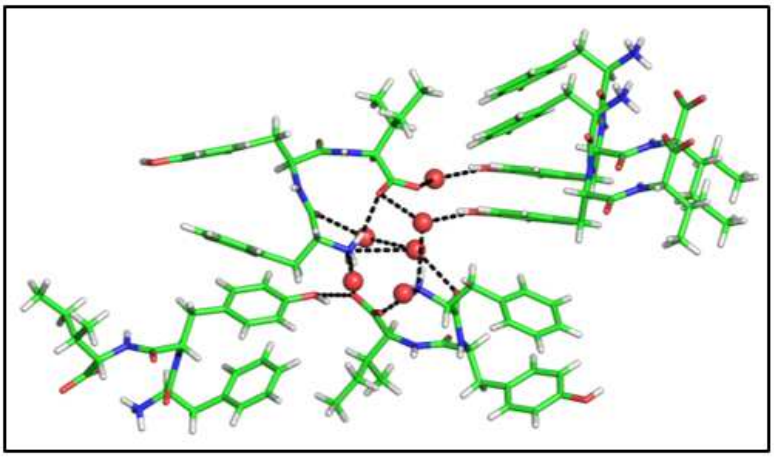

Figure 3.42: Hydrophobic interactions in the crystal structure of peptide fYI, grown in methanol and water. Hydrophilic interactions involve N- and C- termini of the peptide, hydroxyl group of the tyrosine residue and the solvent molecules. Additional hydrogen

bonding interactions involving the carboxyl and the amino groups of the peptide backbone are omitted for clarity. Hydrogen bond and salt bridges interactions are shown as black dashes. Distance between donor and acceptor atoms range between 2.7 and 3.2 Å.

On the opposite side, the hydrophobic groups show CH-π interactions and weaker π-π interactions, both within the same peptide (*e.g.*, the π-π interaction between the phenyl rings of tyrosine and phenylalanine residues) and between adjacent peptides (*Figure 3.43*).

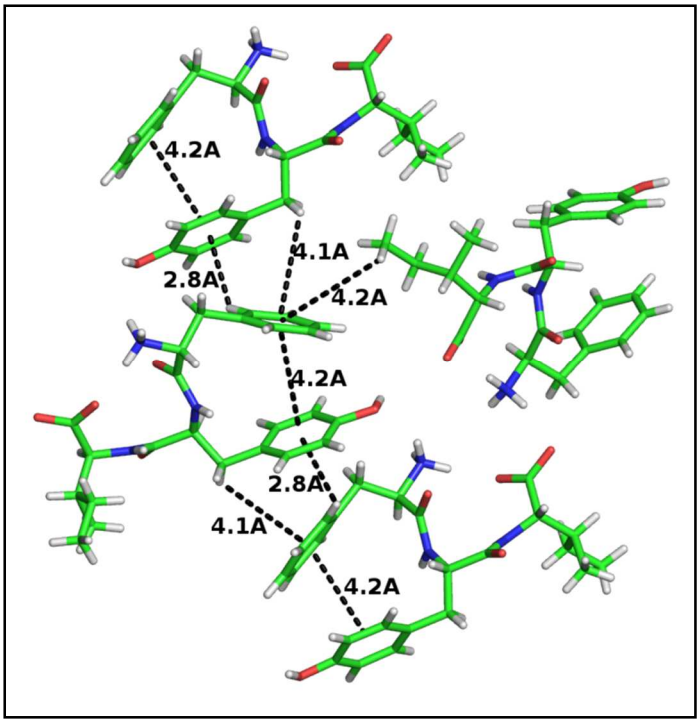

Figure 3.43: Hydrophobic interactions in the crystal structure of peptide fYI, grown in methanol and water. Hydrophilic interactions involve N- and C- termini of the peptide, hydroxyl group of the tyrosine residue and the solvent molecules. Additional hydrogen bonding interactions involving the carboxyl and the amino groups of the peptide backbone are omitted for clarity. Hydrogen bond and salt bridges interactions are shown as black dashes. Distance between donor and acceptor atoms range between 2.7 and 3.2 Å.

Vff (enantiomer of vFF)

The asymmetric unit contains a single molecule of the peptide in its zwitterion form and a molecule of methanol, used as solvent in the crystallization experiment. A total of 4 molecules of peptide, related by symmetry operators of the $P2_12_12_1$ space group, are present in the unit cell.

The crystal packing shows a clear separation between regions with prevalence of hydrophobic groups and regions with hydrophilic interactions (*Figure 3.44*). Hydrophilic interactions are present between the peptides, namely hydrogen bonds between the carbonyl and the amide moieties (*Figure 3.45*, black dashes) and salt bridges between the N-terminus and the C-terminus of different peptides (*Figure 3.46*). In addition, a weaker hydrogen bonding interaction is present between the carbonyl moiety and the hydrogen of the CH-π (*Figure 3.45*, cyan dashes). Notable hydrophobic interactions in the structure of Vff are π-π stacking interactions between the phenyl rings of neighbouring peptides (*Figure 3.45*, blue dashes) and CH-π interactions (*Figure 3.47a*). The peptide interacts also with the

methanol molecule present in the unit cell, through two salt bridges between the hydroxyl group of the alcohol and the C- and N-termini of the peptide (*Figure 3.47b*).

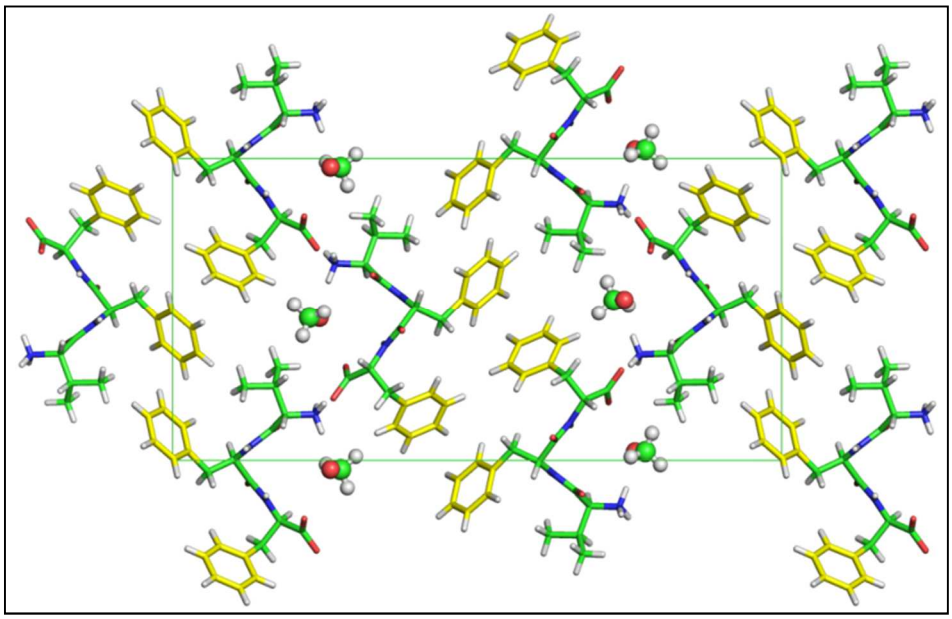

Figure 3.44: Crystal packing in the crystal of the peptide Vff, grown in acetonitrile and water. Views along the crystallographic axis a (peptide molecules are shown as sticks, methanol molecules are shown as spheres, carbon atoms are shown in green, except carbons of the phenyl rings shown in yellow; oxygen atoms are shown in red, nitrogen in blue and hydrogen in white).

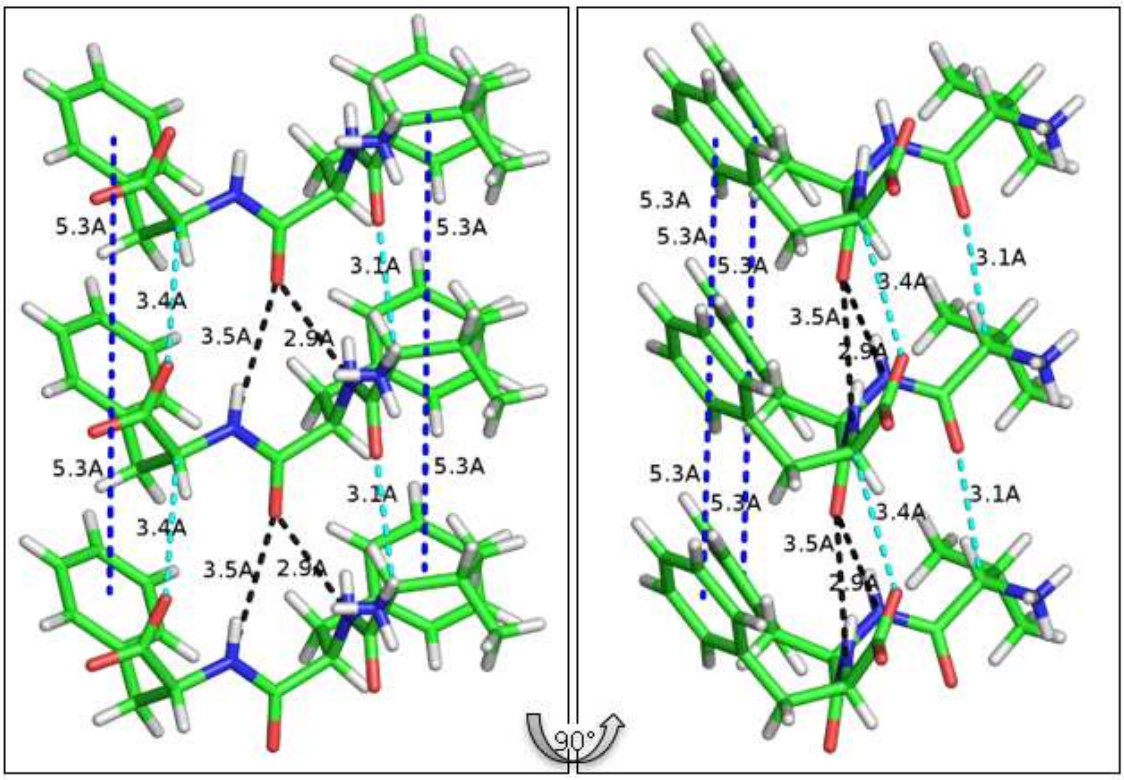

Figure 3.45: Hydrophilic and hydrophobic interactions between adjacent peptides. The two panels show views 90° apart around the vertical axis of the figure. Hydrogen bonding interactions are marked with black dashes and donor-acceptor distances are reported. Interactions between a Cα and a carbonyl moiety can be described as a weak type of hydrogen bonding interactions; these are marked with cyan dashes and the Cα-O distances are reported. Hydrophobic interactions between the phenyl rings are marked with blue dashes and distances between the centres of interacting phenyl rings are shown. Carbon atoms are shown in green, oxygen atoms in red, nitrogen in blue and hydrogen in white.

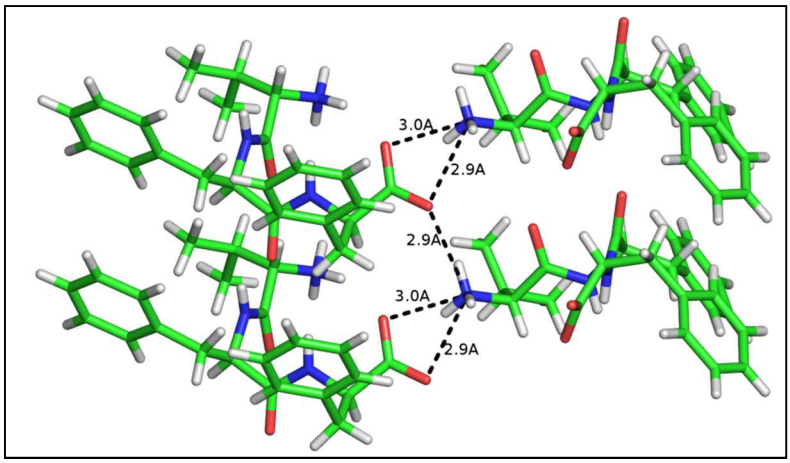

Figure 3.46: Salt bridges interactions involving the N- and C- termini of the peptides. Distances between carbon and nitrogen atoms are shown.

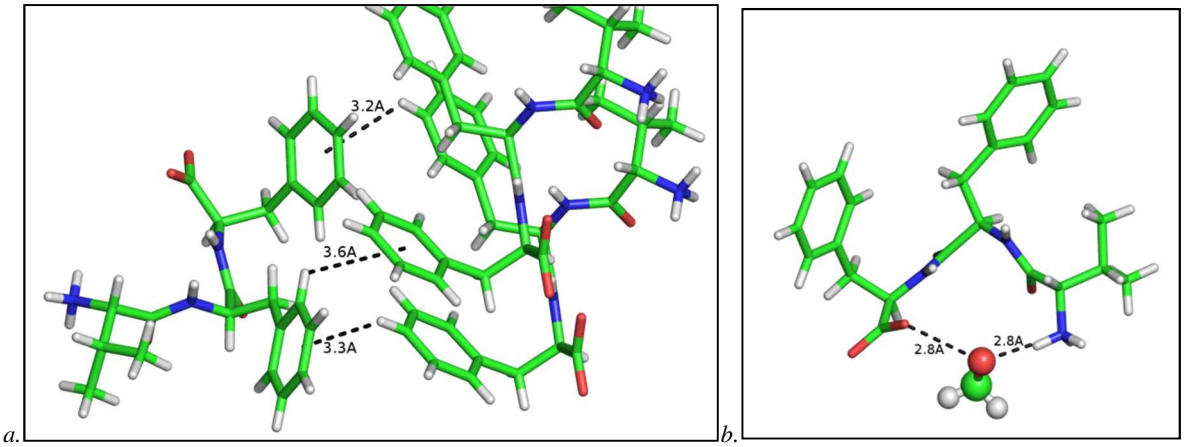

a. *b.*

Figure 3.47: CH-π interactions involving the phenyl rings of the Vff peptide in the crystal structure. Distances from the hydrogen atom to the centre of the phenyl ring are shown (a). Salt bridge interactions involving the peptide Vff and the solvent molecule present in the asymmetric unit (methanol). Distances from the oxygen atom of the hydroxyl group to the charged atoms of the termini are shown (b).

Iff (enantiomer of iFF)

The asymmetric unit contains three molecules of the peptide in its zwitterion form. The additional electron densities present in the asymmetric unit were recognized as a molecule of methanol and 6 molecules of water, used as solvent and precipitant in the crystallization experiment, respectively. The crystal packing (*Figure 3.48*) shows a close packing of the peptide molecules, interacting through their hydrophilic groups on one side, and through their hydrophobic groups on the opposite side. In particular, the three independent peptide molecules are arranged around a C_3 non-crystallographic symmetry (NCS) axis (shown in projection in *Figure 3.49*).

Peptides are held together to form the structure by hydrophilic interactions (*Figure 3.50*), namely hydrogen bonds and salt bridges, and hydrophobic interactions between the side chains of the peptides. *Figure 3.51* shows some of the hydrophobic interactions present in the structure of Iff. Phenyl rings form CH-π interactions with aromatic or aliphatic hydrogen atoms belonging to different peptides (*Figure 3.51*), while no π-π interactions can be observed between the phenyl rings.

a.

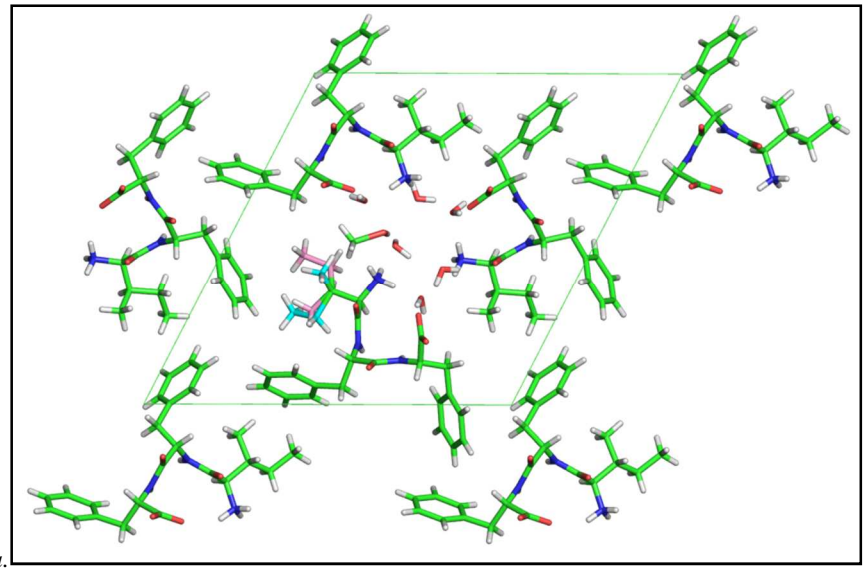

b.

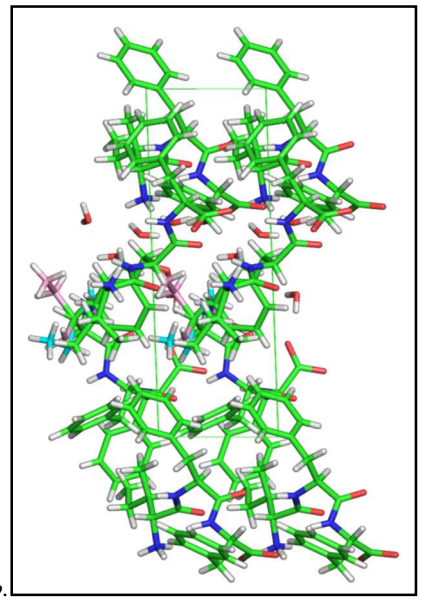

Figure 3.48: Crystal packing in the crystal of the peptide Iff, grown in methanol and water. Views along the a crystallographic axis (a), the b crystallographic axis (b), (peptide molecules are shown as sticks). Carbon atoms are shown in green, except atoms of the disordered isoleucine side chain, which is shown in pink (54% occupancy factor) and cyan (46% occupancy factor) for the two different conformations; oxygen atoms are depicted in red, nitrogen in blue and hydrogen in white.

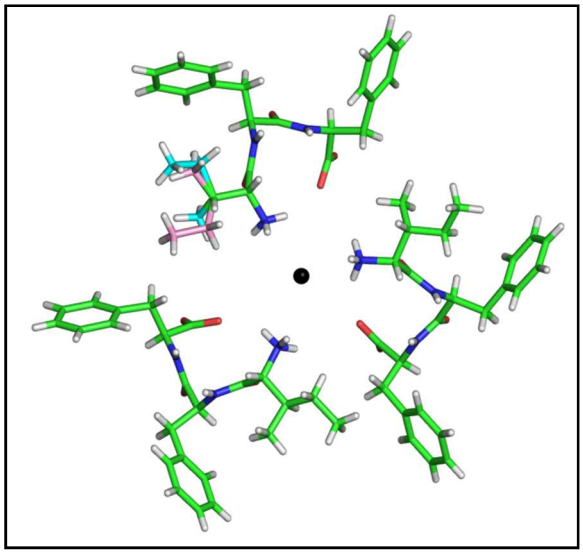

Figure 3.49: Arrangement of the three independent peptides present in the asymmetric unit of crystals of Iff. The black dot indicated the approximate position of the non-crystallographic symmetry axis C_3 present in the structure. While positions of the phenylalanine side chains are similar for all the independent molecules, the isoleucine side chains display different rotamers in the three molecules.

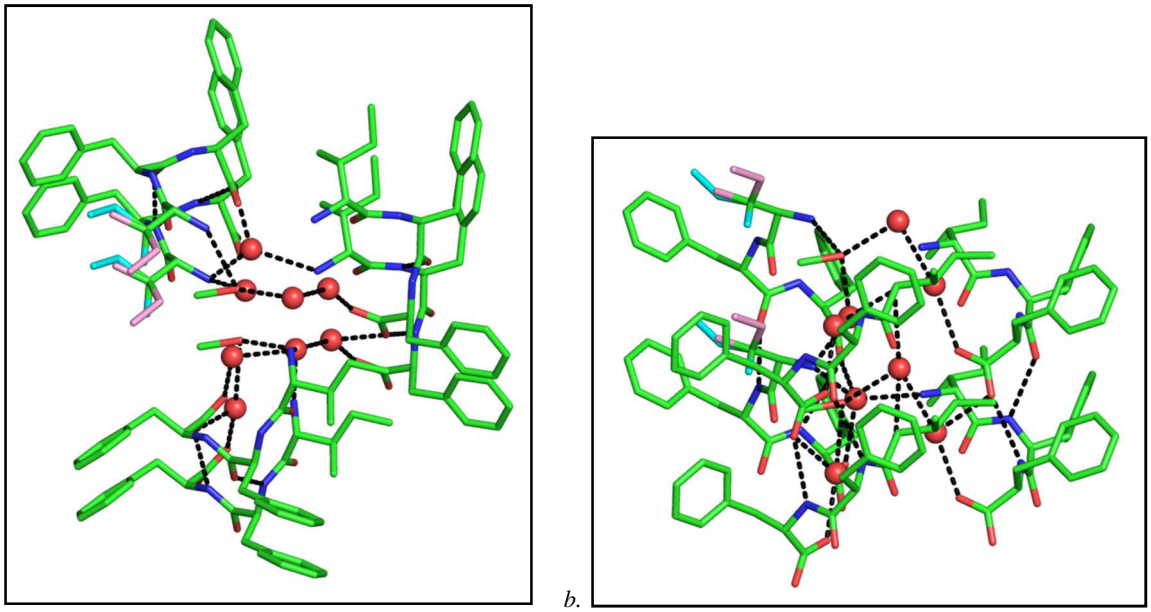

a. *b.*

Figure 3.50: Hydrophilic interactions present in the structure of iFF. Donor-acceptor distances are shown in dashes for hydrogen bonds and salt bridges. The main interactions involve a moiety of the peptide (charged N- and C- terminal groups, or non-charged carboxyl or amino groups) and a molecule of solvent/precipitant (methanol or water). All distances displayed are in the range of 2.7-3.3 Å, compatible with strong interactions.

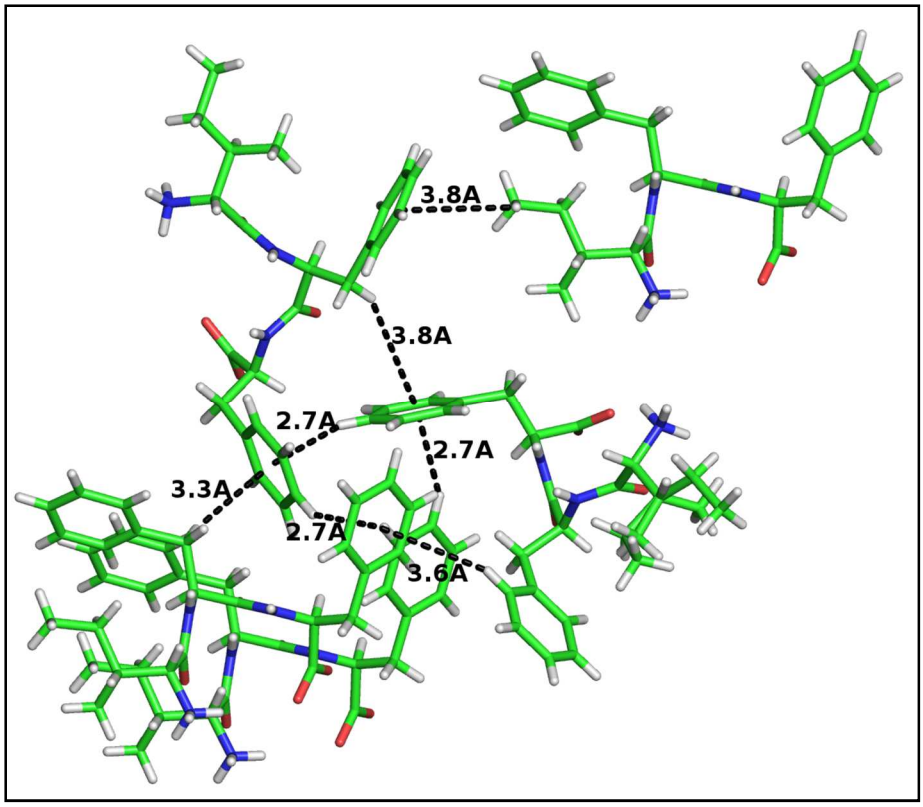

Figure 3.51: Some of the CH-π hydrophobic interactions involving peptides in the structure of Iff. Distances between the hydrogen atom and the centre of the phenyl ring are shown.

fFF

The asymmetric unit contains a single molecule of the peptide in its zwitterion form. The additional electron densities present in the asymmetric unit were recognized as a molecule of 2-propanol and 2 molecules of water, used as solvent and precipitant in the crystallization experiment, respectively. A total of 2 molecules of peptide are present in the unit cell, each related to the others by the symmetry elements of the $P2_1$ space group.

In the crystal packing (*Figure 3.52*), mainly hydrophobic and mainly hydrophilic regions are separated. Hydrophilic interactions, namely hydrogen bonding and salt bridges, between carbonyl and amino moieties of the peptides form a pattern resembling the hydrogen bonding pattern of parallel β-sheets (*Figure 3.53*). In addition, a wide pattern of hydrophobic interactions, involving also 2-propanol molecules, contributes to the close packing of the structure (*Figure 3.54*): intramolecular and intermolecular π-π interactions, CH-π interactions between phenyl groups, and CH-π interactions between methyl moieties of 2-propanol molecules and phenyl groups. The overall packing is also stabilized by extensive hydrophilic interactions between the zwitterionic peptide and the solvent and precipitant molecules, 2-propanol and water, respectively (*Figure 3.55*). Both water molecules are involved in 4 hydrogen bonds, two as donors and two as acceptors, in a coordination geometry closely

resembling a tetrahedron. Hydrogen bonding distances between the peptide, the 2-propanol molecules and the water molecules are in the 2.7-3.0 Å range.

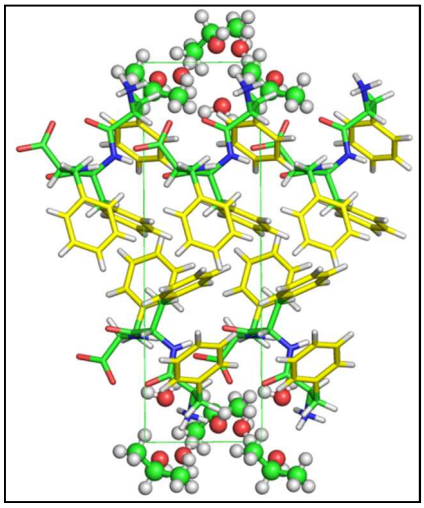

a.

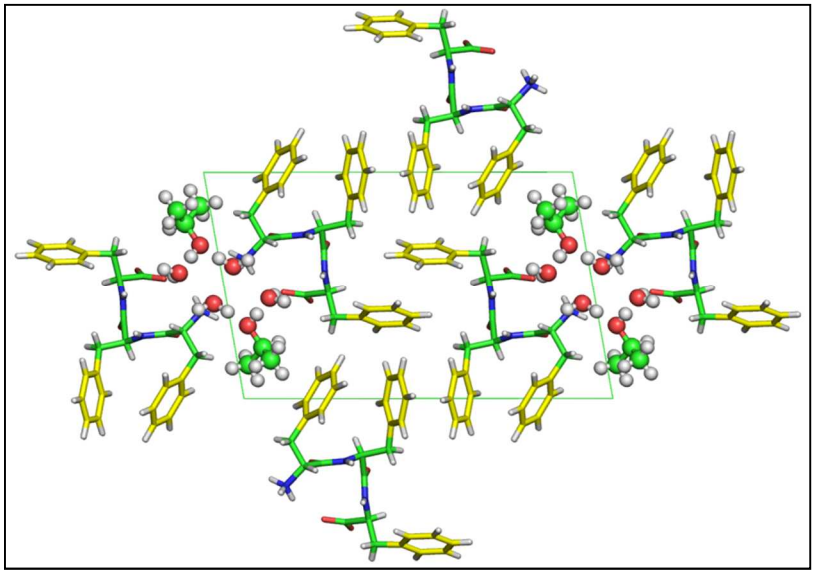

b.

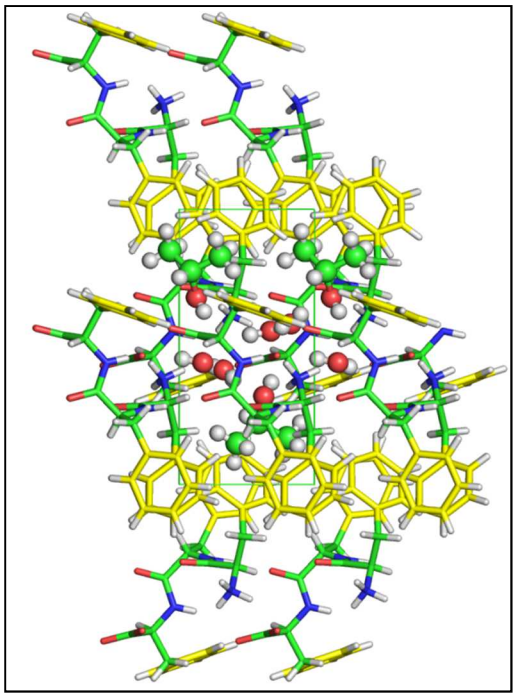

c.

Figure 3.52: Crystal packing in the crystal of the peptide fFF, grown in 2-propanol and water. Views along the crystallographic axis (a), the b crystallographic axis (b) and the c crystallographic axis (c). Peptide molecules are shown as sticks, solvent and precipitant molecules are shown as spheres. Carbon atoms are shown in green, except carbons of the phenyl groups shown in yellow; oxygen atoms are shown in red, nitrogen in blue and hydrogen in white.

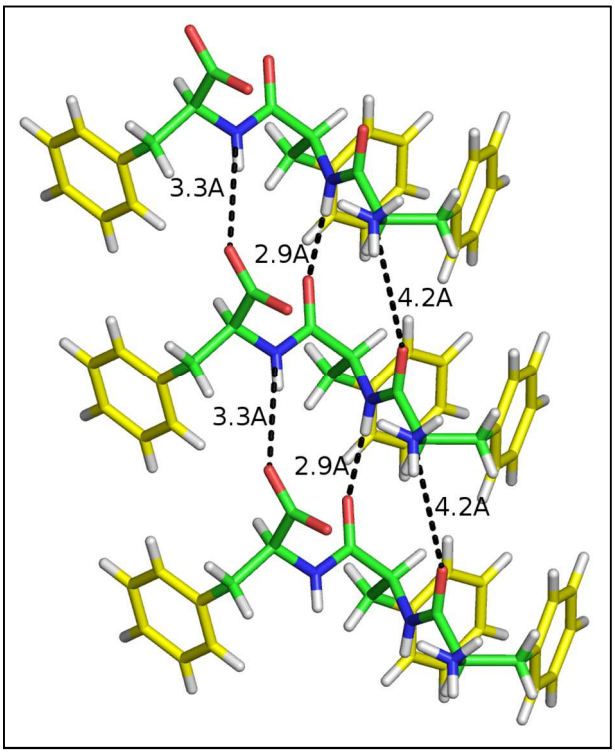

Figure 3.53: Hydrogen bonding and slat bridge interactions between the peptides, resembling the parallel β-sheet pattern in proteins. Interactions are marked with black dashes and donor-acceptor distances are reported.

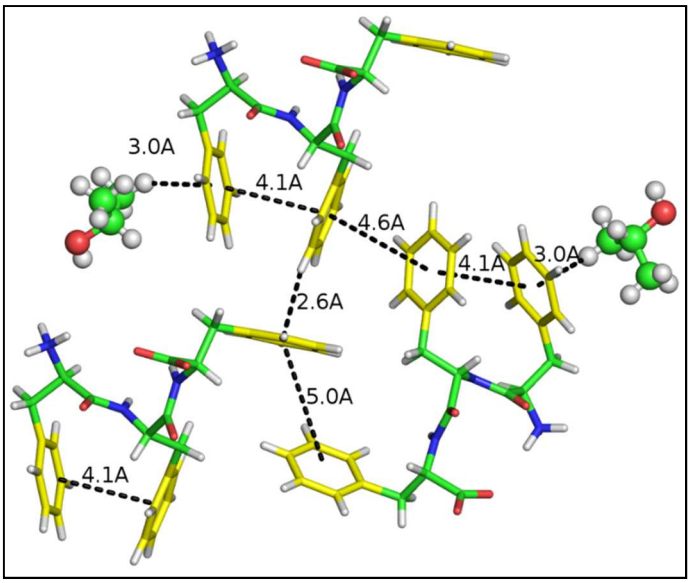

Figure 3.54: Pattern of hydrophobic interactions in the crystal involving peptide molecules and 2-propanol molecules. Interactions are marked with black dashes and distances between the centres of the phenyl rings, or between the hydrogen atom and the centre of the phenyl ring, are reported.

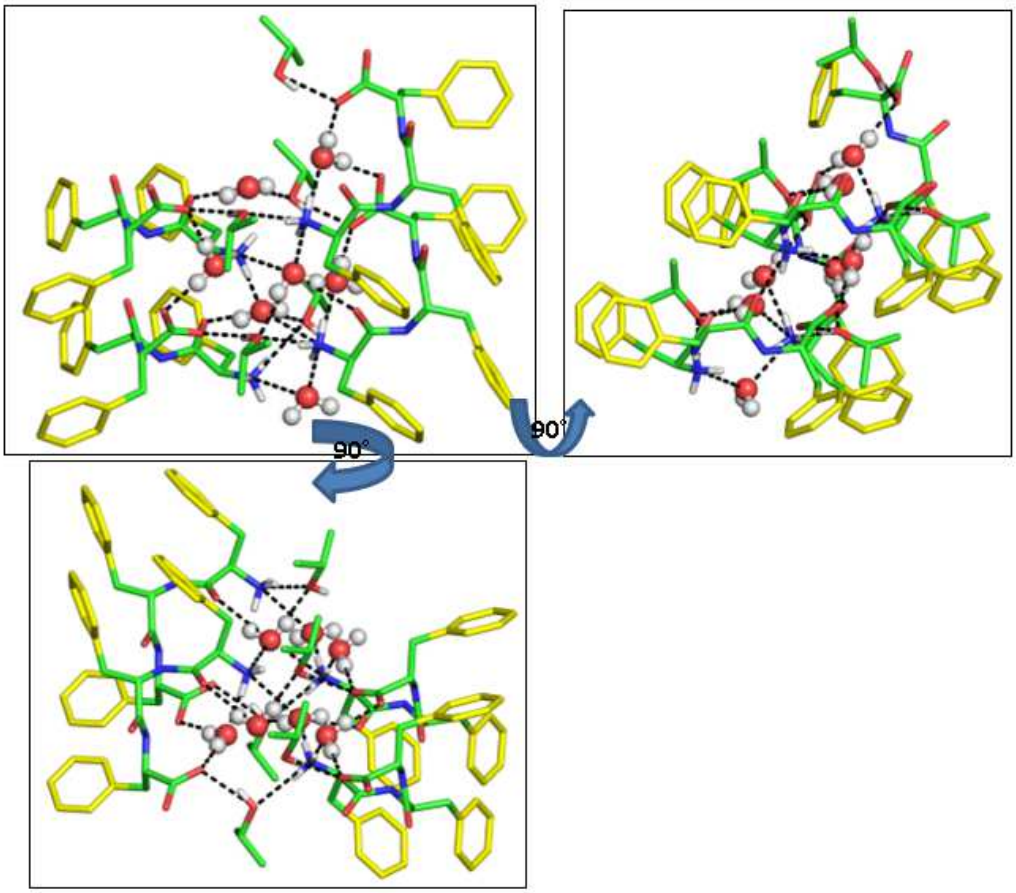

Figure 3.55: Hydrophilic interactions between the peptide molecules and the solvent and precipitant molecules in the structure of fFF. All hydrogen bonding distances marked as dashes are in the 2.7-3.0 Å range. Hydrogen atoms not involved in hydrogen bonding formation between the peptide, the solvent and the precipitant are omitted for clarity. Upper right panel shows a view rotated of 90° along the vertical axis compared to the upper left panel. Lower left panel shows a view rotate of 90°C along the horizontal axis compared to the upper left panel.

VFF

The asymmetric unit contains a single molecule of the peptide in its zwitterion form. The additional electron densities present in the asymmetric unit were recognized as two molecules of methanol, used as solvent in the crystallization experiment. A total of 4 molecules are present in the unit cell, each related to the others by the symmetry elements of the *C2* space group.

The crystal packing shows a clear separation between regions with prevalence of hydrophobic groups and regions with hydrophilic interactions (*Figure 3.56*). Hydrophilic interactions are present between the peptides, namely hydrogen bonds between the carbonyl and the amide moieties (*Figure 3.57*, black dashes) and salt bridges between the N-terminus and the C-terminus of different peptides (*Figure 3.58a*). In addition, weaker hydrogen bonding interactions are present between the carbonyl/carboxyl moieties and hydrogen atoms bound to Cα atoms (*Figure 3.57*, cyan dashes). The patter of salt bridge interactions is completed by the presence of two methanol molecules, each interacting with a terminus of the peptide and forming an additional hydrogen bonding between their hydroxyl groups (*Figure 3.58b*). Notable hydrophobic interactions in the structure of VFF are π-π stacking interactions between the phenyl rings of neighbouring peptides (*Figure 3.57*, blue dashes), and CH-π interactions between the aliphatic chain of the valine residues and the phenyl rings (*Figure 3.59*).

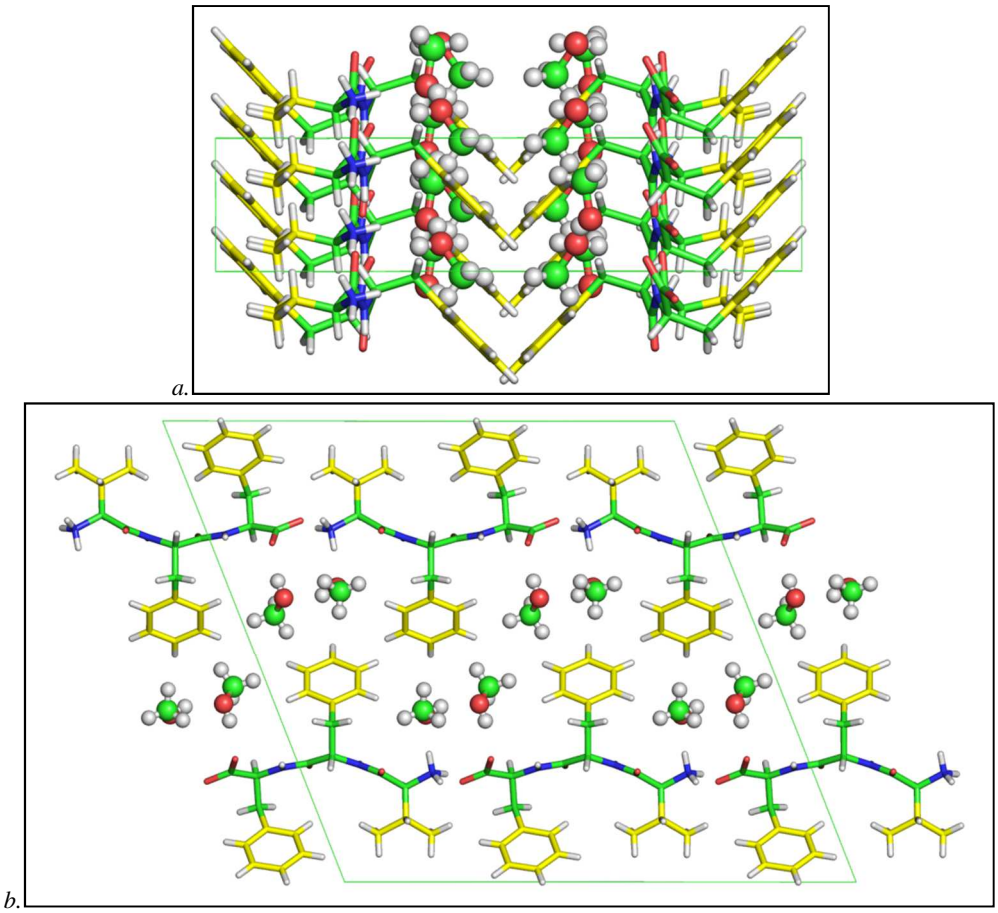

Figure 3.56: Crystal packing in the crystal of the peptide VFF, grown in methanol and water. Views along the a crystallographic axis (a), the b crystallographic axis (b) (peptide molecules are shown as sticks, methanol molecules are shown as spheres). Carbon atoms are shown in green, except carbons of the hydrophobic groups, i.e. phenyl groups of the phenylalanine residues and methylethyl groups of the valine residues, shown in yellow; oxygen atoms are shown in red, nitrogen in blue and hydrogen in white.

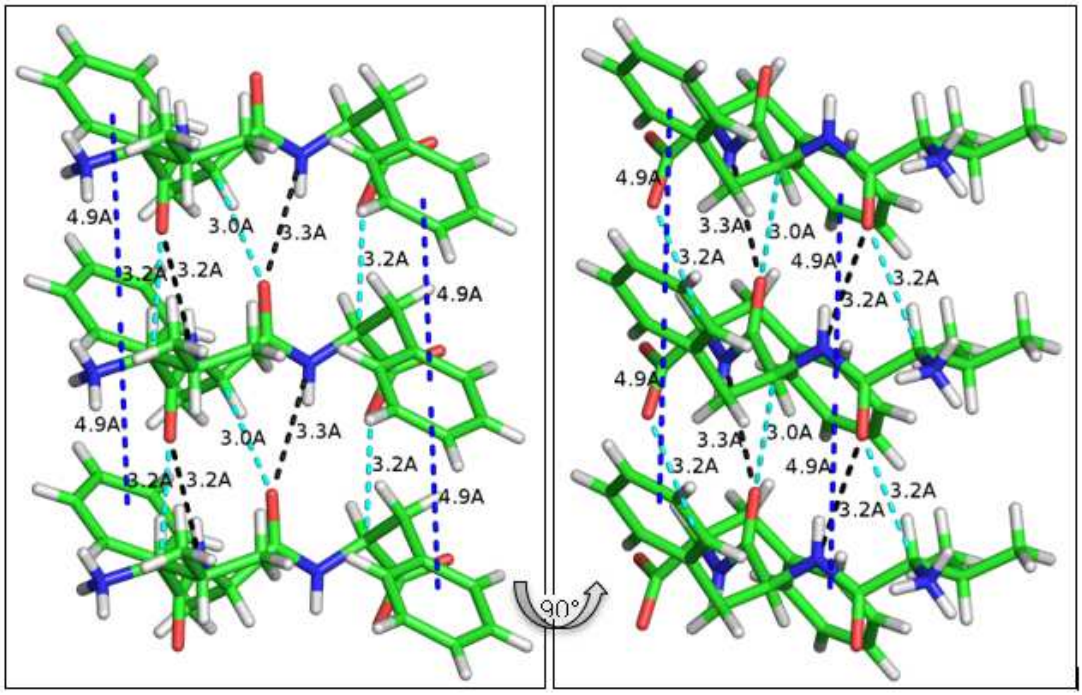

Figure 3.57: Hydrophilic and hydrophobic interactions between adjacent peptides. The two panels show views 90° apart around the vertical axis of the figure. Hydrogen bonding interactions are marked with black dashes and donor-acceptor distances are reported. Interactions between a Cα and a carbonyl moiety can be described as a weak type of hydrogen bonding interactions; these are marked with cyan dashes and the Cα-O distances are reported. Hydrophobic interactions between the phenyl rings are marked with blue dashes and distances between the centres of interacting phenyl rings are shown. Carbon atoms are shown in green, oxygen atoms in red, nitrogen in blue and hydrogen in white.

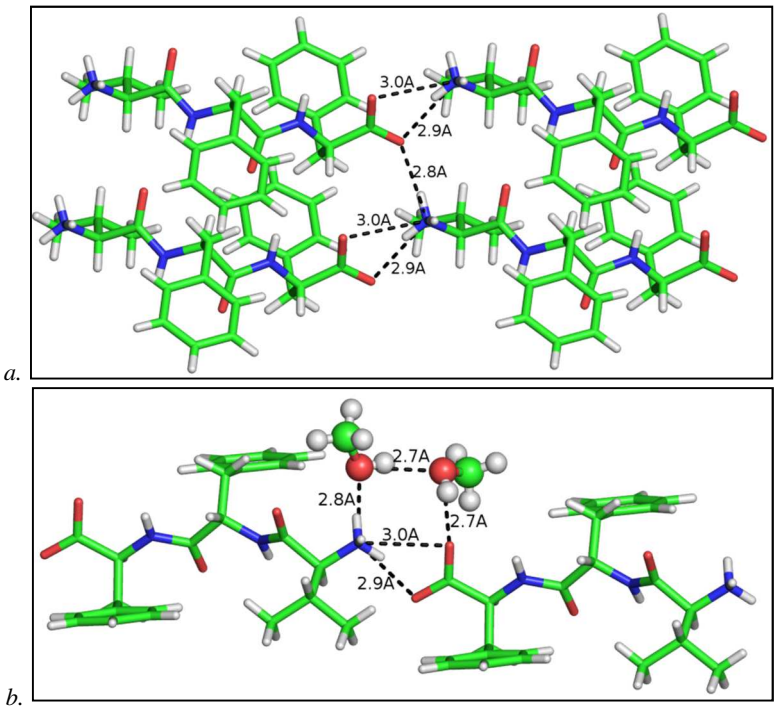

Figure 3.58: Salt bridges interactions involving (a) the N- and C- termini of the peptides, and (b) the same terminal groups and the solvent molecules present in the crystal. In the first panel, methanol molecules are omitted for clarity; in the second methanol molecules are shown as spheres. Distances between carbon and nitrogen atoms involved in the salt bridge interactions, and oxygen atoms involved in the hydrogen bond are shown.

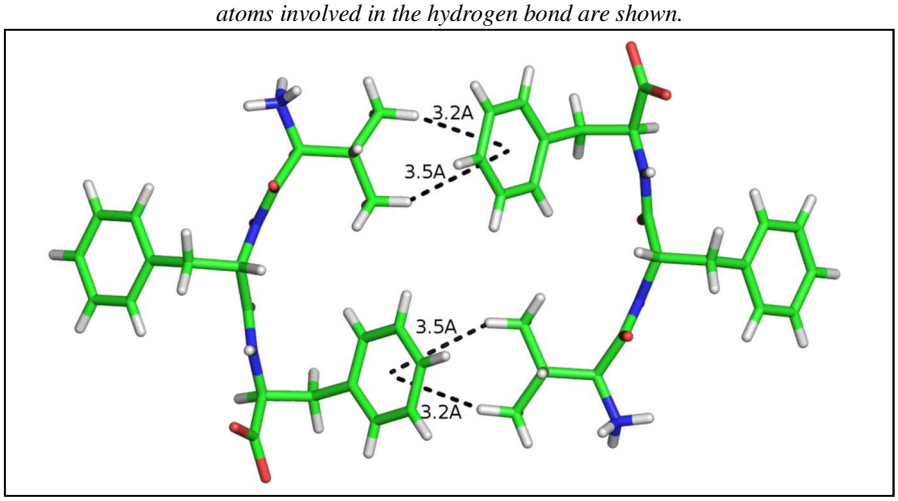

Figure 3.59: CH-π interactions involving the phenyl ring of the terminal phenylalanine residue, and the methyl groups of the valine residue of a different VFF peptide in the crystal structure. Distances from the hydrogen atom to the centre of the phenyl ring are shown.

IFF

The asymmetric unit contains a single molecule of the peptide in its zwitterion form. The additional electron densities present in the asymmetric unit were recognized as 2 molecules of methanol, used as solvent in the crystallization experiment. A total of 4 molecules of peptide, related by symmetry operators of the *C2* space group, are present in the unit cell.

The crystal is formed by a close packing of the peptide, with methanol molecules filling the void spaces between peptide molecules (*Figure 3.60*). The peptide is rather elongated and the N- and C-termini of adjacent peptides interact with each other forming long rows of molecules (*Figure 3.61*,

purple dashes). In a perpendicular direction, piles of peptides are formed by hydrogen bonding interactions (*Figure 3.61*, black dashes). Hydrophilic interactions are present also between the peptide molecules are the alcohol molecules (*Figure 3.62*). Hydrophobic interactions are present between the side chains of the peptide residues, but they are rather weak, i.e. with long distances. The only significant hydrophobic interactions observed are π-π stacking interactions between the phenyl groups belonging to the same pile of peptides (*Figure 3.63*).

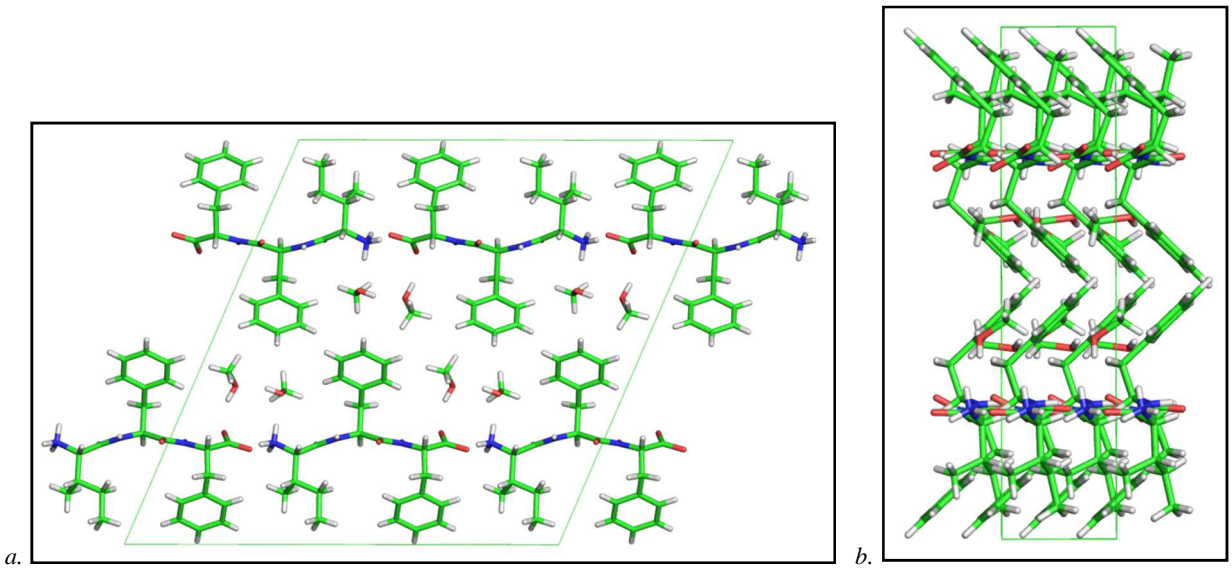

Figure 3.60: Crystal packing in the crystal of the peptide FFF, grown in methanol and water. Views along the b crystallographic axis (a) and the c crystallographic axis (b), (peptide and alcohol molecules are shown as sticks, carbon atoms are shown in green, oxygen in red, nitrogen in blue and hydrogen in white).

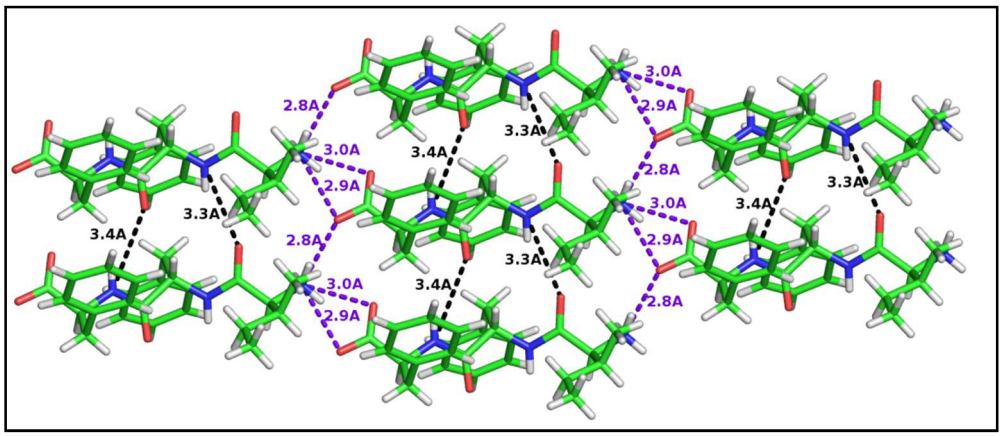

Figure 3.61: Hydrophilic interactions between peptide molecules in the crystal of FFF. Hydrogen bonding interactions are shown as black dashes, while salt bridge interactions are shown as purple dashes. Distances are measured from donor to acceptor atoms in both the H-bond and the salt bridge interactions.

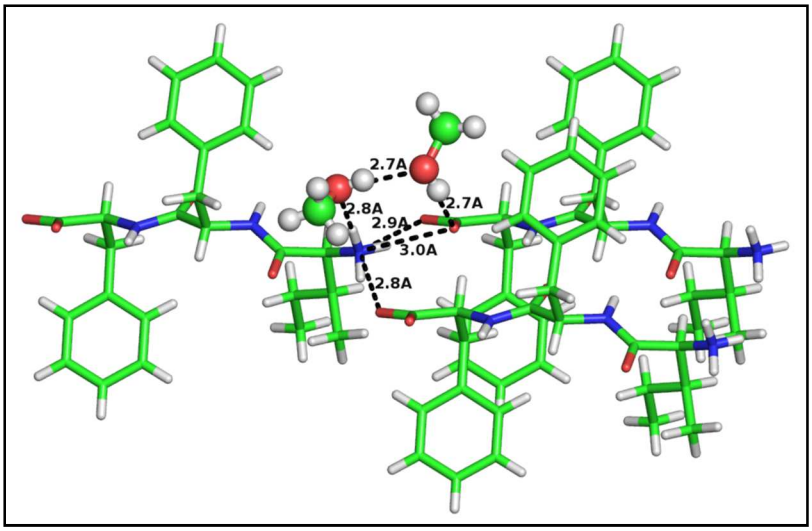

Figure 3.62: Peptide-solvent interactions in the structure of FFF. The alcoholic groups of different methanol molecules bind the N- and C- termini of peptides, in addition to the hydrogen bond formed between the same solvent molecules. Solvent molecules are depicted as ball-and-stick, peptide molecules are depicted as sticks. Donor-acceptor distances are shown.

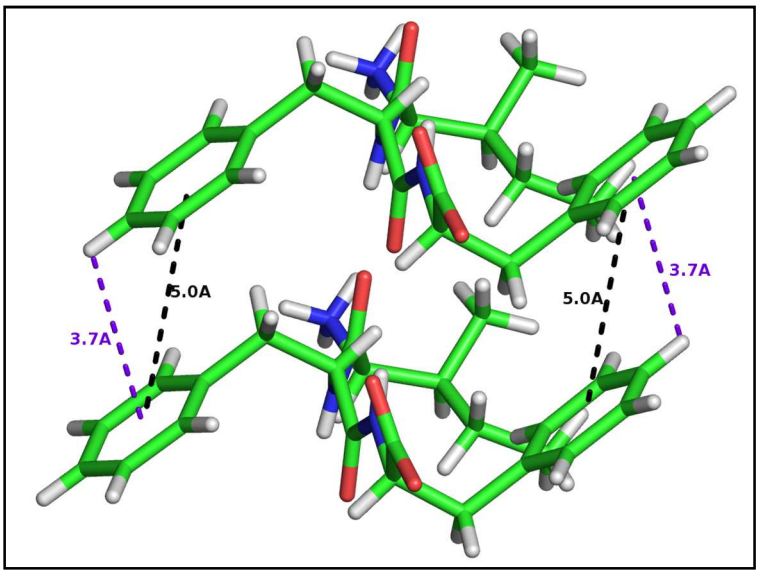

Figure 3.63: Hydrophobic interactions in the structure of FFF. Phenyl groups present form □-□ interactions with a centre-to-centre distance of 5.0 Å (black dashes) and a offset distance of about 3 Å. The distance between the closest hydrogen atom of one phenyl group and the centre of the other phenyl group is also shown (purple dashes)

FFF

The asymmetric unit contains a single molecule of the peptide in its zwitterion form and 2 molecules of methanol, used as solvent in the crystallization experiment. A total of 4 peptide molecules are present in the unit cell, due to the symmetry elements of the *C2* space group.

The crystal packing shows both hydrophilic, namely H-bonds and salt bridges, and hydrophobic interactions, namely π-π stacking interactions, forming hydrophilic and hydrophobic regions within the crystal. *Figure 3.64* shows the crystal packing of FFF in the 3 crystallographic directions. Hydrogen bond interactions hold together peptides in a parallel β sheet-like orientation (*Figure 3.65*),

with 2 hydrogen bonds for each couple of parallel adjacent peptides. In addition, amino- and carbonyl-terminal groups form salt bridges with peptides belonging to different β-sheet bundles (*Figure 3.65*). Hydrophobic interactions are weaker, with a distance of 5.0 Å between the centres of the phenyl rings, but their arrangement shows a probable synergy in their formation (*Figure 3.66*). In addition, methanol molecules interact with peptide molecules through salt bridges between the hydroxyl function of the alcohol and the N- and C-termini, and with other methanol molecules through hydrogen bonds (*Figure 3.67*).

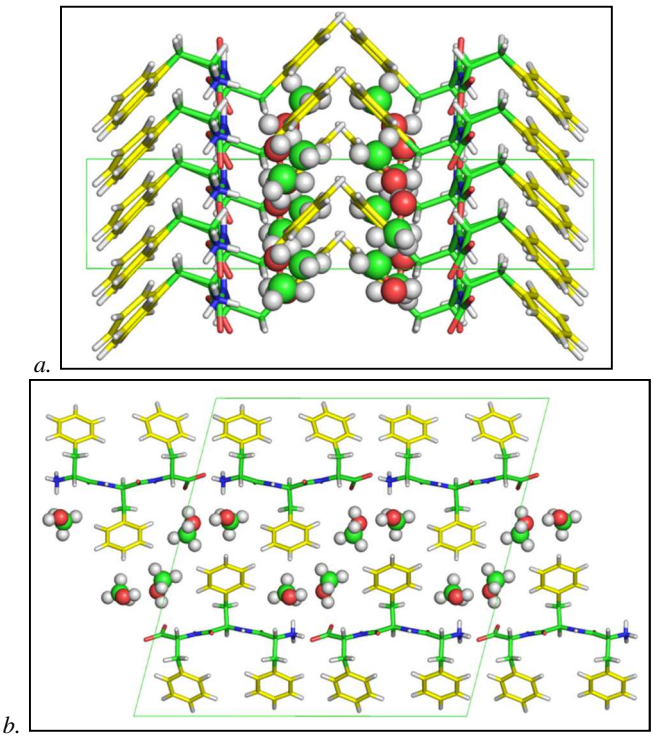

Figure 3.64: Crystal packing in the crystal of the peptide FFF, grown in methanol and acetonitrile. Views along the crystallographic axis (a), the b crystallographic axis (b), (peptide molecules are shown as sticks, methanol molecules are shown as spheres, carbon atoms are shown in green, except carbons of the phenyl rings shown in yellow; oxygen atoms are shown in red, nitrogen in blue and hydrogen in white).

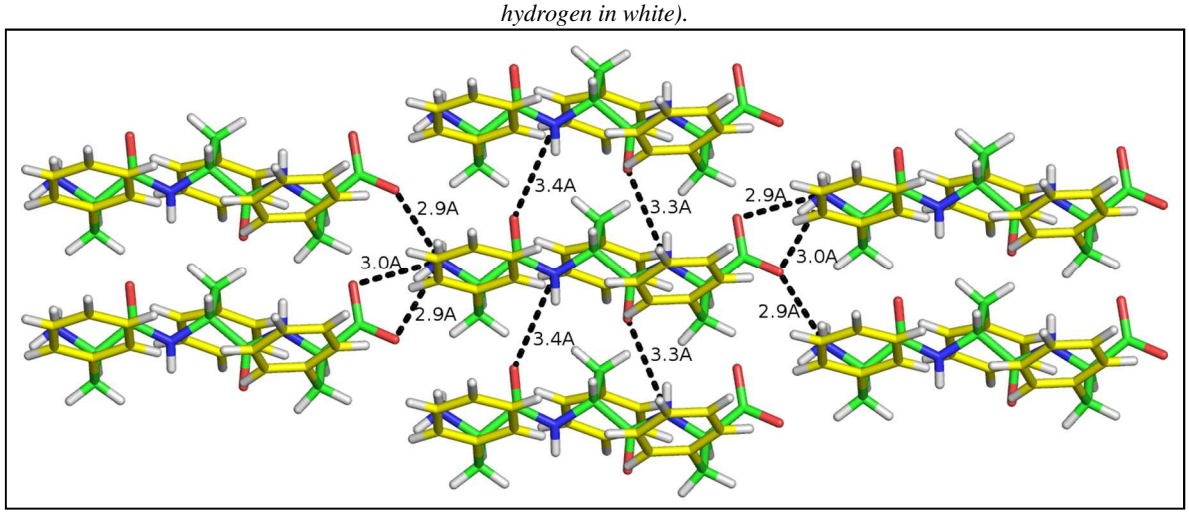

Figure 3.65: Hydrogen bonds and salt bridges between molecules of the peptide FFF in the crystal structure. For each interaction, distance in Å between donor and acceptor atoms is shown. Hydrogen bond interactions (distances 3.3-3.4 Å) between adjacent peptides show a pattern similar to parallel β-sheet secondary structure in proteins. Each N- and C-terminal group interacts through salt bridges with 2 peptide molecules (distances 2.9-3.0 Å).

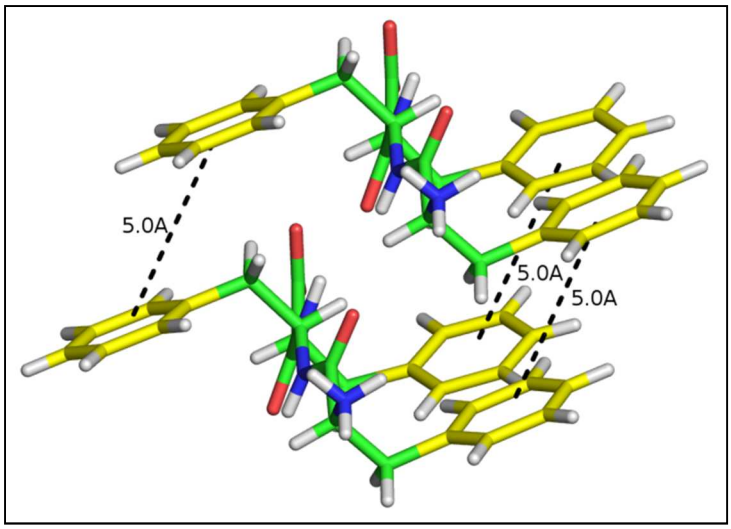

Figure 3.66: Hydrophobic interactions between two adjacent peptides. Distances between the centres of interacting phenyl rings are shown.

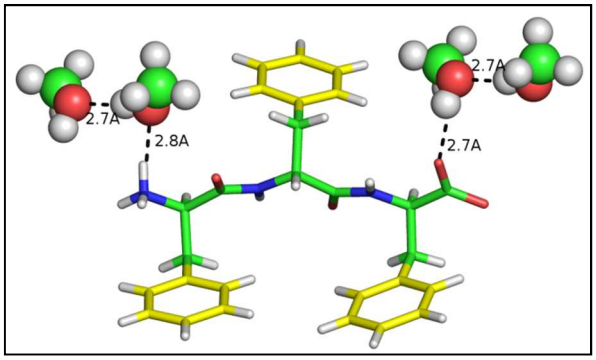

Figure 3.67: Salt bridge and hydrogen bond interactions involving methanol molecules in the crystal structure of the peptide FFF. Distances between donor and acceptor atoms are shown. Methanol molecules are shown as spheres, while a peptide molecule is shown as sticks.

Comparison between homochiral XFF peptides

Considering homochiral peptides VFF and IFF, a relatively small change consists in the addition of a methyl group, from a valine residue to a isoleucine residue, in the side chain of the N-terminal residue shown a very small effect on the arrangement of the peptide backbone, as well as in the orientation of the side chains, as proven by the superimposition of the crystallographic independent units of the crystals of VFF and IFF (*Figure 3.68*). The measurement of the Ramachandran torsional angles for the two structures confirms this observation. As regards the crystal packing, the structures of VFF and IFF show similar unit cell parameters (see Table in Supplementary) that reflect a similar arrangement of the peptides to form the crystal packing, as shown by the superimposition of the two lattices (*Figure 3.69*).

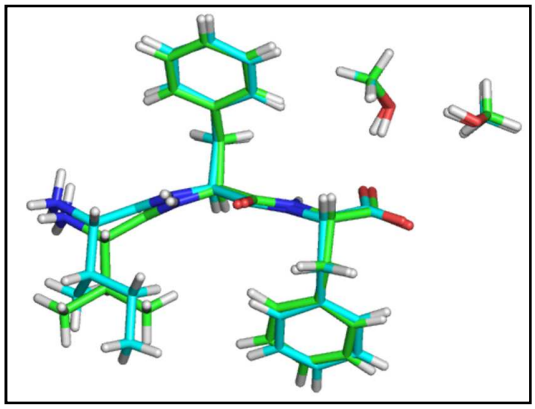

Figure 3.68: Superimposition of the crystallographic independent units of the structures of VFF (green) and IFF (cyan). The figure highlights the very similar arrangement of the backbone, for which the most remarkable difference is observed for the N-terminal residue, as well as the almost perfect superimposition of the side chains, particularly the phenyl rings.

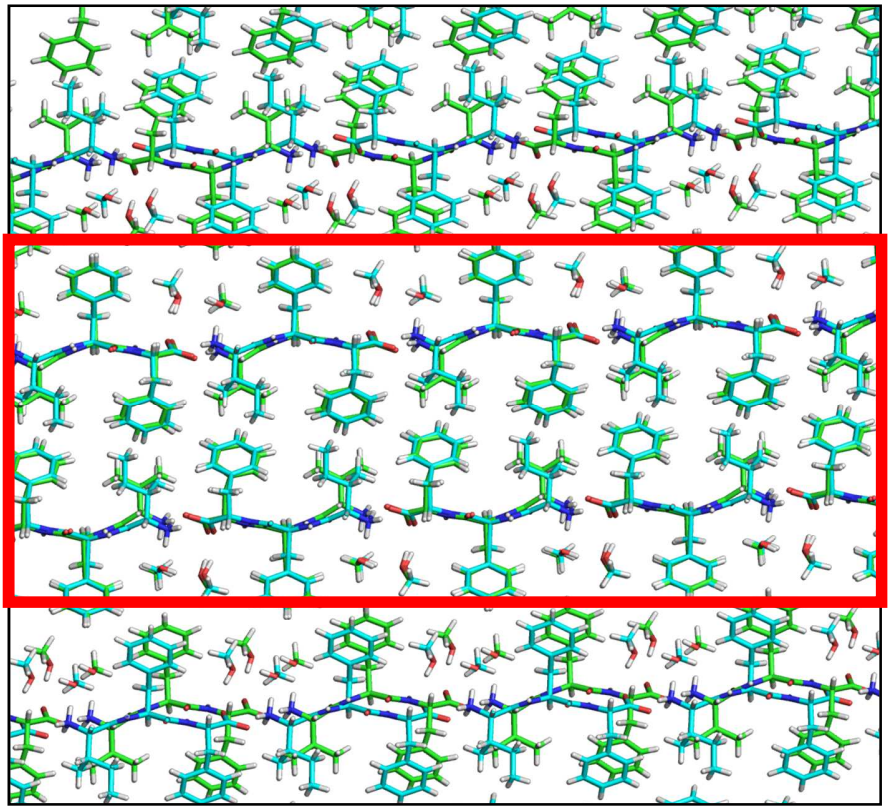

Figure 3.69: Crystal packing in the structures of VFF (green) and IFF (cyan). The figure highlights the presence of two peptide rows that can be exactly superimposed (red rectangle). The adjacent rows, above and below the red rectangle, are shifted in one structure compared to the other, causing a lack of superimposition between the two models.

A further change in the nature of the N-terminal residue, *i.e.* from an aliphatic to an aromatic side chain, causes a severe change in the arrangement of the peptide, as shown in *Figure 3.70* where crystallographically independent peptides of the structures of VFF, IFF and FFF are superimposed. The presence of the aromatic moiety in the first position affects the conformation of the backbone of the peptide, and consequently the side chains arrange in a similar alternate fashion, but with opposite orientation. As a result, despite the apparent resemblance of the peptide arrangement in rows in the three structures (*Figure 3.71*), a superimposition between the crystal packing of VFF and FFF highlights the crucial differences (*Figure 3.72*).

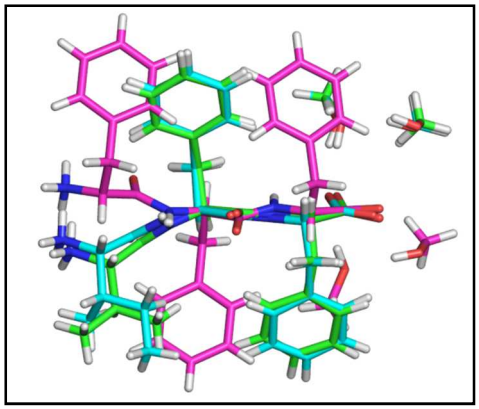

Figure 3.70: Superimposition of the crystallographic independent units of the structures of VFF (green), IFF (cyan) and FFF (magenta). Differences between the structure of FFF and the other two are clearly observable in both the backbone arrangement and the side chain orientation.

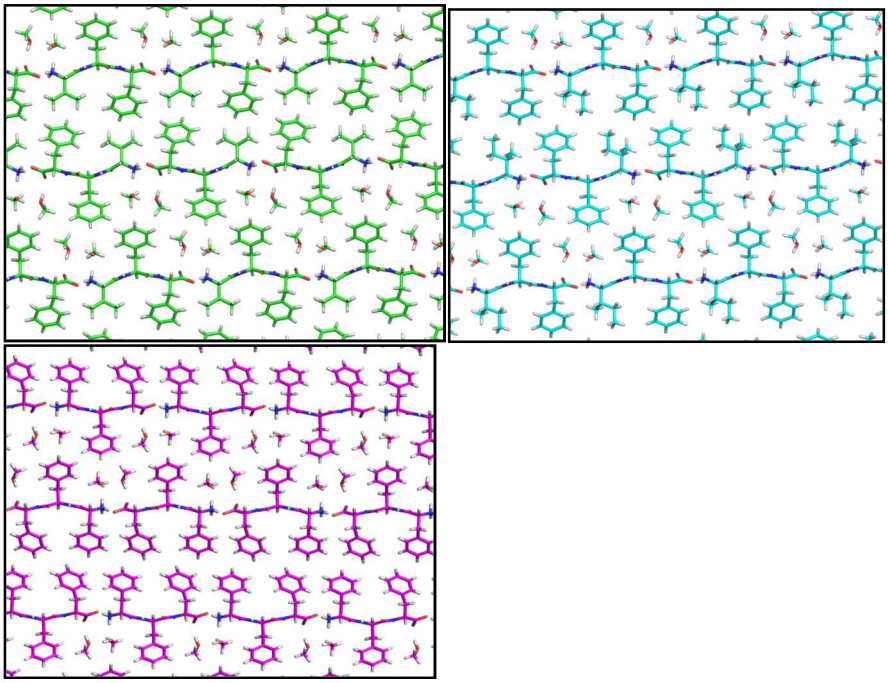

Figure 3.71: Comparison between the peptide arrangement in the structures of VFF (green, left), IFF (cyan, center) and FFF (magenta, right). Peptides display a similar organization in rows with the N- and C-termini of adjacent peptides forming salt bridges. The hydrophobic side chains are organized on opposite sides of each peptide and their interaction is responsible for the packing of rows.

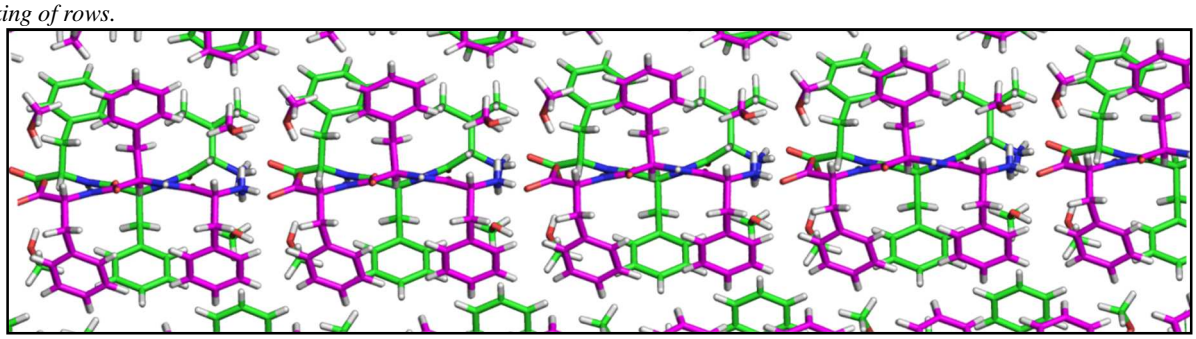

Figure 3.72: Superimposition of the structures of VFF (green) and FFF (magenta), showing that despite a similar arrangement in rows of peptides, the overall crystal packing is different between the structures.

3.3.4.2. XRD structures of xFW group sequences

In this section are reported the XRD structures for vFW and iFW peptides of xFW group, crystallisation trials for the other two peptides of the group are still ongoing.

vFW

The asymmetric unit contains a single molecule of the peptide in its zwitterion form. The additional electron densities present in the asymmetric unit were recognized as 3 molecules of water, used as precipitant in the crystallization experiment. A total of 6 molecules of peptide, related by symmetry operators of the $P6_5$ space group, are present in the unit cell. The overall structure is very similar to that of iFW, differing only for the presence in the latter of an additional methyl group belonging to the isoleucine residue.

The crystal packing shows the presence of large channels filled with solvent molecules along the *c* crystallographic direction (*Figure 3.73*). N- and C- termini of the peptides face the inner part of channels, as water molecules bridging between peptides, making the surface of the channel very hydrophilic. *Figure 3.74* shows the hydrophilic interactions, hydrogen bonds and salt bridges, exposed on the channel surface. Hydrophobic moieties are arranged on the opposite side of the large hydrophilic channel, surrounding a 3_2 crystallographic symmetry axis. Among the hydrophobic interactions, C-H$\cdots_\pi$ interactions involving aromatic or aliphatic carbon atoms are present, as well as a N-H$\cdots_\pi$ interaction involving the nitrogen atom of the indole moiety of the tryptophan residue (*Figure 3.75*). Solvent molecules fill the channels of the crystal, as indicated by the presence of large blobs of electron density in the region surrounded by the hydrophilic groups of the peptides. However, the exact positions of solvent molecules could be determined only for those that have strong hydrogen bonding interactions with the peptide, as highlighted in *Figure 3.76*. All other solvent molecules could not be located.

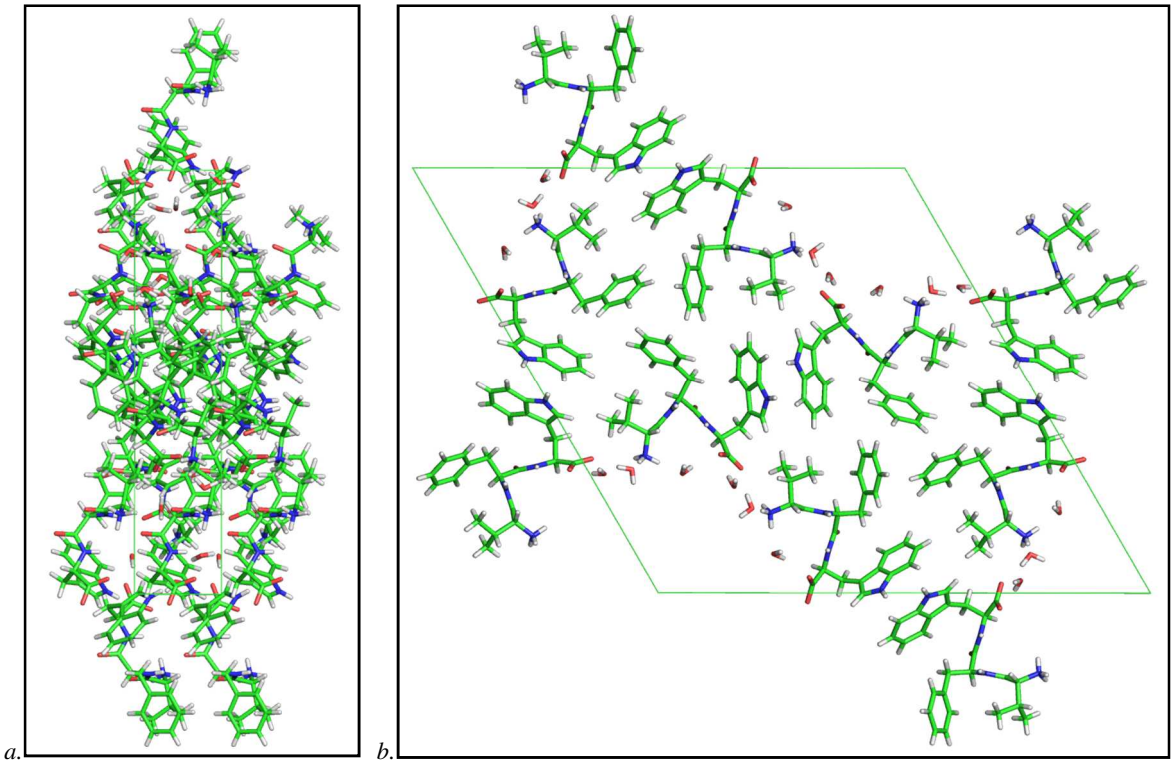

Figure 3.73: Crystal packing in the crystal of the peptide vFW, grown in acetonitrile and water. Views along the a and b crystallographic axes (a) and the c crystallographic axis (b), (peptide molecules are shown as sticks, carbon atoms are shown in green, oxygen in red, nitrogen in blue and hydrogen in white).

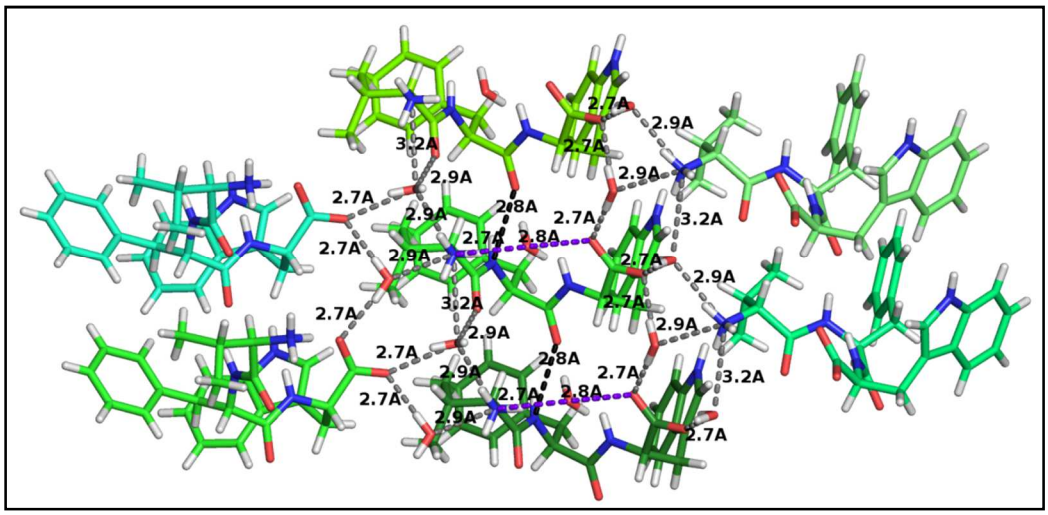

Figure 3.74: Hydrophilic interactions along the channel walls. Hydrogen bonding interactions connecting peptides along the channel axis (c crystallographic axis) are marked with black dashes and donor-acceptor distances are reported. Hydrogen bonding and salt bridging interactions mediated by a water molecule, involving adjacent peptides either along the channel direction (c crystallographic axis) or in a perpendicular direction, are marked with grey dashes and donor-acceptor distances are reported. Salt bridges involving a water molecule and the N- and C- termini of the same peptide are marked with purple dashes and donor-acceptor distances are reported. Carbon atoms are shown in different shades of green for different peptides, oxygen atoms in red, nitrogen in blue and hydrogen in white.

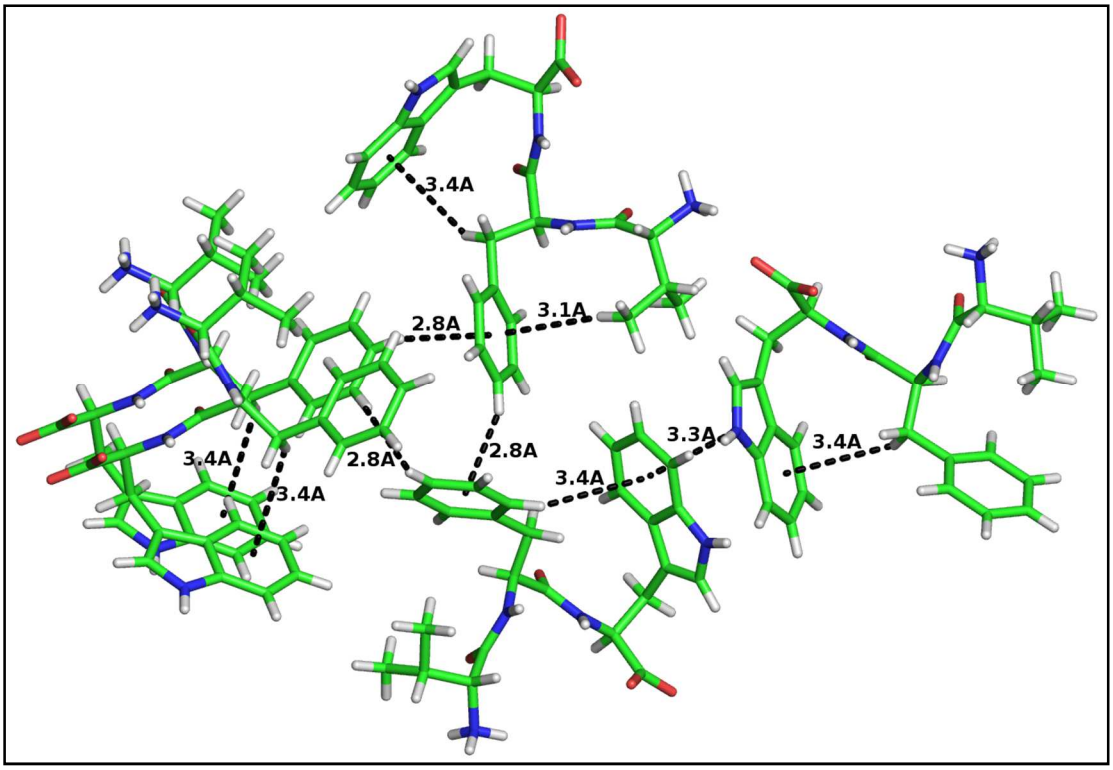

Figure 3.75:CH-π involving aromatic and aliphatic carbon atoms, and the NH- π interaction involving the nitrogen atom of the indole moiety. Distances from the hydrogen atom to the centre of the phenyl ring are shown.

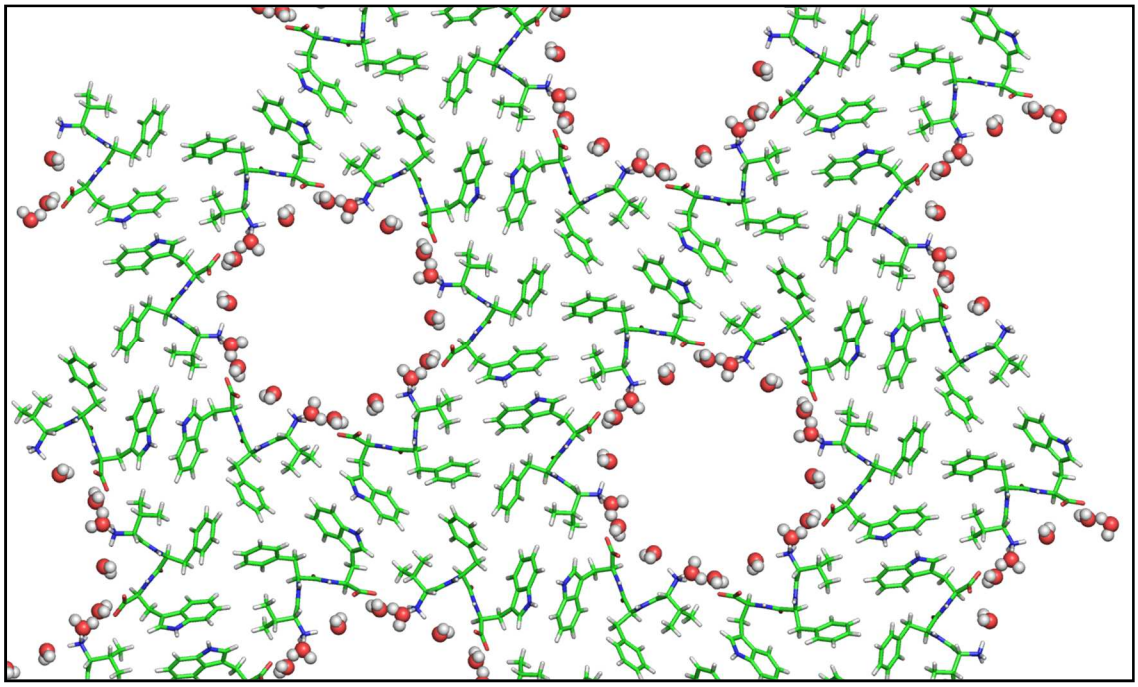

Figure 3.76: Channels present in the structure of vFW. Water molecules that could be precisely located are depicted as spheres. Peptide molecules are represented as sticks. Electron density blobs located in the channel voids indicate the presence of disordered solvent filling the channels.

iFW

The asymmetric unit contains a single molecule of the peptide in its zwitterion form. The additional electron densities present in the asymmetric unit were recognized as 3 molecules of water,

used as precipitant in the crystallization experiment. A total of 6 molecules of peptide, related by symmetry operators of the $P6_5$ space group, are present in the unit cell.

The crystal packing shows the presence of large channels filled with solvent molecules along the *c* crystallographic direction (*Figure 3.77*). N- and C- termini of the peptides face the inner part of channels, as water molecules bridging between peptides, making the surface of the channel very hydrophilic. *Figure 3.78* shows the hydrophilic interactions, hydrogen bonds and salt bridges, exposed on the channel surface. Hydrophobic moieties are arranged on the opposite side of the large hydrophilic channel, surrounding a 3_2 crystallographic symmetry axis. Among the hydrophobic interactions, C-H$\cdots_\pi$ interactions involving aromatic or aliphatic carbon atoms are present, as well as a N-H$\cdots_\pi$ interaction involving the nitrogen atom of the indole moiety of the tryptophan residue (*Figure 3.79*). Solvent molecules fill the channels of the crystal, as indicated by the presence of large blobs of electron density in the region surrounded by the hydrophilic groups of the peptides. However, the exact positions of solvent molecules could be determined only for those that have strong hydrogen bonding interactions with the peptide, as highlighted in *Figure 3.80*. All other solvent molecules could not be located.

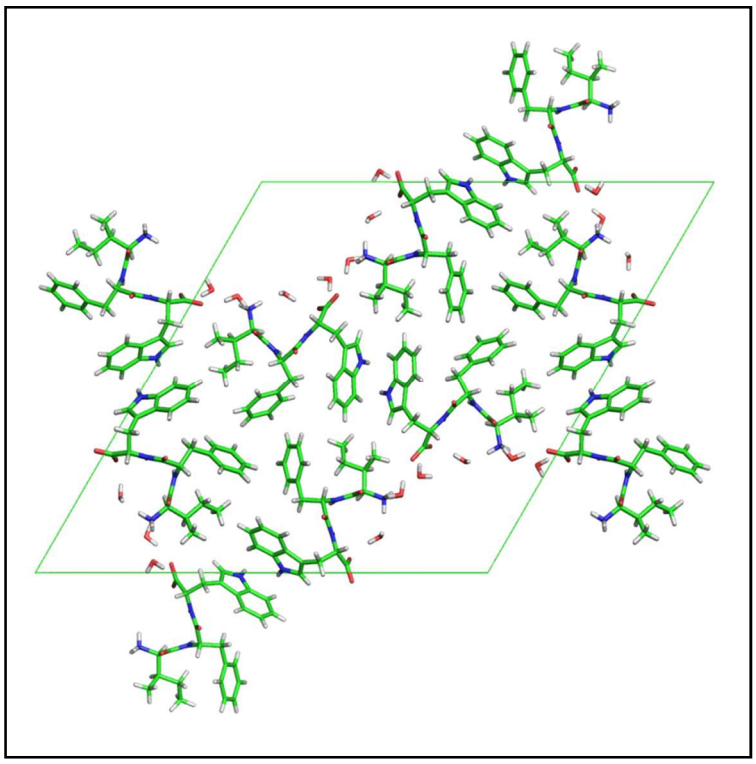

Figure 3.77: Crystal packing in the crystal of the peptide iFW, grown in methanol and water. Views along the c crystallographic axis (peptide molecules are shown as sticks, carbon atoms are shown in green, oxygen in red, nitrogen in blue and hydrogen in white).

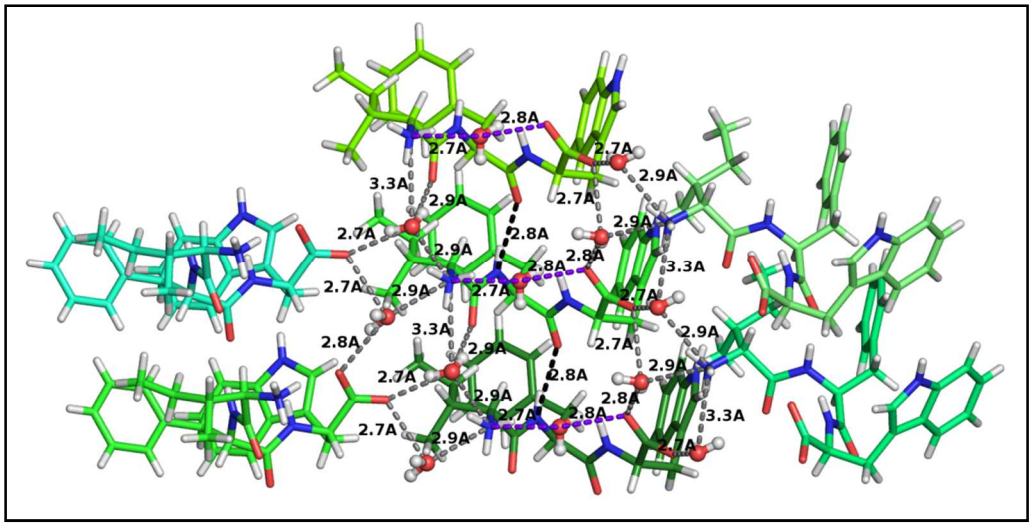

Figure 3.78: Hydrophilic interactions along the channel walls. Hydrogen bonding interactions connecting peptides along the channel axis (c crystallographic axis) are marked with black dashes and donor-acceptor distances are reported. Hydrogen bonding and salt bridging interactions mediated by a water molecule, involving adjacent peptides either along the channel direction (c crystallographic axis) or in a perpendicular direction, are marked with grey dashes and donor-acceptor distances are reported. Salt bridges involving a water molecule and the N- and C- termini of the same peptide are marked with purple dashes and donor-acceptor distances are reported. Carbon atoms are shown in different shades of green for different peptides, oxygen atoms in red, nitrogen in blue and hydrogen in white.

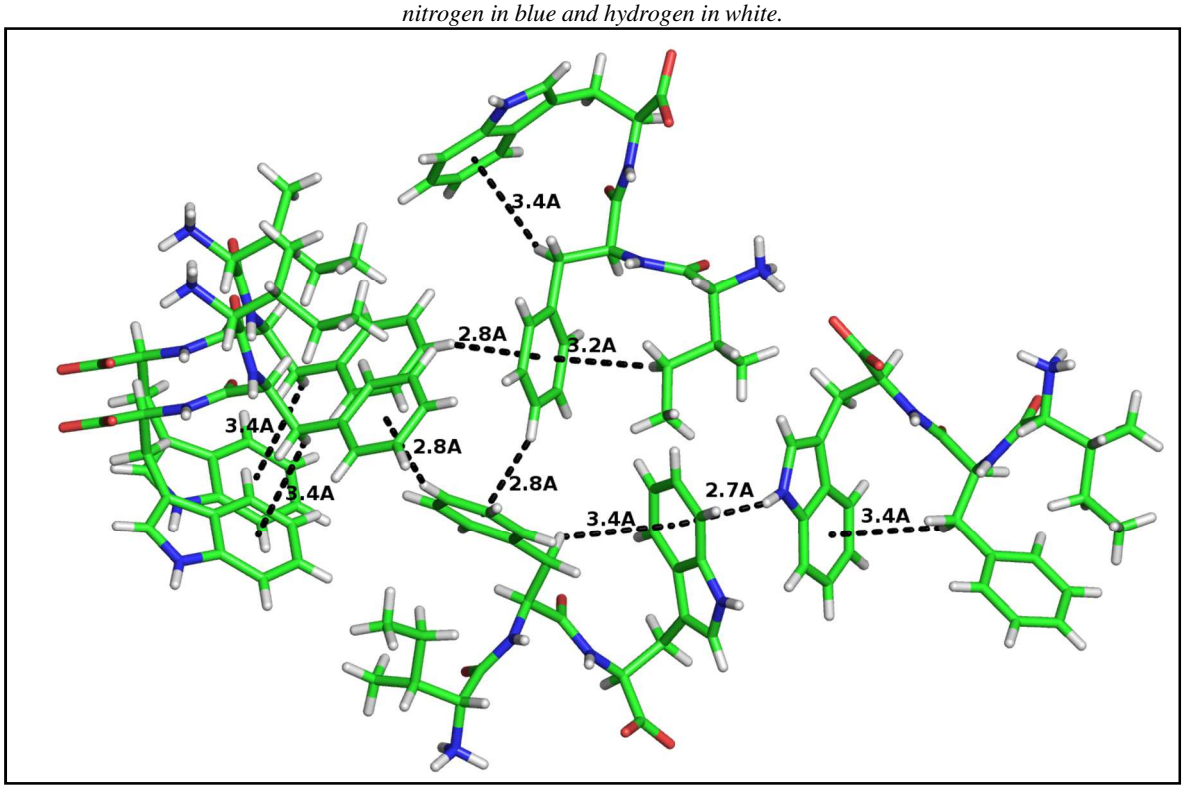

Figure 3.79:CH-π involving aromatic and aliphatic carbon atoms, and the NH-π interaction involving the nitrogen atom of the indole moiety. Distances from the hydrogen atom to the centre of the phenyl ring are shown.

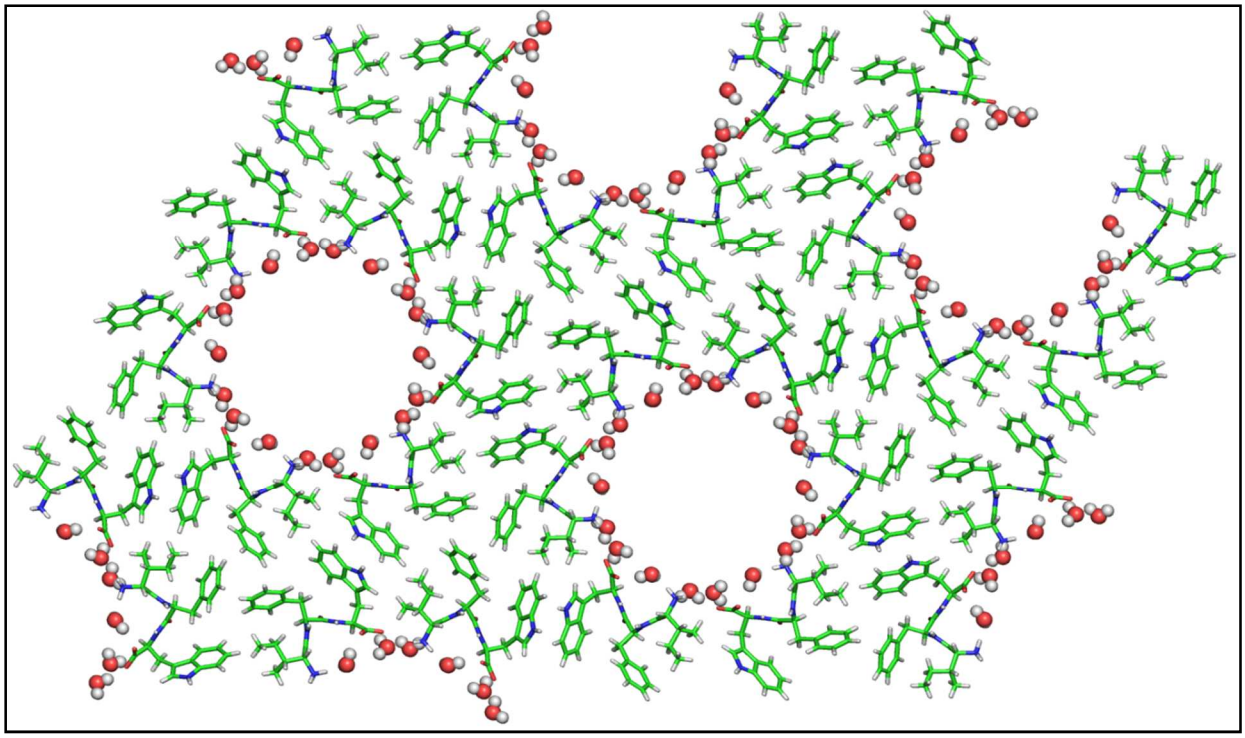

Figure 3.80: Channels present in the structure of iFW. Water molecules that could be precisely located are depicted as spheres. Peptide molecules are represented as sticks. Electron density blobs located in the channel voids indicate the presence of disordered solvent filling the channels.

The superimposition between the crystallographic structures of iFW and vFW shows a perfect match between the two peptides as regards the main chain and the side chains of the aromatic residues (*Figure 3.81*). Slight differences are observed in the region of the aliphatic side chain of the valine residue in vFW, and the isoleucine residue of iFW.

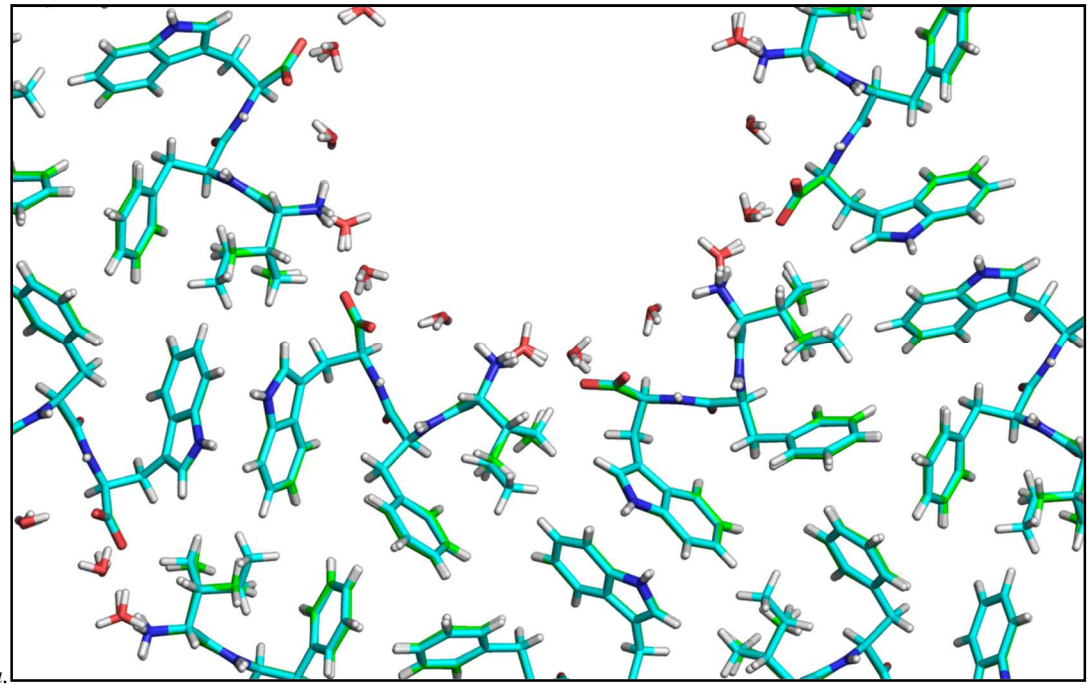

a.

b.

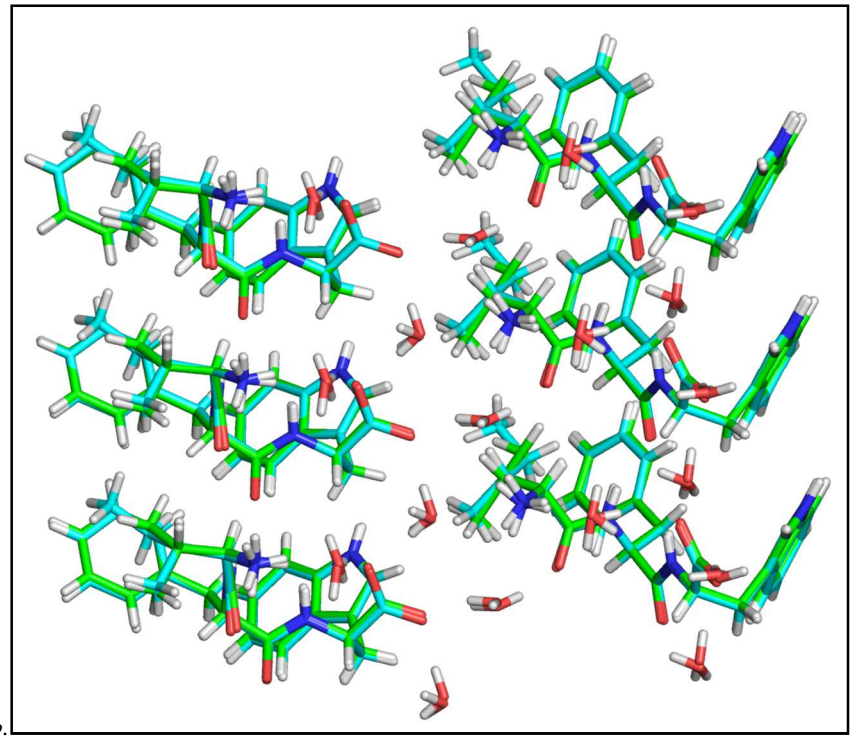

Figure 3.81: Superimposition between the structures of iFW (cyan) and vFW (green). The (a) and (b) views are related by a 90° rotation along the horizontal axis of the figure. Carbon atoms are represented in cyan for iFW and green for vFW, nitrogen atoms are in blue, oxygen in red and hydrogen in white.

3.3.4.3. XRD structures of xXX group sequences

Below are reported the XRD structures for the two peptides of xXX group that are not self-assembling into hydrogels: pWF and wFF. Proline is a known β-breaker, thus it is not too surprising that a hydrogel is not obtained, considering that pWF has a two-fold disadvantage, having both a proline and WF motif, which has less self-assembling propensity than FF. On the contrary, it is difficult to rationalise the lack of hydrogelation of wFF, other than noting that presence of three aromatic residues results in very good and tight molecular packing, leaving little space for water molecules.

pWF

The asymmetric unit contains a single molecule of the peptide in its zwitterion form. No additional electron density was observed in the unit cell. A total of 2 molecules of peptide, related by symmetry operators of the $P2_1$ space group, are present in the unit cell.

The crystal is formed by a close packing of the peptide (*Figure 3.82*). Hydrophilic interactions are present between the peptide molecules, involving the N- and C-termini, the carboxylic and the amino group of the backbone, and the nitrogen of the indole group of the tryptophan residue (*Figure 3.83*). Few hydrophobic interactions are present in the structure. The π- π stacking interactions between aromatic rings are weak, as shown by the rather long distance and the non-ideal geometry (*Figure*

3.84). A strong CH- π interaction is present between one of the aliphatic carbons of the proline residue and the aromatic ring of a neighbouring phenylalanine residue.

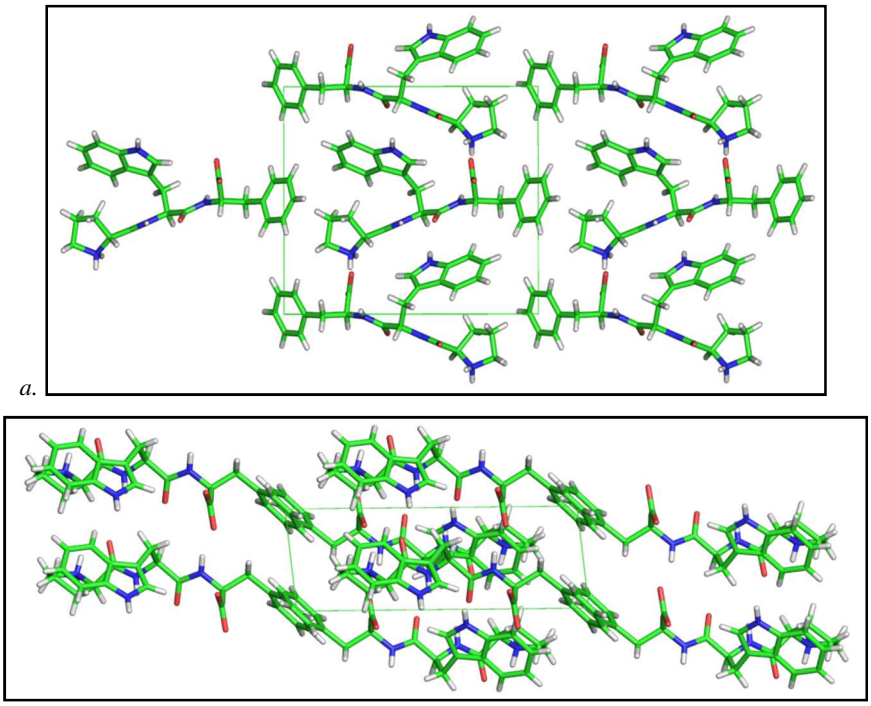

Figure 3.82: Crystal packing in the crystal of the peptide pWF, grown in methanol and water. Views along the a crystallographic axis (a), the b crystallographic axis (b), (peptide molecules are shown as sticks, carbon atoms are shown in green, oxygen in red, nitrogen in blue and hydrogen in white).

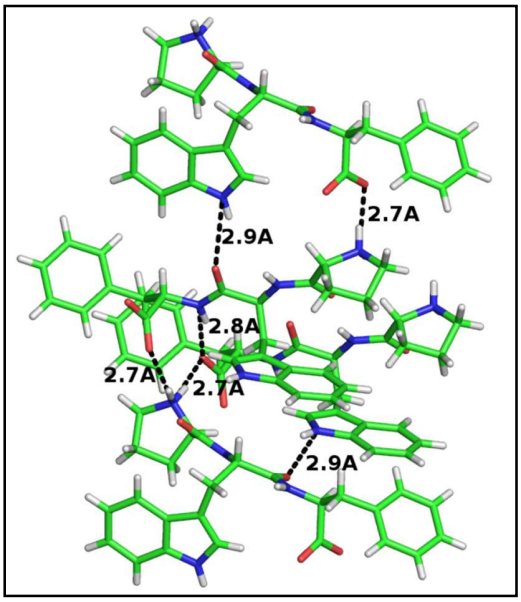

Figure 3.83: Hydrophilic interactions between peptide molecules in the crystal of pWF. Hydrogen bonding interactions and salt bridge interactions are shown as black dashes. Distances are measured from donor to acceptor atoms in both the H-bond and the salt bridge interactions.

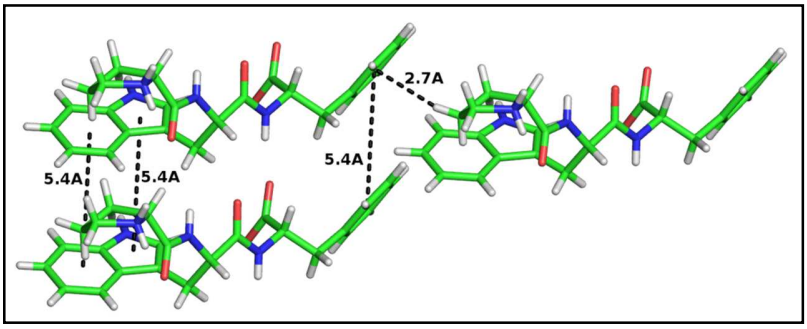

Figure 3.84: Hydrophobic interactions in the structure of pWF. The π - π stacking interactions are weak, as demonstrated by the rather long distances between centres of aromatic rings. A stronger interaction of the CH- π kind is present between a carbon atom of the side chain of the proline residue and the aromatic ring of the phenylalanine side chain.

wFF

The asymmetric unit contains a single molecule of the peptide in its zwitterion form. An additional electron density in the centre of the unit cell was interpreted as a water molecule statistically disordered in two positions at partial occupancy. A total of 2 molecules of peptide, related by symmetry operators of the $P2_1$ space group, are present in the unit cell.

The crystal is formed by a close packing of the peptide (*Figure 3.85*). Hydrophilic interactions are present between the peptide molecules, involving the N- and C-termini, the carboxylic and the amino groups of the backbone, and the water molecules present between the peptides (*Figure 3.86*). Strong CH-p interactions are present between aromatic CH groups and the aromatic rings of phenylalanine or tryptophan residues. The π-π stacking interactions between aromatic rings are weak, as shown by the rather long distance and the non-ideal geometry (*Figure 3.87*).

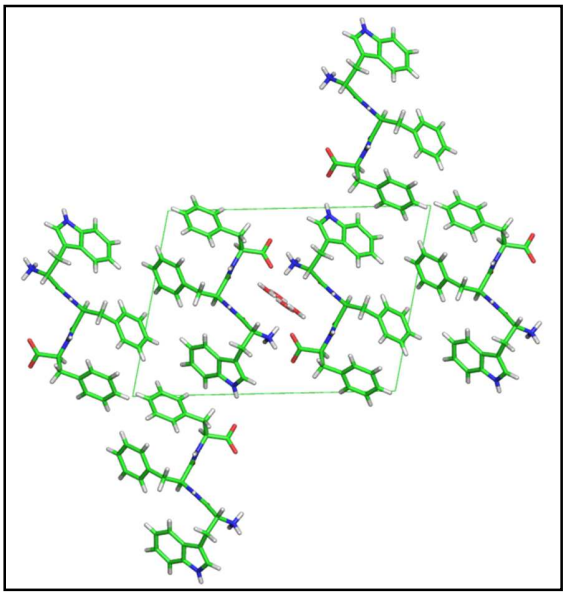

Figure 3.85: Crystal packing for the peptide wFF, grown in methanol and water. Views along the b crystallographic axis (peptide and water molecules are shown as sticks, carbon atoms are shown in green, oxygen in red, nitrogen in blue and hydrogen in white).

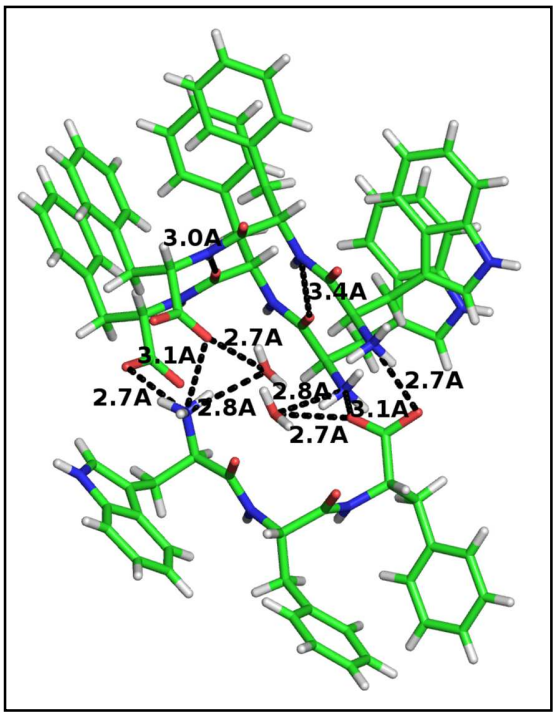

Figure 3.86: Hydrophilic interactions between peptide molecules and solvent in the crystal of wFF. Hydrogen bonding interactions and salt bridge interactions are shown as black dashes. Distances are measured from donor to acceptor atoms in both the H-bond and the salt bridge interactions. Water molecules are shown in the highest occupancy statistical position.

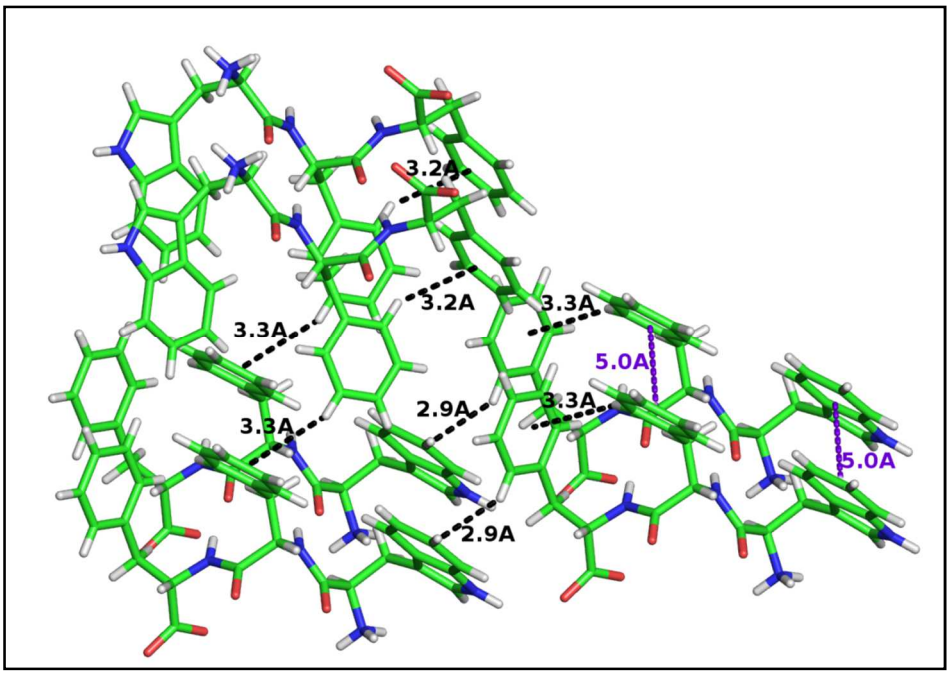

Figure 3.87: Hydrophobic interactions in the structure of wFF. CH-π interactions, shown as black dashes, are present among different aromatic rings and their distances, measured from the hydrogen atom to the centre of the aromatic ring, are compatible with strong interactions. π- π stacking interactions, shown as purple dashes, are weak, as demonstrated by the rather long distances between centres of aromatic rings.

4.PEPTIDE-HYDROGEL APPLICATION

4.1. Peptide hydrogel potential bio-application

Hydrogels obtained from heterochiral tripeptides could be an innovative and promising material for several bio-applications, such as preparation of scaffolds for cell growth [78] (and eventually for tissue engineering in the future) or for drug delivery [94]. In particular, in case of a previously reported system based on a short heterochiral tripeptide combined with an antimicrobial drug (*e.g.*, ciprofloxacin), it was shown how the hydrogel in itself was also able to explicate a mild antimicrobial activity [61]. The first step to consider any of these potential applications is to perform basic starting studies about the toxicity of the material once in contact with living cells. Usually, the first cell line used for these tests are fibroblast cells from mouse. Their choice is directly correlated to time factor, the cells can spread and grow quickly in a material favourable for them (*Figure 4.1*), and to the ease in identifying the cell type and relative condition even for a novice operator.

Fibroblast cells are the more active cells in connective tissue, their morphology present a large, flat, elongated (spindle-shaped) form with processes that are extending themselves far from the end of body cells. This kind of cells, regulated in turn by fibrocytes present in stroma tissue, explicate a fundamental role in wound healing since they are the producer of tropocollagen, the precursor of collagen, and ground substance, a gel matrix that fills the portion included between fibres and cells in connective tissue. Typically, after an injury, fibroblast cells can migrate directly to the damage site toward soluble factors released by damaged tissue and start to deposit collagen and healing process.

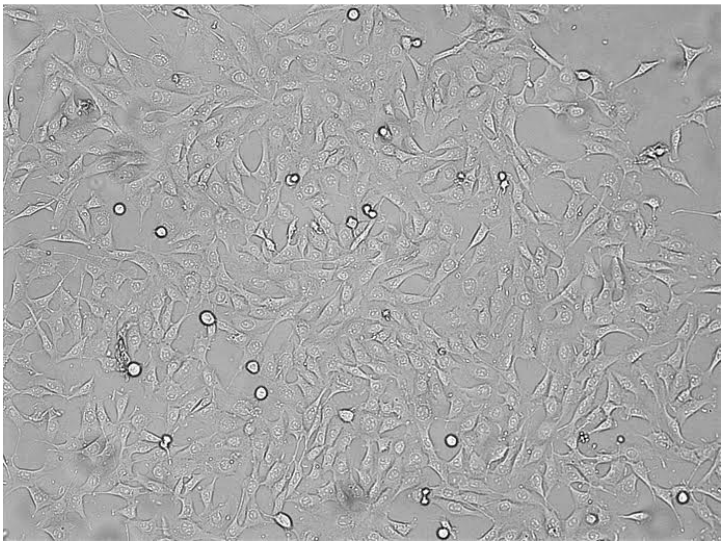

Figure 4.1: Fibroblast cells (commons.wikimedia.org source).

In this project, the first group of heterochiral peptides xFF was selected for LIVE/DEAD® viability/cytotoxicity tests and MTS (3-(4,5-dimethylthiazol-2-yl)-5-(3-

carboxymethoxyphenyl)-2-(4-sulfophenyl)-2H-tetrazolium,inner salt) cell proliferation assays that were performed during a short-term research period of 7 weeks at Biokeskus 1 at Helsinki University, Biocenter 1 in prof. Carl G. Gahmberg's laboratory under the supervision of prof. Mikaela Grönholm.

4.2. Preparation of the hydrogels for cell assays

Each peptide hydrogel was prepared according to the protocol described in previous session inside microwells of µ-slide Angiogenesis uncoated (Ibidi) in a laminar-flow cabinet and left for 24 hours before the addition of cells. Considering the capacity and geometry of the microwells, initial trials were performed to understand the optimal volume of hydrogel that could be located inside the wells to permit and monitor the cell growth properly and to allow easy completion of the protocol procedures for each assay. One slide was used for one complete trial for each peptide hydrogel and the contents of microwells were distributed as follows:

- column 1: 20µl of hydrogel + 30µl specifically prepared medium for fibroblast cells (control),
- column 2: 20µl of hydrogel + 30µl of water (control),
- column 3, 4, 5: 20µl of hydrogel + 30µl of cells appropriately counted in their medium (sample in triplicates).

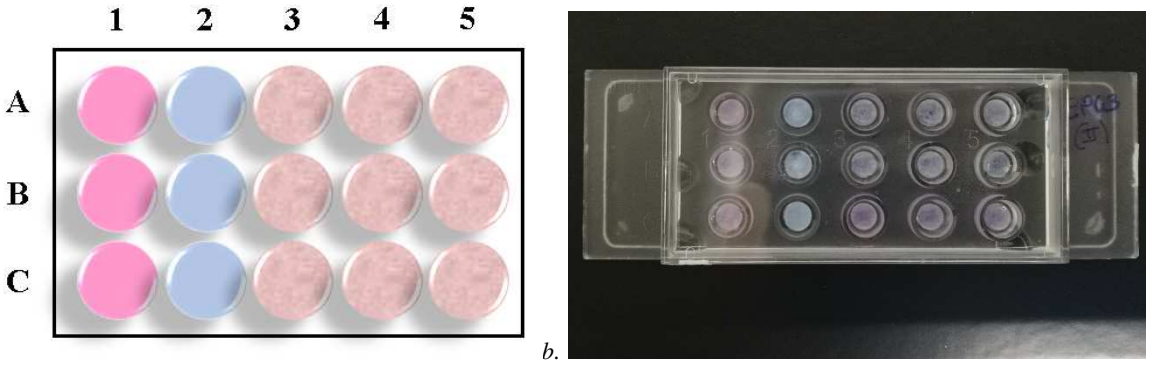

a. *b.*

Figure 4.2: Schematic representation of microwells of µ-slide Angiogenesis uncoated (Ibidi) fillings (a.), picture of real slide containing hydrogels and cells after 72 hours(b.).

Cells were left free to spread and growth on the hydrogels inside the microwell for 24 hours at 37 ° C in a humidified incubator.

4.3. Cell count

Before to perform every LIVE/DEAD viability/cytotoxicity and MTS cell proliferation assays the number of cells that will be moved in each microwell was fixed at 15,000 cells for

microwell for the following experiments. The cell count was performed before every cell transfer from their growth plates (maintained for the whole period of all experiments at 37°C in humidified incubator) through trypan blue exclusion test of cell viability using a Countess ™ Automated Cell Counter. This dye exclusion test is based on the principle that dead cells cannot exclude dyes (*e.g.*, trypan blue) while live cells with intact cell membranes can. In the adopted procedure a small volume of cell suspension was mixed 1 to 1 with the dye, moved inside a Countess slide and measure through the Countess ™ Automated Cell Counter (*Figure 4.3*).

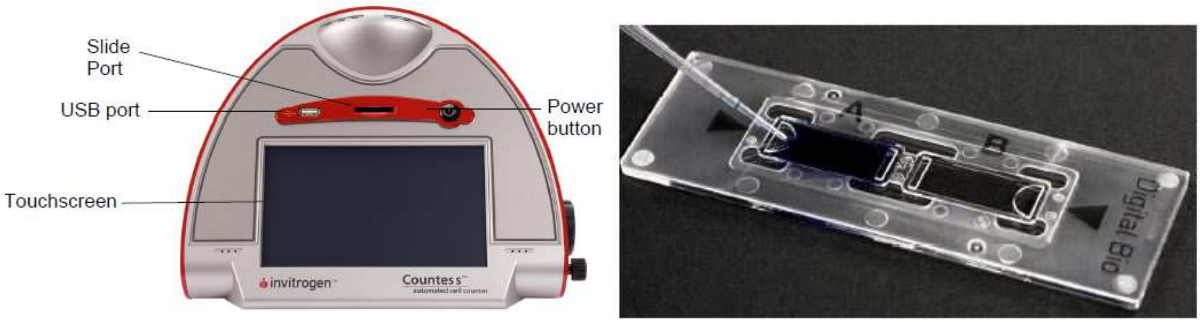

Figure 4.3: Countess ™ Automated Cell Counter (Invitrogen) used for these experiments (left), countess slide in which the cells-dye solution is placed to be analysed (Invitrogen Countess ™ Automated Cell Counter User Manual source).

The cells appeared as reported in *Figure 4.4*, indeed live cells had bright centres and dark edges and dead cells presented uniform blue colour, although the dye was not sensitive enough to discriminate between healthy cells and the alive cells that were losing cell functions.

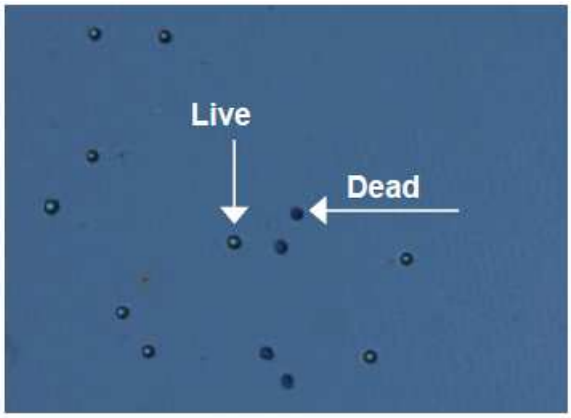

Figure 4.4: Aspect of live and dead cells (Invitrogen Countess ™ Automated Cell Counter User Manual source).

Once counted, an average of 15,000 cells were placed on hydrogels after 24 hours from their preparations and left to spread at 37°C in the humidified incubator for 24 hours before performing the cytotoxicity assays described in the next sections.

4.4. Cytotoxicity assays

4.4.1. LIVE/DEAD® viability/cytotoxicity assay

The assay was performed using a kit containing two fluorescent colour assays that allow the detection of live and dead cells simultaneously, which involves the action of calcein AM and ethidium homodimer (Eth D-1) dye [95] and the use of a fluorescence microscope. In particular, in living cells is present a ubiquitous intracellular esterase activity that can be exploited to catalyse enzymatically the transformation of cell-permeant calcein AM to the fluorescent calcein determining an intense green fluorescence (ex/em ~495 nm/~515 nm). EthD-1, instead, can enter only inside cells with damaged membranes and whether bounded to nucleic acid in dead cells determines a consistent improvement in bright red fluorescence (ex/em ~495 nm/~635 nm, *Figure 4.5*).

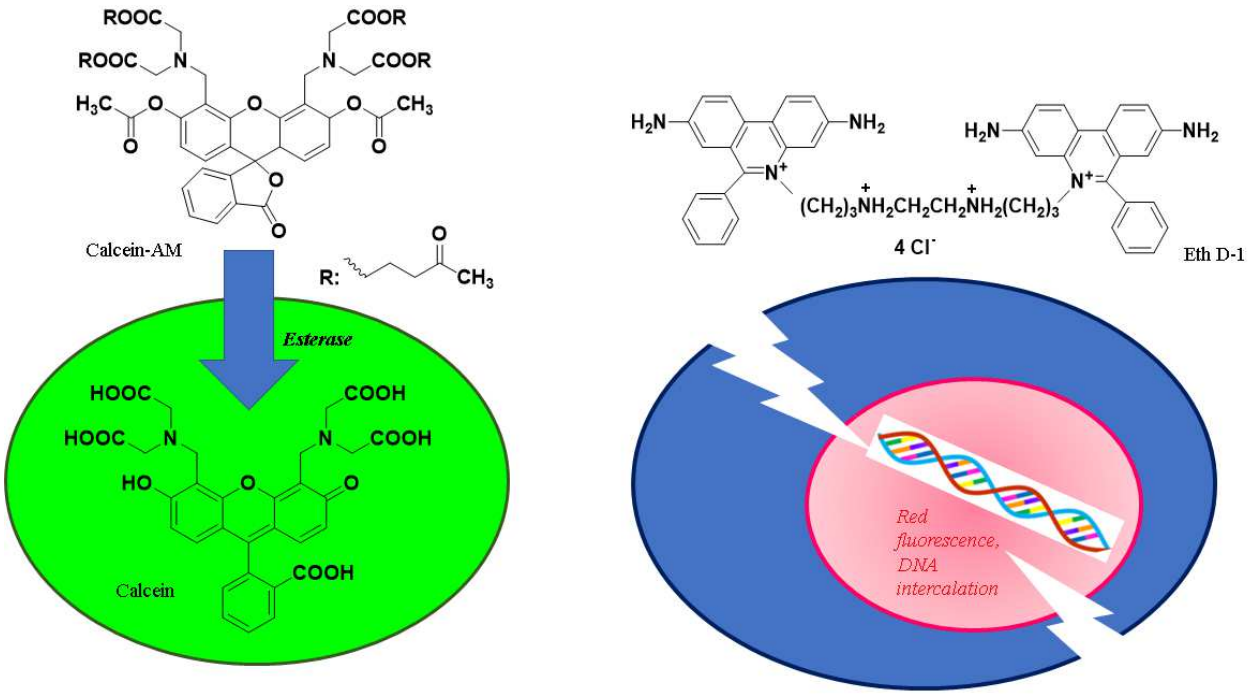

Figure 4.5: Mechanism of action of Calcein AM fluorescent coloration (left) and Eth D-1 (right).

Considering the schematic representation of the slide previously reported in *Figure 4.2a*, it should be noted that line A refers to cell spreading for 24 hours, line B to 48 hours, and line C to 72 hours.

Below are reported the images at different magnification collected for all xFF tripeptides tested before and after the experiments.

pFF

The final hydrogel was a high-density fibrous material of white colour and this led to a challenging focus procedure. The cells were growing closely to the fibres of the hydrogel, forming also some clusters, visible once that the fluorescent dyes were applied to the samples (*Figure 4.6, 4.7*). Also, after 72 hours, the cells presented a good viability and the hydrogel did not lead to cytotoxicity.

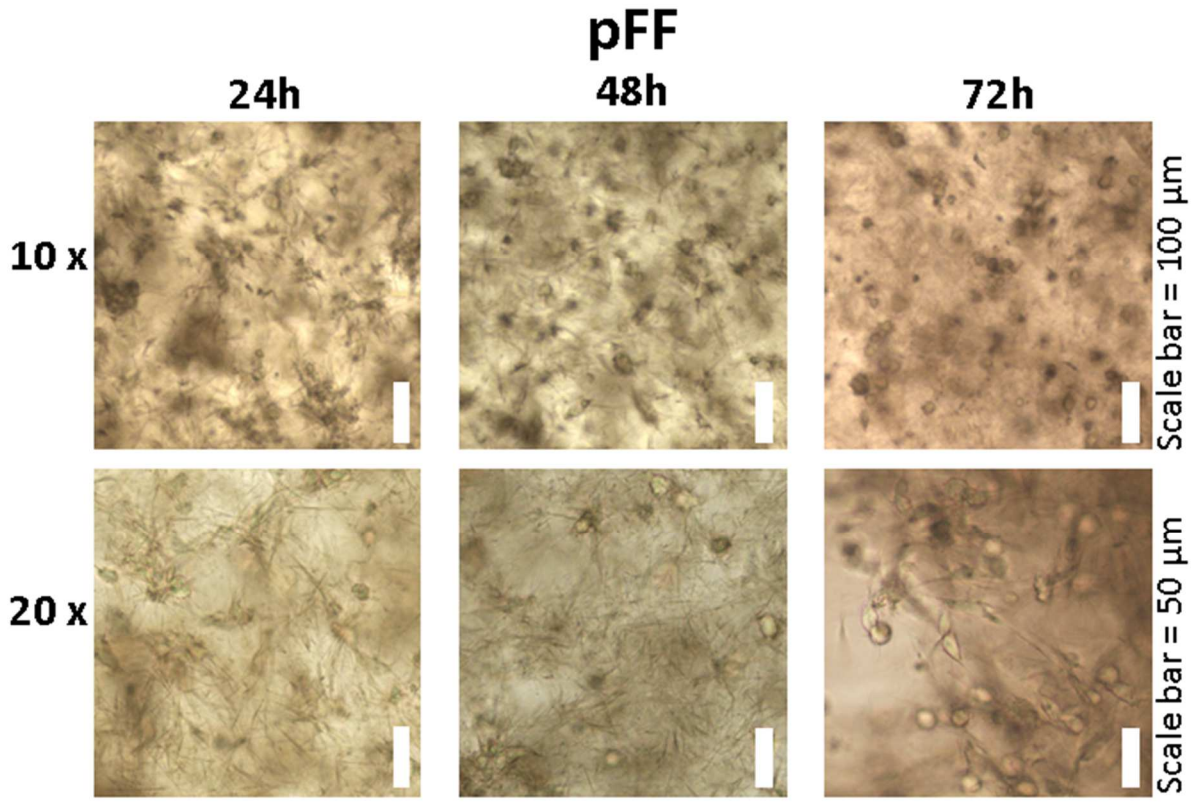

Figure 4.6: Fibroblast cells growth on pFF hydrogel as scaffold support (bright field).

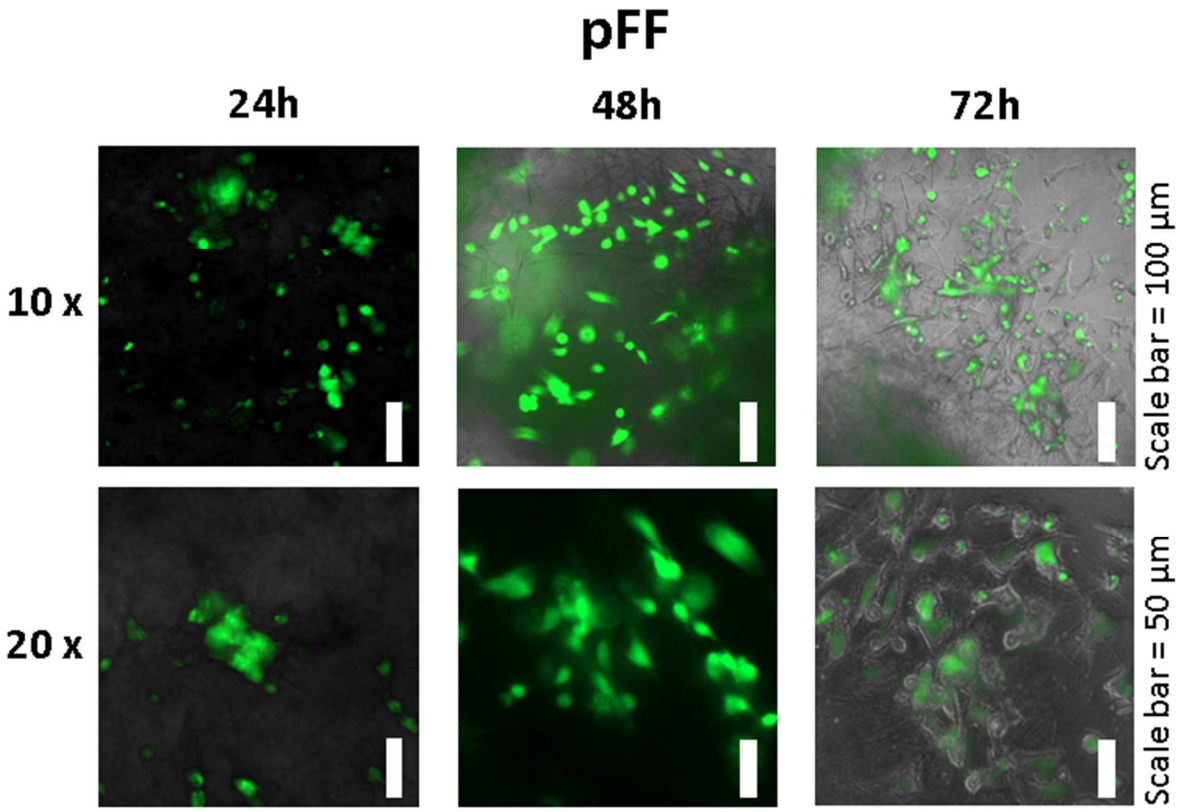

Figure 4.7: Fibroblast cells growth on pFF hydrogel as scaffold support (fluorescence), alive cells (green).

vFF

The hydrogel prepared was characterised by a system of fibres well visible at microscope and it seems formed by more layers of gel. The cells were able to spread consistently on the hydrogel surface already, although they moved through inside the gel. At the end of 72 hours period of tests, the cells presented good viability and not cytotoxicity signals (*Figure 4.8, 4.9*), confirming the previous experiments reported in literature [78].

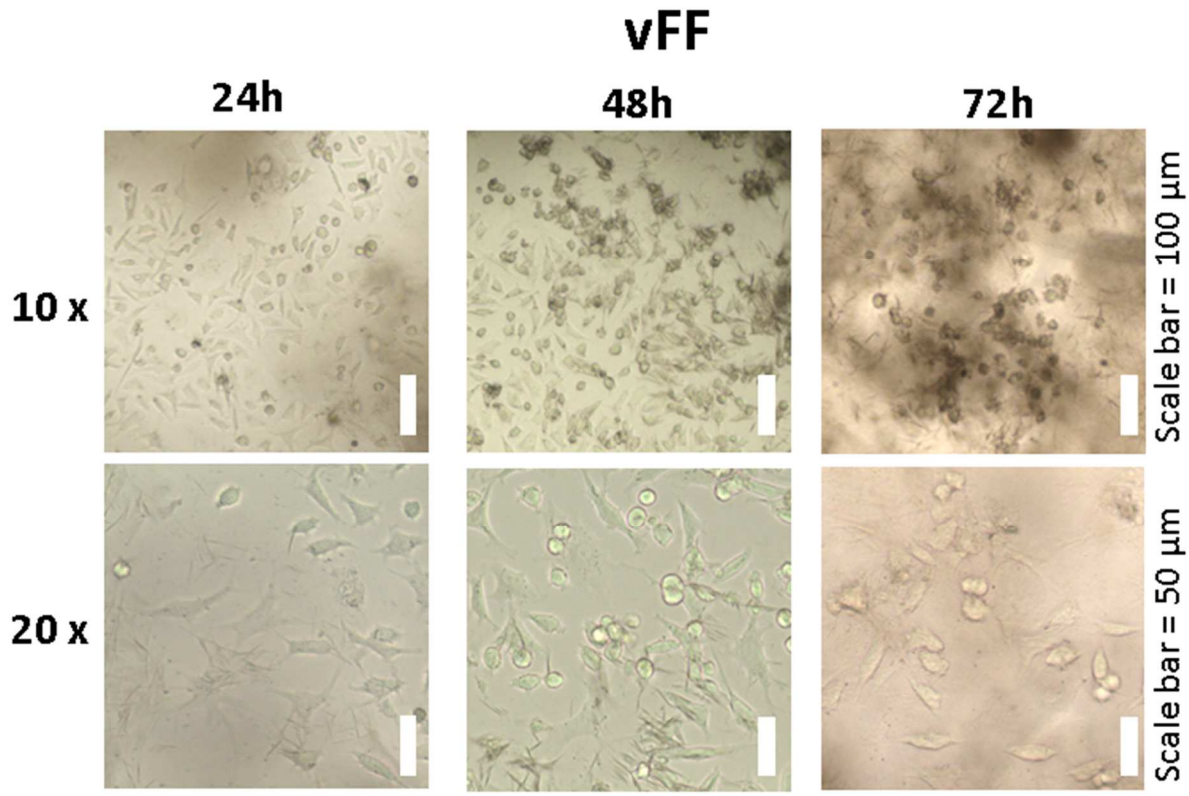

Figure 4.8: Fibroblast cells growth on vFF hydrogel as scaffold support (bright field).

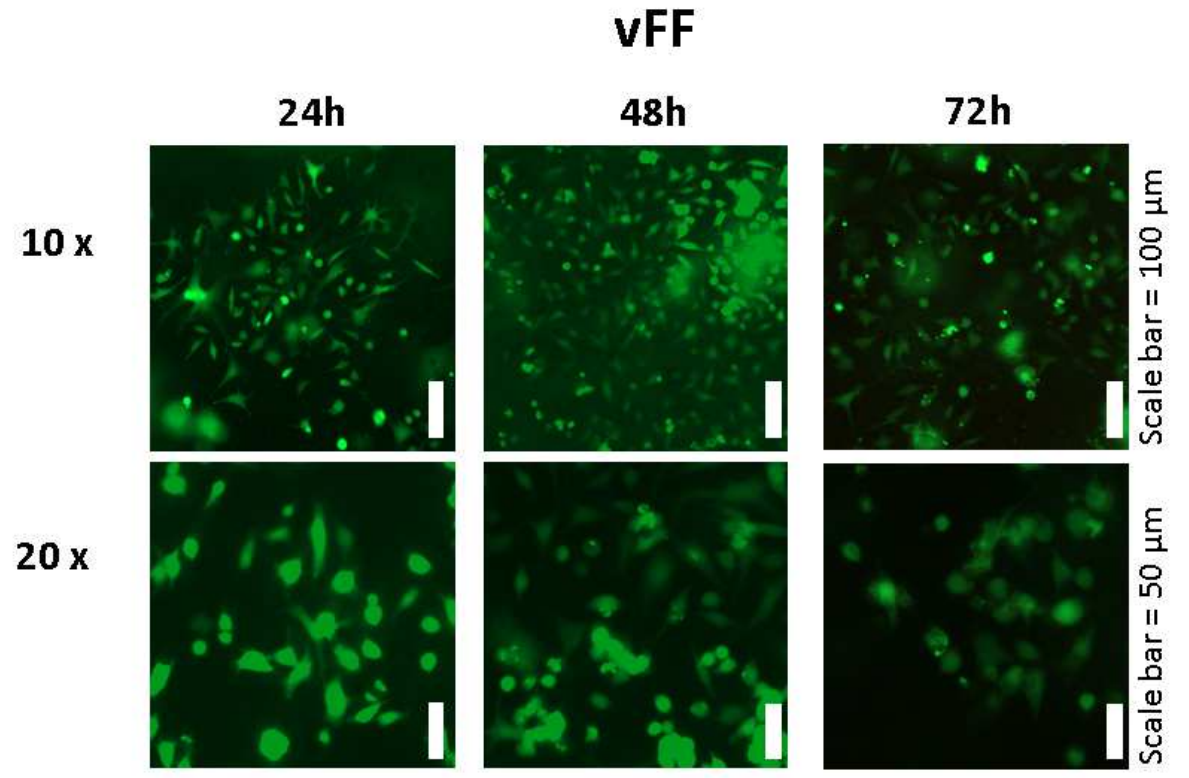

Figure 4.9: Fibroblast cells growth on vFF hydrogel as scaffold support (fluorescence), alive cells (green).

iFF

Hydrogel prepared from this peptide was strong and transparent and the cells were able to spread both isolated and in small clusters already after the first 24 hours. The gel maintained its strength until the end of the experiments and the cells presented a good viability, continuing to spread preferably associated in small clusters, with just very few of them dead (*Figure 4.10, 4.11*).

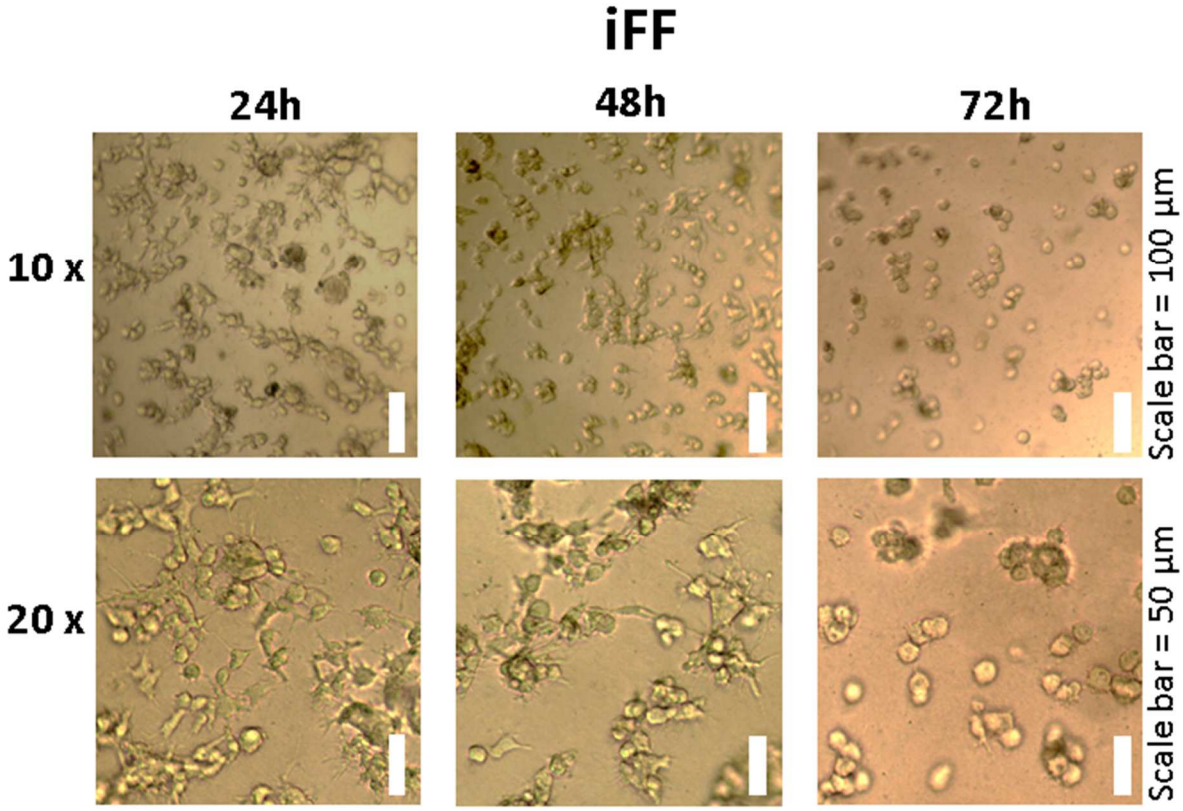

Figure 4.10: Fibroblast cells growth on iFF hydrogel as scaffold support (bright field).

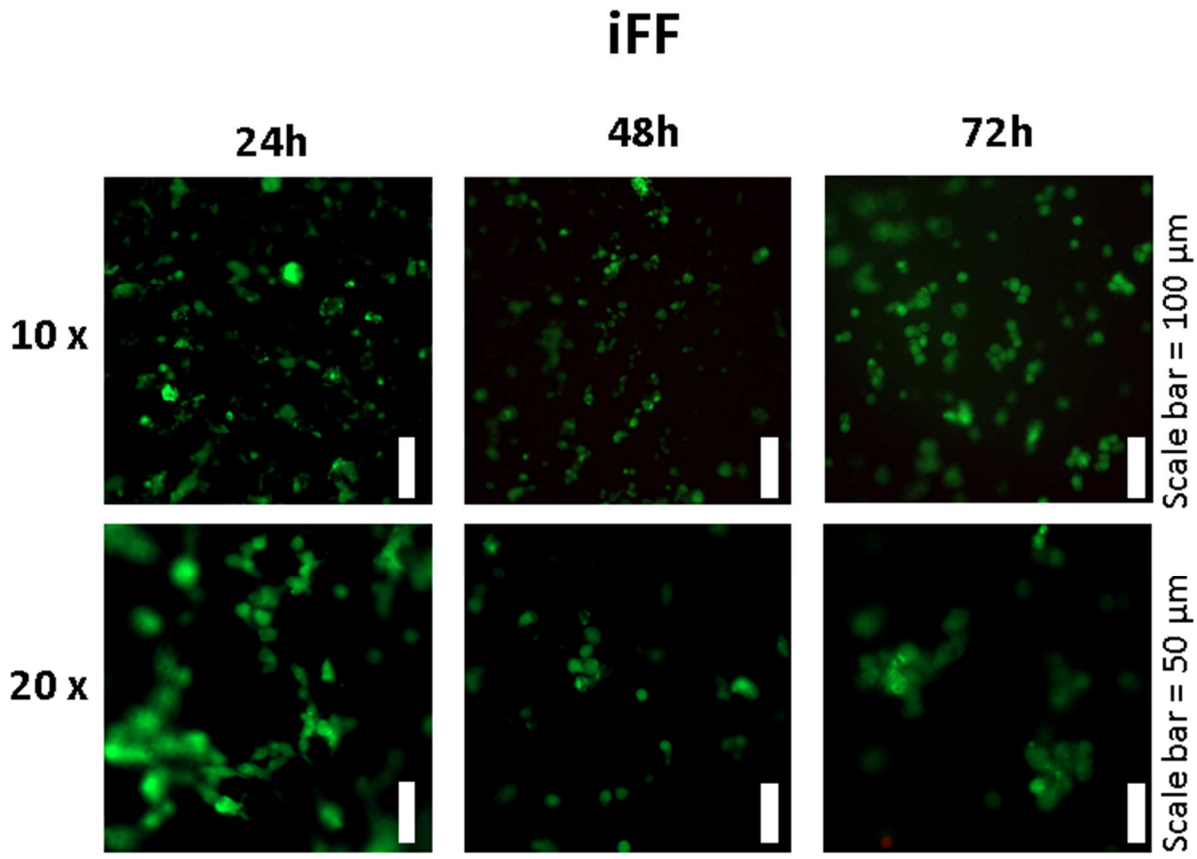

Figure 4.11: Fibroblast cells growth on iFF hydrogel as scaffold support (fluorescence), alive cells (green).

fFF

Also, the hydrogel prepared from this peptide presented a high very density of fibres present. The major difficulty of this sample was the weakness of the hydrogel in itself and for this reason it was necessary to pipette very gently every component added or removed during the different steps of the test. The spreading of the cells on the hydrogel increased over time and it seemed that the cell extensions developed along the directions of the gel fibres. Moreover, the cell viability was confirmed after the live/dead test although they are moved inside the gel to the bottom of the microwells.

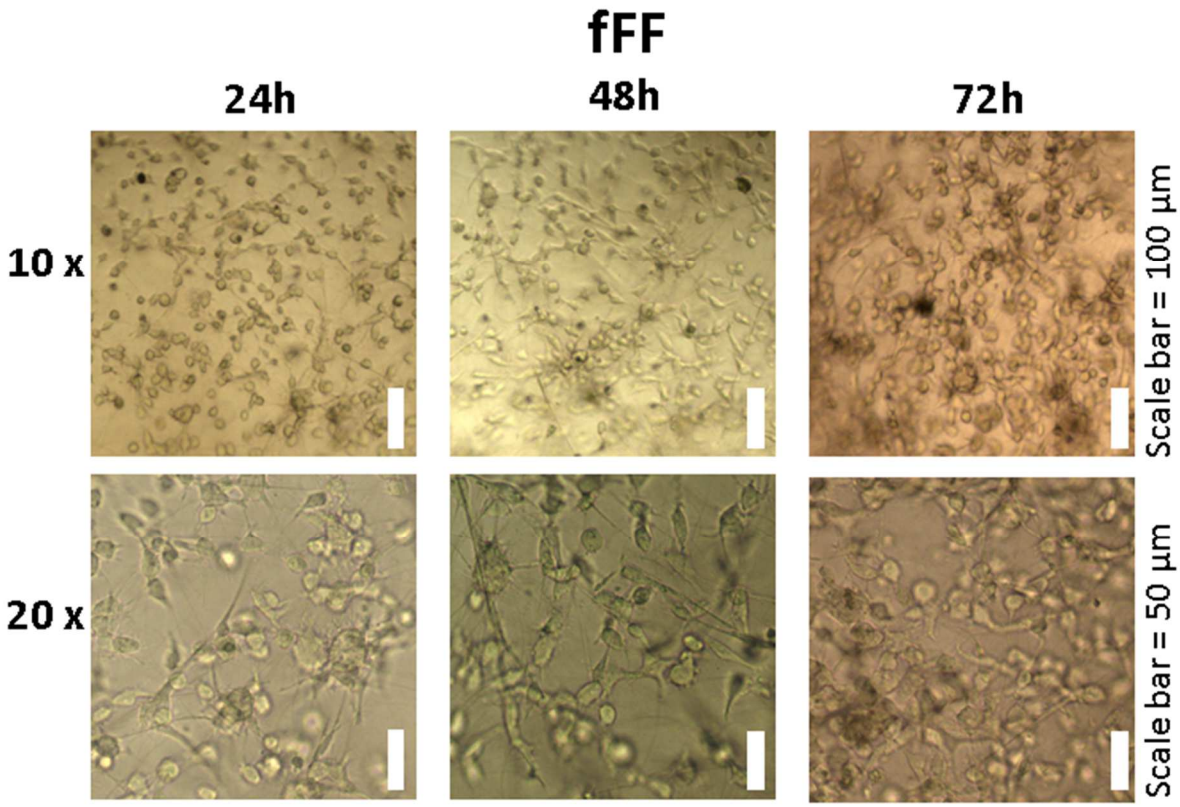

Figure 4.12: Fibroblast cells growth on fFF hydrogel as scaffold support (bright field).

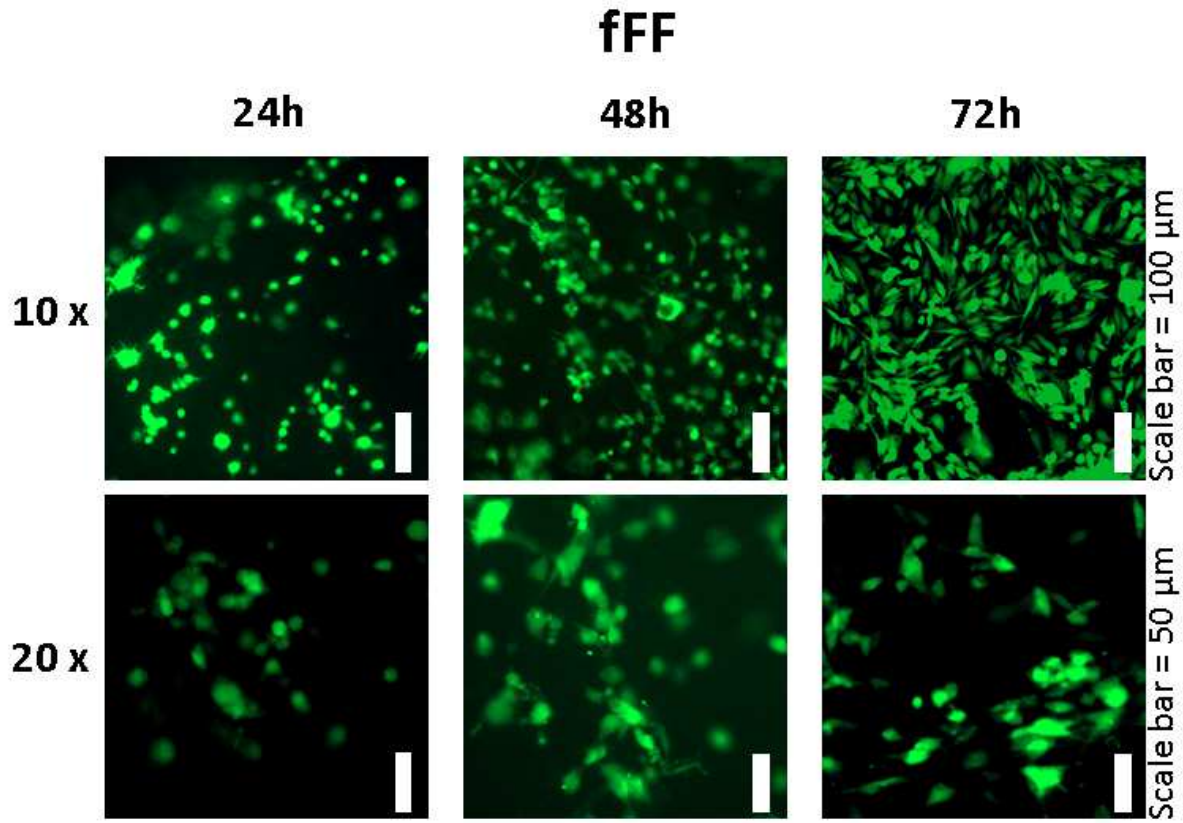

Figure 4.13: Fibroblast cells growth on fFF hydrogel as scaffold support (fluorescence), alive cells (green).

Moreover, all the hydrogels maintained their integrity for all the period for the whole duration of the experiments with behaviours compatible with *storage modulus* G' values recorded during rheological analyses.

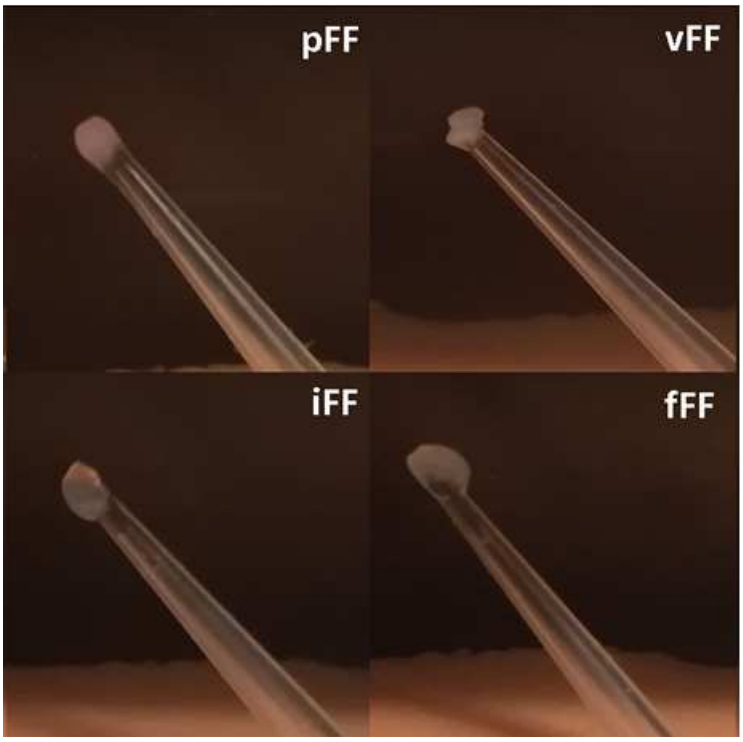

Figure 4.14: Hydrogel after 72 hours.

4.4.2. MTS Cell Proliferation Assay

MTS Cell Proliferation Assay is a colorimetric method employed to determine the number of viable cells in proliferation. The Abcam kit used for the tests provided a reagent containing the novel tetrazolium compound 3-(4,5-dimethylthiazol-2-yl)-5-(3-carboxymethoxyphenyl)-2-(4-sulfophenyl)-2H-tetrazolium, inner salt, MTS. The method is based on the reduction of MTS tetrazolium by viable cells with the final formation of a coloured formazan product soluble in cell medium. The MTS assay did not require intermittent steps, usually present in the routine MTT (3-(4,5-dimethylthiazol-2-yl)-2,5-diphenyltetrazolium bromide) assay and it was chosen with the aim to preserve the hydrogels structure for the duration of the experiments since no washing or solubilization steps were required.

The hypothesised mechanism of MTS reaction involves a conversion carried out by NAD(P)H-dependent dehydrogenase enzymes in metabolically active cells (*Figure 4.15*). The assay was performed adding a precise amount of the kit solution inside the cell culture medium placed on each hydrogel samples, incubating for 2 hours and recording the absorbance at 490

nm using a Nanodrop ND-2000c Spectrophotometer to determine the quantity of formazan producted [96] (Figure 4.16).

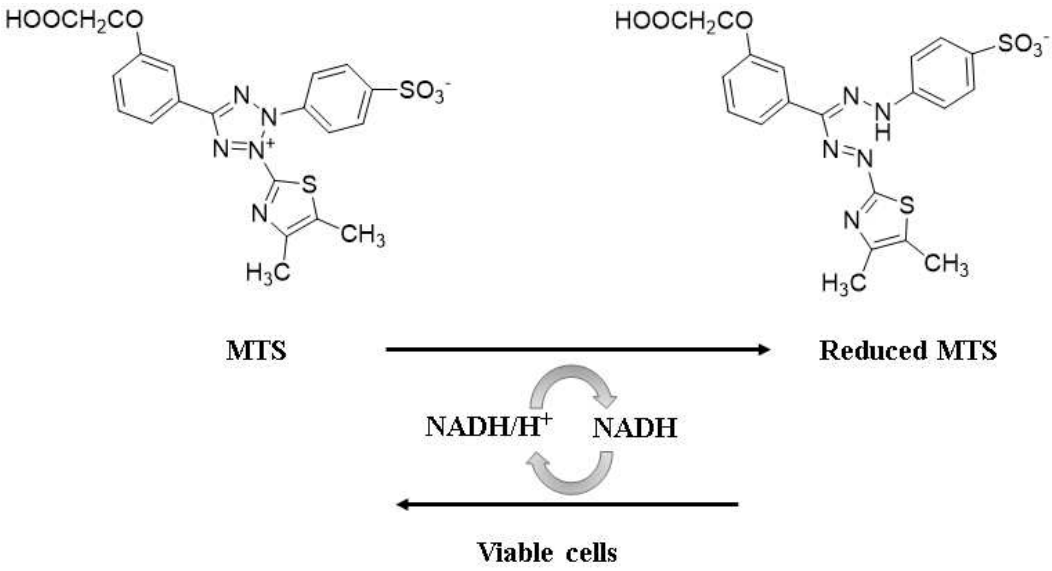

Figure 4.15: MTS proposed mechanism reaction.

Figure 4.16: Nanodrop ND™-2000c Spectrophotometer allows to measure Absorbance in very small samples volumes, without the use of cuvettes (www.thermofisher.com source).

Data were represented for pFF, iFF and fFF peptides, normalising them considering the measured values for vFF as control, which was shown to lead to analogous viability as tissue culture plastic (*Figure 4.17*). fFF was the worst performer of the series, while the other three performed all similarly well.

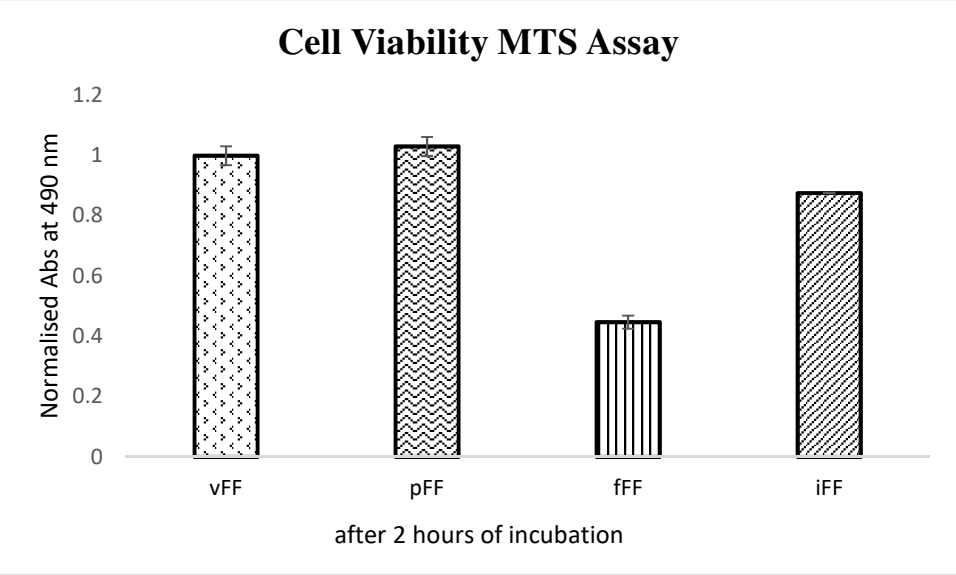

Figure 4.17: MTS assay results for xFF peptides.

5.CONCLUSIONS

5.1. Conclusions

This project aimed at the investigation of the effects on self-assembly of changing the chirality of the N-terminal amino acid in 16 L-tripeptide sequences with high AP score of which those tested previously by other research groups did not gel [7]. All of the 16 D-L-L heterochiral tripeptides were successfully synthesised by SPPS and purified by RP-HPLC, as confirmed by NMR and MS data. They were all tested for hydrogelation following a protocol that involves dissolution in an alkaline phosphate buffer and subsequent dilution with a idly acidic phosphate buffer to reach neutral pH of 7.3 ± 0.1 [78,86].

12 out of the 16 tripeptides proved to be hydrogelators under these conditions, as confirmed by the inversion test tube, and by oscillatory rheology data. This is quite remarkable considering that in the literature usually far fewer hydrogelators are found when unprotected L-tripeptide series are tested. The 12 tripeptides were very diverse in terms of amino acid sequence, thus they were divided in the three sub-groups xFF (without tryptophan), xFW, and the remaining xXX. In this manner, it was possible to rationalise some of their properties and find trends within each sub-group. In particular, the MGC revealed to be quite in good agreement with the inverse relation to hydrophobicity (based on HPLC R_t), especially for the more homogenous first two sub-groups. Notable exceptions included sequences with proline, which is a peculiar amino acid, and with those containing hydroxyl functional groups on the amino acid side chain, which hindered hydrogelation. At MGC, the elastic modulus G' was also found to be quite in good agreement with a direct relation to the width of the individual fibrils, at least for the first two sub-groups.

In terms of secondary structure, FT-IR and CD spectra proved to be of difficult interpretation. However, CD at the concentration of 1 mM for xFF tripeptides were remarkably similar to the recently published FxF [59]. In this study, it was shown that at 1 mM the tripeptides did not self-assemble and the resulting most stable conformation corresponded to a slightly bent backbone into half-turn. All hydrophobic side chains featured on the same side of the backbone, thus allowing a net segregation between the hydrophobic (*i.e.*, side chains) and hydrophilic (*i.e.*, peptide bonds and termini) components on opposite faces, thus creating an amphipathic spatial conformation. It was thus hypothesised that a similar conformation was to be found for xFF peptides, and indeed this was confirmed by single-crystal XRD data, with the main difference being that in the latter case a sharper angle was noted in the peptide backbone corresponding to the point of change of amino acid chirality, thus yielding more kinked structures. This was in sharp contrast with the homochiral VFF, IFF, and FFF tripeptides that showed an almost linear backbone with alternation of the side chains on each side. We were,

overall, very pleased to be able to obtain good-quality single crystals and solve the relevant structures for 11 tripeptides in total, which is quite remarkable considering how difficult it is to crystallise peptides that tend to form gels instead.

The hierarchical assembly of the D-L-L tripeptides though varied greatly. For all the 12 gelling tripeptides, anisotropic fibrous structures were noted, but with homogenous sizes and size distributions, which could not easily be related to differences in peptide sequence for a rational design. Interestingly, in the case of iFW and vFW, water channels were visible, and they arose from the disposition of 6 peptides along the channel, with almost superimposable structures for the two tripeptides.

Finally, preliminary tests for cytotoxicity were performed for vFF, iFF, pFF and fFF on murine fibroblasts for 72 hours, and both MTS and live/dead fluorescence tests led to encouraging results for all the tripeptides tested. In particular, the first three performed analogously well, while fFF showed a significantly worse performance in the MTS assay.

5.2. Future perspective

Future investigations will be required to overcome the technical challenges noticed during this project, researching the most advanced technologies for an adequate study of these systems (*e.g.*, ATR-IR instead of FT-IR, cryo-TEM instead of TEM) and to complete the cytotoxicity evaluation for xFW and xXX peptides. Further investigations will be needed to better rationalise the existing relationship between amino acid sequence and ability to self-assemble and gel. Clearly, there are many factors that come into play and thus far have hindered the identification of very general rules for self-assembly and hydrogelation of such flexible minimalistic sequences. In particular, it would be very interesting to better understand why certain heterochiral tripeptides can form water channels, while others don't. Even more appealing would be the possibility to control the length and the width of such channels, for instance for applications in innovative therapeutic solutions, targeting cell membranes. It could be envisaged that ions or bioactive small molecules could be shuttled through the channels.

Finally, these tripeptides are interesting candidates for tissue regeneration applications, although in this scenario the level of complexity of the materials must be increased, for instance through the addition of bioadhesive motifs, growth factors, etc. The potential applications are overall vast and diverse, but far more research is needed to advance our understanding of these systems and fine-tune their properties *ad hoc* based on the intended use.

6.MATERIALS AND METHODS

6.1. Peptide synthesis

6.1.1. Peptide synthesis

All the peptides in this work were synthesized using standard Fmoc-based solid phase peptide synthesis (SPPS) using 2-Chlorotrityl chloride resin as solid support and activation via uronium salt of *O*-(Benzotriazol-1-yl)-*N,N,N′,N′*-tetramethyluronium hexafluorophosphate (HBTU) and 1-Hydroxy-7-azabenzotriazole (HOAt)**.**

6.1.2. Loading of the first amino acid on the resin

1 g of 2-Chlorotrityl chloride resin were swelled for 10 minutes using Dichloromethane (DCM) in a plastic reaction vessel. After the swelling, the resin was treated with 0.1 mL of thionyl chloride ($SOCl_2$) in DCM and leave to react, mild stirring for 1h at room temperature. After 1h the solution inside the plastic reaction vessel was removed and the resin was washed with DCM and *N,N*-Dimethylformamide (DMF) twice. Fmoc-amino acid (2.0 mmol) solution in DCM and half part of DMF was prepared and added to the activated resin in the plastic reaction vessel, followed by the addition of 0.9 mL of *N,N*-Diisopropylethylamine (DIPEA) and left to stir for 1.5h at room temperature. After this reaction time, without remove the mixture, 0.5 mL of methanol was added, and the vessel was spinned for 5 min. After that, the resin was dripped and washed with DCM and DMF twice. Fmoc protecting group was removed after two deprotection steps of 10min each using a solution of 20% piperidine in DMF. After that, the resin was newly dripped and washed with DCM and DMF twice.

6.1.3. Calculation of the first amino acid loading on the resin

Before to perform the Fmoc deprotection step after the loading of the first amino acid, triplicate samples of 5 to 10 mg of loaded resin were weighed and stored in Eppendorf tubes. To each sample 1.00 mL of deprotection solution of 20% piperidine in DMF was added and left to mild shake for 20min. After that time, each Eppendorf tube containing the resin were centrifuged for 5 min at 12.000 rpm and 100 μL were transferred into a vial glass tube containing 10 mL DMF and mixed well. The absorbance at λ=301 nm was measured in triplicate samples, considering DMF solvent for baseline and calculating the average substitution, according to the formula below:

$$Substitution\ (mmol/g) = (101 * A_{301}) / (7.8 * w),$$

where A_{301} is the absorbance at λ=301 nm, w = exact mass weighted of resin sample (mg), and considering the initial Lambert-Beer law formula:

$$A = C*l*\varepsilon,$$

where C is the concentration of the solution, l is the optical pathway (1 cm) and ε is the molar extinction coefficient.

6.1.4. Colorimetric tests

Before and after every Fmoc deprotection step, few beads of loaded resin in Eppendorf tubes were to perform the colorimetric tests.

6.1.4.1. Chloranil test

This test was developed to detect secondary amino group, indeed it is very specific and used not only for primary amine detection. In case of positive test, few beads of resin placed in a small test tube will be coloured, after the addition of two solutions, appropriately prepared: solution 1 (2% acetaldehyde in DMF) and solution 2 (2% chloranil in DMF), left to react for 5 min at room temperature.

Positive (free amine)	Negative
Dark blue to green beads	Colourless to yellowish

6.1.4.2. Bromophenol Blue test

Bromophenol blue test is an immediate test to detect all types of amines, but it has to be performed carefully because traces of acid can provide false negative results. Few beads of the resin were placed in a small test tube and few drops of reagent solution were added.

Positive (free amine)	Negative
Blue beads	Colourless

6.1.5. Cleavage of peptide from the resin

Considering the use of 2-chlorotrityl chloride resin, the cleavage solution of the peptides was prepared using 49.5% TFA, 49.5% DCM with 0.5% TIPS and 0.5% H_2O as

scavengers after the last Fmoc group removal and a proper dehydration of the resin. A fresh prepared cleavage solution was added to the resin and left to react under mild shaking for 2 hours (1.5 hours for W-containing peptides, to reduce the side reactions of the electronic doublet of the indole nitrogen, once that the Boc orthogonal protection has been removed). After the reaction time, the resin was washed with DCM and well dried. The peptide cleaved from resin was collected and leave under evaporation in a flask under air. The obtained oil after the completion of the evaporation was then dissolved in the HPLC mixture for purification (MeCN/ H_2O with 0.05% TFA).

6.1.6. Peptide purification

Each peptide was purified using reverse-phase HPLC (1260 Agilent Infinity system) equipped with a preparative gradient pump (G1311B), semipreparative C-18 column (Kinetex, 5 μm, 100 Å, 250 x 10 mm, Phenomenex) and Photodiode Array detector (G1315C). The gradient used consisted of acetonitrile (MeCN)/ H_2O with 0.05% TFA with the following program: t = 0–2 min, 30% MeCN; t = 9 min, 65% MeCN; t = 11 min, 95% MeCN; t = 14 min, 95% MeCN. The liquid collected was then freeze-dried to yield the corresponding peptide as a white fluffy powder.

6.1.7. Peptide characterisation

All the synthesised peptides were characterised by ESI-MS (Electrospray Ionisation Mass Spectroscopy) and ^{1}H-NMR and ^{13}C-NMR (Nuclear Magnetic Resonance Spectroscopy). The ESI-MS spectra were recorded in MeCN/ H_2O 1:1 with 0.1% of Formic acid, using am analytic C-18 column (Luna, 5 μm, 100 Å, 150 x 2 mm, Phenomenex) and Quadrupole LC/MS (6120). The ^{1}H-NMR and ^{13}C-NMR spectra were recorded in deuterated dimethyl sulfoxide (DMSO-d6), with tetramethylsilane (TMS) as internal standard at the frequency of 400MHz, using a Varian Innova Instrument spectrometer.

6.2. Peptide hydrogel preparation

Attempts of self-assembly have been made on each peptide, based on the transition of the peptide from a condition of maximum solubility to reduced solubility one. Peptides were dissolved in an alkaline saline buffer (sodium phosphate 0.1M, 11.8<pH<12, depending from the sequence) in ultrasonic bath, then the peptide solution was diluted 1:1 using a mild acid

saline buffer (0.1 M sodium phosphate, pH~5.8). The pH trigger was used to drive the self-assembly of peptide zwitterions, to achieve final supramolecular hydrogel at neutral pH (~7).

6.3. Hydrogel characterisation

Hydrogel nature of the peptide was confirmed by Oscillatory Rheometry measurements whereas secondary structures of the heterochiral tripeptides were determined by FT-IR (Fourier-Transformed Infrared Spectroscopy) and Circular Dichroism (CD) Spectroscopy. Morphology of the nanostructures were assessed by Transmission Electron Microscopy (TEM).

6.3.1. Oscillatory Rheometry

Dynamic time sweep rheological analyses were conducted on a Malvern Kinexus Ultra Plus Rheometer (Alfatest) with a 20 mm stainless steel parallel plate geometry, at fix temperature of 25°C using a Peltier temperature controller (Alfatest). All the samples were prepared in situ, and immediately analysed with a gap of 1.00 mm. Time sweeps were recorded for 1 hour, using 1.00 Hz frequency and 1.00, 2.00 or 5.00 Pa (depending from the sequence) controlled stress conditions. After 1h, frequency sweeps were recorded using a 1.00, 2.00 or 5.00 (depending from the sequence) Pa controlled stress and final stress sweeps were recorded using 1.00 Hz frequency.

6.3.2. Transmission Electron Microscopy (TEM)

Nanostructure morphology of each peptide was assessed by TEM analyses. Small aliquot of gels prepared 24 hours before were deposited on a TEM grid (carbon-coated 300-mesh copper grid), dried opportunely and contrasted by aqueous tungsten phosphate solution (pH ~7.3±0.1). Grids were maintained air-dried until their examination using Jeol, JEM 2100 instrument at 100 kV. The average size of the nanostructures was determined by considering at least 100 measurements.

6.3.3. Circular Dichroism (CD) Spectroscopy

The secondary structure of peptides was analysed using a 0.1 mm quartz cell on a Jasco J815 Spectropolarimeter, with 1 s integrations, one accumulation and a step size of 1 nm with a bandwidth of 1 nm over a range of wavelengths from 185 to 320 nm at 25°C. All

the samples were freshly prepared *in situ*, mixing the peptide dissolved in alkaline buffer, after the addition of the second mild acid buffer directly in the CD cell. Spectra were recorded after 2 min. Measurements were repeated at least 3 times.

6.3.4. Fourier-Transformed Infrared Spectroscopy (FT-IR)

FT-IR spectra were registered using the KBr pellet method. The gel was prepared, and after 24 h it was dried under vacuum. Then, it was mixed with KBr to make the pellet. Spectra were acquired at 1 cm^{-1} resolution and 128 accumulations on a Perkin Elmer System 2000.

6.3.5. X-Ray Diffraction (XRD) single crystal structures

Crystals of heterochiral and homochiral tripeptides were grown using the sitting-drop vapour diffusion method. Each peptide was dissolved in a specific organic solvent at very low concentration. 1.5 mL were deposited and put in vapour diffusion with a reservoir containing 3 mL a mixture at different ratio of the solvents in which the peptide was dissolved and another solvent or MilliQ water. Single crystals were grown upon a range of few weeks or even 6 months period, depending from the sequence.

6.3.5.1. Crystallographic details

fYI

Similar needle-shaped single crystals of the peptide were collected with a loop from both the methanol: water and the phosphate buffer mother waters. In both cases, cryoprotection obtained by dipping the crystal in glycerol allowed to store the frozen samples in liquid nitrogen. Crystals were mounted on the diffractometer at the synchrotron Elettra, Trieste (Italy), beamline XRD1, using the robot present at the facility. Temperature was kept at 100 K by a stream of nitrogen on the crystal during each data collection session. Diffraction data were collected by the rotating crystal method using synchrotron radiation, wavelength 0.70 Å, rotation interval 1°/image, crystal-to-detector distance of 85 mm. A total of 180 images were collected for each of the crystals. Separately for the two different datasets, reflections were indexed and integrated using the XDS package [97], space group $P2_1$ was determined using POINTLESS [98] and the resulting data set was scaled using AIMLESS [99]. Phase information were obtained by direct methods using the software SHELXT [100]. Refinements

cycles were conducted with SHELXL-14 [101], operating through the WinGX GUI [102], by full-matrix least-squares methods on F^2. Unit cell parameters and scaling statistics for each of the data collections are reported in Table S3. The asymmetric unit contains two molecules of the peptide and 3 molecules of water in the same position for both the structures. All the atoms, except the hydrogen atoms, within the asymmetric unit have been refined with anisotropic thermal parameters. Hydrogen atoms of the peptide were added at geometrically calculated positions and refined isotropically. Refinement statistics are reported in Table S1.

Vff

A needle-shaped single crystal of the peptide was collected with a loop, cryoprotected by dipping the crystal in glycerol and stored frozen in liquid nitrogen. The crystal was mounted on the diffractometer at the synchrotron Elettra, Trieste (Italy), beamline XRD1, using the robot present at the facility. Temperature was kept at 100 K by a stream of nitrogen on the crystal. Diffraction data were collected by the rotating crystal method using synchrotron radiation, wavelength 0.70 Å, rotation interval 1°/image, crystal-to-detector distance of 85 mm. A total of 180 images were collected. Reflections were indexed and integrated using the XDS package [97], space group $P2_12_12_1$ was determined using POINTLESS [98] and the resulting data set was scaled using AIMLESS [99]. Phase information were obtained by direct methods using the software SHELXT [100]. Refinements cycles were conducted with SHELXL-14 [101], operating through the WinGX GUI [102], by full-matrix least-squares methods on F^2. Unit cell parameters and scaling statistics are reported in Table S1. The asymmetric unit contains a molecule of the peptide and a molecule of methanol. All the atoms, except the hydrogen atoms, within the asymmetric unit have been refined with anisotropic thermal parameters. During refinement, restraints were added for the C-O distance of the methanol molecule and for its thermal parameters, using the DFIX and SIMU cards of SHELXL-14 [101], respectively. Hydrogen atoms of the peptide and of the methyl moiety of the alcohol molecule were added at geometrically calculated positions and refined isotropically, with thermal parameters dependent on those of the attached atom. The hydrogen atom of the hydroxyl moiety of the alcohol could not be located, possibly due to a statistical disordered caused by different hydrogen bonding patterns involving the solvent molecule. A small amount of additional electron density is present in the unit cell and reveals the presence of more solvent (methanol) or precipitant (water) molecules, in statistically disordered positions that could not be identified. Refinement statistics are reported in Table S2.

Iff

A needle-shaped single crystal of the peptide was collected with a loop, cryoprotected by dipping the crystal in glycerol and stored frozen in liquid nitrogen. The crystal was mounted on the diffractometer at the synchrotron Elettra, Trieste (Italy), beamline XRD1, using the robot present at the facility. Temperature was kept at 100 K by a stream of nitrogen on the crystal. Diffraction data were collected by the rotating crystal method using synchrotron radiation, wavelength 0.70 Å, rotation interval 1°/image, crystal-to-detector distance of 85 mm. A total of 360 images were collected. Reflections were indexed and integrated using the XDS package [97], space group *P1* was determined using POINTLESS [98] and the resulting data set was scaled using AIMLESS [99]. Phase information were obtained by direct methods using the software SHELXT [100]. Refinements cycles were conducted with SHELXL-14 [101], operating through the WinGX GUI [102], by full-matrix least-squares methods on F^2. Unit cell parameters and scaling statistics are reported in Table S2. The asymmetric unit contains three molecules of the peptide, a molecule of methanol and 6 molecules of water. During refinement, a disorder for the isoleucine side chain of one of the crystallographically independent monomers was notices and two different positions were refined at 54% and 46% occupancy factor, respectively. All the atoms, except the hydrogen atoms, within the asymmetric unit have been refined with anisotropic thermal parameters. Hydrogen atoms of the peptide and of the alcohol molecule were added at geometrically calculated positions and refined isotropically. Hydrogen atoms of the water molecules were added with restrains on bond lengths and bond angle, using the DFIX and DANG cards of SHELXL-14 [101], respectively. Refinement statistics are reported in Table S2.

fFF

A needle-shaped single crystal of the peptide was collected with a loop, cryoprotected by dipping the crystal in glycerol and stored frozen in liquid nitrogen. The crystal was mounted on the diffractometer at the synchrotron Elettra, Trieste (Italy), beamline XRD1, using the robot present at the facility. Temperature was kept at 100 K by a stream of nitrogen on the crystal. Diffraction data were collected by the rotating crystal method using synchrotron radiation, wavelength 0.70 Å, rotation interval 3°/image, crystal-to-detector distance of 85 mm. A total of 90 images were collected. Reflections were indexed and integrated using the XDS package [97], space group $P2_1$ was determined using POINTLESS [98] and the resulting data set was scaled using AIMLESS [99]. Phase information were obtained by direct methods using the software SHELXT [100]. Refinements cycles were conducted with SHELXL-14 [101],

operating through the WinGX GUI [102], by full-matrix least-squares methods on F^2. Unit cell parameters and scaling statistics are reported in Table S2. The asymmetric unit contains a molecule of the peptide, 2 molecules of water and a molecule of 2-propanol. All the atoms, except the hydrogen atoms, within the asymmetric unit have been refined with anisotropic thermal parameters. Hydrogen atoms of the peptide and of the alcohol molecule were added at geometrically calculated positions and refined isotropically. Hydrogen atoms of the water molecules were added with restrains on bond lengths and bond angle, using the DFIX and DANG cards of SHELXL-14 [101], respectively. Refinement statistics are reported in Table S2.

VFF

A needle-shaped single crystal of the peptide was collected with a loop, cryoprotected by dipping the crystal in glycerol and stored frozen in liquid nitrogen. The crystal was mounted on the diffractometer at the synchrotron Elettra, Trieste (Italy), beamline XRD1, using the robot present at the facility. Temperature was kept at 100 K by a stream of nitrogen on the crystal. Diffraction data were collected by the rotating crystal method using synchrotron radiation, wavelength 0.70 Å, rotation interval 1°/image, crystal-to-detector distance of 85 mm. A total of 180 images were collected. Reflections were indexed and integrated using the XDS package [97], space group *C2* was determined using POINTLESS [98] and the resulting data set was scaled using AIMLESS [99]. Phase information were obtained by direct methods using the software SHELXT [100]. Refinements cycles were conducted with SHELXL-14 [101], operating through the WinGX GUI [102], by full-matrix least-squares methods on F^2. Unit cell parameters and scaling statistics are reported in Table S1. The asymmetric unit contains a molecule of the peptide and 2 molecules of methanol. All the atoms, except the hydrogen atoms, within the asymmetric unit have been refined with anisotropic thermal parameters. Hydrogen atoms of the peptide and of the alcohol molecules were added at geometrically calculated positions and refined isotropically, with thermal parameters dependent on those of the attached atom. Refinement statistics are reported in Table S3.

IFF

A needle-shaped single crystal of the peptide was collected with a loop, cryoprotected by dipping the crystal in glycerol and stored frozen in liquid nitrogen. The crystal was mounted on the diffractometer at the synchrotron Elettra, Trieste (Italy), beamline XRD1, using the robot present at the facility. Temperature was kept at 100 K by a stream of nitrogen on the crystal. Diffraction data were collected by the rotating crystal method using synchrotron radiation,

wavelength 0.70 Å, rotation interval 1°/image, crystal-to-detector distance of 85 mm. A total of 180 images were collected. Reflections were indexed and integrated using the XDS package [97], space group *C2* was determined using POINTLESS [98] and the resulting data set was scaled using AIMLESS [99]. Phase information were obtained by direct methods using the software SHELXT [100]. Refinements cycles were conducted with SHELXL-14 [101], operating through the WinGX GUI [102], by full-matrix least-squares methods on F^2. Unit cell parameters and scaling statistics are reported in Table S3. The asymmetric unit contains a molecule of the peptide and 2 molecules of methanol. All atoms, except hydrogen atoms, within the asymmetric unit have been refined with anisotropic thermal parameters. Hydrogen atoms of the peptide and of the alcohol molecules were added at geometrically calculated positions and refined isotropically. Refinement statistics are reported in Table S3.

FFF

A needle-shaped single crystal of the peptide was collected with a loop, cryoprotected by dipping the crystal in glycerol and stored frozen in liquid nitrogen. The crystal was mounted on the diffractometer at the synchrotron Elettra, Trieste (Italy), beamline XRD1, using the robot present at the facility. Temperature was kept at 100 K by a stream of nitrogen on the crystal. Diffraction data were collected by the rotating crystal method using synchrotron radiation, wavelength 0.70 Å, rotation interval 1°/image, crystal-to-detector distance of 85 mm. A total of 180 images were collected. Reflections were indexed and integrated using the XDS package [97], space group *C2* was determined using POINTLESS [98] and the resulting data set was scaled using AIMLESS [99]. Phase information were obtained by direct methods using the software SHELXT [100]. Refinements cycles were conducted with SHELXL-14 [101], operating through the WinGX GUI [102], by full-matrix least-squares methods on F^2. Unit cell parameters and scaling statistics are reported in Table S1. The asymmetric unit contains a molecule of the peptide and 2 molecules of methanol. All the atoms, except the hydrogen atoms, within the asymmetric unit have been refined with anisotropic thermal parameters. Hydrogen atoms of the peptide and of the alcohol molecule were added at geometrically calculated positions and refined isotropically, with thermal parameters dependent on those of the attached atom. Refinement statistics are reported in Table S3.

vFW

A needle-shaped single crystal of the peptide was collected with a loop, cryoprotected by dipping the crystal in glycerol and stored frozen in liquid nitrogen. The crystal was mounted

on the diffractometer at the synchrotron Elettra, Trieste (Italy), beamline XRD1, using the robot present at the facility. Temperature was kept at 100 K by a stream of nitrogen on the crystal. Diffraction data were collected by the rotating crystal method using synchrotron radiation, wavelength 0.70 Å, rotation interval 1°/image, crystal-to-detector distance of 85 mm. A total of 181 images were collected. Reflections were indexed and integrated using the XDS package [97], space group $P6_5$ was determined using POINTLESS [98] and the resulting data set was scaled using AIMLESS [99]. Phase information were obtained by direct methods using the software SHELXT [100]. Refinements cycles were conducted with SHELXL-14 [101], operating through the WinGX GUI [102], by full-matrix least-squares methods on F^2. Unit cell parameters and scaling statistics are reported in Table S2. The asymmetric unit contains a molecule of the peptide and 3 molecules of water. All the atoms, except the hydrogen atoms, within the asymmetric unit have been refined with anisotropic thermal parameters. Hydrogen atoms of the peptide molecule were added at geometrically calculated positions and refined isotropically. Hydrogen atoms of the water molecules were added with restrains on bond lengths and bond angle, using the DFIX and DANG cards of SHELXL-14 [101], respectively. Disordered solvent molecules present in the large cavities of the structure were too difficult to be modelled, but their contribution was taken into account using the SQUEEZE/PLATON procedure [8]. Residual electron densities corresponding to 332 electrons/cell were found in the voids of vFW crystals, corresponding to 20% of the cell volume. Refinements using reflections modified by the SQUEEZE procedure behaved well and R-factors were reduced from 10% to 6%. Refinement statistics are reported in Table S4.

iFW

A needle-shaped single crystal of the peptide was collected with a loop, cryoprotected by dipping the crystal in glycerol and stored frozen in liquid nitrogen. The crystal was mounted on the diffractometer at the synchrotron Elettra, Trieste (Italy), beamline XRD1, using the robot present at the facility. Temperature was kept at 100 K by a stream of nitrogen on the crystal. Diffraction data were collected by the rotating crystal method using synchrotron radiation, wavelength 0.70 Å, rotation interval 1°/image, crystal-to-detector distance of 85 mm. A total of 175 images were collected. Reflections were indexed and integrated using the XDS package [97], space group $P6_5$ was determined using POINTLESS [98] and the resulting data set was scaled using AIMLESS [99]. Phase information were obtained by direct methods using the software SHELXT [100]. Refinements cycles were conducted with SHELXL-14 [101], operating through the WinGX GUI [102], by full-matrix least-squares methods on F^2. Unit cell

parameters and scaling statistics are reported in Table S2. The asymmetric unit contains a molecule of the peptide and 3 molecules of water. All the atoms, except the hydrogen atoms, within the asymmetric unit have been refined with anisotropic thermal parameters. Hydrogen atoms of the peptide molecule were added at geometrically calculated positions and refined isotropically. Hydrogen atoms of the water molecules were added with restrains on bond lengths and bond angle, using the DFIX and DANG cards of SHELXL-14 [101], respectively. Disordered solvent molecules present in the large cavities of the structure were too difficult to be modelled, but their contribution was taken into account using the SQUEEZE/PLATON procedure [8]. Residual electron densities corresponding to 357 electrons/cell were found in the voids of iFW crystals, corresponding to 21% of the cell volume. Refinements using reflections modified by the SQUEEZE procedure behaved well and R-factors were reduced from 8% to 6%. Refinement statistics are reported in Table S4.

pWF

A needle-shaped single crystal of the peptide was collected with a loop, cryoprotected by dipping the crystal in glycerol and stored frozen in liquid nitrogen. The crystal was mounted on the diffractometer at the synchrotron Elettra, Trieste (Italy), beamline XRD1, using the robot present at the facility. Temperature was kept at 100 K by a stream of nitrogen on the crystal. Diffraction data were collected by the rotating crystal method using synchrotron radiation, wavelength 0.70 Å, rotation interval 1°/image, crystal-to-detector distance of 85 mm. A total of 360 images were collected. Reflections were indexed and integrated using the XDS package [97], space group $P2_1$ was determined using POINTLESS [98] and the resulting data set was scaled using AIMLESS [99]. Phase information were obtained by direct methods using the software SHELXT [100]. Refinements cycles were conducted with SHELXL-14 [101], operating through the WinGX GUI [102], by full-matrix least-squares methods on F^2. Unit cell parameters and scaling statistics are reported in Table S4. The asymmetric unit contains a molecule of the peptide. All atoms, except hydrogen atoms, within the asymmetric unit have been refined with anisotropic thermal parameters. Hydrogen atoms were added at geometrically calculated positions and refined isotropically. Refinement statistics are reported in Table S5.

wFF

A needle-shaped single crystal of the peptide was collected with a loop, cryoprotected by dipping the crystal in glycerol and stored frozen in liquid nitrogen. The crystal was mounted

on the diffractometer at the synchrotron Elettra, Trieste (Italy), beamline XRD1, using the robot present at the facility. Temperature was kept at 100 K by a stream of nitrogen on the crystal. Diffraction data were collected by the rotating crystal method using synchrotron radiation, wavelength 0.70 Å, rotation interval 1°/image, crystal-to-detector distance of 85 mm. A total of 270 images were collected. Reflections were indexed and integrated using the XDS package [97], space group $P2_1$ was determined using POINTLESS [98] and the resulting data set was scaled using AIMLESS [99]. Phase information were obtained by direct methods using the software SHELXT [100]. Refinements cycles were conducted with SHELXL-14 [101], operating through the WinGX GUI [102], by full-matrix least-squares methods on F^2. Unit cell parameters and scaling statistics are reported in Table S4. The asymmetric unit contains a molecule of the peptide and a molecule of water, statistically disordered in two positions at partial occupancy (68% and 32%, respectively). The statistical occupation of the water was refined. All atoms, except hydrogen atoms, within the asymmetric unit have been refined with anisotropic thermal parameters. Hydrogen atoms of the peptide molecule were added at geometrically calculated positions and refined isotropically. Hydrogen atoms of the water molecule were added to each statistical position with restrains on bond lengths and bond angle, using the DFIX and DANG cards of SHELXL-14 [101], respectively. Refinement statistics are reported in Table S5.
More references: [103], [104].

6.3.6. Trypan blue exclusion test of cell viability

To count the cells before to add them on hydrogel surfaces, they need to be counted. Culture medium was removed from cell growth plate and the latter was washed with PBS (Phosphate Buffered Saline 0.0067 M, without Ca and Mg, BioWhittaker by Lonza), then 1.0 ml of trypsin/EDTA (BioWhittaker by Lonza, 170.000 U Trypsin/L, 200mg/L Versene, EDTA), was added and let the cells to detach from the plate for 10-15 min. Suddenly, more medium was added, the suspension was mixed well, and 1.0-1.5 ml were moved into an Eppendorf tube. 10µl from this tube were then transfer in a new tube to whom 10µl of trypan blue (Life Technologies Corporation) were added and mixed 10 times. 10µl of this last mixture were finally added to the Countless slide and the percentage of living and dead cells were measured through the Countess ™ Automated Cell Counter (Invitrogen).

6.3.7. Fibroblast cell culture live/dead assay

Peptide self-assembled hydrogels were prepared as described above (Section X, by using 10 µl of each precursor solution which were filtered 0.2 mm) and added to each microwell of a µ-slide Angiogenesis uncoated (Ibidi) in a laminar-flow cabinet (final gel volume of 20 µl). Hydrogels were left to settle at room temperature for 24 h. 30 µl of milli-Q filtered 0.2 mm water (only for one column) and fresh DMEM/glutamax (Invitrogen) medium containing 10% foetal bovine serum were added and incubated for 30 min at room temperature were gently added on top of gels. Controls consist of hydrogels with 30 µl of media and 30 µl and milli-Q filtered 0.2 mm water. The solution was then replaced with media containing L929 fibroblasts (mouse C3H/An connective tissue from Sigma) at 15,000 cells per well. These were cultured at 37°C in a humidified incubator for up to 3 days, exchanging the media with fresh (30 µl) after 48h. A few drops of sterile PBS were carefully placed between the microwells to reduce evaporation. Live/dead assays were performed at 24 h, 48 h, or 72 h by replacing 30 µl of the media with 15 µl of freshly prepared live/dead solution containing calcein (live) and ethidium-homodimer (dead), (Viability/Cytotoxicity kit for mammalian cell, Invitrogen by Thermo Fisher Scientific) prepared according to the manufacturers' instructions. Following 20 min incubation, cells were imaged on an inverted widefield fluorescence microscope (EVO FL Microscope). Each condition was repeated twice in triplicates. Representative images after 72 h incubation are shown.

6.3.8. MTS assay

Microwells containing hydrogels and cells, cells only (control), hydrogel only with media or milliQ water filtered 0.2 mm were prepared as described in Section X and incubated for 24 h. 25 µl of media were replaced with 25 µl of an MTS solution (ab197010 from Abcam). Absorbance at 490 nm was read by placing 5 µl samples on a Nanodrop ND-2000c Spectrophotometer (Thermo Scientific). Each measurement was repeated at least three times per sample, and each condition was repeated twice in quintuplicate. Absorbance at 490 nm of the blanks was subtracted to the absorbance at 490 nm of the samples and controls. Data are represented as means + standard deviation (SD).

7.SUPPLEMENTARY

Synthesised peptides

1. xFF group

fYI

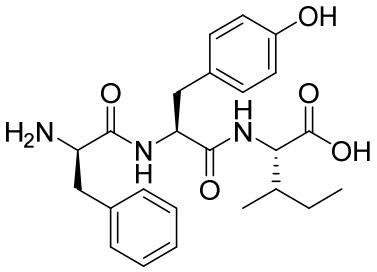

Chemical Formula: $C_{24}H_{31}N_3O_5$
Exact Mass: 441.23
Molecular Weight: 441.53

pFF

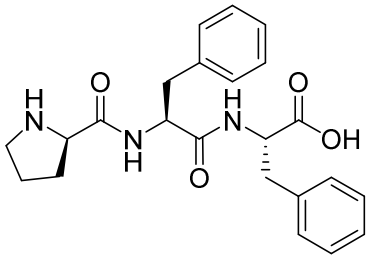

Chemical Formula: $C_{23}H_{27}N_3O_4$
Exact Mass: 409.20
Molecular Weight: 409.49

vFF

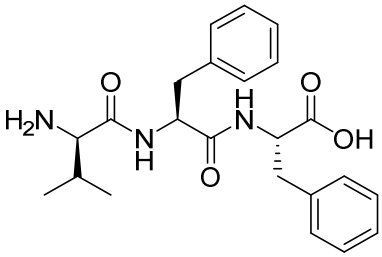

Chemical Formula: $C_{23}H_{29}N_3O_4$
Exact Mass: 411.22
Molecular Weight: 411.50

iFF

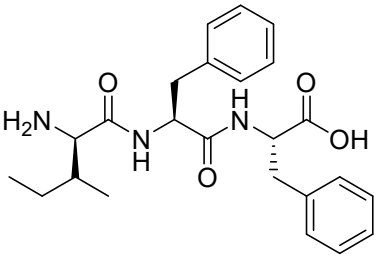

Chemical Formula: $C_{24}H_{31}N_3O_4$
Exact Mass: 425.23
Molecular Weight: 425.53

fFF

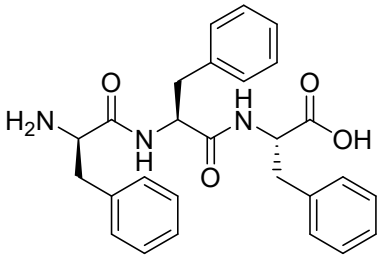

Chemical Formula: $C_{27}H_{29}N_3O_4$
Exact Mass: 459.22
Molecular Weight: 459.55

2. xFW group

sFW

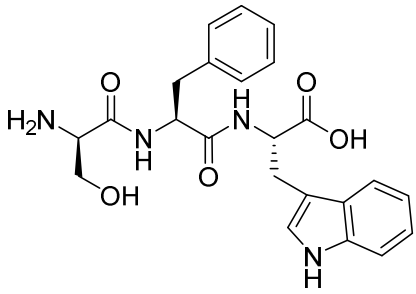

Chemical Formula: $C_{23}H_{26}N_4O_5$
Exact Mass: 438.19
Molecular Weight: 438.48

vFW

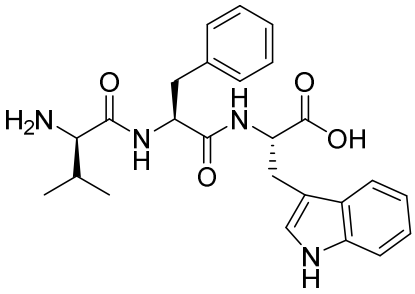

Chemical Formula: $C_{25}H_{30}N_4O_4$
Exact Mass: 450.23
Molecular Weight: 450.54

iFW

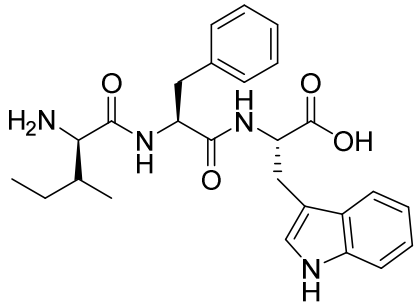

Chemical Formula: $C_{26}H_{32}N_4O_4$
Exact Mass: 464.24
Molecular Weight: 464.57

fFW

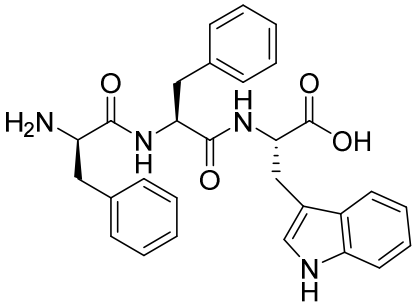

Chemical Formula: $C_{29}H_{30}N_4O_4$
Exact Mass: 498.23
Molecular Weight: 498.58

3. xXX group

pWF

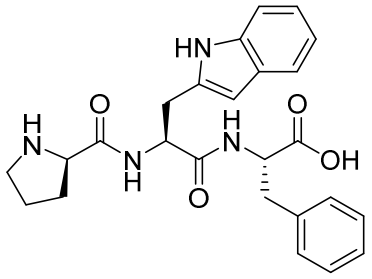

Chemical Formula: $C_{25}H_{28}N_4O_4$
Exact Mass: 448.21
Molecular Weight: 448.52

fWI

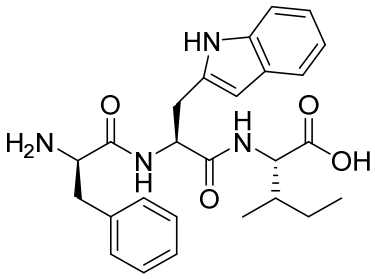

Chemical Formula: $C_{26}H_{32}N_4O_4$
Exact Mass: 464.24
Molecular Weight: 464.57

wLL

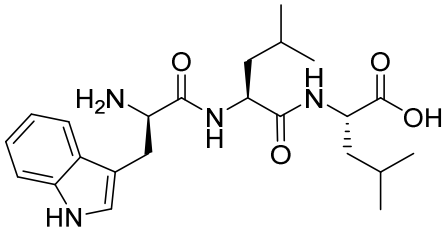

Chemical Formula: $C_{23}H_{34}N_4O_4$
Exact Mass: 430.26
Molecular Weight: 430.55

wFL

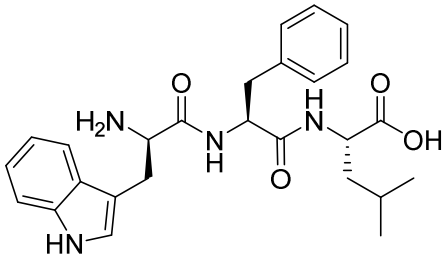

Chemical Formula: $C_{26}H_{32}N_4O_4$
Exact Mass: 464.24
Molecular Weight: 464.57

fWF

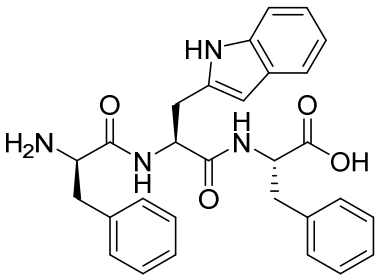

Chemical Formula: $C_{29}H_{30}N_4O_4$
Exact Mass: 498.23
Molecular Weight: 498.58

wWF

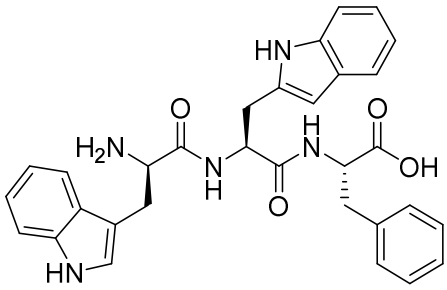

Chemical Formula: $C_{31}H_{31}N_5O_4$
Exact Mass: 537.24
Molecular Weight: 537.62

wFF

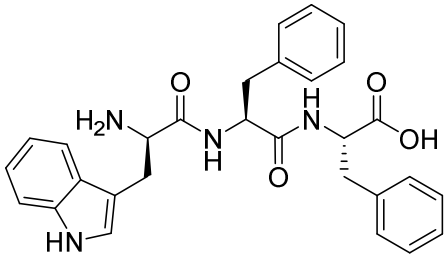

Chemical Formula: $C_{29}H_{30}N_4O_4$
Exact Mass: 498.23
Molecular Weight: 498.58

Spectroscopic Data for fYI

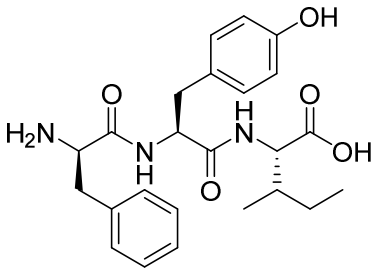

Chemical Formula: $C_{24}H_{31}N_3O_5$
Exact Mass: 441.23
Molecular Weight: 441.53

^{1}H-NMR (400 MHz, DMSO-*d*$_6$, TMS)

^{1}H-NMR (400 MHz, DMSO, TMS), δ (ppm): 9.19 (s, 1H, OH), 8.78 (d, *J* = 8.7 Hz, 1H, NH), 8.39 (d, *J* = 8.3 Hz, 1H, NH), 7.95 (s, 2H, NH_2), 7.26 – 7.17 (m, 4H, Ar), 7.10 (d, *J* = 8.4 Hz, 2H, Ar), 6.92 (m, *J* = 6.3, 2.7 Hz, 2H, Ar), 6.65 (d, *J* = 8.4 Hz, 2H, Ar), 4.78 – 4.70 (m, 1H, αCH), 4.18 (m, *J* = 8.2, 6.0 Hz, 1H, αCH), 4.01 (m, *J* = 7.8, 4.4 Hz, 1H, αCH), 2.95 (m, *J* = 13.8, 3.3 Hz, 1H, βCH_2), 2.84 (m, *J* = 14.2, 4.1 Hz, 1H, βCH_2), 2.57 (m, *J* = 13.9, 8.1 Hz, 2H, βCH_2), 1.80 (m, *J* = 12.9, 6.6 Hz, 1H, βCH), 1.50 – 1.39 (m, 1H, γCH_2), 1.26 – 1.16 (m, 1H, γCH_2), 0.90-0.84 (m, *J* = 7.1, 2.7 Hz, 6H, 3x γCH_3 and 3 x δCH_3).

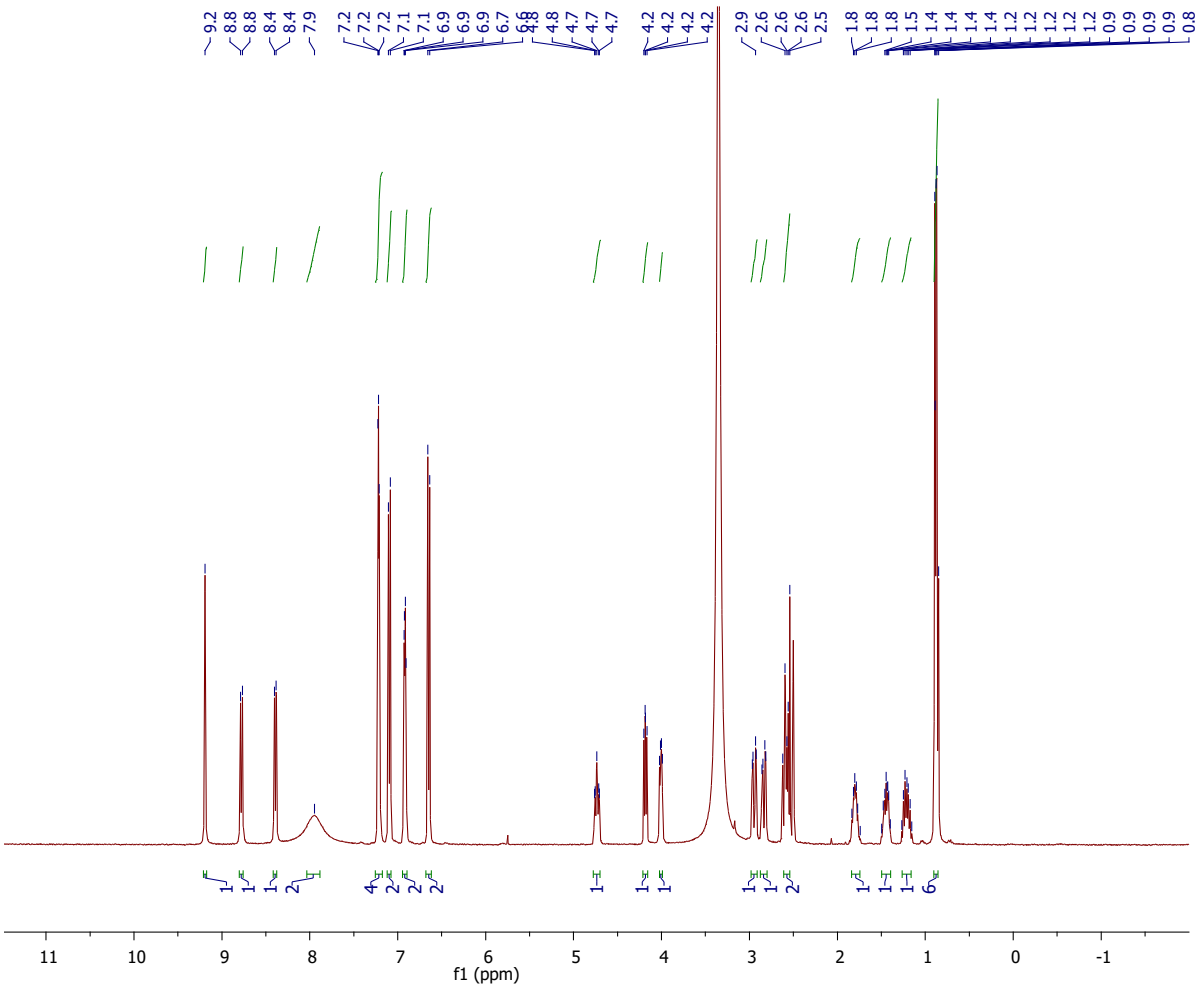

^{13}C-NMR (100MHz, DMSO-*d6*, TMS)

^{13}C-NMR (100 MHz, DMSO, TMS), δ (ppm): 172.8, 171.3, 167.5 (3 x CO); 156.1, 134.6, 130.4, 129.6, 128.4, 127.4, 127.1, 114.8 (Ar); 56.5, 53.9, 53.2 (3 x α C); 37.5, 36.9, 36.3 (2 x βCH_2 and 1 x βCH); 24.8, 15.6 (1 x γCH_2 and 1 x γCH_3); 11.4 (δCH_3).

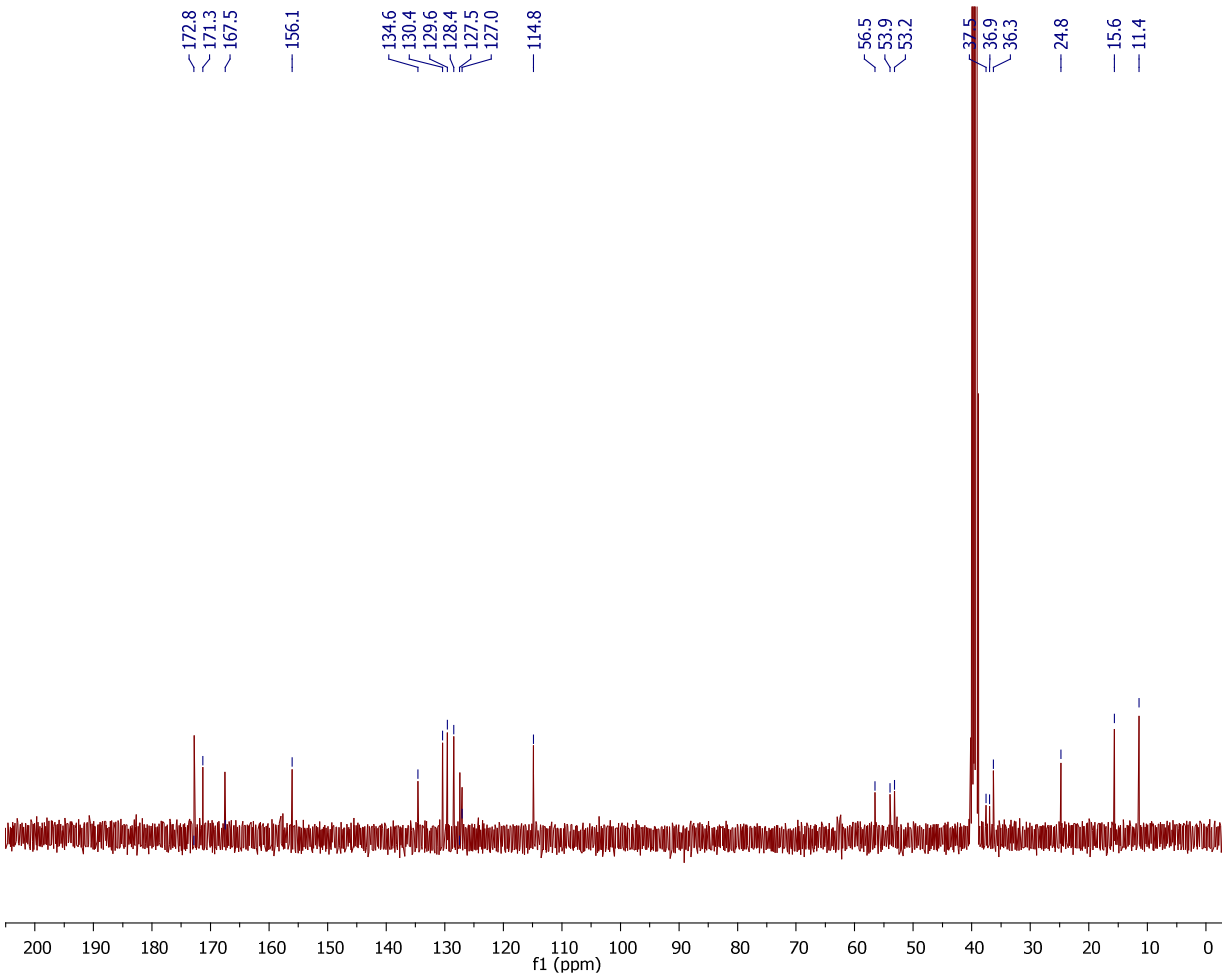

fYI, MS Spectra (Positive and Negative, top and bottom respectively).

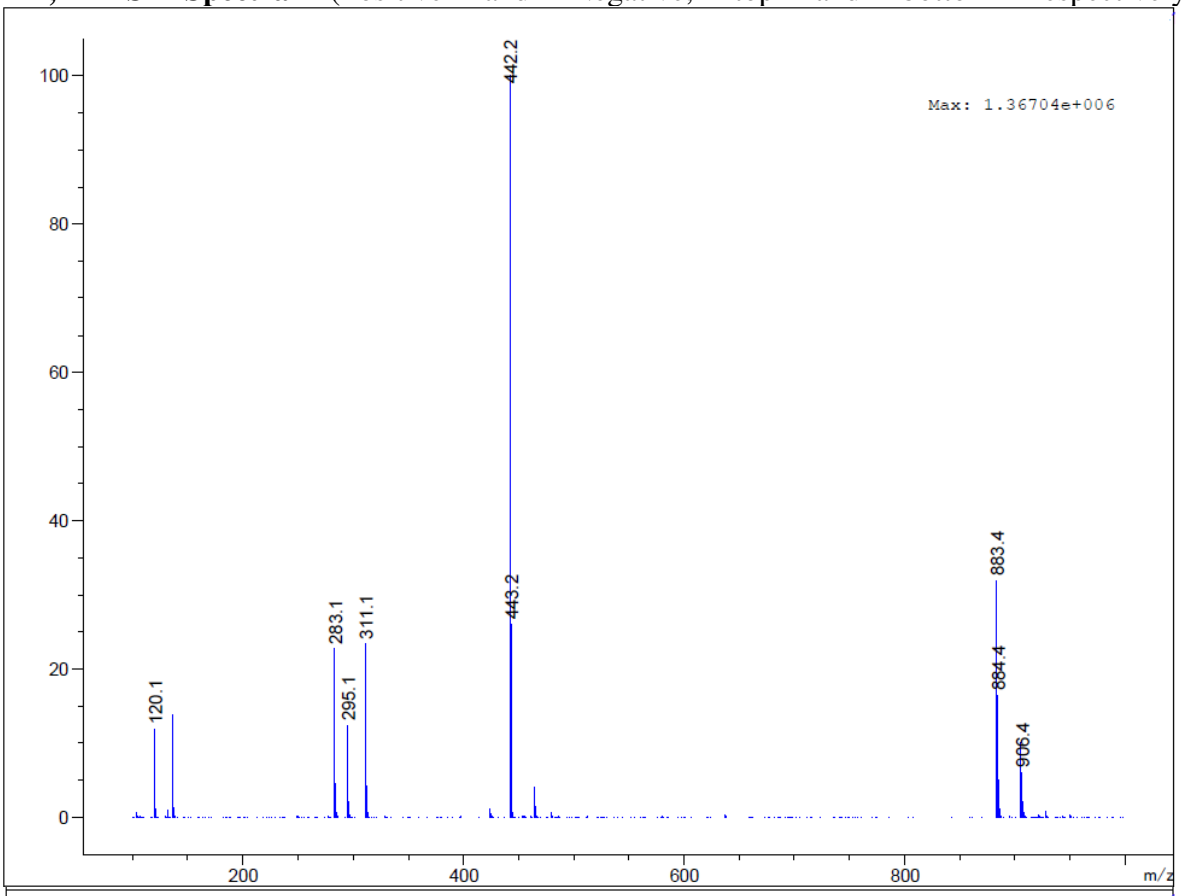

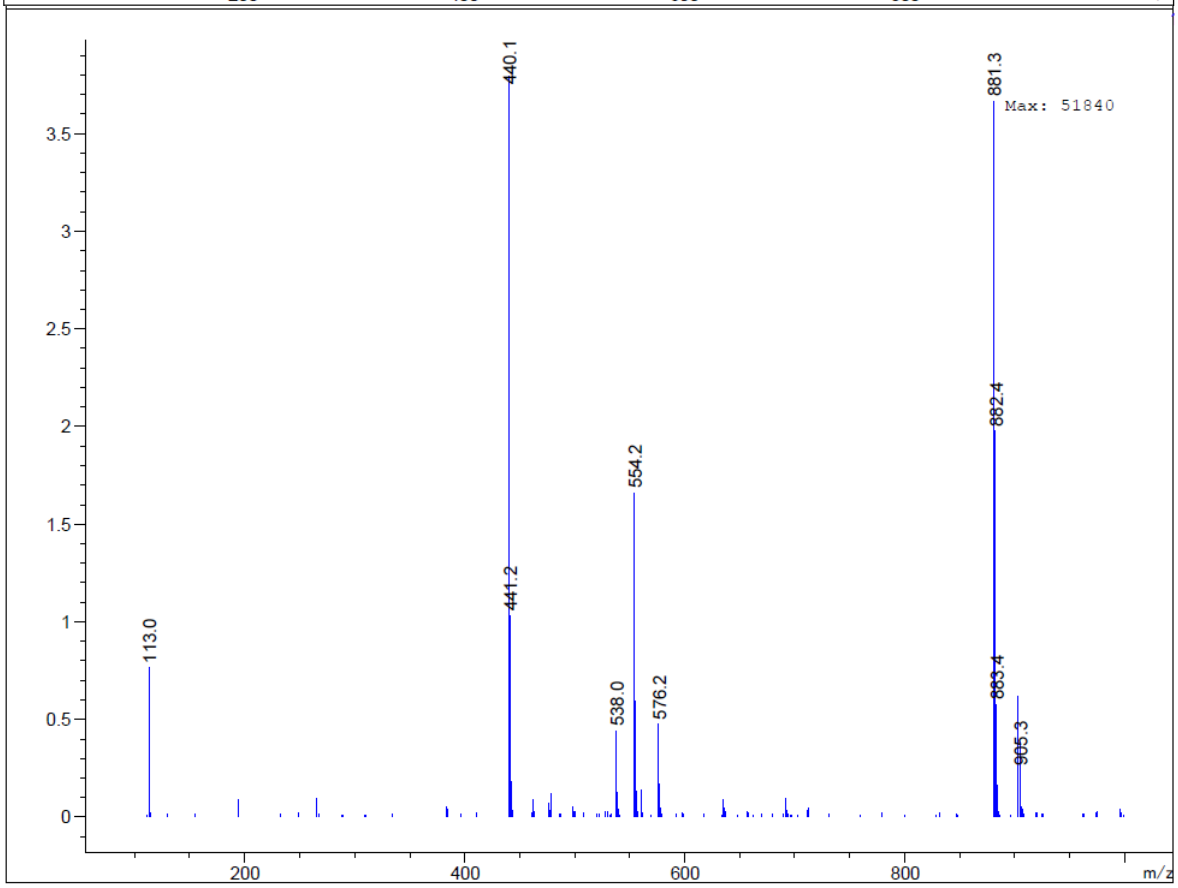

Spectroscopic Data for pFF

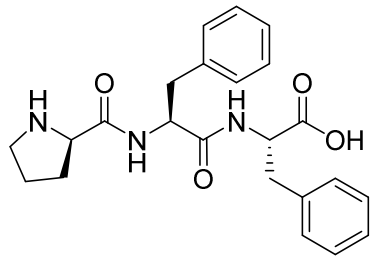

Chemical Formula: $C_{23}H_{27}N_3O_4$
Exact Mass: 409.20
Molecular Weight: 409.49

^{1}H NMR (400 MHz, DMSO-d_6, TMS)

^{1}H-NMR (400 MHz, DMSO, TMS), δ (ppm): 8.73 (d, *J* = 9.1 Hz, 1H, NH), 8.61 (d, *J* = 7.9 Hz, 1H, NH), 7.32 – 7.15 (m, 10H, Ar), 4.74 – 4.68 (m, 1H, αCH), 4.50 – 4.44 (m, 1H, αCH), 4.05 (m, *J* = 8.0, 7.3 Hz, 1H, αCH), 3.09 (m, *J* = 12.3, 10.0, 5.4 Hz, 4H, 2 x δCH_2 and 2 x βCH_2), 2.93 (m, *J* = 14.0, 9.3 Hz, 1H, βCH_2), 2.66 (m, *J* = 13.7, 11.0 Hz, 1H, βCH_2), 2.10 – 1.99 (m, 1H, βCH_2), 1.72 (m, *J* = 14.4, 7.3 Hz, 1H, βCH_2), 1.58 – 1.45 (m, 1H, γCH_2), 1.24 (m, *J* = 14.6, 7.1 Hz, 1H, γCH_2).

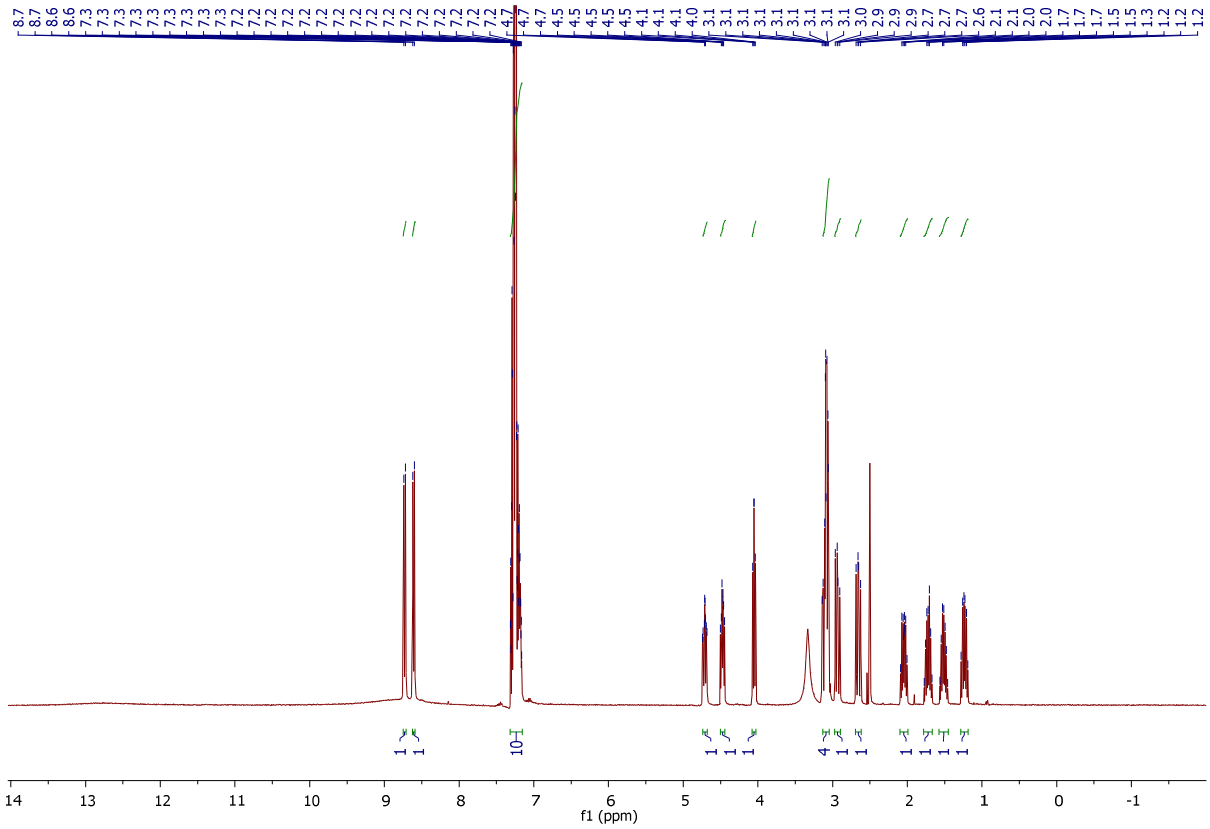

^{13}C-NMR (100MHz, DMSO-*d6*, TMS)

^{13}C-NMR (100 MHz, DMSO, TMS), δ (ppm): 172.7, 170.8, 167.5 (3 x CO); 137.5, 137.3, 129.3, 129.09, 128.25, 127.96, 126.5, 126.4 (Ar); 59.0, 53.6, 53.4 (3 x α C); 45.5 (δCH_2 pro), 38.2, 36.6, 29.6 (3 x βCH_2); 23.1 (γCH_2).

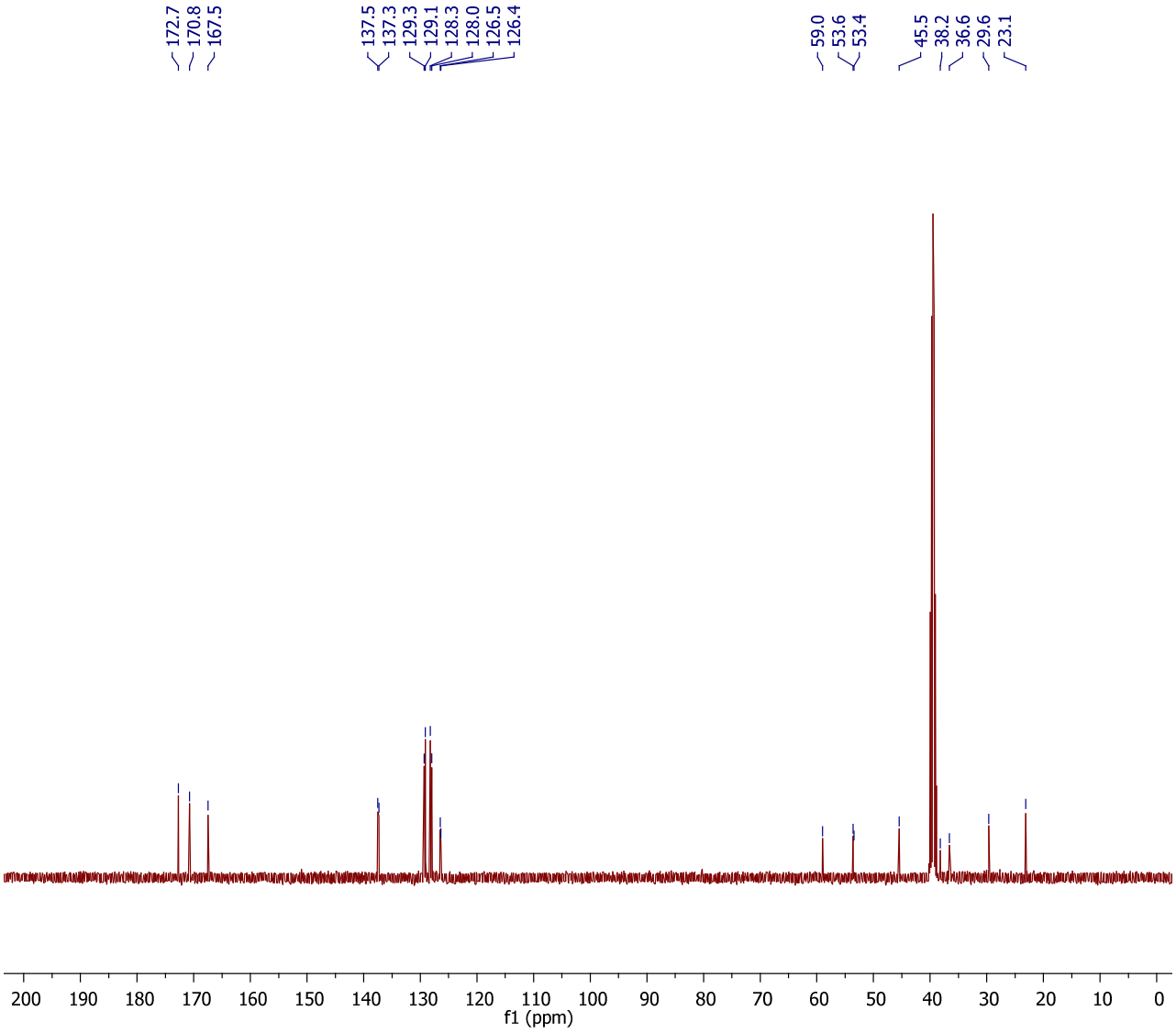

pFF, MS Spectra (Positive and Negative, top and bottom respectively).

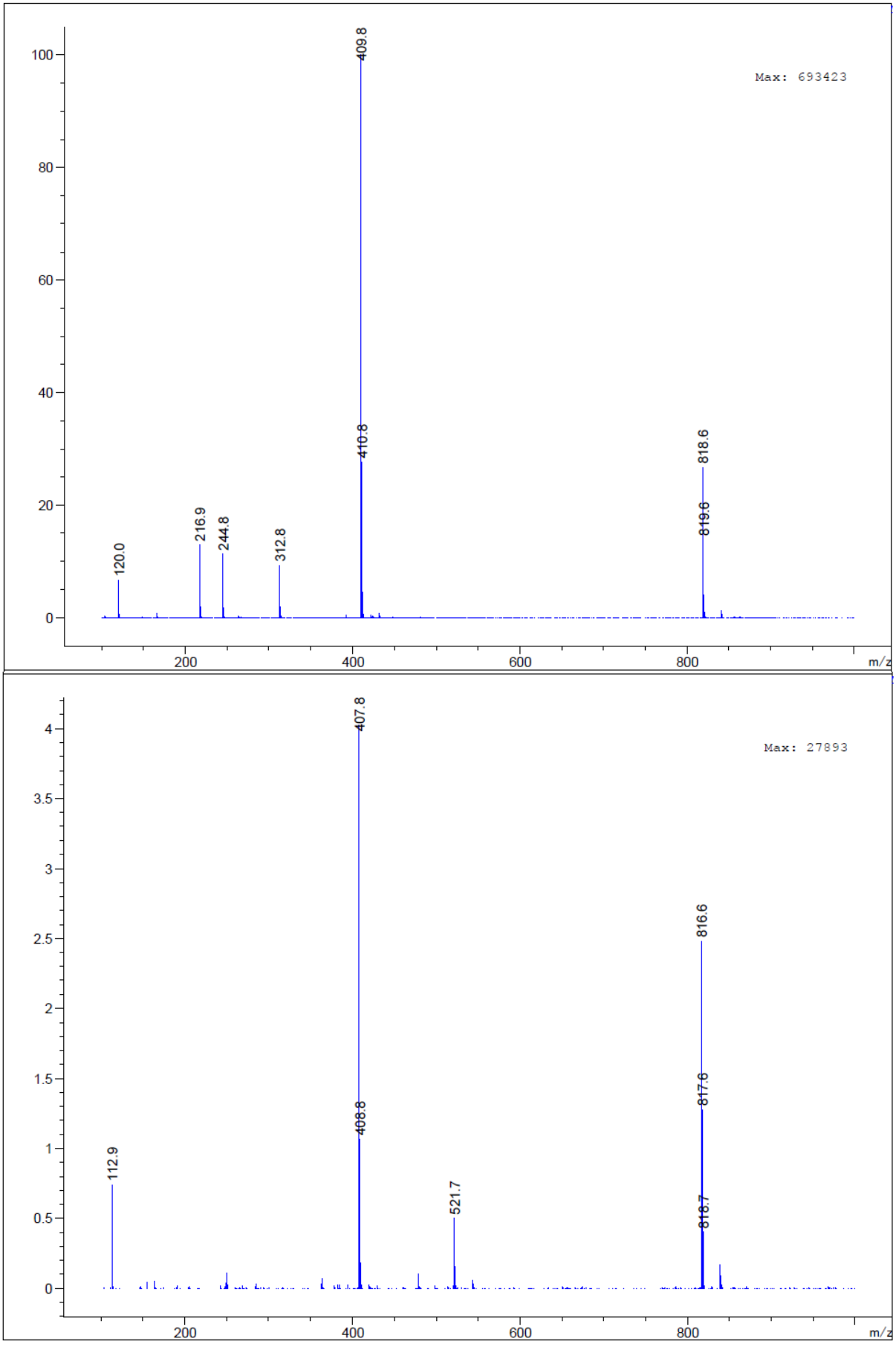

Spectroscopic Data for vFF

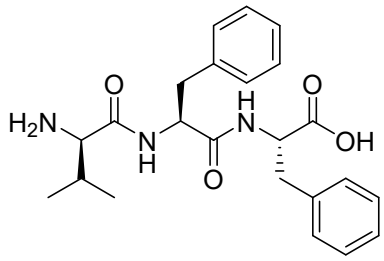

Chemical Formula: $C_{23}H_{29}N_3O_4$
Exact Mass: 411.22
Molecular Weight: 411.50

^{1}H-NMR (400 MHz, DMSO-d_6, TMS)

^{1}H-NMR (400 MHz, DMSO, TMS), δ (ppm): 12.86 (s, 1H, OH), 8.65 – 8.60 (m, 2H, NH), 7.89 (s, 2H, NH_2), 7.34 – 7.13 (m, 10H, Ar), 4.79 – 4.73 (m, 1H, αCH), 4.49 – 4.43 (m, 1H, αCH), 3.54 (s, 1H, αCH), 3.10 (m, J = 13.7, 4.6 Hz, 2H, βCH_2), 2.94 (m, J = 14.0, 9.2 Hz, 1H, βCH_2), 2.71 – 2.59 (m, 1H, βCH_2), 1.79 (m, J = 11.5, 6.9 Hz, 1H, βCH), 0.64 (d, J = 7.0 Hz, 3H, γCH_3), 0.37 (d, J = 7.0 Hz, 3H, γCH_3).

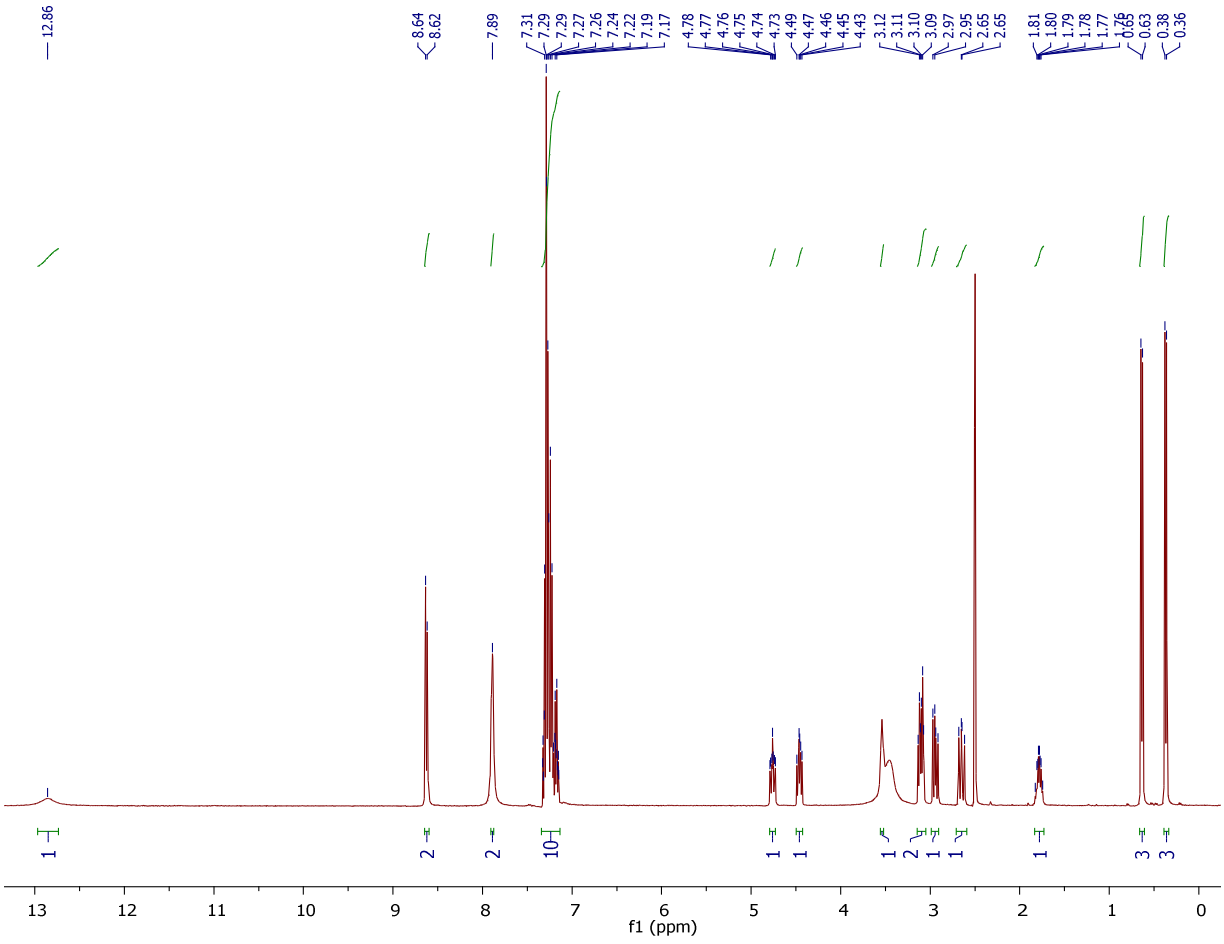

^{13}C-NMR (100MHz, DMSO-*d6*, TMS)

^{13}C-NMR (100 MHz, DMSO, TMS), δ (ppm): 172.8, 171.3, 167.5 (3 x CO), 137.5, 137.4, 129.2, 129.1, 128.3, 128.0, 126.5, 126.4 (Ar); 57.2, 53.8, 53.6 (3 x αC); 38.2, 36.6, 29.6 (2 x βCH$_2$ and 1 x βCH); 18.2, 16.3 (2 x γ CH$_3$).

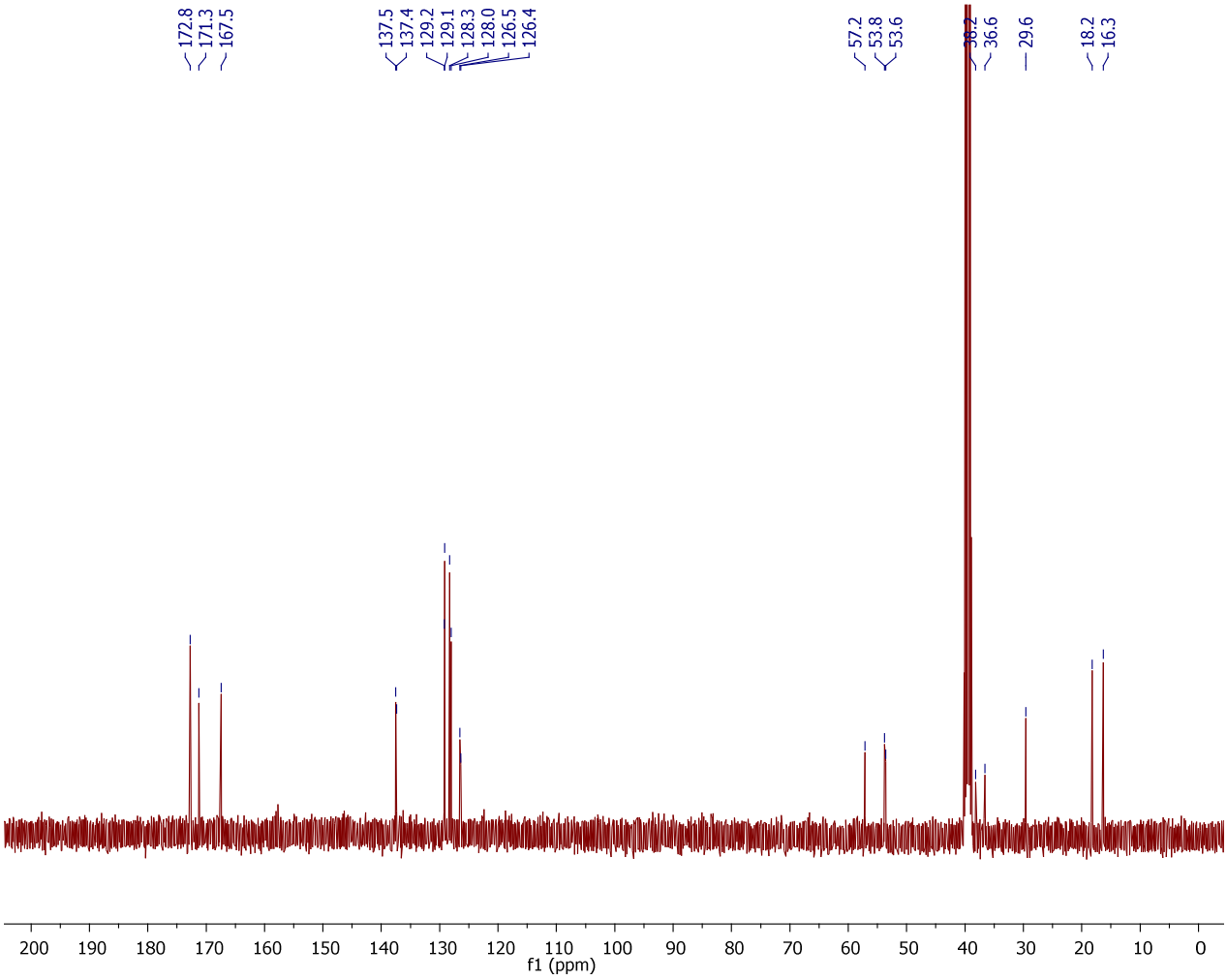

vFF, MS Spectra (Positive and Negative, top and bottom respectively).

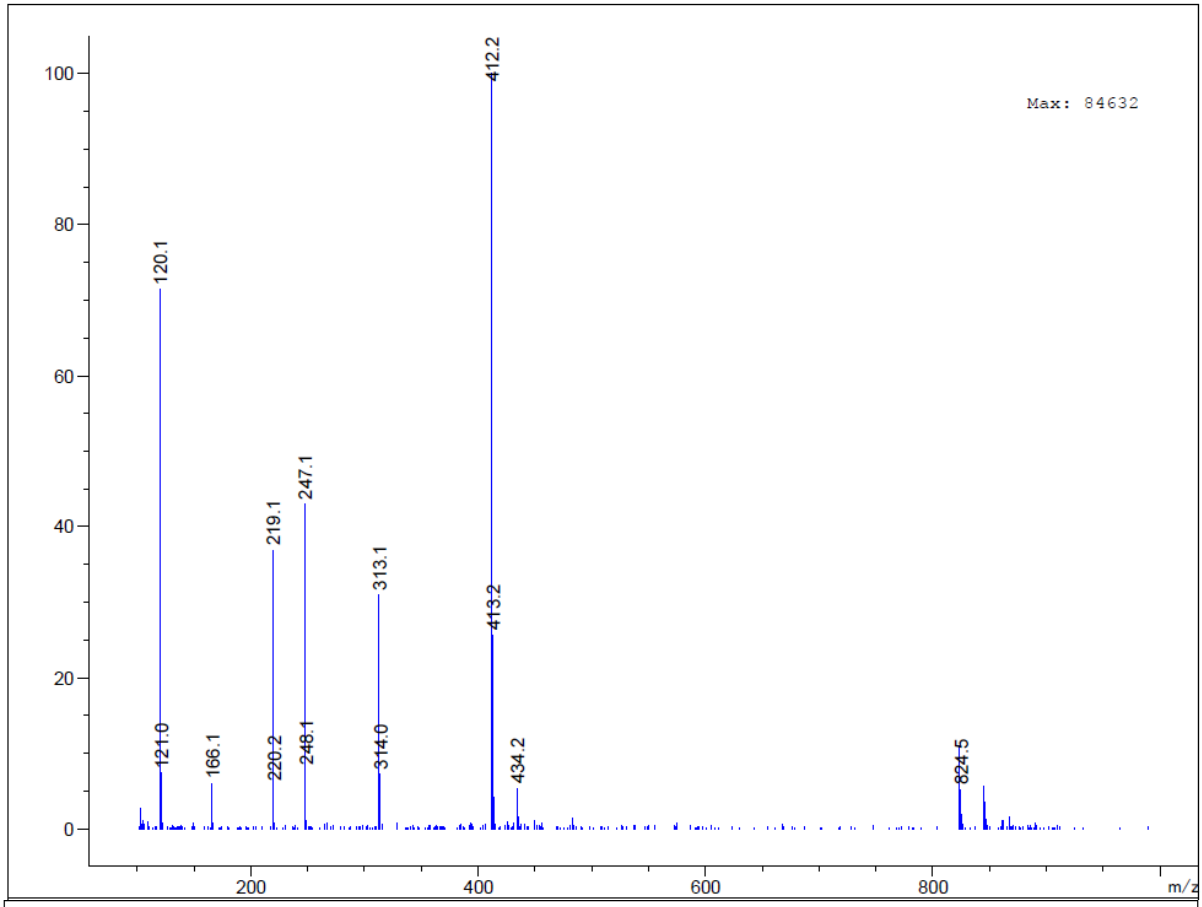

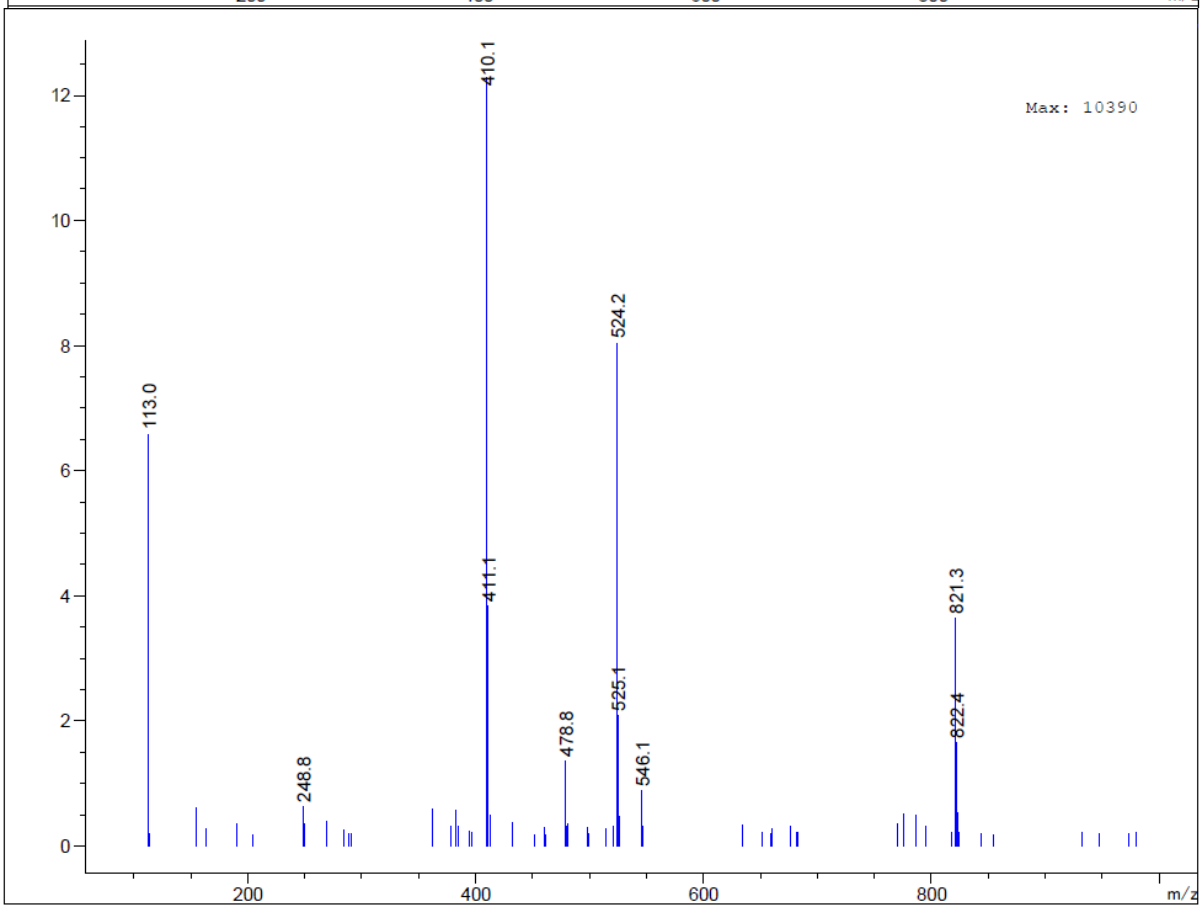

Spectroscopic Data for iFF

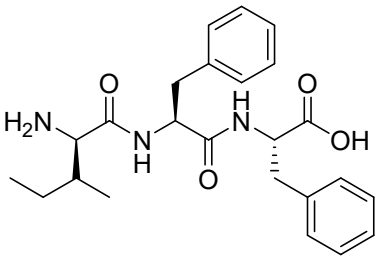

Chemical Formula: $C_{24}H_{31}N_3O_4$
Exact Mass: 425.23
Molecular Weight: 425.53

^{1}H-NMR (400 MHz, DMSO-*d*$_6$, TMS)

^{1}H-NMR (400 MHz, DMSO, TMS), δ (ppm): 8.60 (m, *J* = 8.1, 5.4 Hz, 2H, NH), 7.33 – 7.15 (m, 10H, Ar), 4.77 – 4.71 (m, 1H, αCH), 4.45 (m, *J* = 8.8, 5.1 Hz, 1H, αCH), 3.57 (d, *J* = 4.3 Hz, 1H, αCH), 3.13 – 3.07 (m, 2H, βCH$_2$), 2.94 (m, *J* = 14.0, 9.1 Hz, 1H, βCH$_2$), 2.66 (m, *J* = 13.9, 11.6 Hz, 1H, βCH$_2$), 1.57 – 1.46 (m, 1H, βCH), 0.96 – 0.84 (m, 1H, γCH$_2$), 0.65-0.60 (m, 1H, γCH$_2$), 0.59 – 0.54 (m, 6H, 3x γCH$_3$ and 3 x δCH$_3$).

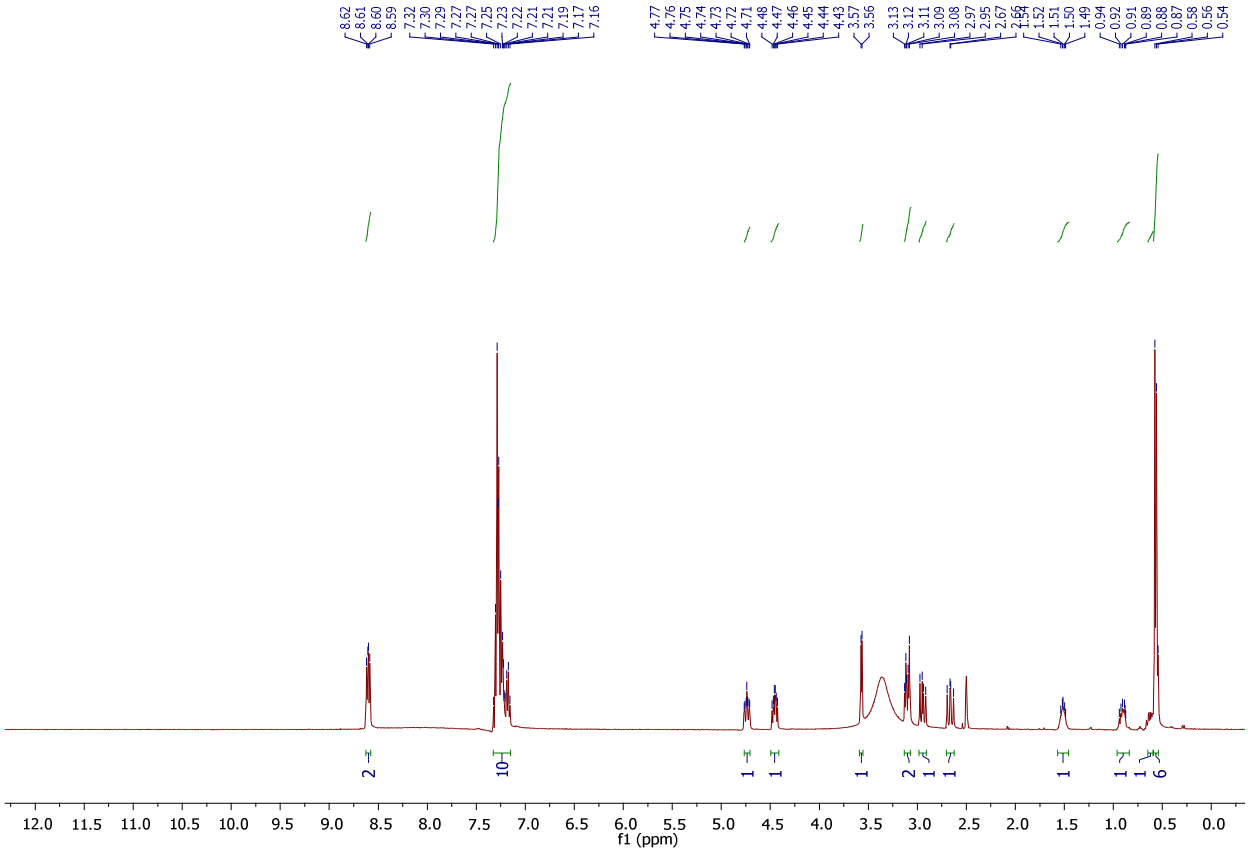

^{13}C-NMR (100MHz, DMSO-*d6*, TMS)

^{13}C-NMR (101 MHz, DMSO, TMS), δ (ppm): 172.8, 171.3, 167.5 (3 x CO); 137.5, 137.5, 129.2, 128.3, 128.03 126.53 126.4 (Ar); 56.7, 53.8, 53.8 (3 x αC); 38.0, 36.6, 36.0 (3 x βCH_2); 23.0 (γCH_2); 14.2 (γCH_3), 11.3 (δCH_3).

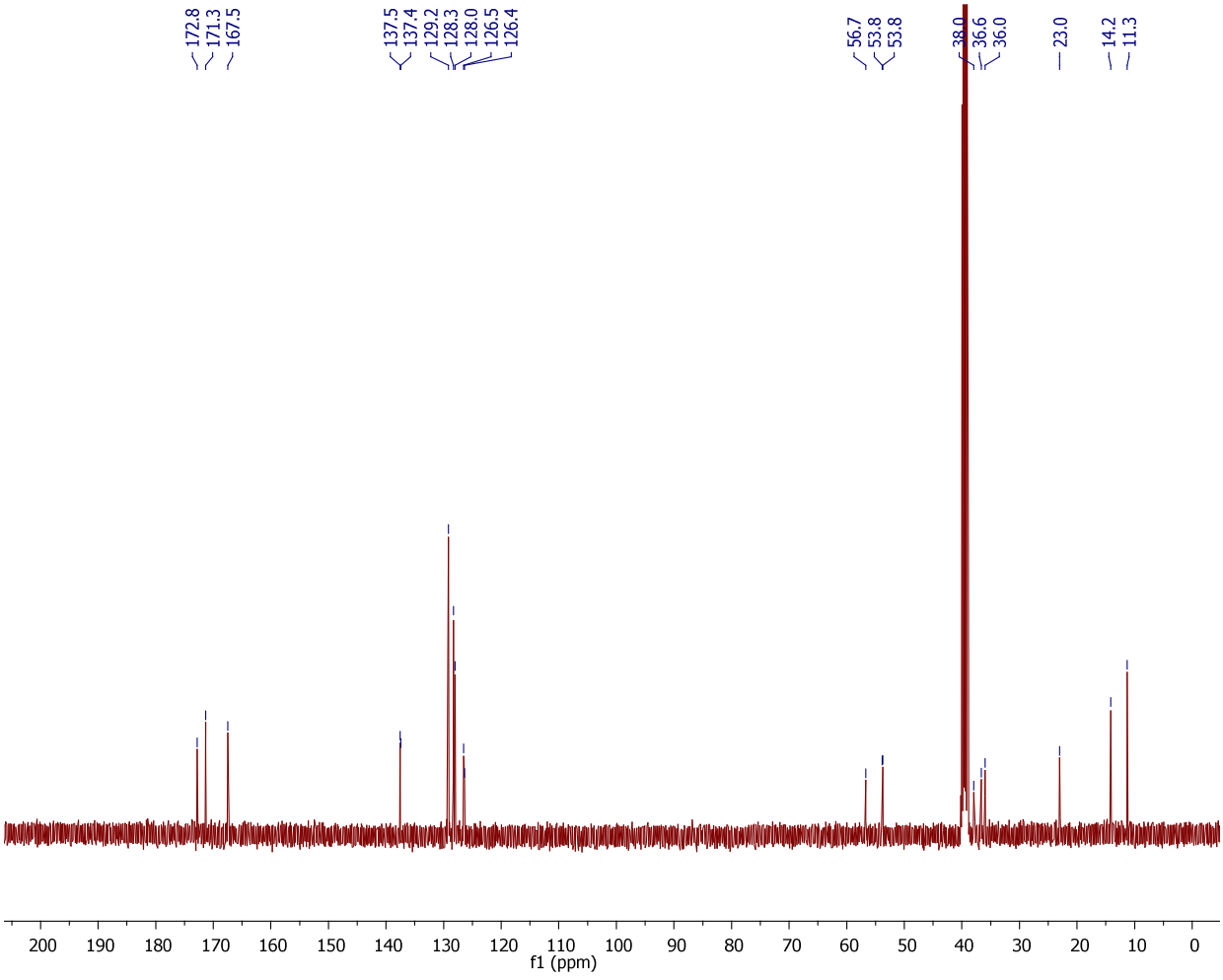

iFF, MS Spectra (Positive and Negative, top and bottom respectively).

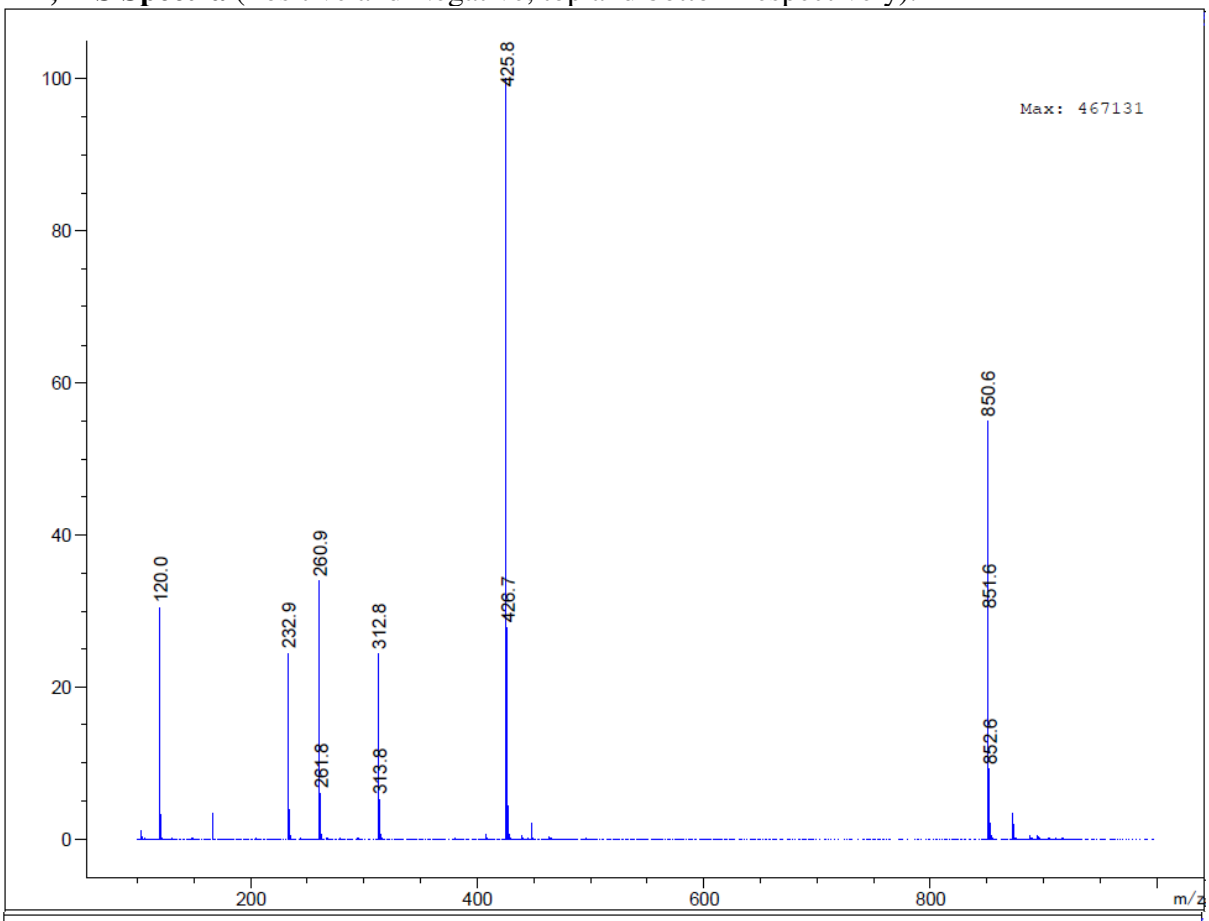

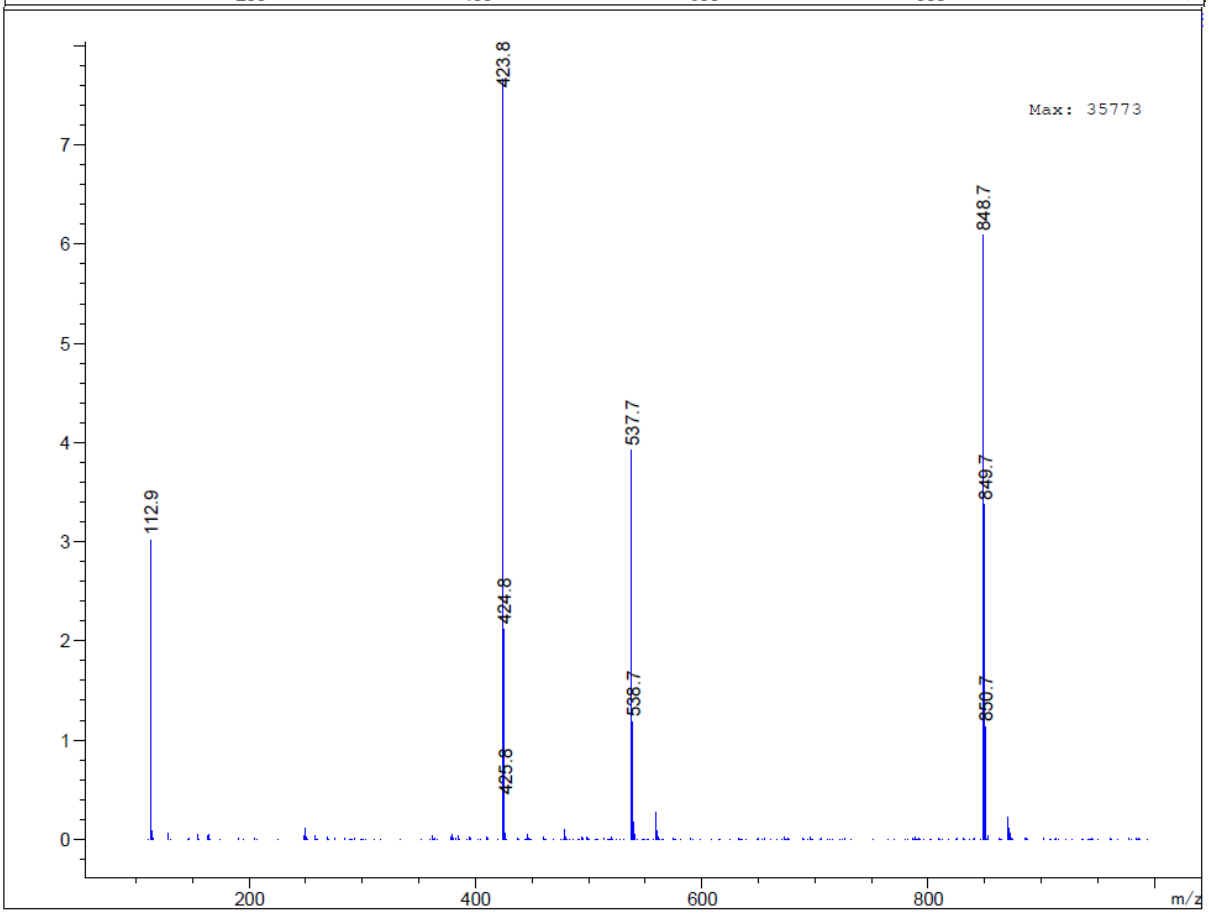

Spectroscopic Data for fFF

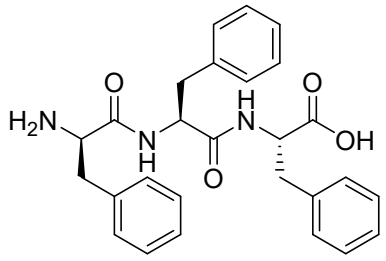

Chemical Formula: $C_{27}H_{29}N_3O_4$
Exact Mass: 459.22
Molecular Weight: 459.55

^{1}H-NMR (400 MHz, DMSO-d_6, TMS)

^{1}H-NMR (400 MHz, DMSO, TMS), δ (ppm):8.86 (d, J = 8.8 Hz, 1H, NH), 8.66 (d, J = 7.8 Hz, 1H, NH), 7.92 (s, 2H, NH_2), 7.33 – 7.15 (m, 13H, Ar), 6.89 (m, J = 6.5, 2.9 Hz, 2H, Ar), 4.72 (m, J = 10.7, 3.7 Hz, 1H, αCH), 4.49 – 4.43 (m, 1H, αCH), 3.96 (s, 1H, αCH), 3.15 – 3.05 (m, 2H, βCH_2), 2.96-2.91 (m, J = 14.0, 9.3 Hz, 1H, βCH_2), 2.78-2.65 (m, J = 24.5, 13.9, 7.4 Hz, 2H, βCH_2), 2.49 – 2.44 (m, 1H, βCH_2).

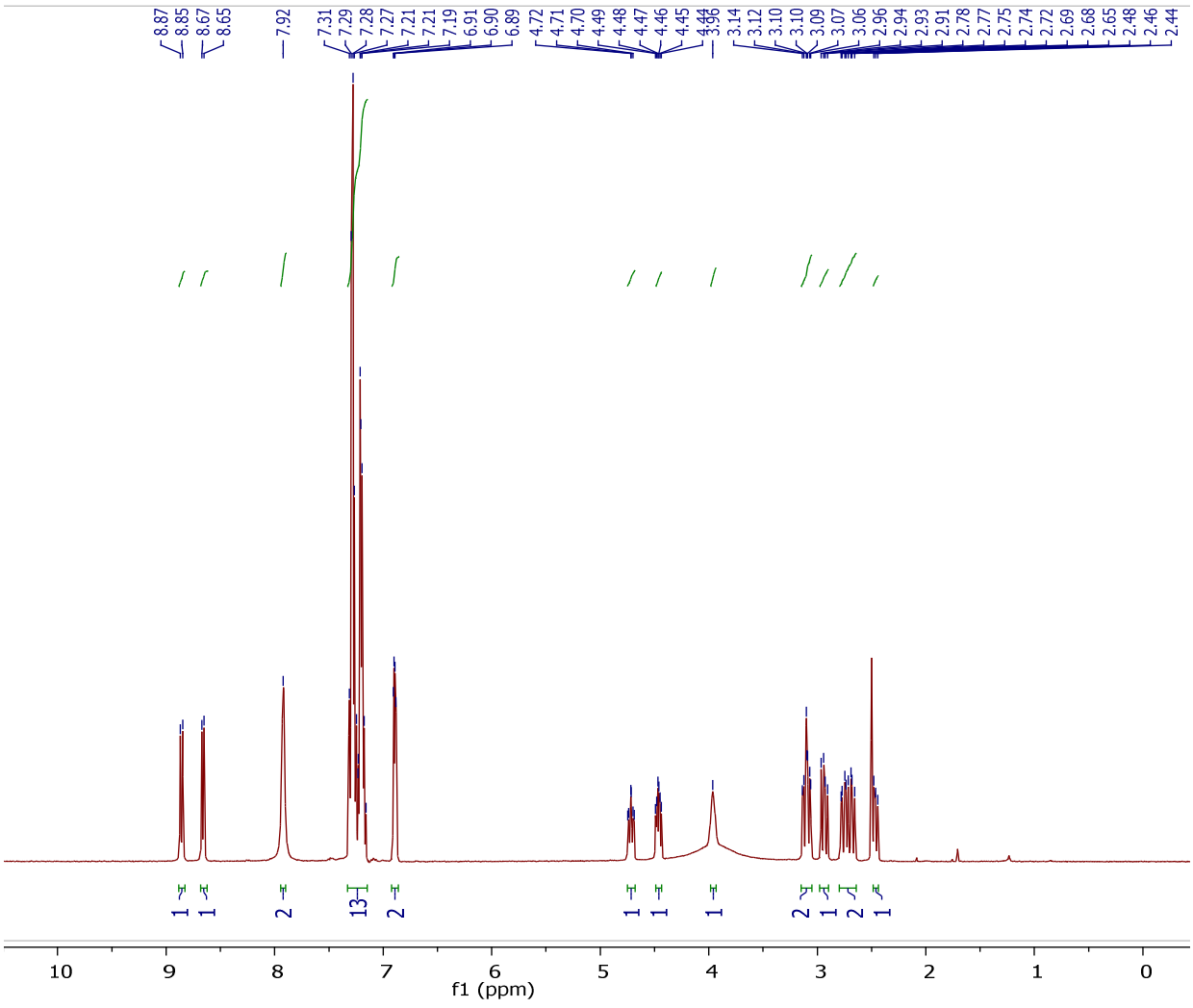

^{13}C-NMR (100MHz, DMSO-*d6*, TMS)

^{13}C-NMR (100 MHz, DMSO, TMS), δ (ppm): 172.7, 171.5, 168.0 (3 x CO); 137.5, 137.4, 134.5, 129.5, 129.1, 128.4, 128.3, 128.1, 127.0, 126.5, 126.5 (Ar); 53.7, 53.6, 53.2 (3 x αC); 38.3, 36.9, 36.6 (3 x βCH_2).

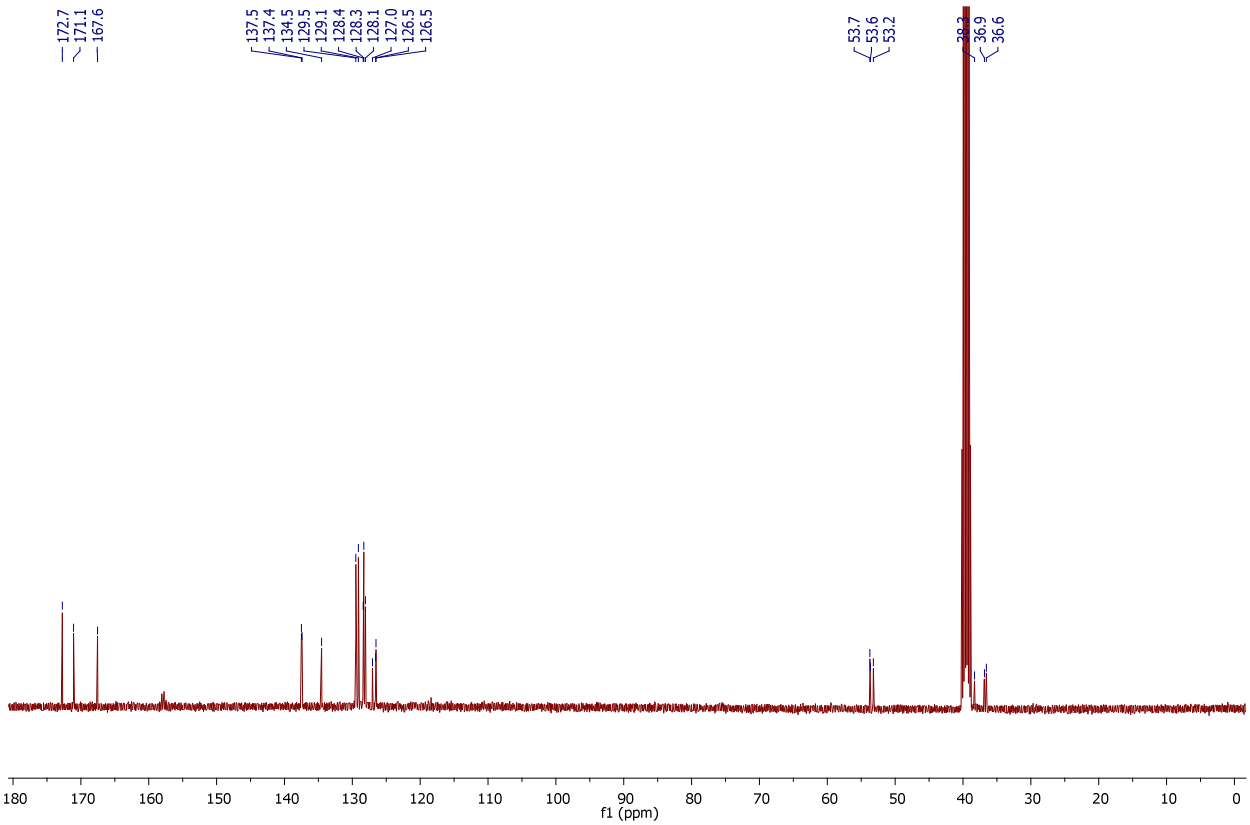

fFF, MS Spectra (Positive and Negative, top and bottom respectively).

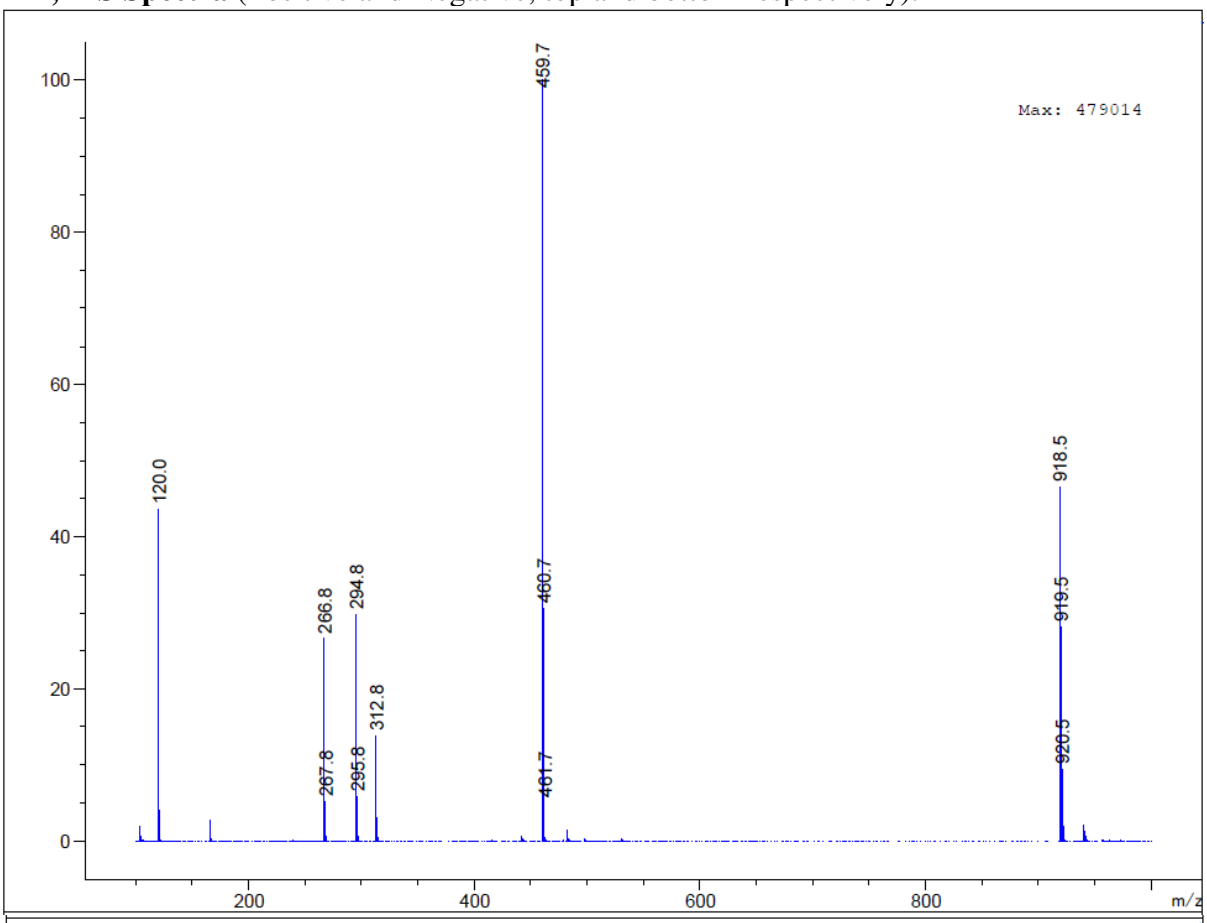

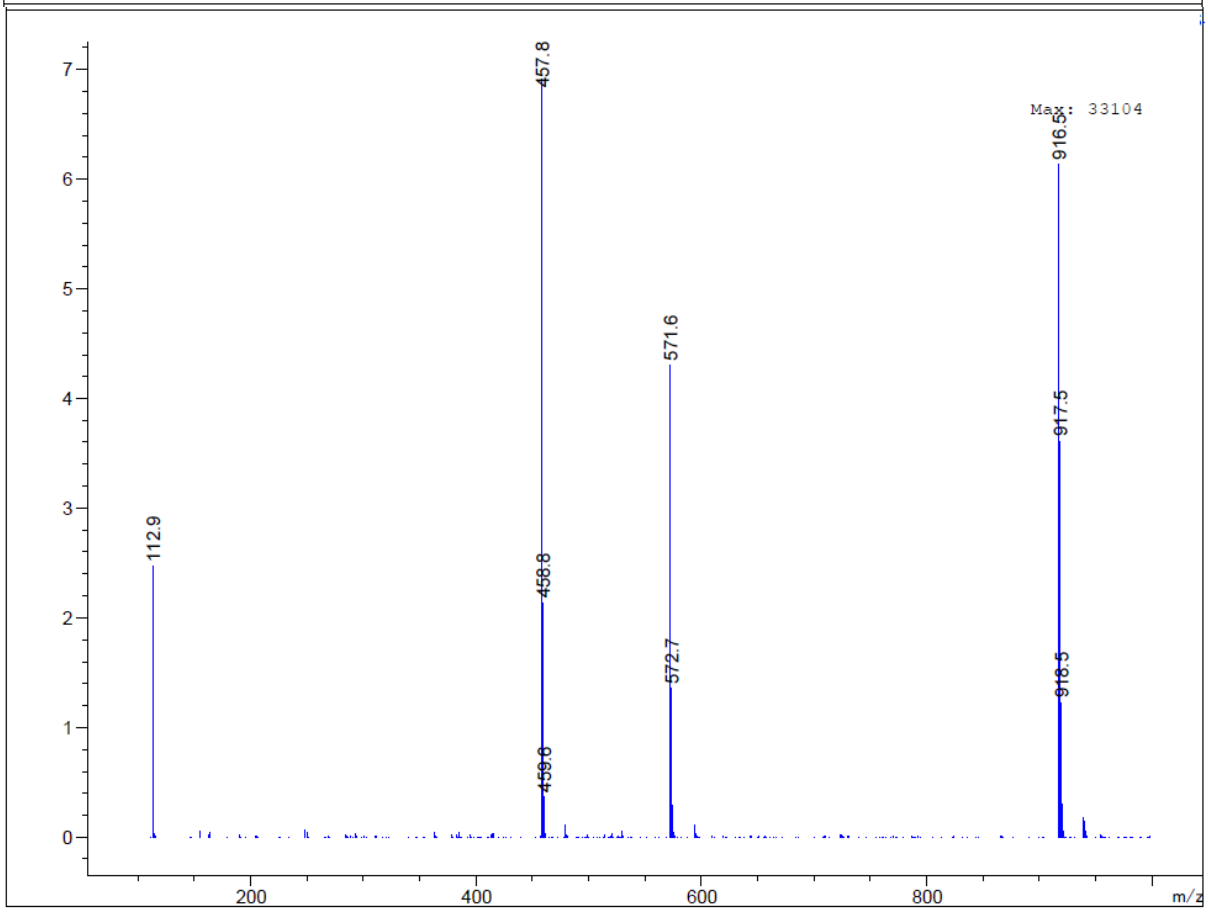

Spectroscopic Data for sFW

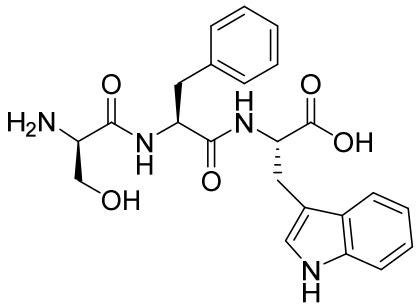

Chemical Formula: $C_{23}H_{26}N_4O_5$
Exact Mass: 438.19
Molecular Weight: 438.48

^{1}H-NMR (400 MHz, DMSO-d_6, TMS)

^{1}H-NMR (400 MHz, DMSO, TMS), δ (ppm): 10.89 (d, *J* = 2.1 Hz, 1H, NH), 8.59 (m, *J* = 13.8, 8.2 Hz, 2H, NH), 7.56 (d, *J* = 7.9 Hz, 1H, Ar), 7.34 (m, *J* = 8.1, 0.9 Hz, 1H, Ar), 7.26 – 7.15 (m, 6H, Ar), 7.10-7.05 (m, *J* = 8.1, 7.1, 1.2 Hz, 1H, Ar), 7.02-6.97 (m, *J* = 8.0, 7.0, 1.1 Hz, 1H, Ar), 5.38 (s, 1H, OH), 4.74 – 4.68 (m, 1H, αCH), 4.56-4.49 (m, *J* = 8.3, 5.2 Hz, 1H, αCH), 3.75-3.71 (m, *J* = 8.1, 4.1 Hz, 1H, αCH), 3.49 – 3.44 (m, 1H, βCH$_2$), 3.24 – 3.19 (m, 1H, βCH$_2$), 3.16 – 3.11 (m, 1H, βCH$_2$), 3.10 – 3.03 (m, 2H, βCH$_2$), 2.75 – 2.66 (m, 1H, βCH$_2$).

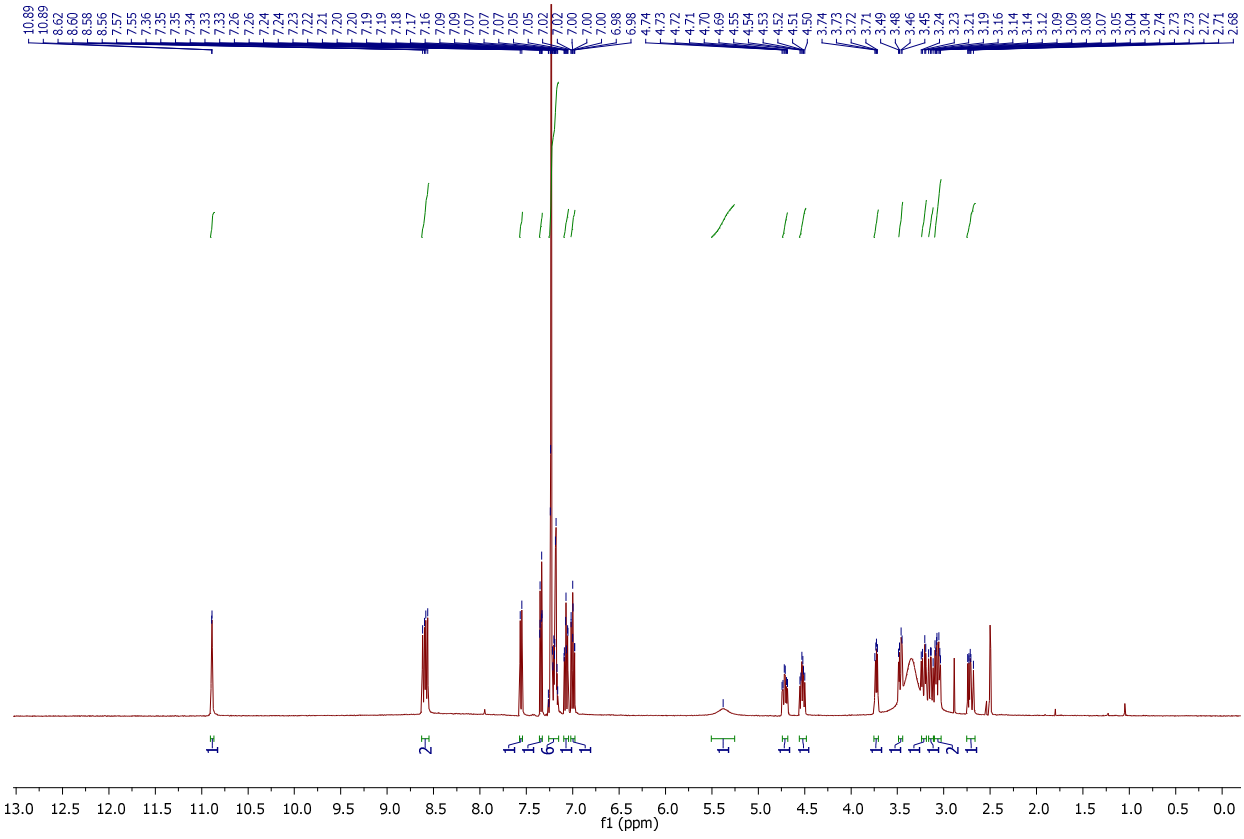

^{13}C-NMR (100MHz, DMSO-*d6*, TMS)

^{13}C-NMR (100 MHz, DMSO, TMS), δ (ppm): 173.20, 170.75, 166.17 (3 x CO), 137.24, 136.12, 129.36, 127.94, 127.12, 126.37, 123.75, 120.99, 118.46, 118.18, 111.43, 109.71 (Ar), 60.26, 54.44, 53.37 (3 x αC), 53.07, 38.15, 27.12 (3 x βCH_2).

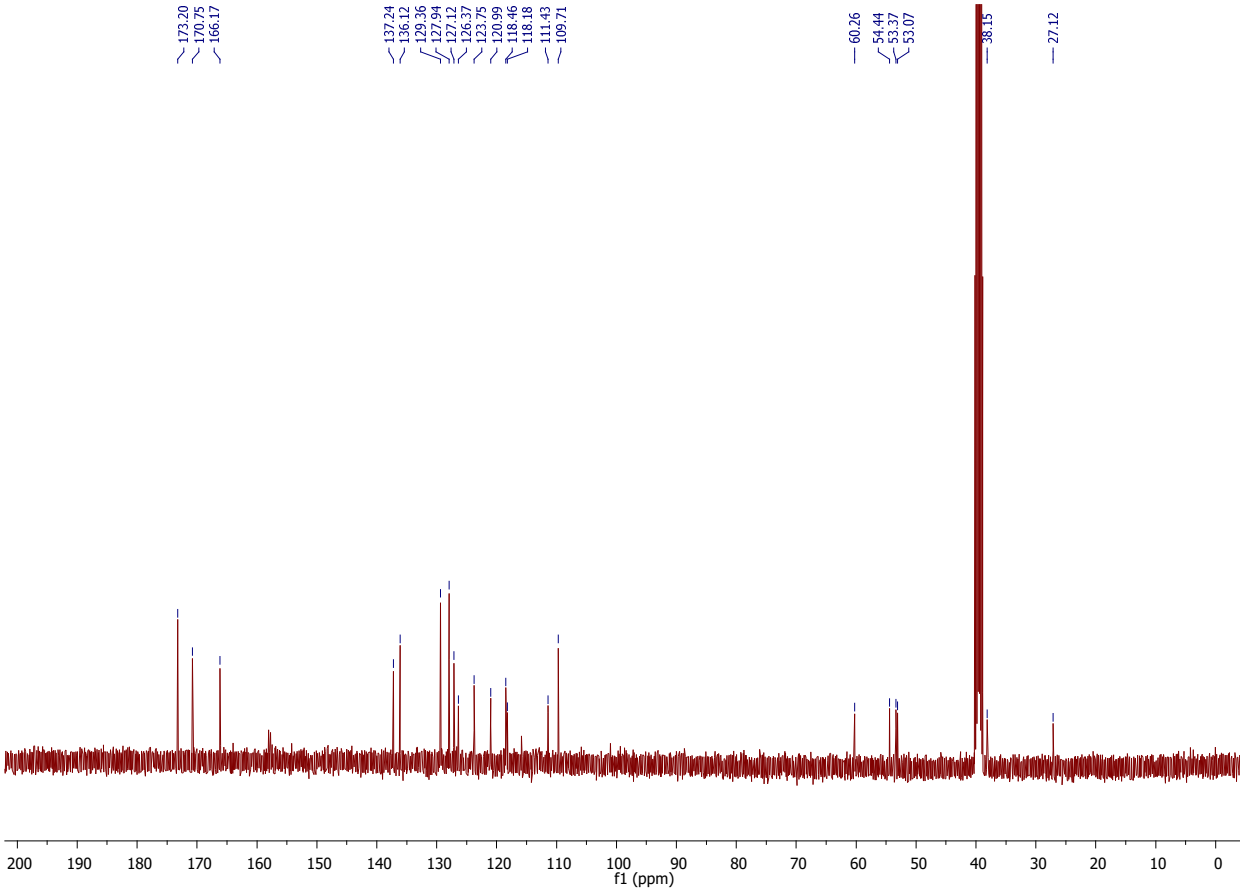

sFW, MS Spectra (Positive and Negative, top and bottom respectively).

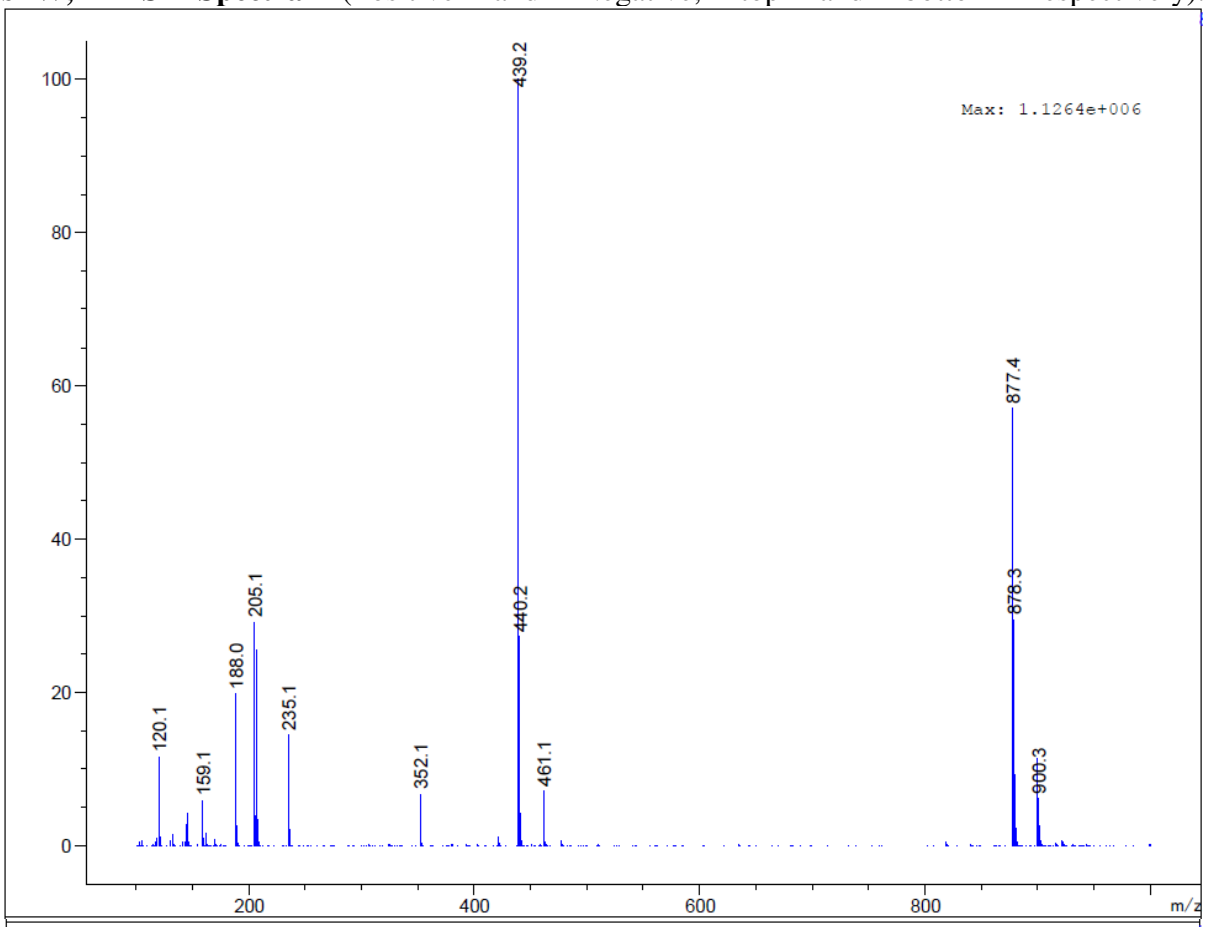

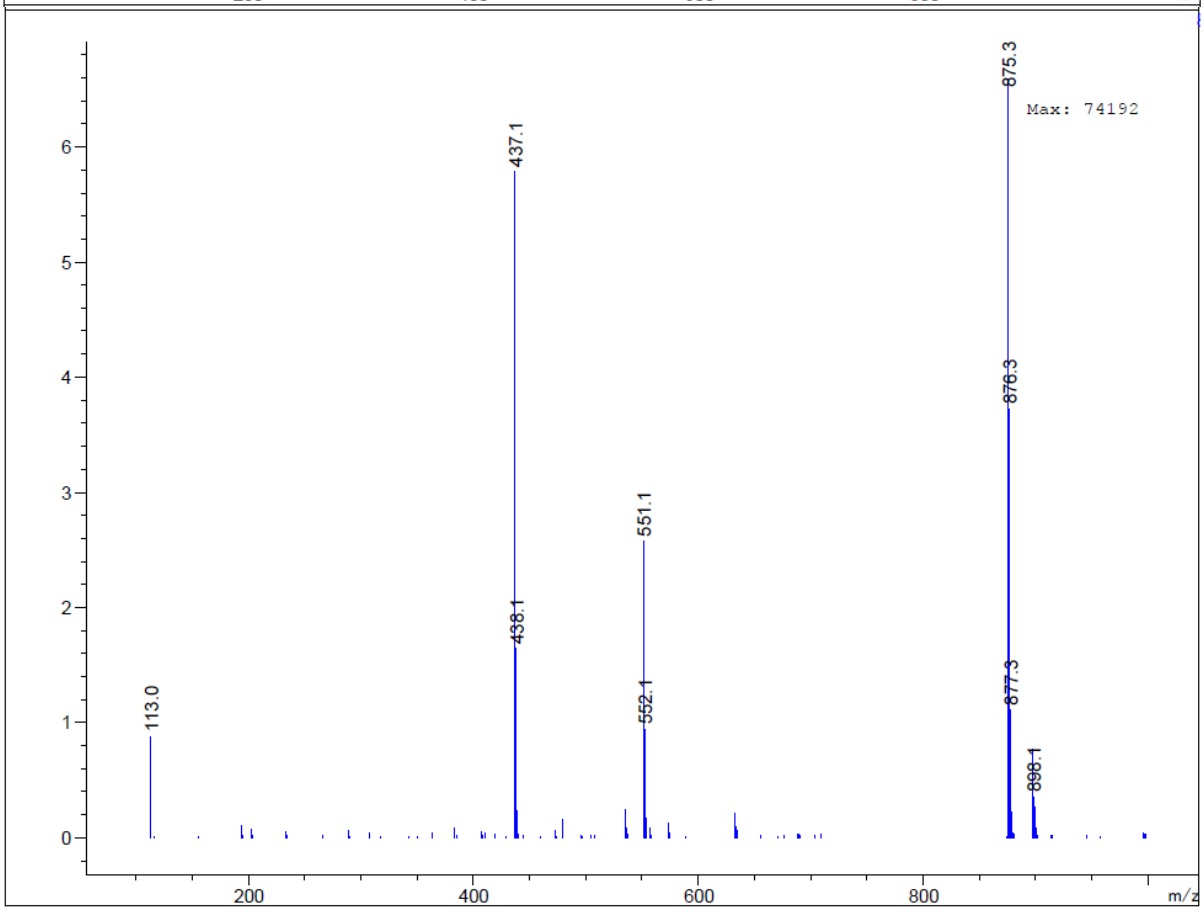

Spectroscopic Data for vFW

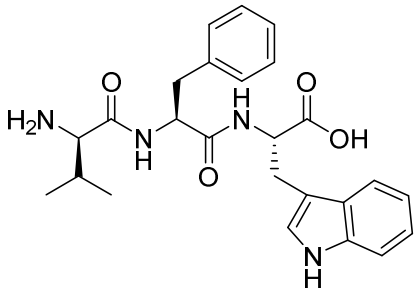

Chemical Formula: $C_{25}H_{30}N_4O_4$
Exact Mass: 450.23
Molecular Weight: 450.54

^{1}H-NMR (400 MHz, DMSO-*d*$_6$, TMS)

^{1}H-NMR (400 MHz, DMSO, TMS), δ (ppm): 10.88 (d, *J* = 2.0 Hz, 1H, NH), 8.60 (m, *J* = 8.3, 2.5 Hz, 2H, NH), 7.84 (d, *J* = 3.9 Hz, 2H, NH_2), 7.55 (d, *J* = 7.9 Hz, 1H, Ar), 7.33 (m, *J* = 4.8, 4.0 Hz, 1H, Ar), 7.28 – 7.12 (m, 6H, Ar), 7.02 (m, *J* = 15.9, 7.0, 1.1 Hz, 2H, Ar), 4.81 – 4.75 (m, 1H, αCH), 4.51 (m, *J* = 8.2, 5.2 Hz, 1H, αCH), 3.56 – 3.46 (m, 1H, αCH), 3.20 (m, *J* = 14.7, 5.0 Hz, 1H, βCH$_2$), 3.15 – 3.01 (m, 2H, βCH$_2$), 2.65 (m, *J* = 13.8, 11.4 Hz, 1H, βCH$_2$), 1.82 – 1.70 (m, 1H, βCH), 0.62 (d, *J* = 7.0 Hz, 3H, γCH$_3$), 0.36 (d, *J* = 7.0 Hz, 3H, γCH$_3$).

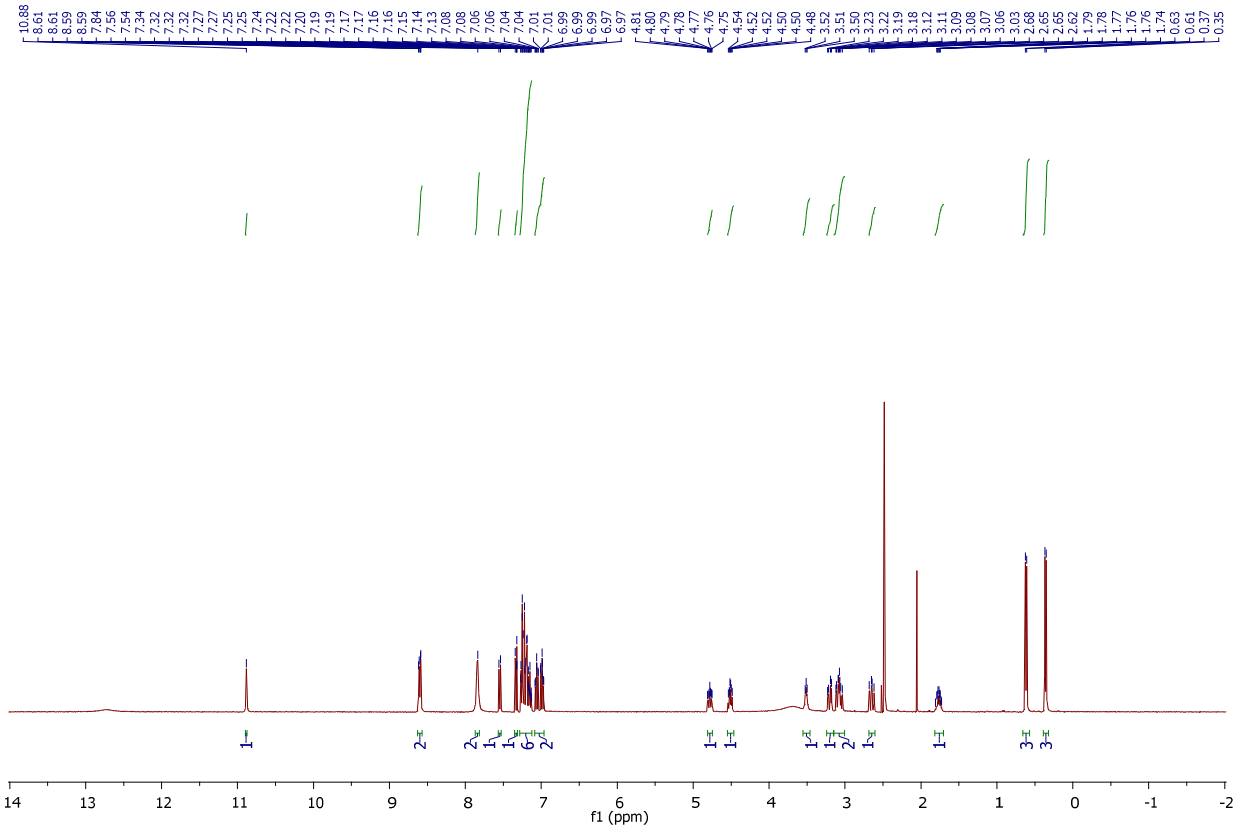

^{13}C-NMR (100MHz, DMSO-*d6*, TMS)

^{13}C-NMR (100 MHz, DMSO, TMS), δ (ppm): 173.2, 171.2, 167.4 (3 x CO); 137.4, 136.1, 129.2, 128.0, 127.1, 126.4, 123.8, 121.0, 118.5, 118.2, 111.4, 109.7 (Ar); 57.2, 53.5, 53.1 (3 x α C); 38.2, 29.5, 27.1 (2 x βCH_2 and 1 x βCH), 18.2, 16.3 (2 x γCH_3).

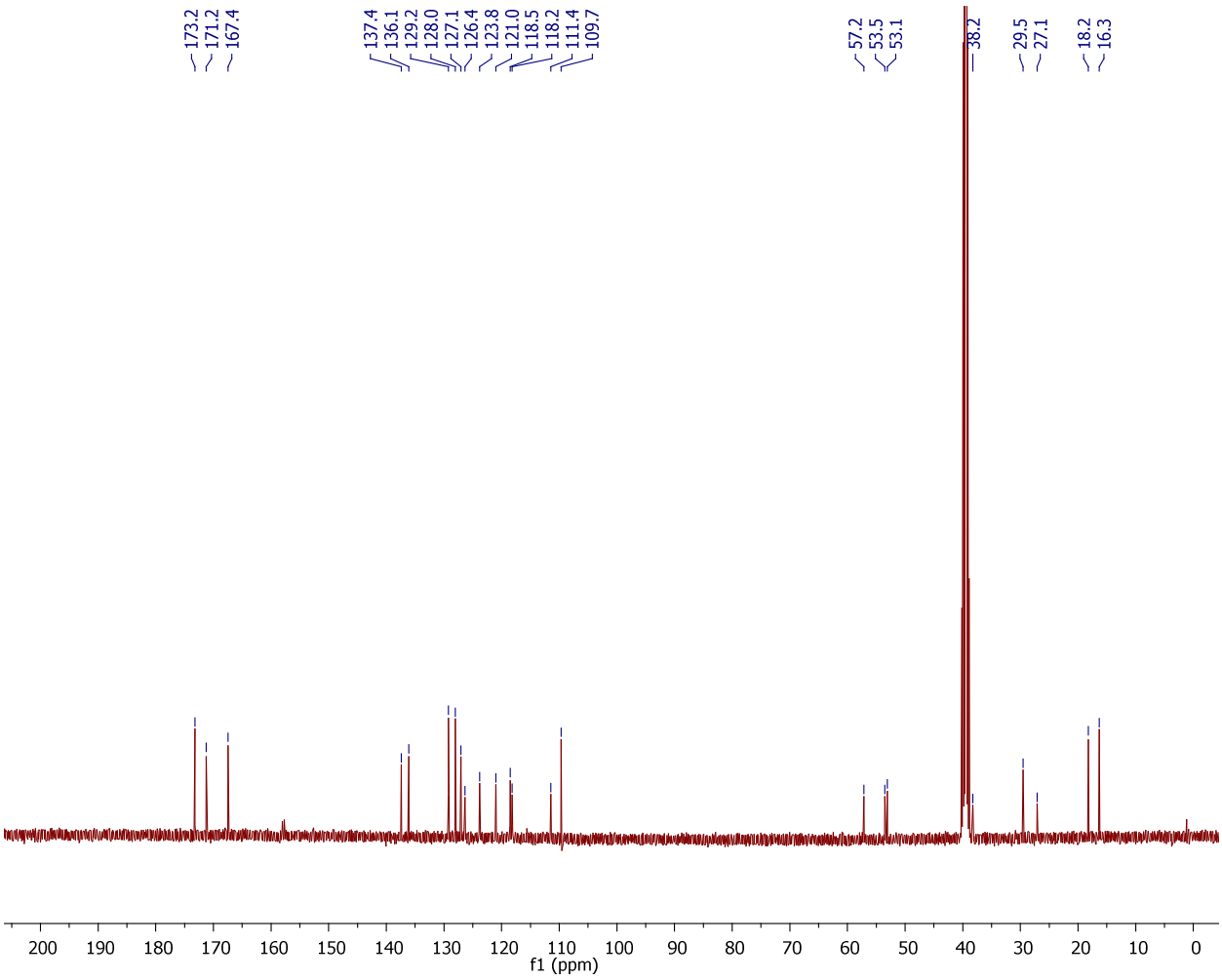

vFW, MS Spectra (Positive and Negative, top and bottom respectively).

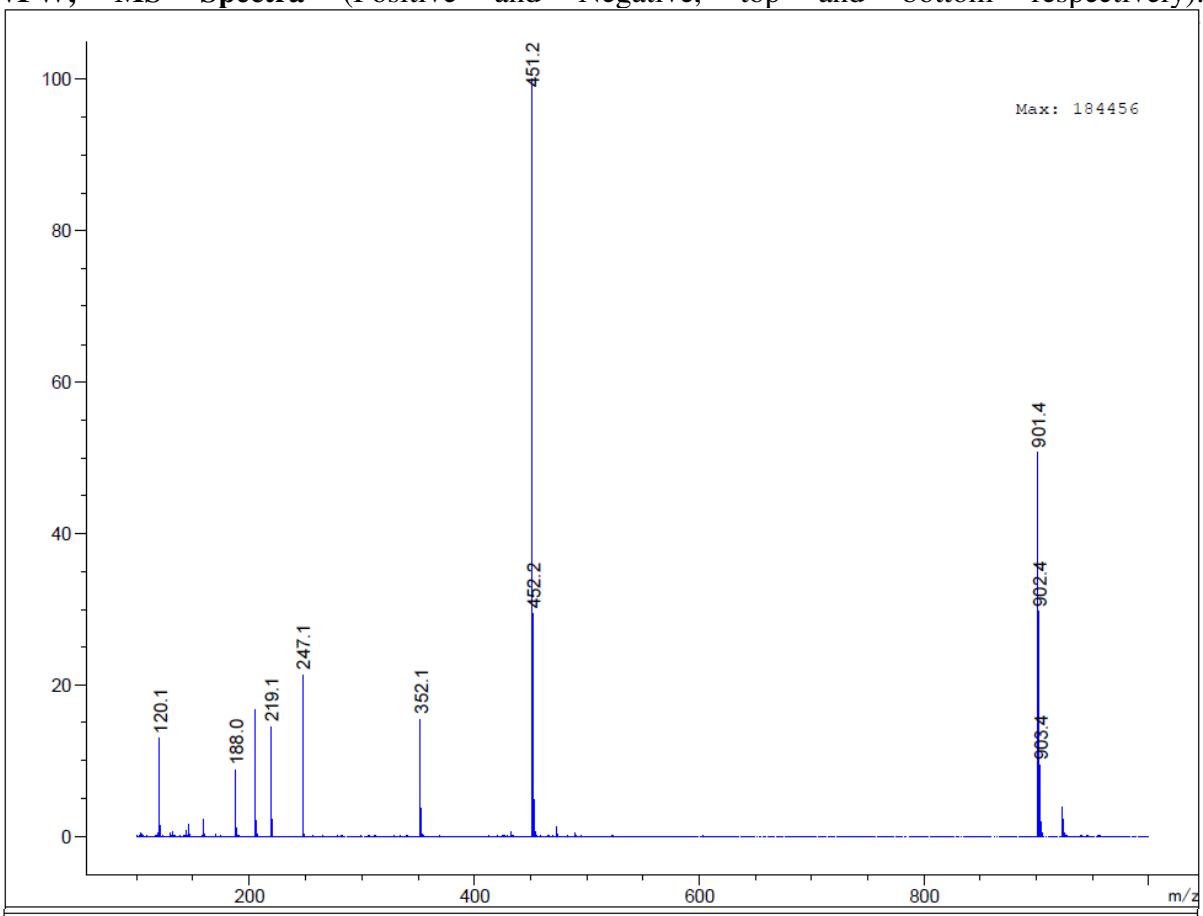

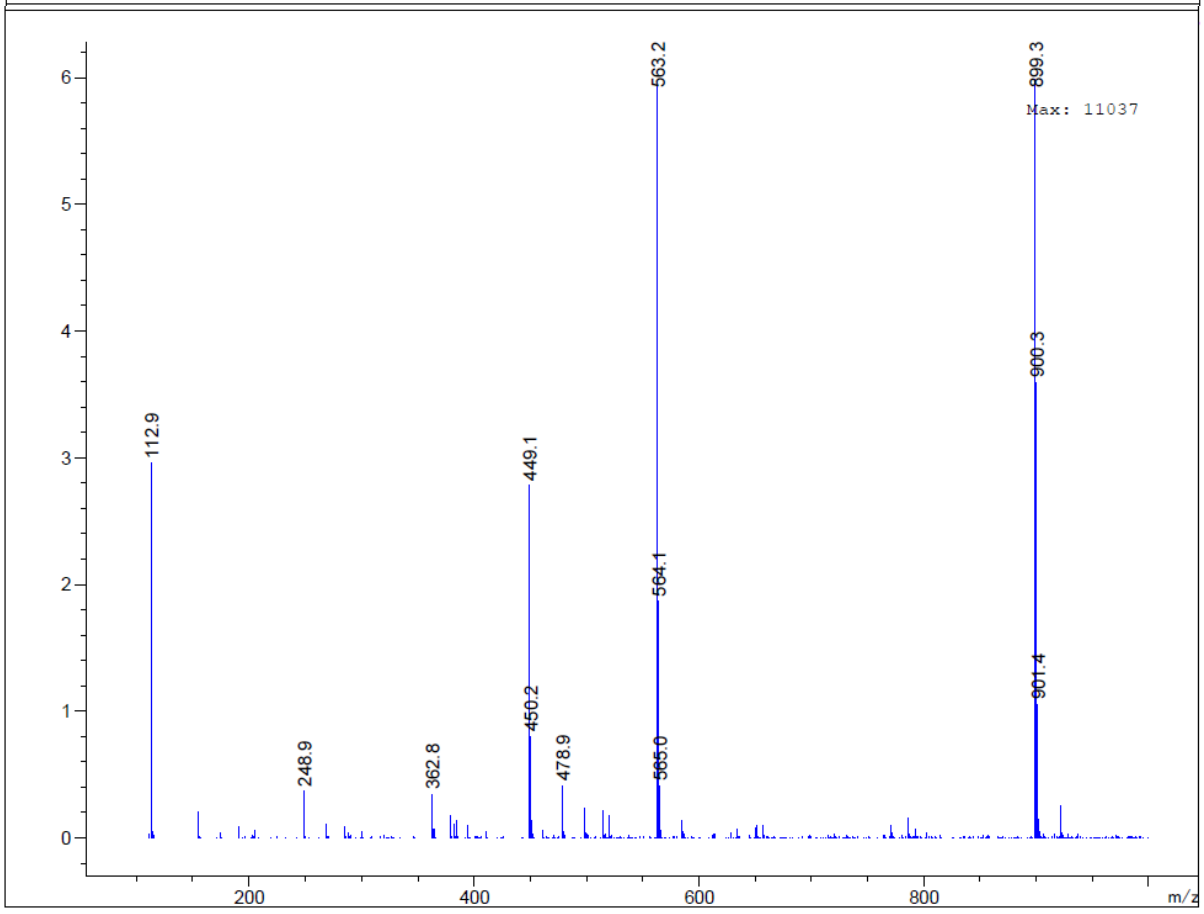

Spectroscopic Data for iFW

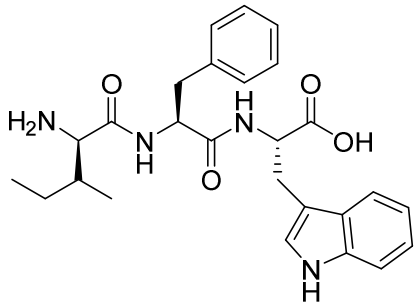

Chemical Formula: $C_{26}H_{32}N_4O_4$
Exact Mass: 464.24
Molecular Weight: 464.57

^{1}H-NMR (400 MHz, DMSO-*d*$_6$, TMS)

^{1}H-NMR (400 MHz, DMSO, TMS), δ (ppm):10.91 (d, *J* = 2.0 Hz, 1H, NH), 8.64-8.57 (m, 2H, NH), 7.90 (d, *J* = 3.8 Hz, 2H, NH_2), 7.57 (d, *J* = 7.8 Hz, 1H, Ar), 7.35 (d, *J* = 8.0 Hz, 1H, Ar), 7.31 – 7.15 (m, 6H, Ar), 7.11-6.98 (m, *J* = 15.9, 7.1, 1.1 Hz, 2H, Ar), 4.81 – 4.76 (m, 1H, αCH), 4.53 (m, *J* = 8.2, 5.2 Hz, 1H, αCH), 3.56 (m, 1H, αCH), 3.22 (m, *J* = 14.7, 5.1 Hz, 1H, βCH_2), 3.10 (m, *J* = 17.9, 11.8, 5.9 Hz, 2H, βCH_2), 2.68 (m, *J* = 13.9, 11.5 Hz, 1H, βCH_2), 1.57 – 1.46 (m, 1H, βCH), 0.96 – 0.86 (m, 1H, γCH_2), 0.63 (m, *J* = 8.2, 7.6, 4.9 Hz, 1H, γCH_2), 0.60 – 0.54 (m, 6H, 3 x γCH_3, 3 x δCH_3).

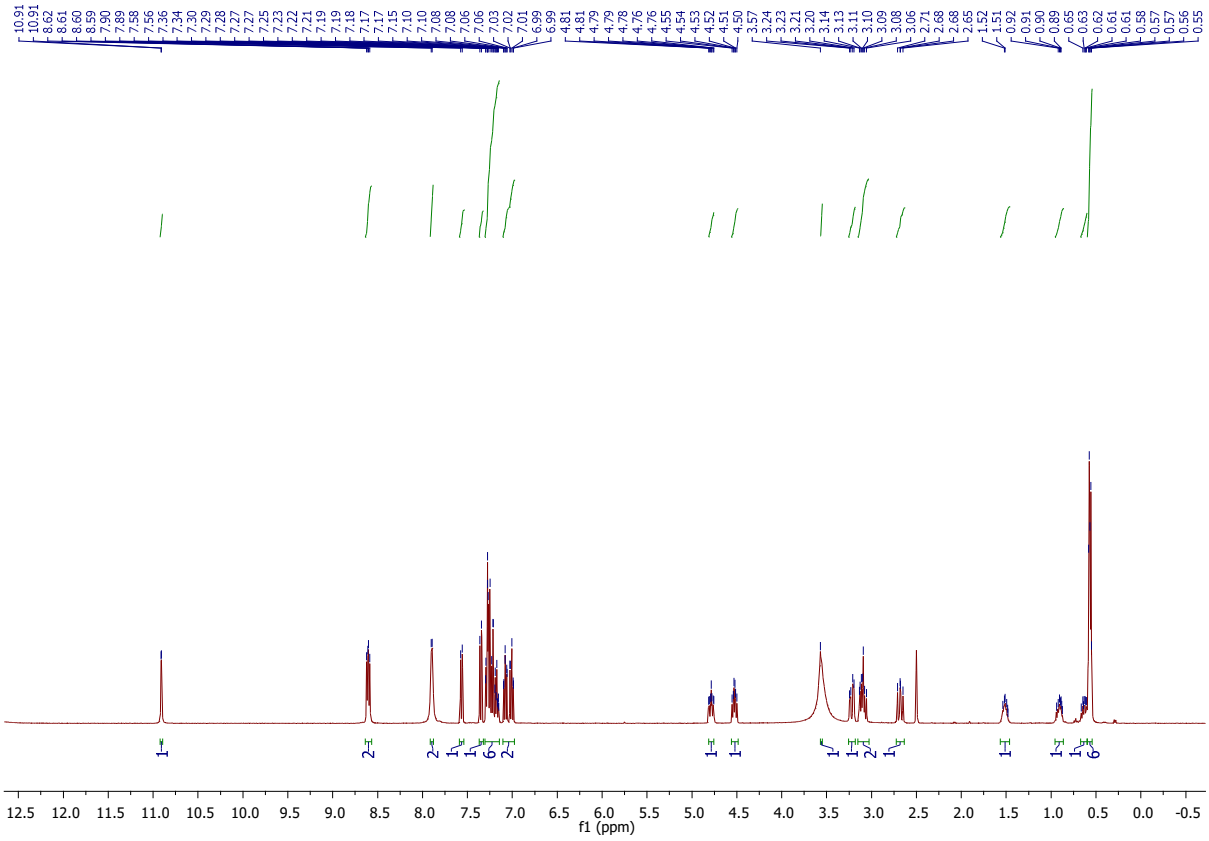

^{13}C-NMR (100MHz, DMSO-*d6*, TMS)

^{13}C-NMR (100 MHz, DMSO, TMS), δ (ppm): 173.2, 171.3, 167.4 (3 x CO); 137.4, 136.1, 129.2, 128.0, 127.1, 126.4, 123.9, 121.0, 118.5, 118.2, 111.4, 109.7 (Ar); 56.67, 53.65, 53.13 (3 x αC); 38.04, 35.93, 27.10 (2 x βCH_2 and 1 x βCH); 23.0 (γCH_2); 14.1 (γCH_3), 11.3 (δCH_3).

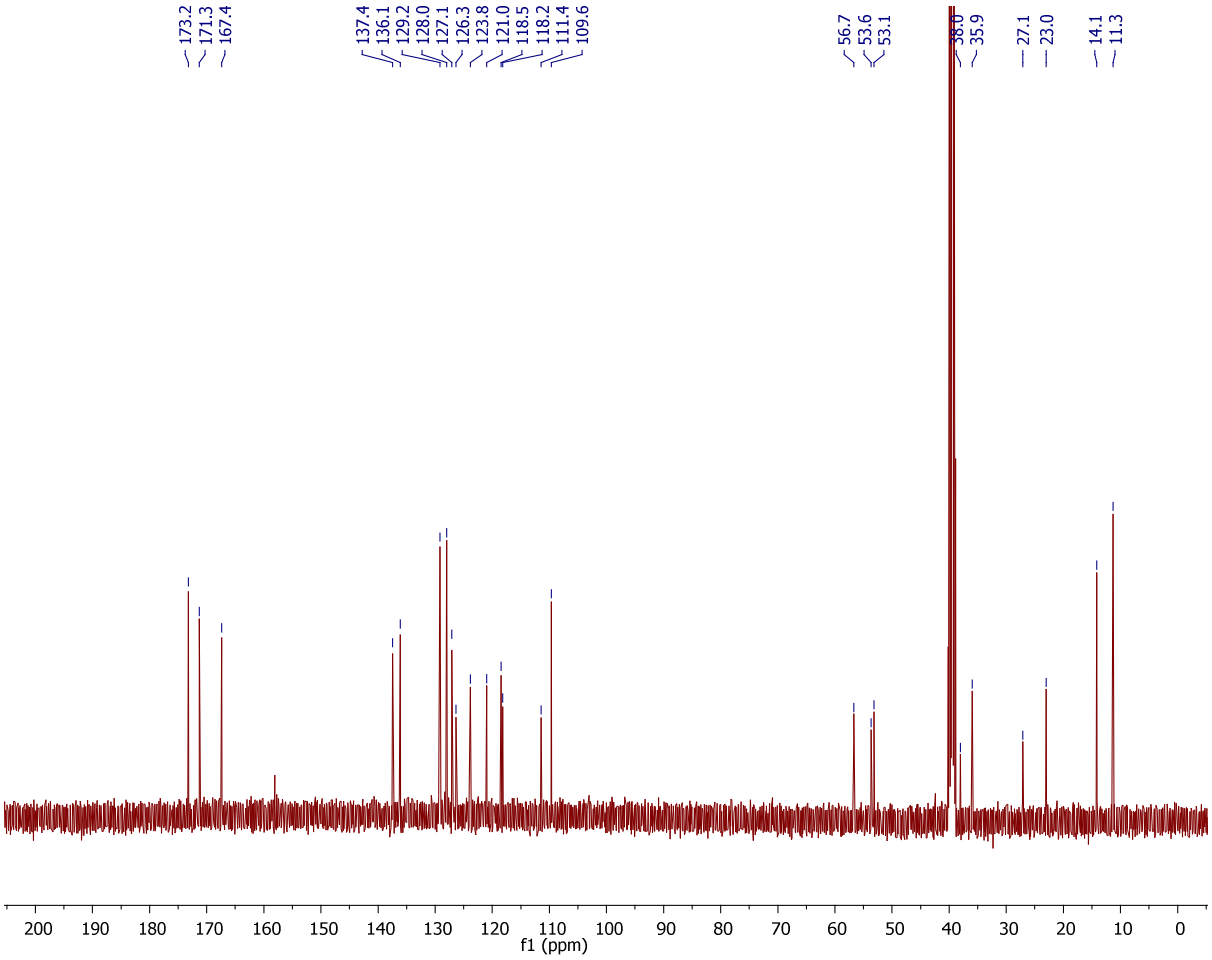

iFW, MS Spectra (Positive and Negative, top and bottom respectively).

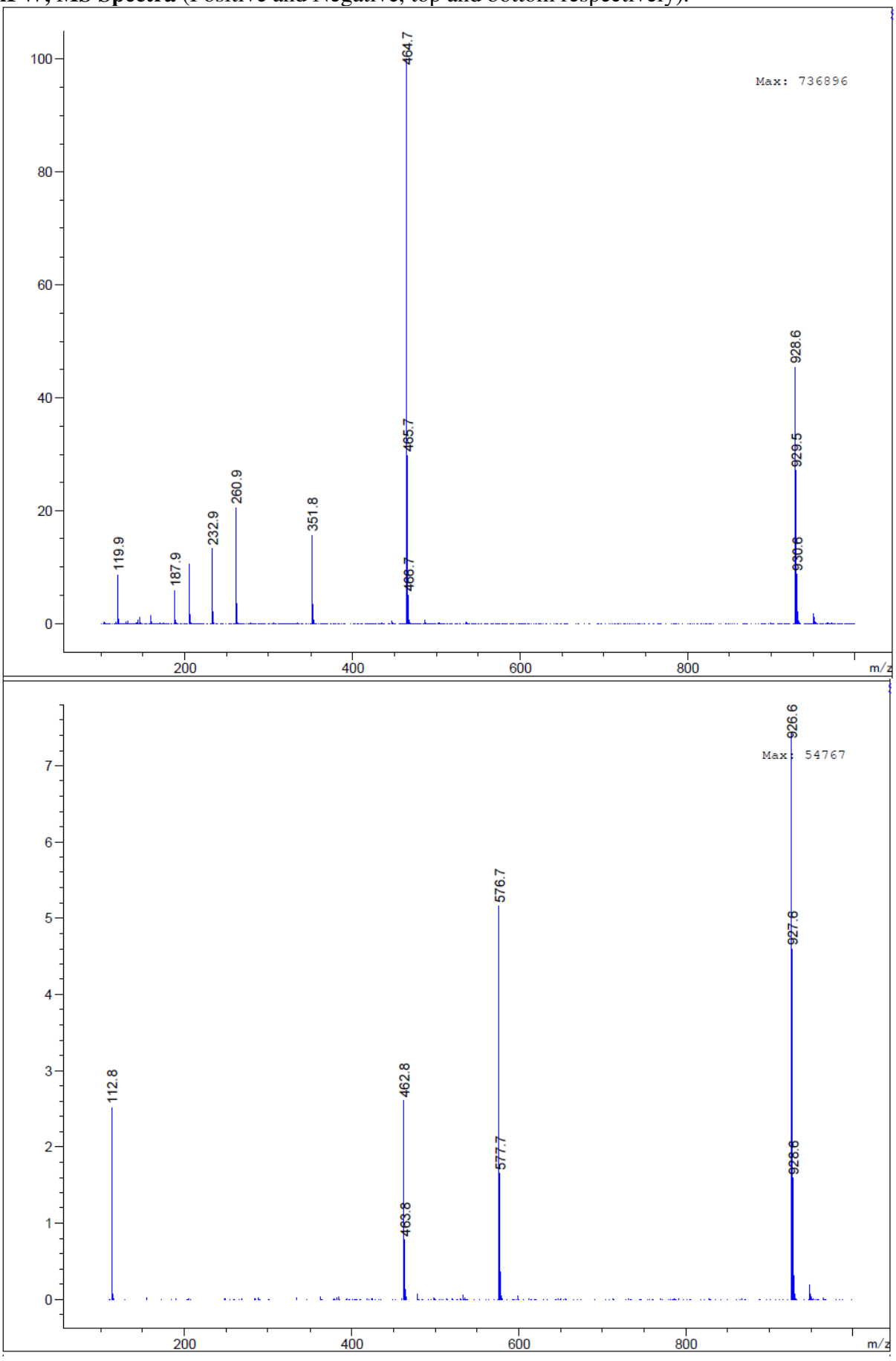

Spectroscopic Data for fFW

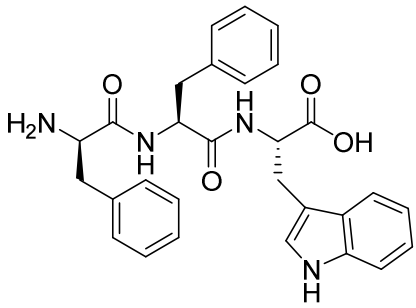

Chemical Formula: $C_{29}H_{30}N_4O_4$
Exact Mass: 498.23
Molecular Weight: 498.58

^{1}H-NMR (400 MHz, DMSO-d_6, TMS)

^{1}H-NMR (400 MHz, DMSO, TMS), δ (ppm): 10.89 (d, *J* = 2.0 Hz, 1H, NH), 8.85 (d, *J* = 8.8 Hz, 1H, NH), 8.65 (d, *J* = 7.7 Hz, 1H, NH), 7.90 (s, 2H, NH_2), 7.58-7.55 (d, *J* = 7.8 Hz, 1H, Ar), 7.37 – 7.14 (m, 10H, Ar), 7.10 – 6.98 (m, 2H, Ar), 6.95-6.90 (m, *J* = 6.5, 3.0 Hz, 2H, Ar), 4.79 – 4.73 (m, 1H, αCH), 4.54 (m, *J* = 8.3, 5.2 Hz, 1H, αCH), 3.96 (m, 1H, αCH), 3.26-3.19 (m, *J* = 14.7, 5.1 Hz, 1H, βCH_2), 3.13-3.04 (m, *J* = 10.9, 6.7 Hz, 2H, βCH_2), 2.79 – 2.66 (m, 2H, βCH_2), 2.48 – 2.42 (m, 1H, βCH_2).

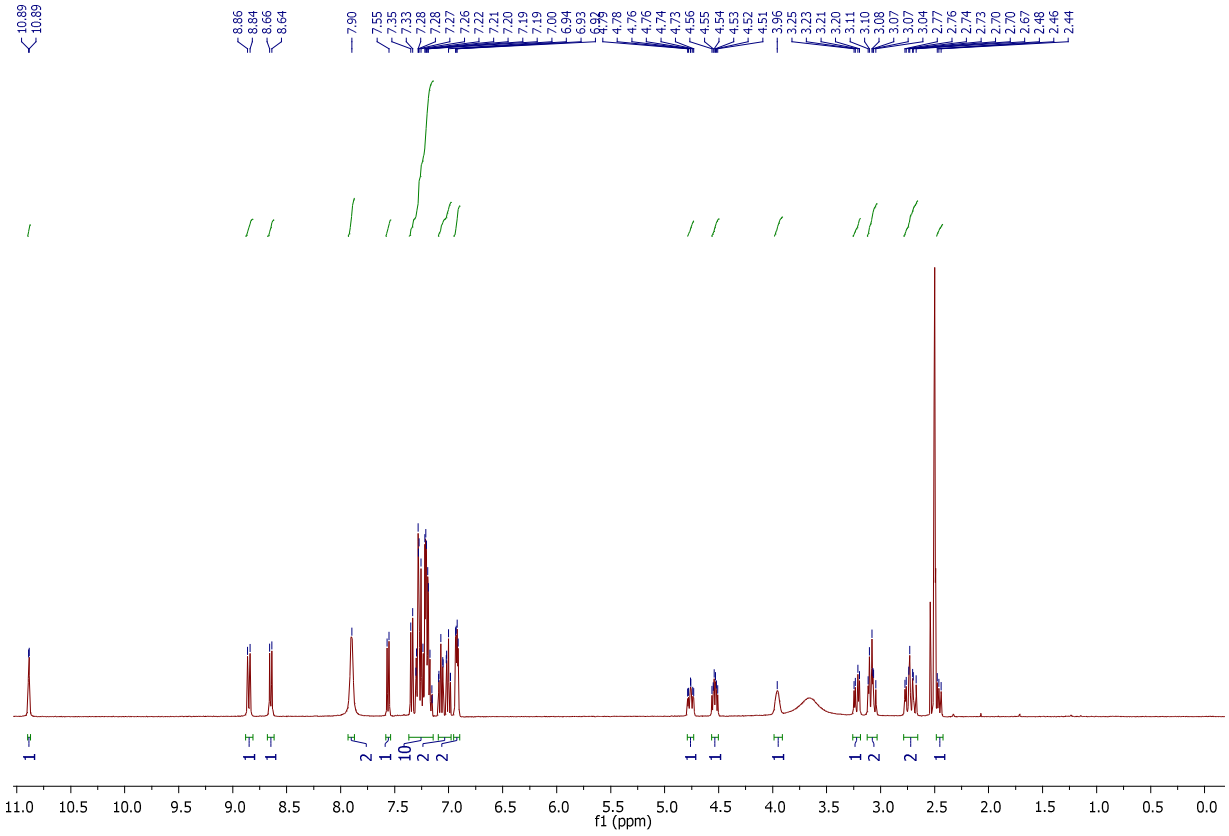

^{13}C-NMR (100MHz, DMSO-*d6*, TMS)

^{13}C-NMR (100 MHz, DMSO, TMS), δ (ppm): 173.2, 171.0, 167.6 (3 x CO); 137.4, 136.1, 134.6, 129.5, 128.4, 128.1, 127.1, 126.5, 123.8, 121.0, 118.5, 118.2, 111.4, 109.7 (Ar); 53.54, 53.23, 53.08 (3 x αC); 38.40, 36.84, 27.10 (3 x βCH_2).

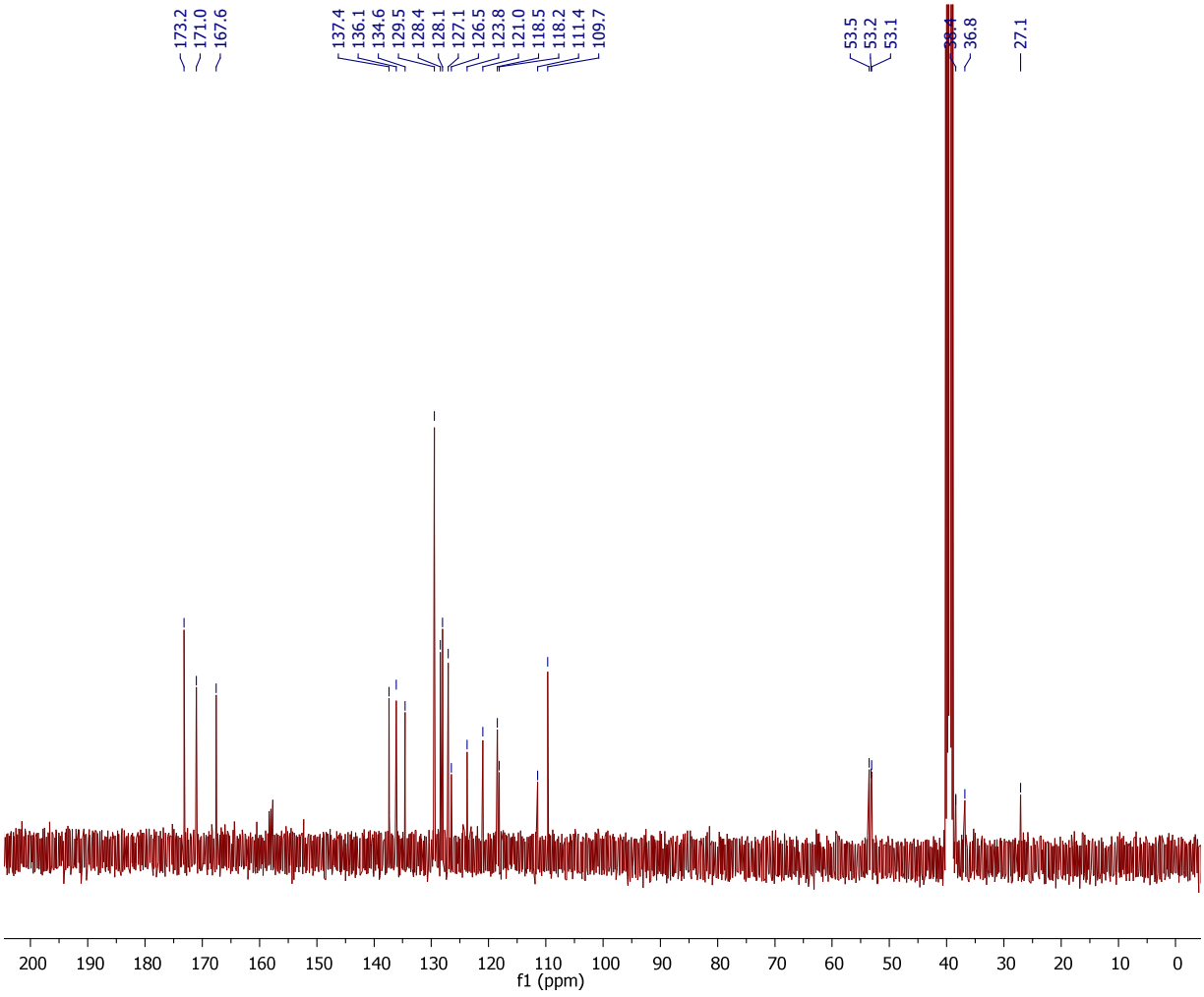

fFW, MS Spectra (Positive and Negative, top and bottom respectively).

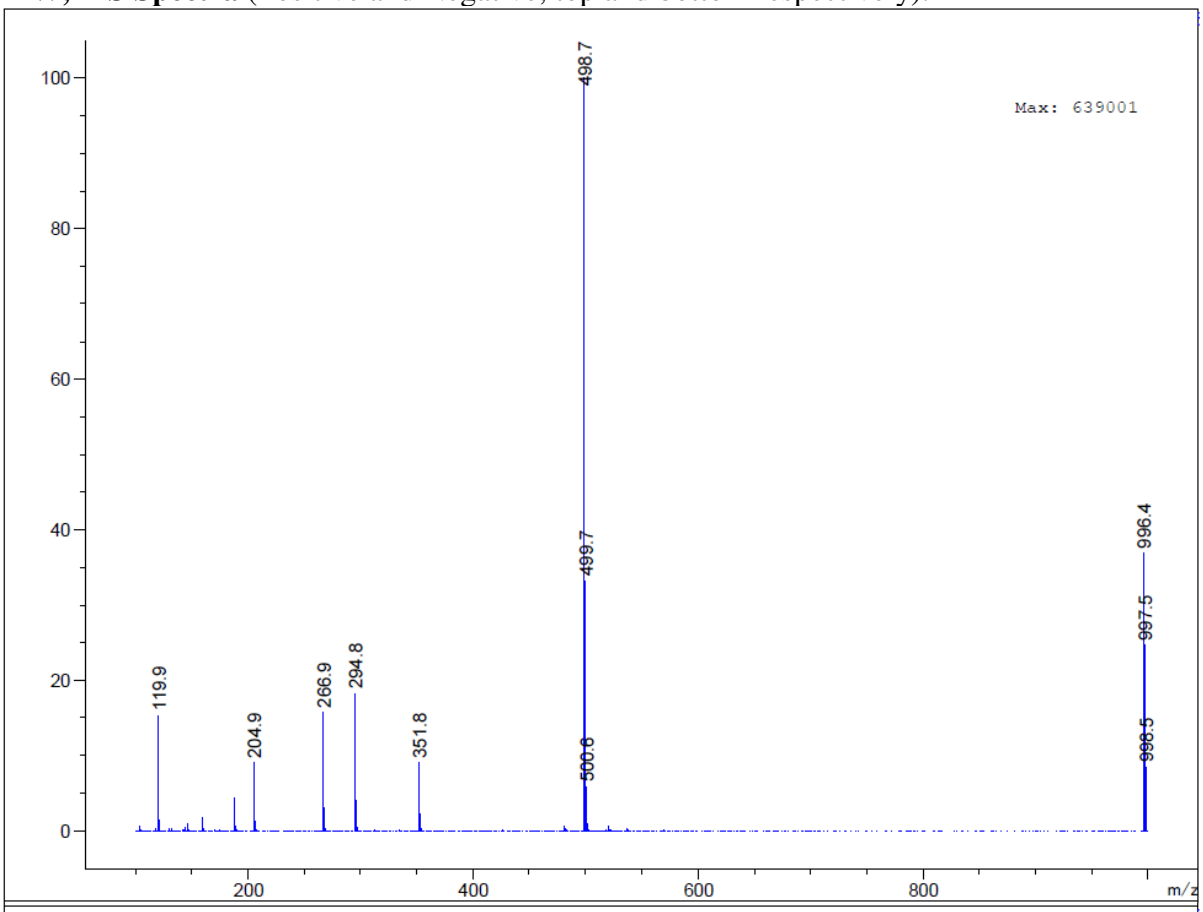

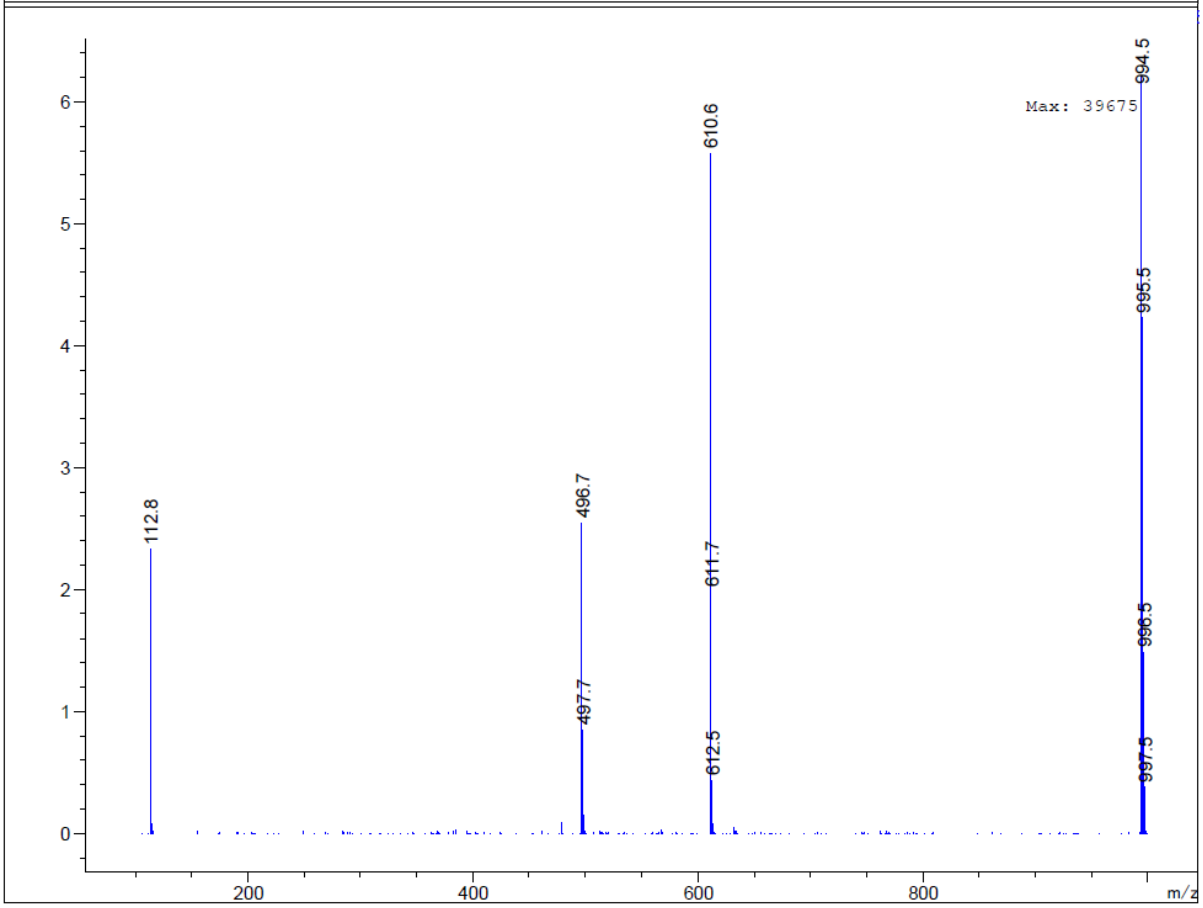

Spectroscopic Data for pWF

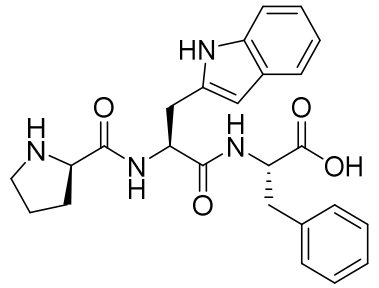

Chemical Formula: $C_{25}H_{28}N_4O_4$
Exact Mass: 448.21
Molecular Weight: 448.52

^{1}H-NMR (400 MHz, CD_3OD, TMS)

^{1}H-NMR (400 MHz, CD_3OD, TMS), δ (ppm): 7.62 – 7.59 (m, 1H, Ar), 7.34-7.32 (d, *J* = 8.1 Hz, 1H, Ar), 7.29 – 7.17 (m, 5H, Ar), 7.11 – 7.06 (m, 2H, Ar), 7.03 – 6.98 (m, 1H, Ar), 4.84 (d, *J* = 5.1 Hz, 1H, αCH), 4.70-4.66 (m, *J* = 8.6, 5.1 Hz, 1H, αCH), 4.13-4.07 (m, *J* = 8.5, 6.3 Hz, 1H, αCH), 3.34-3.32 (m, *J* = 5.0, 0.7 Hz, 1H, δCH_2), 3.26-3.11 (m, *J* = 18.8, 14.7, 10.9, 6.3 Hz, 3H, δCH_2 and 2 x βCH_2), 3.07 – 2.98 (m, 2H, βCH_2), 2.08-1.96 (m, *J* = 15.8, 13.3, 7.3 Hz, 1H, βCH_2), 1.83 – 1.71 (m, 1H, βCH_2), 1.60 – 1.47 (m, 1H, γCH_2), 1.39-1.28 (m, *J* = 13.4, 6.2 Hz, 1H, γCH_2).

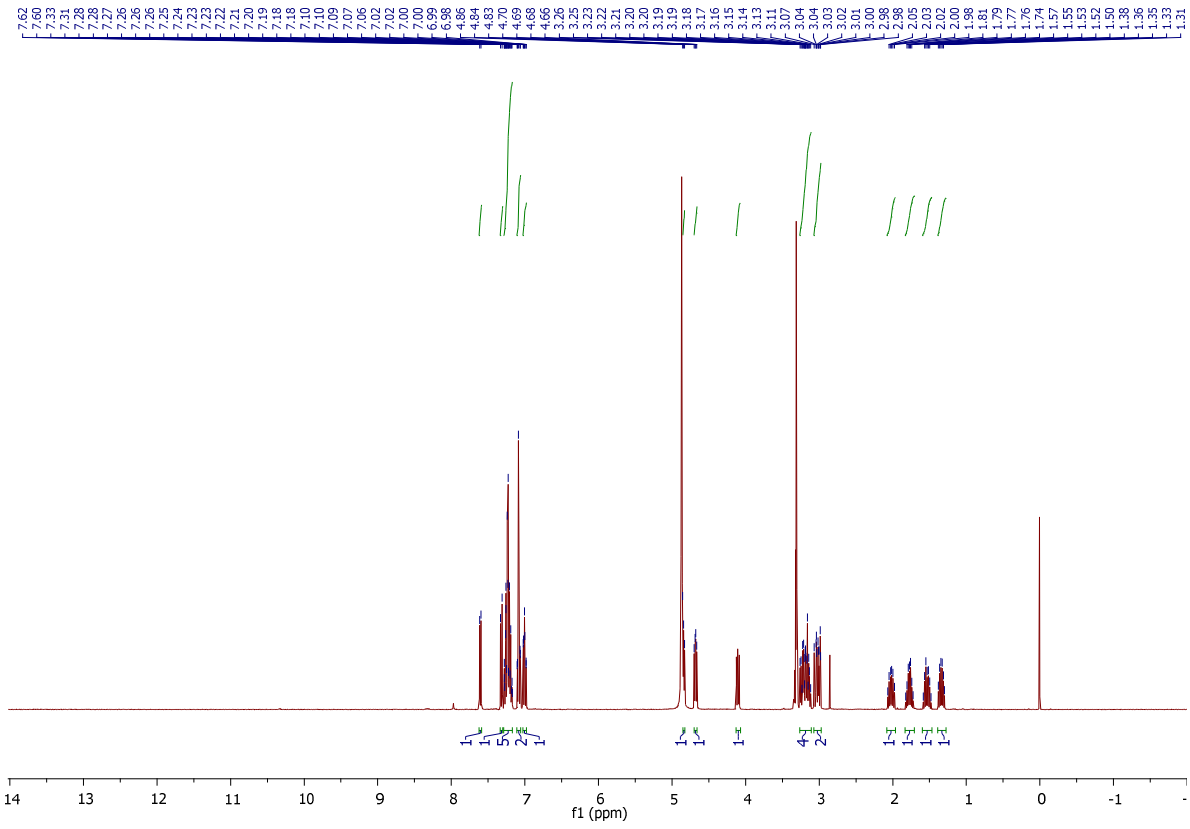

^{13}C-NMR (400 MHz, CD_3OD, TMS)

^{13}C-NMR (101 MHz, CD_3OD, TMS), δ (ppm): 174.3, 173.5, 169.2 (3 x CO); 138.3, 138.0, 130.3, 129.4, 128.7, 127.8, 124.8, 122.5, 119.8, 119.4, 112.3, 110.8 (Ar); 60.9, 55.2, 55.1 (3 x αC); 47.23 (δCH_2 pro); 38.28, 30.85, 29.28 (3 x βCH_2); 24.56 (γCH_2).

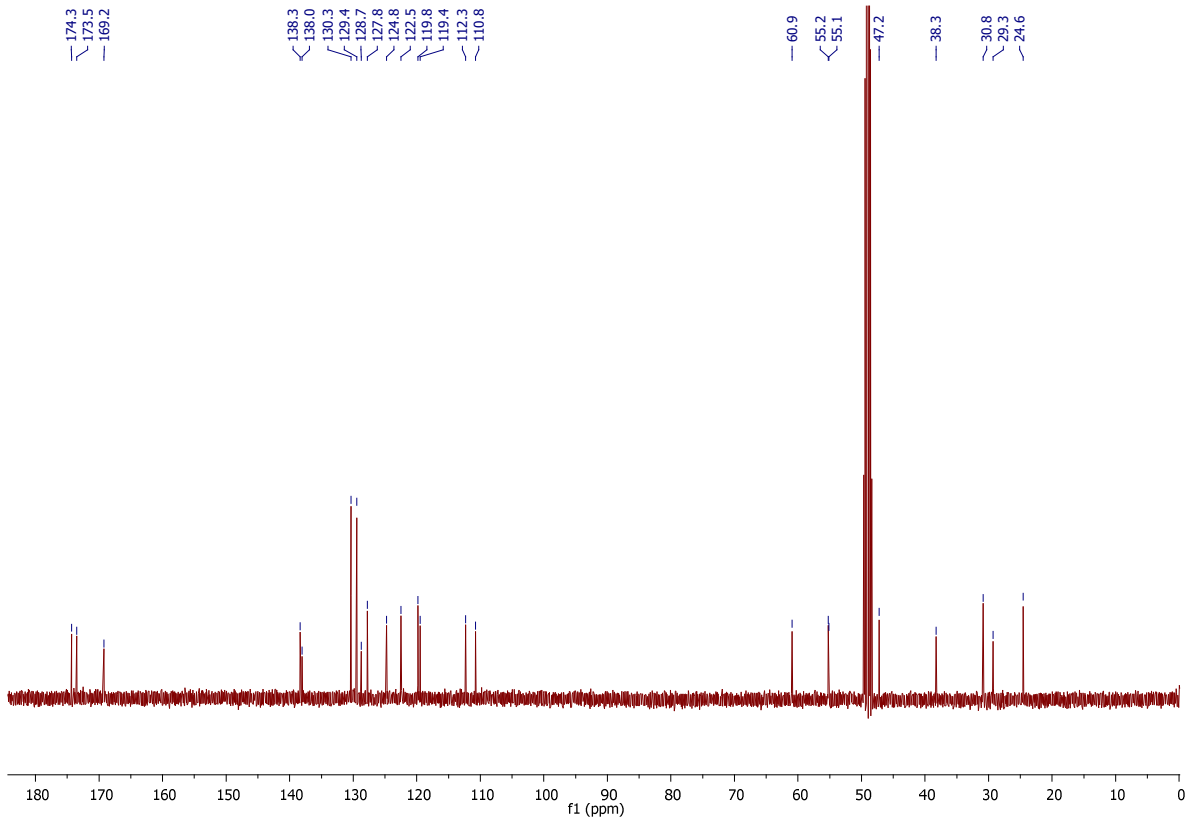

pWF, MS Spectra (Positive and Negative, top and bottom respectively).

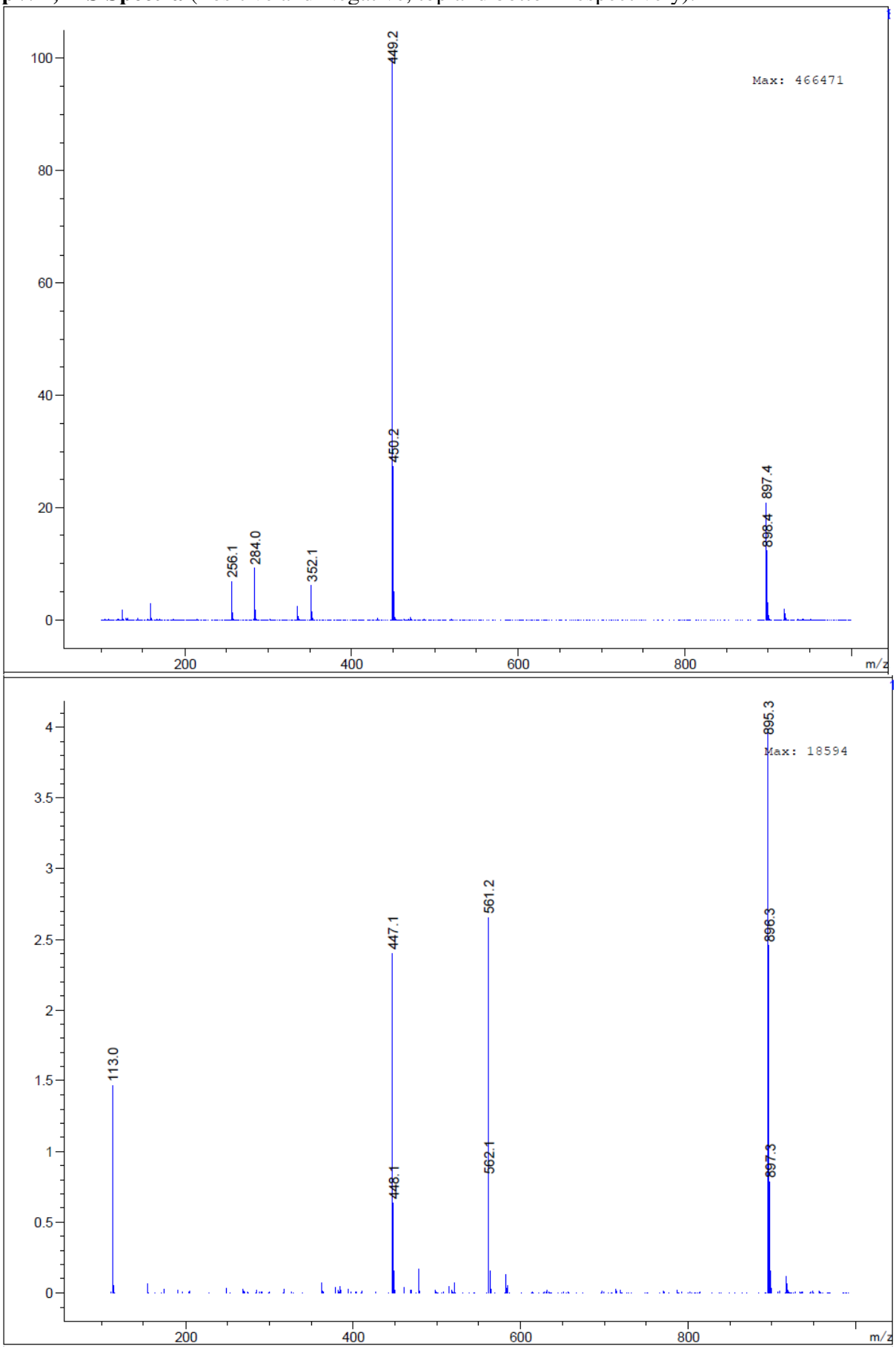

Spectroscopic Data for fWI

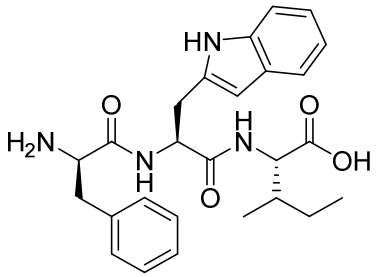

Chemical Formula: $C_{26}H_{32}N_4O_4$
Exact Mass: 464.24
Molecular Weight: 464.57

^{1}H-NMR (400 MHz, DMSO-*d_6*, TMS)

^{1}H-NMR (400 MHz, DMSO, TMS), δ (ppm): 10.84 (s, 1H, NH), 8.75 (d, *J* = 8.4 Hz, 1H, NH), 8.50 (d, *J* = 8.2 Hz, 1H, NH), 7.93 (s, 2H,NH_2), 7.81-7.78 (d, *J* = 7.7 Hz, 1H, Ar), 7.32-7.29 (d, *J* = 8.0 Hz, 1H,Ar), 7.18 – 6.96 (m, 6H, Ar), 6.78-6.73 (d, *J* = 7.4 Hz, 2H, Ar), 4.85-4.79 (m, *J* = 10.0, 4.1 Hz, 1H, αCH), 4.23-4.18 (m, *J* = 8.0, 6.2 Hz, 1H, αCH), 4.03-3.98 (s, 1H, αCH), 3.17-3.10 (m, *J* = 14.5, 3.9 Hz, 1H, βCH_2), 2.94-2.85 (m, *J* = 14.5, 10.4 Hz, 1H, βCH_2), 2.78-2.70 (m, *J* = 14.1, 4.2 Hz, 1H, βCH_2), 2.56-2.52 (m, *J* = 5.0 Hz, 1H, βCH_2), 1.87 – 1.75 (m, 1H, βCH), 1.53 – 1.41 (m, 1H, γCH_2), 1.29 – 1.16 (m, 1H, γCH_2), 0.92-0.84 (m, *J* = 13.5, 7.0 Hz, 6H, 3 x γCH_3, 3 x δCH_3).

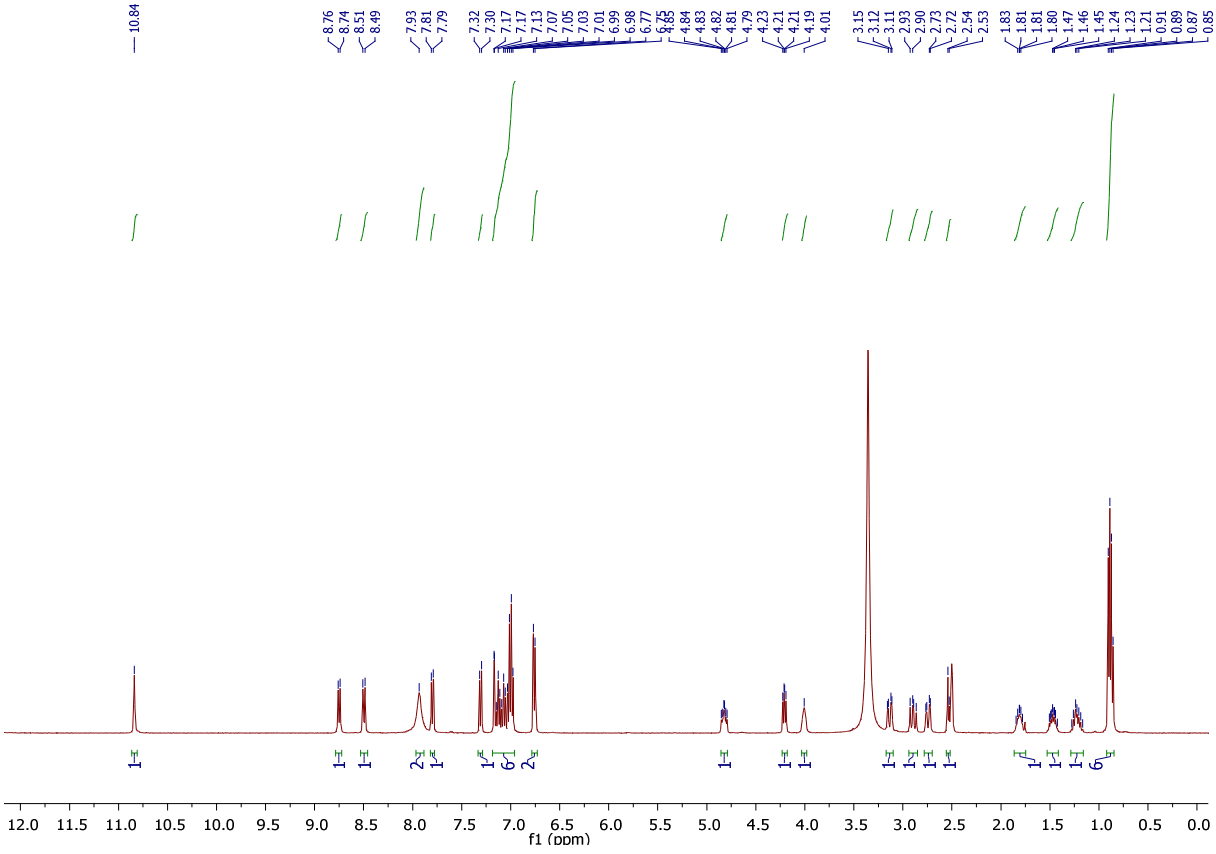

^{13}C-NMR (100MHz, DMSO-*d6*, TMS)

^{13}C-NMR (100 MHz, DMSO, TMS), δ (ppm): 172.8, 171.7, 167.4 (3 x CO); 136.2, 134.4, 129.5, 128.2, 127.2, 126.9, 124.3, 121.0, 119.0, 118.1, 111.3, 109.6 (Ar); 56.6, 53.0, 52.8 (3 x αC), 36.7, 36.3, 28.5 (2 x βCH_2 and 1 x βCH), 24.9 (γCH_2), 15.6 (γCH_3), 11.4 (δCH_3).

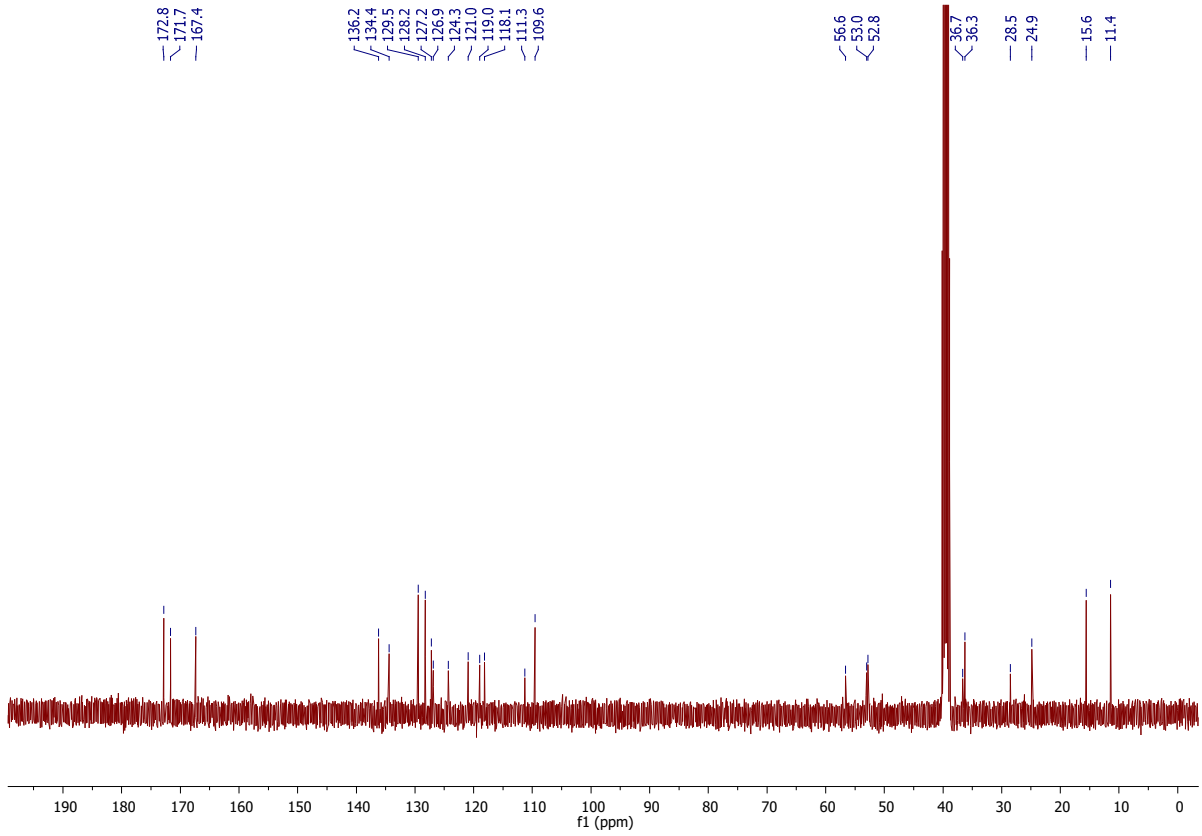

fWI, MS Spectra (Positive and Negative, top and bottom respectively).

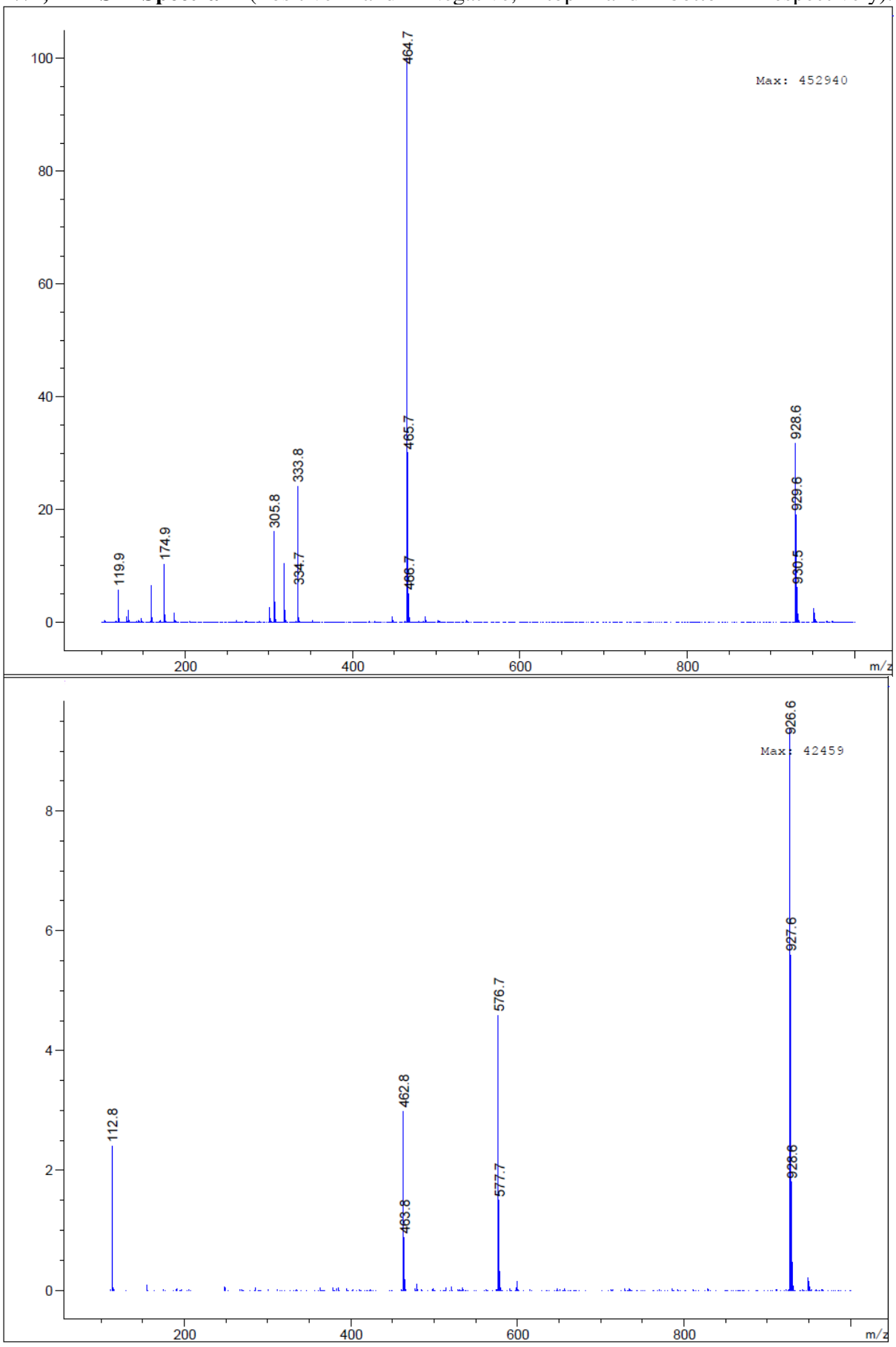

Spectroscopic Data for wLL

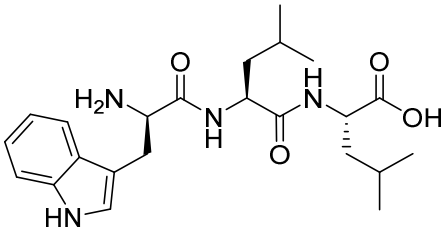

Chemical Formula: $C_{23}H_{34}N_4O_4$
Exact Mass: 430.26
Molecular Weight: 430.55

^{1}H-NMR (400 MHz, DMSO-*d*$_6$, TMS)

^{1}H-NMR (400 MHz, DMSO, TMS), δ (ppm): 11.04 (s, 1H, NH), 8.70 (d, *J* = 8.4 Hz, 1H, NH), 8.31 (d, *J* = 7.6 Hz, 1H, NH), 8.08 (s, 2H, NH_2), 7.72 (d, *J* = 7.9 Hz, 1H, Ar), 7.36 (d, *J* = 8.0 Hz, 1H, Ar), 7.21 (s, 1H, Ar), 7.09 (m, *J* = 7.5 Hz, 1H, Ar), 7.01 (m, *J* = 7.4 Hz, 1H, Ar), 4.43-4.36 (d, *J* = 8.5 Hz, 1H, αCH), 4.20 – 4.14 (m, 1H, αCH), 4.13-4.04 (m, 1H, αCH), 3.26-3.18 (m, *J* = 14.4, 5.7 Hz, 1H, βCH), 3.08-3.00 (m, *J* = 14.4, 8.6 Hz, 1H, βCH), 1.68 – 1.44 (m, 3H, 3 x βCH_2), 1.44-1.28 (m, 3H, βCH_2 and 2 x γCH), 0.92-0.82 (m, *J* = 23.3, 6.4 Hz, 6H, 4 x $3\delta CH_3$), 0.82-0.72 (m, *J* = 22.1, 4.3 Hz, 6H, 2 x $3\delta CH_3$).

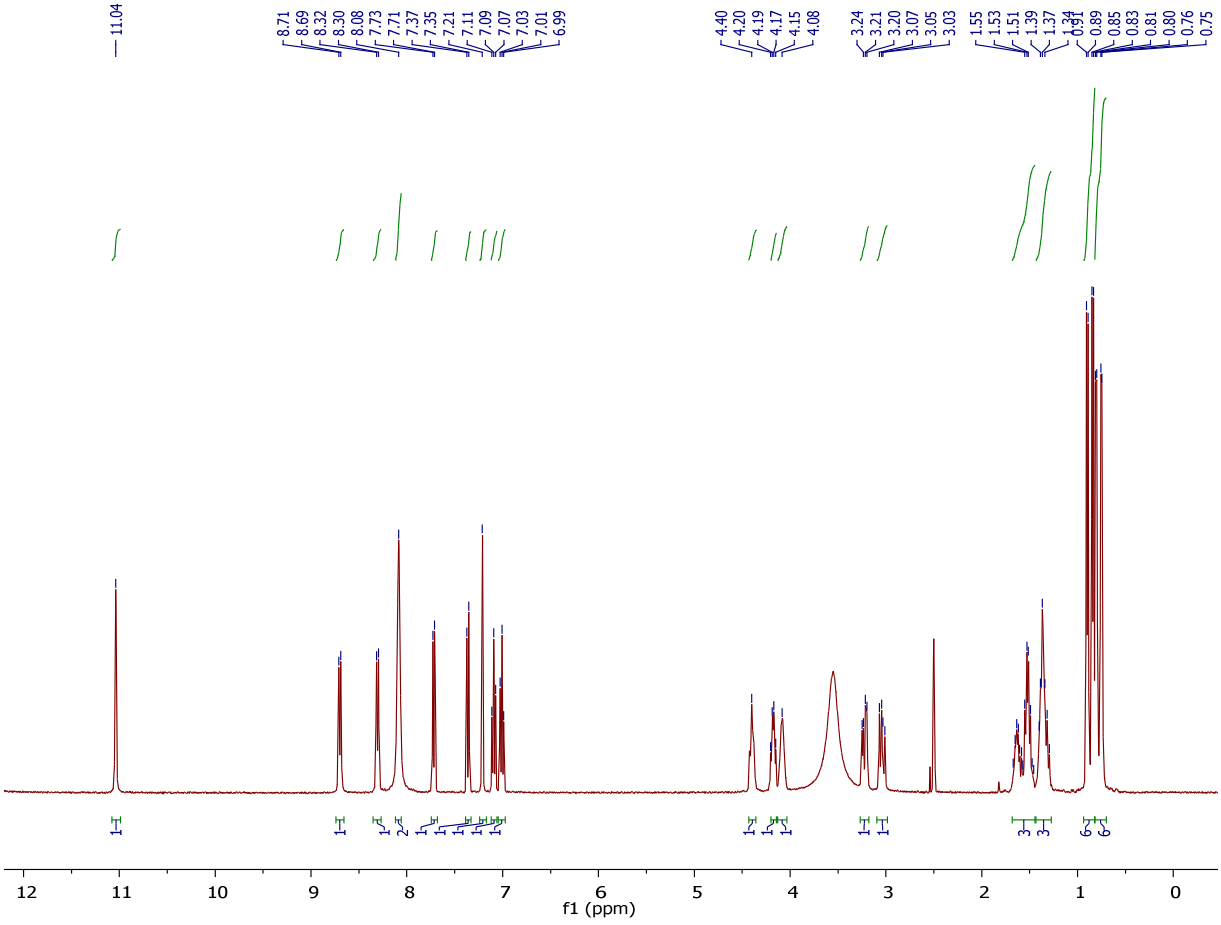

^{13}C-NMR (100MHz, DMSO-*d6*, TMS)

^{13}C NMR (101 MHz, dmso) δ 173.8, 171.7, 168.1 (3 x CO), 136.3, 127.0, 124.9, 121.1, 118.6, 118.4, 111.4, 106.8 (Ar); 52.6, 50.8, 50.3 (3 x αC); 41.4, 27.7 (3 x βCH_2); 24.3, 23.9 (2 x γCH); 23.1, 22.9, 21.4, 21.4 (4 x δCH_3).

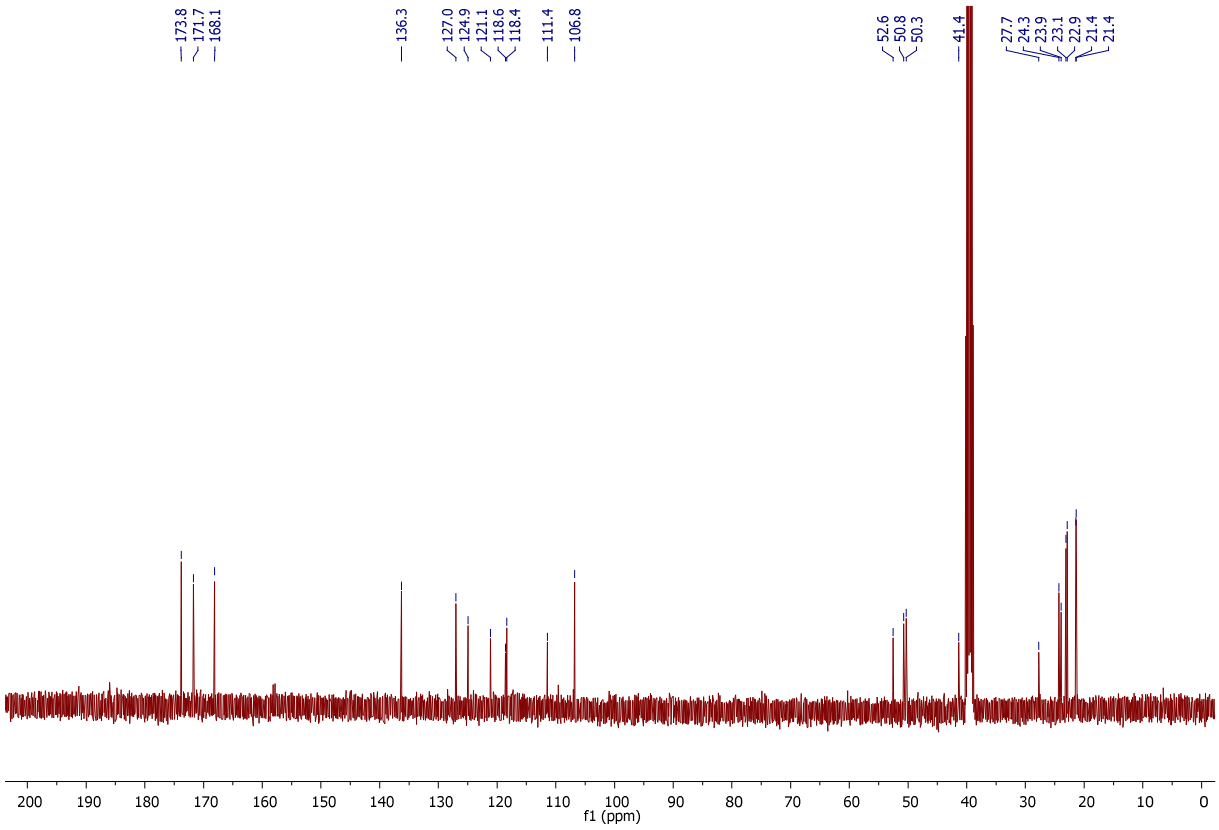

wLL, MS Spectra (Positive and Negative, top and bottom respectively).

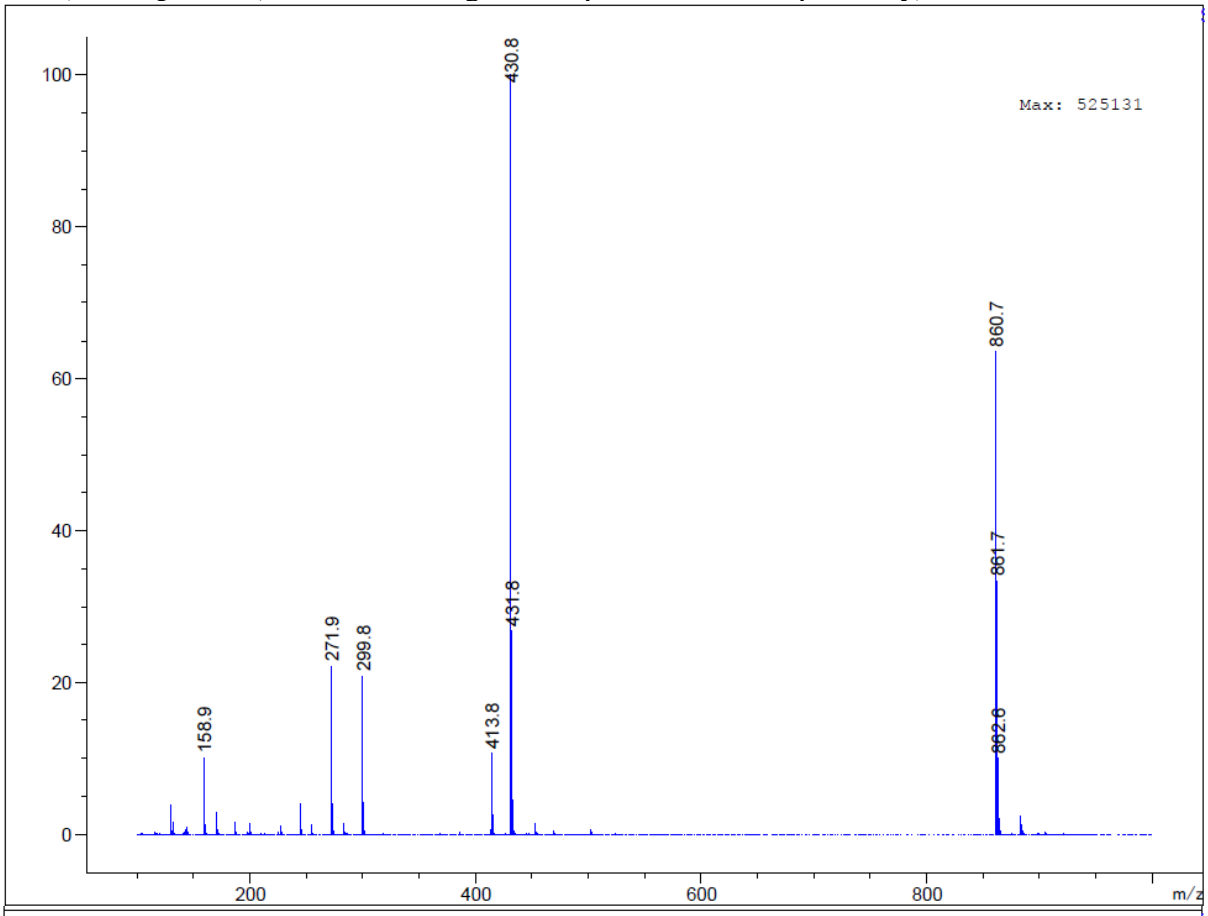

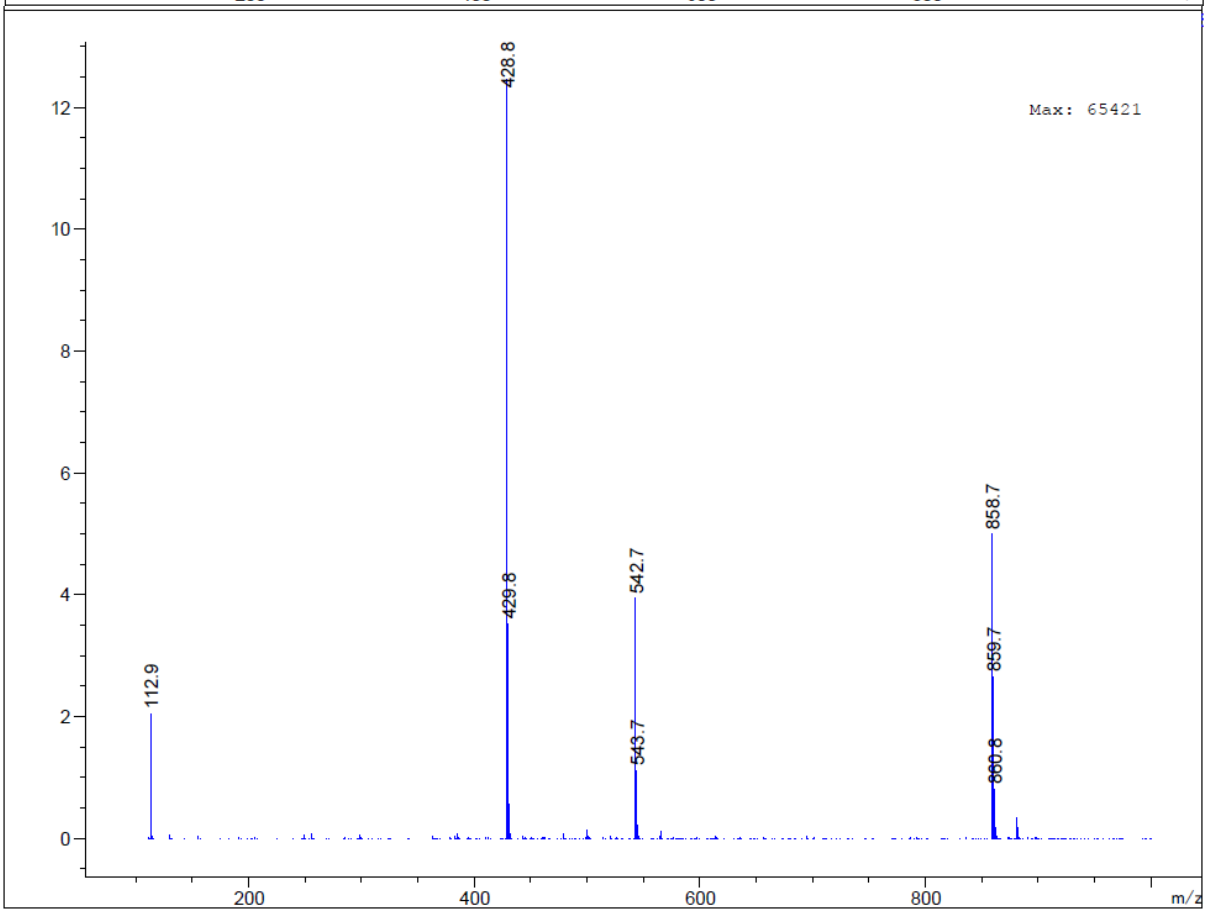

Spectroscopic Data for wFL

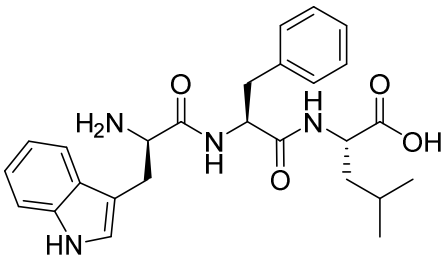

Chemical Formula: $C_{26}H_{32}N_4O_4$
Exact Mass: 464.24
Molecular Weight: 464.57

^{1}H-NMR (500 MHz, DMSO-*d_6*, TMS)

^{1}H-NMR (500 MHz, DMSO, TMS), δ (ppm): 12.67 (s, 1H, OH), 10.94 (s, 1H, NH), 8.95 (d, *J* = 8.7 Hz, 1H, NH), 8.51 (d, *J* = 7.7 Hz, 1H, NH), 7.84 (s, 2H, NH_2), 7.60 (d, *J* = 7.9 Hz, 1H, Ar), 7.35-6.93 (m, *J* = 61.1, 53.1, 19.1, 10.2 Hz, 9H, Ar), 4.78-4.72 (m, *J* = 12.9, 6.3 Hz, 1H, αCH), 4.25-4.19 (m, *J* = 15.1, 7.4 Hz, 1H, αCH), 3.97-3.91 (s, 1H, αCH), 3.12-3.05 (d, *J* = 13.5 Hz, 1H, βCH_2), 2.87-2.81 (d, *J* = 14.6 Hz, 1H, βCH_2), 2.75-2.68 (t, *J* = 12.2 Hz, 1H, βCH_2), 2.56 – 2.49 (m, 1H, βCH_2), 1.71 – 1.52 (m, 3H, 2 x βCH_2, 1 x γCH), 0.92-0.88 (d, *J* = 6.5 Hz, 3H3 x δCH_3), 0.86-0.82 (d, *J* = 6.4 Hz, 3H, 3 x δCH_3).

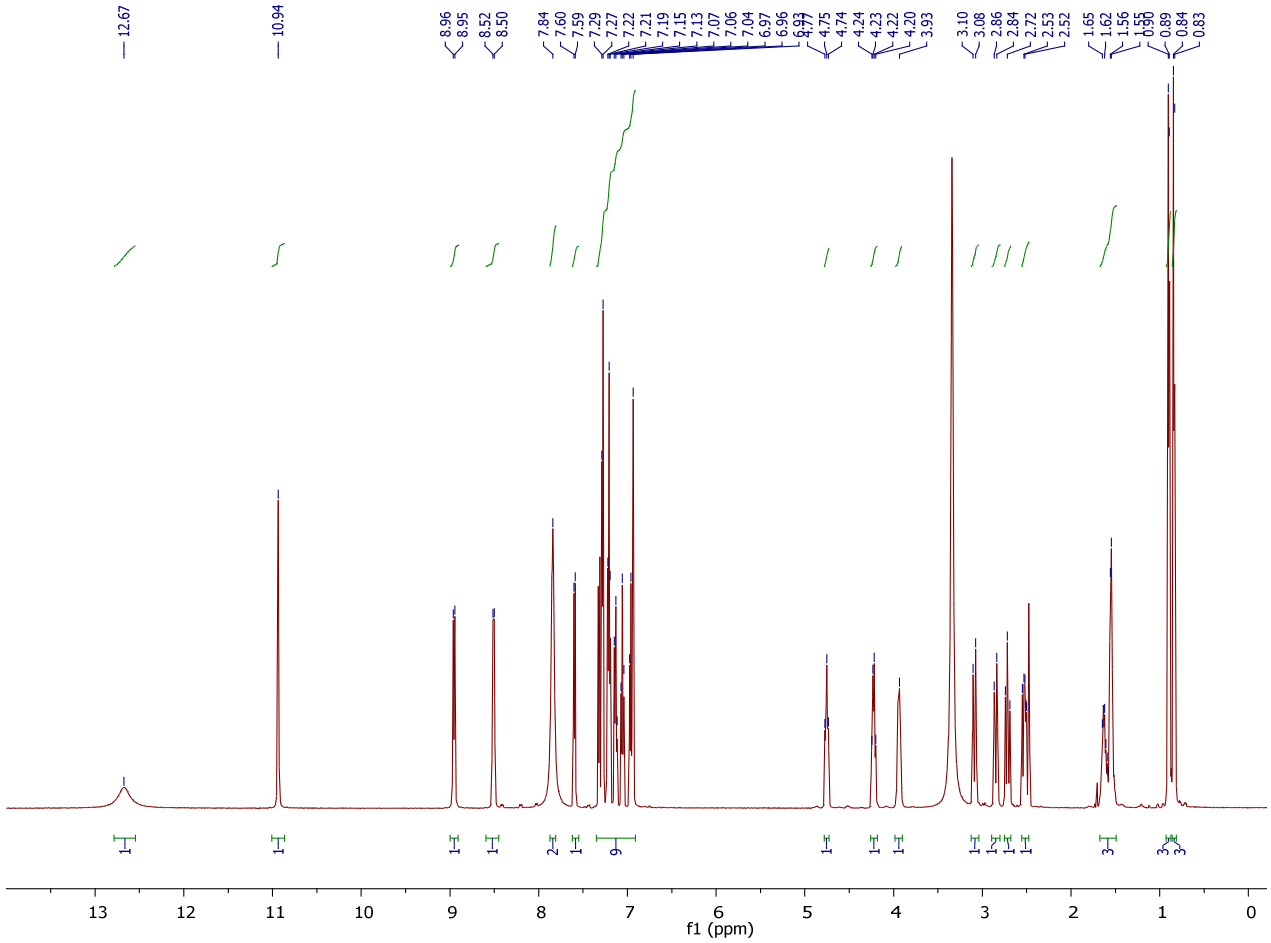

^{13}C-NMR (100MHz, DMSO-*d6*, TMS)

^{13}C-NMR (101 MHz, DMSO, TMS), δ (ppm) 173.86, 171.01, 168.28 (3 x CO); 137.44, 136.34, 129.45, 128.03, 126.97, 126.45, 125.01, 121.13, 118.68, 118.39, 111.39, 106.73 (Ar); 53.59, 52.41, 50.41 (3 x αC); 24.38 (γCH), 22.88, 21.34 (2 x δCH_3).

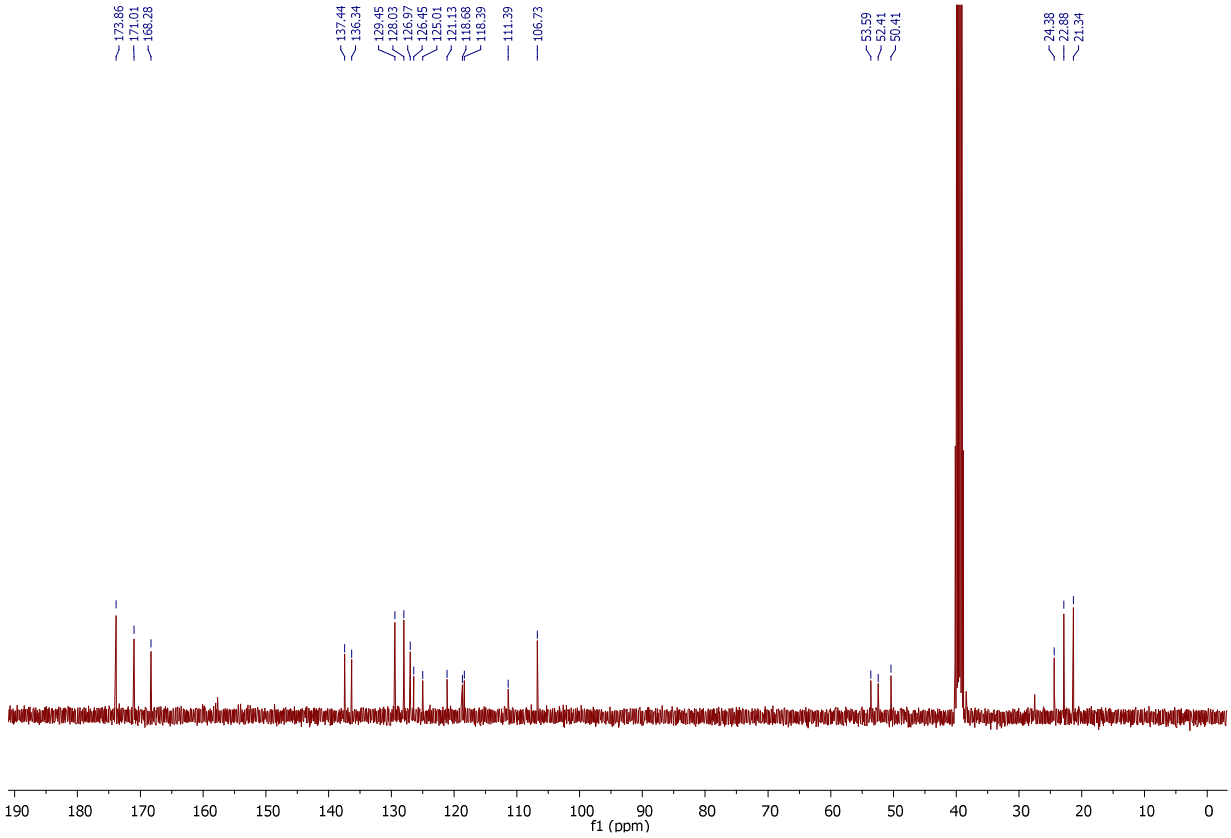

wFL, MS Spectra (Positive and Negative, top and bottom respectively).

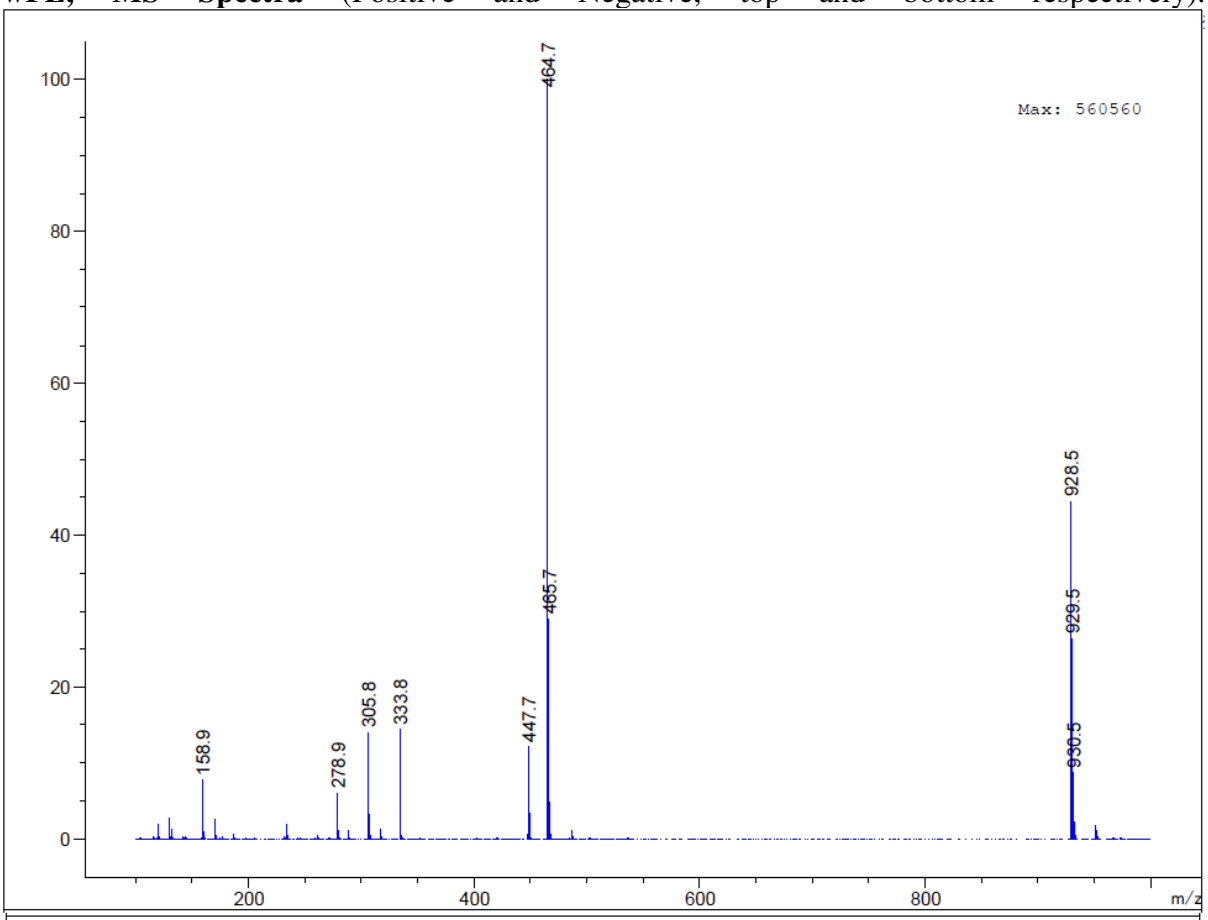

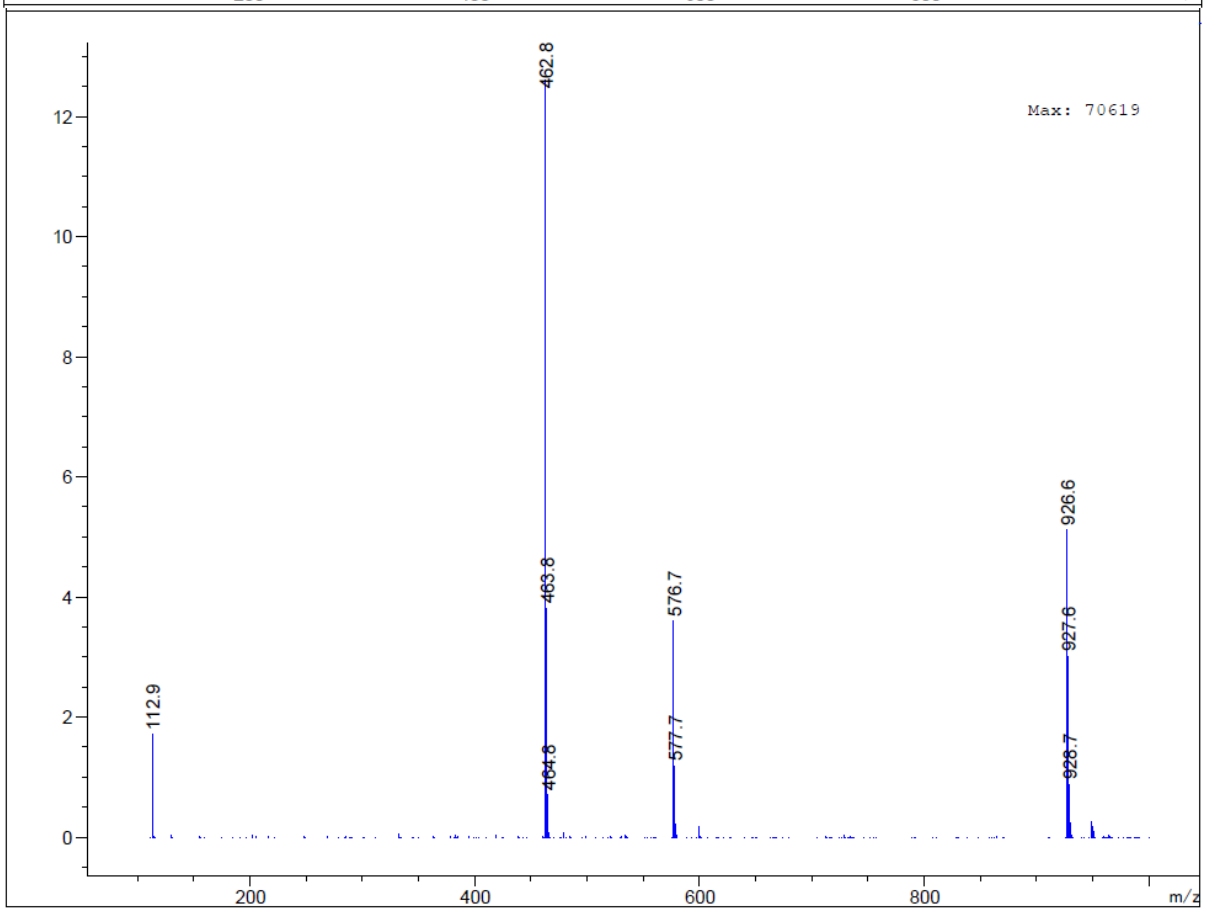

Spectroscopic Data for fWF

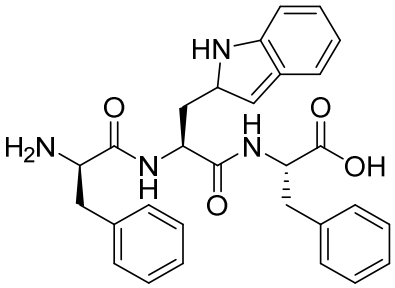

Chemical Formula: $C_{29}H_{31}N_4O_4$
Exact Mass: 499.23
Molecular Weight: 499.59

^{1}H-NMR (400 MHz, DMSO-d_6, TMS)

^{1}H-NMR (400 MHz, DMSO, TMS), δ (ppm):10.84 (d, *J* = 2.1 Hz, 1H, NH), 8.77 (d, *J* = 8.5 Hz, 1H, NH), 8.70 (d, *J* = 7.7 Hz, 1H, NH), 7.90 (s, 2H, NH_2), 7.78 (d, *J* = 7.7 Hz, 1H, Ar), 7.33 – 6.96 (m, 12H, Ar), 6.77 – 6.72 (m, 2H,Ar), 4.75 – 4.69 (m, 1H, αCH), 4.50-4.45 (m, *J* = 9.1, 7.8, 5.2 Hz, 1H, αCH), 3.99-3.93 (m, 1H, αCH), 3.20 – 3.09 (m, 2H, βCH_2), 3.00-2.82 (m, *J* = 25.1, 14.3, 9.8 Hz, 3H, βCH_2), 2.77 – 2.67 (m, 1H, βCH_2).

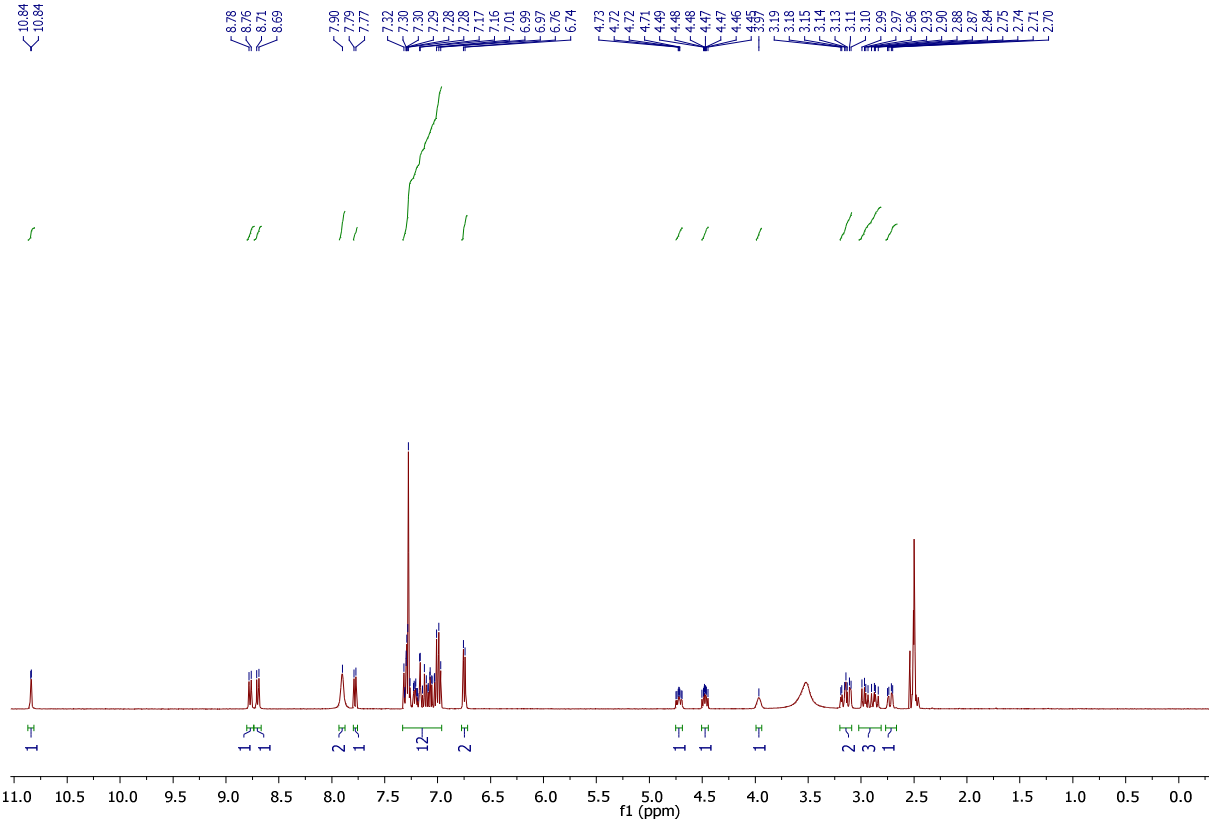

^{13}C-NMR (100MHz, DMSO-*d6*, TMS)

^{13}C-NMR (100 MHz, DMSO, TMS), δ (ppm): 172.8, 171.6, 167.4 (3 x CO); 137.6, 136.2, 134.4, 129.5, 129.1, 128.3, 128.2, 127.2, 126.9, 126.5, 124.3, 121.0, 118.9, 118.2, 111.3, 109.5 (Ar); 53.8, 53.1, 52.9 (3 x αC); 36.60, 36.52, 28.51 (3 x βCH_2).

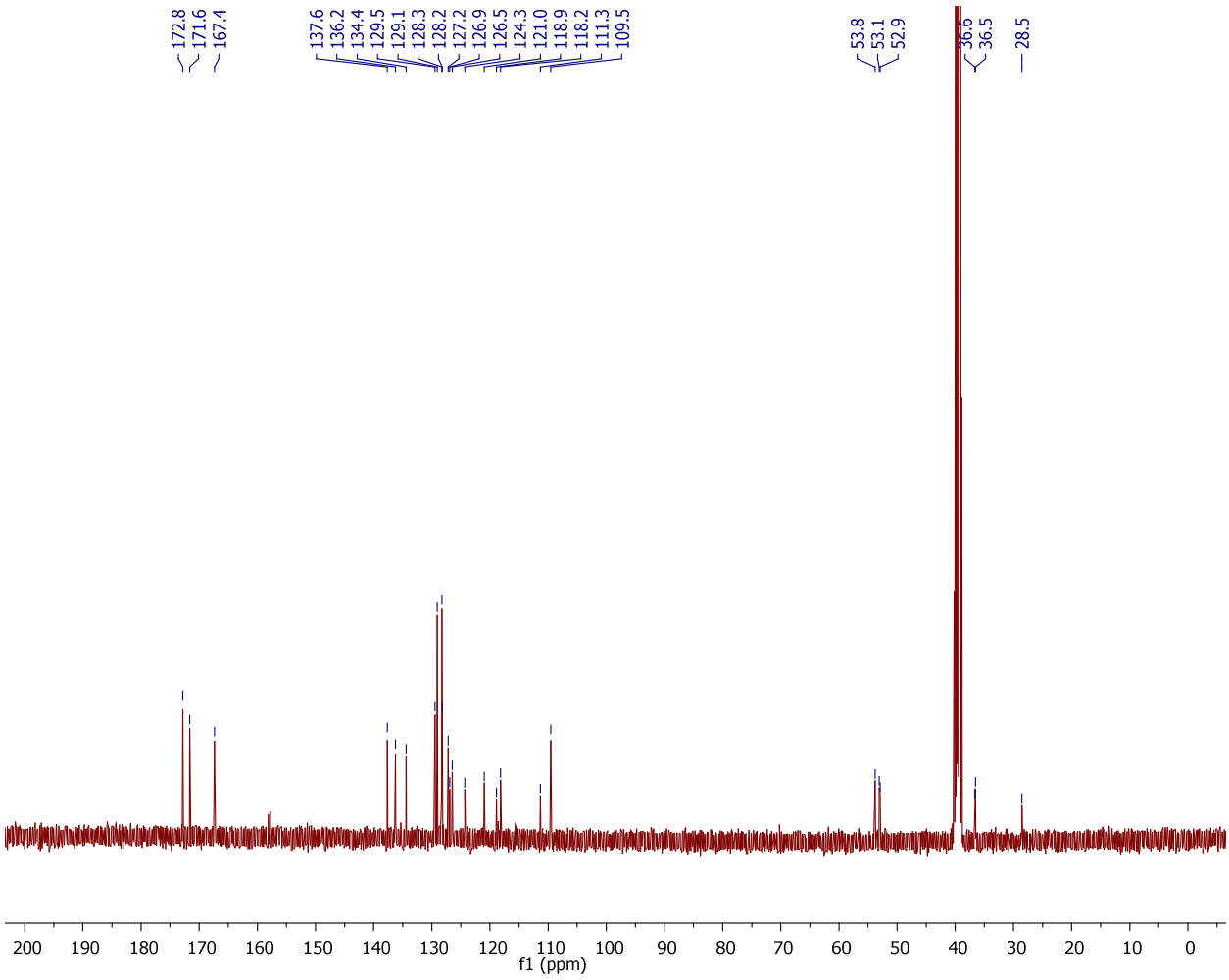

fWF, MS Spectra (Positive and Negative, top and bottom respectively).

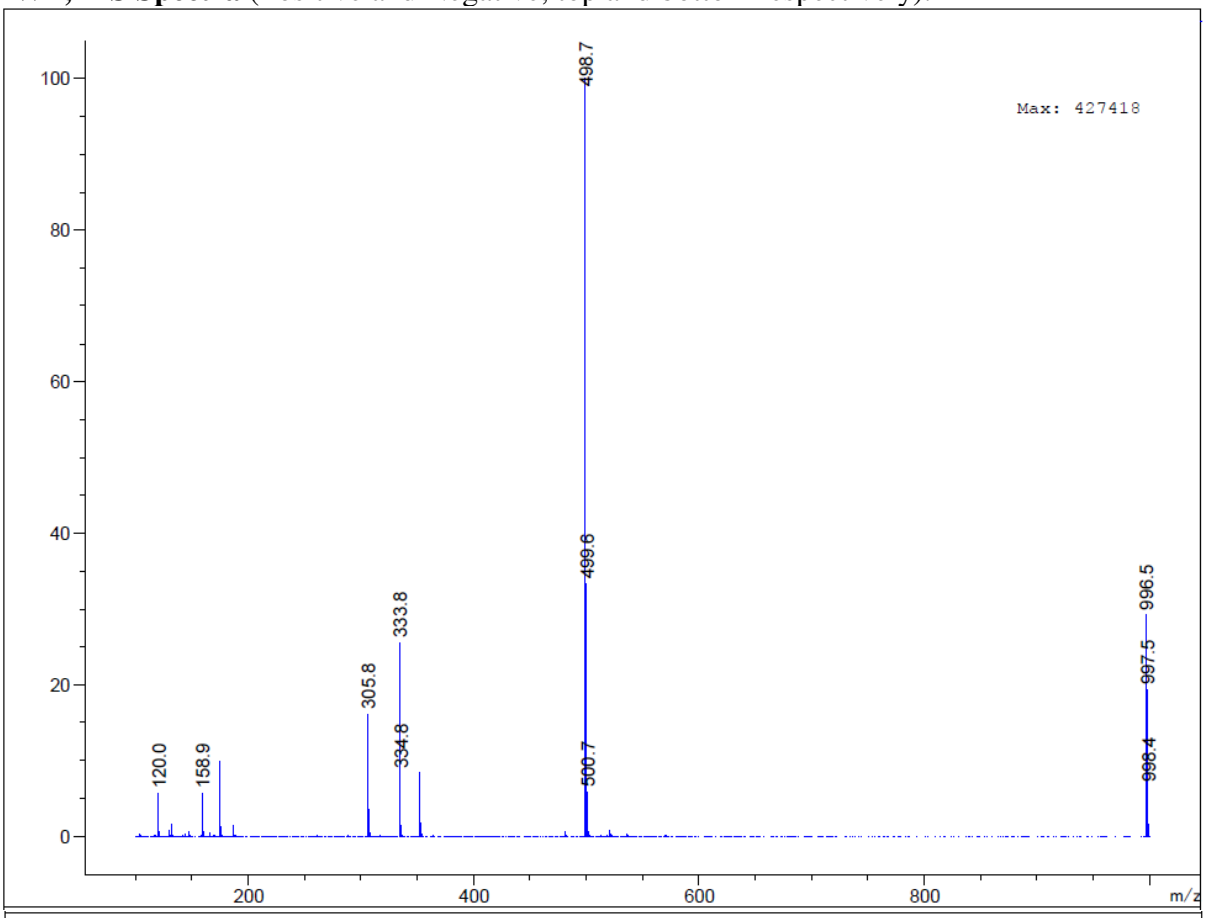

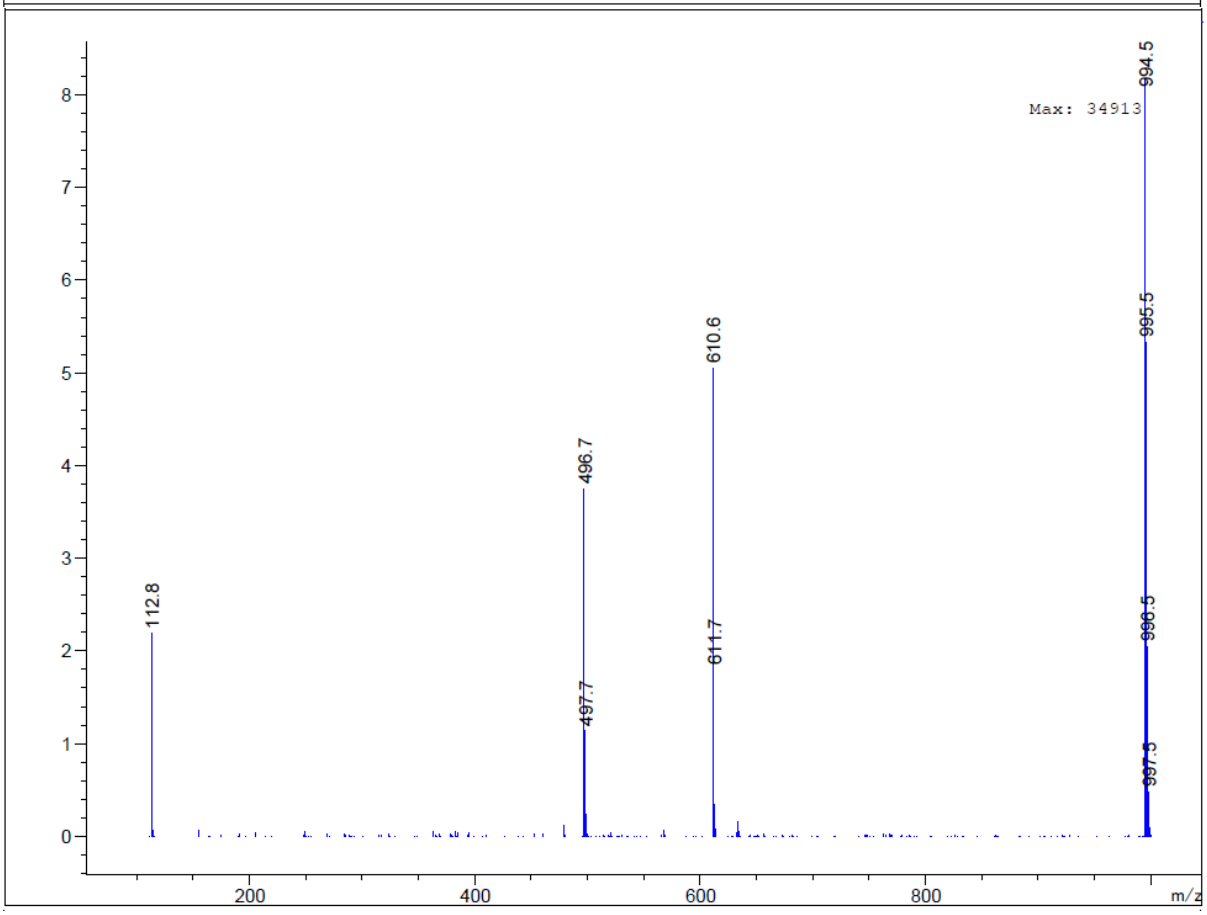

Spectroscopic Data for wWF

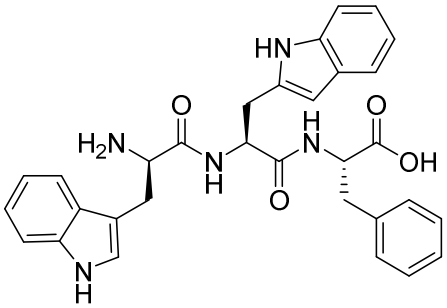

Chemical Formula: $C_{31}H_{31}N_5O_4$
Exact Mass: 537.24
Molecular Weight: 537.62

^{1}H-NMR (400 MHz, DMSO-*d*$_6$, TMS)

^{1}H-NMR (400 MHz, DMSO, TMS), δ (ppm):10.90 (d, *J* = 2.1 Hz, 1H, NH), 10.82 (d, *J* = 2.0 Hz, 1H, NH), 8.92 (d, *J* = 8.7 Hz, 1H, NH), 8.69 (d, *J* = 7.7 Hz, 1H, NH), 7.81-7.77 (s, 2H, NH_2), 7.76 (s, 1H, Ar), 7.56-7.53 (d, *J* = 7.9 Hz, 1H, Ar), 7.34 – 7.17 (m, 8H, Ar), 7.06 – 6.95 (m, 4H, Ar), 6.86 – 6.80 (m, 1H, Ar), 4.81 – 4.75 (m, 1H, αCH), 4.52 – 4.46 (m, 1H, αCH), 3.95 – 3.89 (m, 1H, αCH), 3.16 (m, *J* = 19.2, 14.3, 4.5 Hz, 2H, βCH_2), 3.01 – 2.79 (m, 4H, βCH_2).

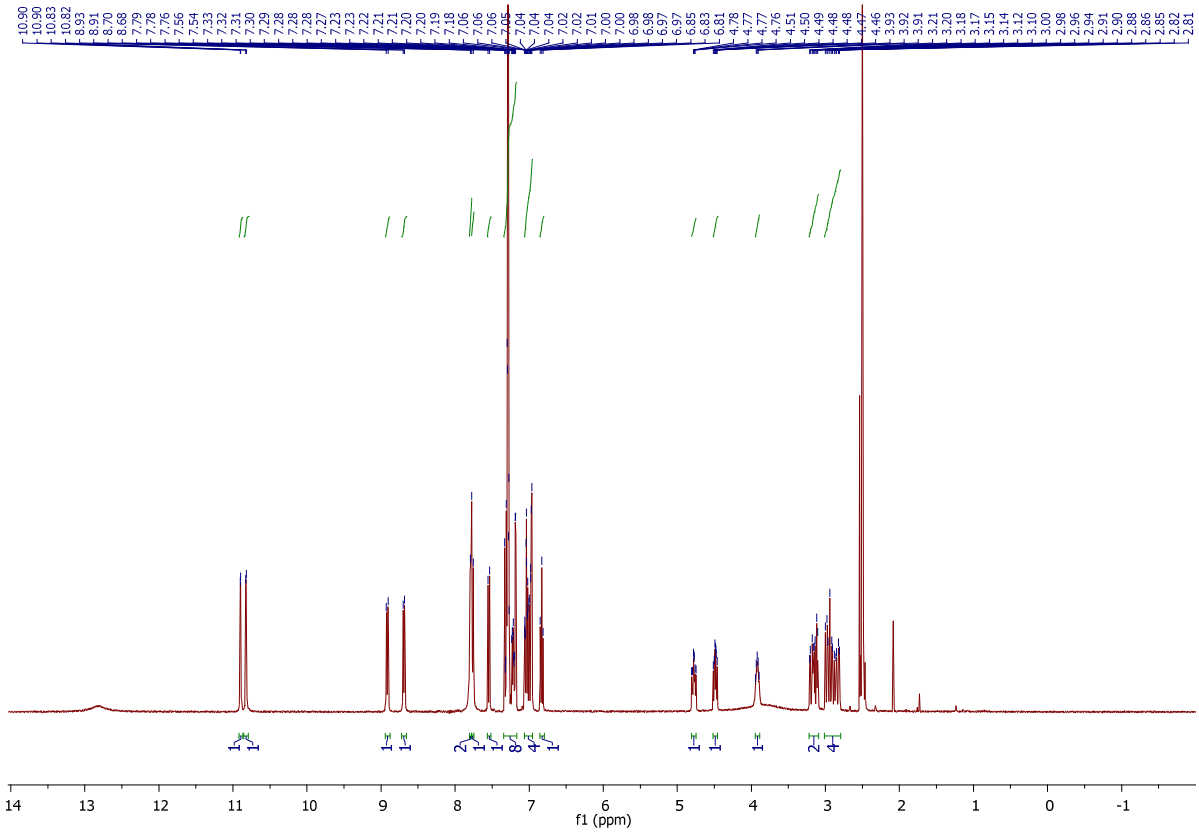

^{13}C-NMR (100MHz, DMSO-*d6*, TMS)

^{13}C-NMR (100 MHz, DMSO, TMS), δ (ppm): 172.85, 171.64, 168.18 (3 x CO), 137.67, 136.33, 136.16, 129.11, 128.32, 127.28, 126.94, 126.52, 125.04, 124.19, 121.10, 120.92, 118.79, 118.33, 118.19, 111.27, 109.64, 106.78 (Ar); 53.85, 53.02, 52.34 (3 x αC); 36.55, 28.58, 27.29 (3 x βCH$_2$).

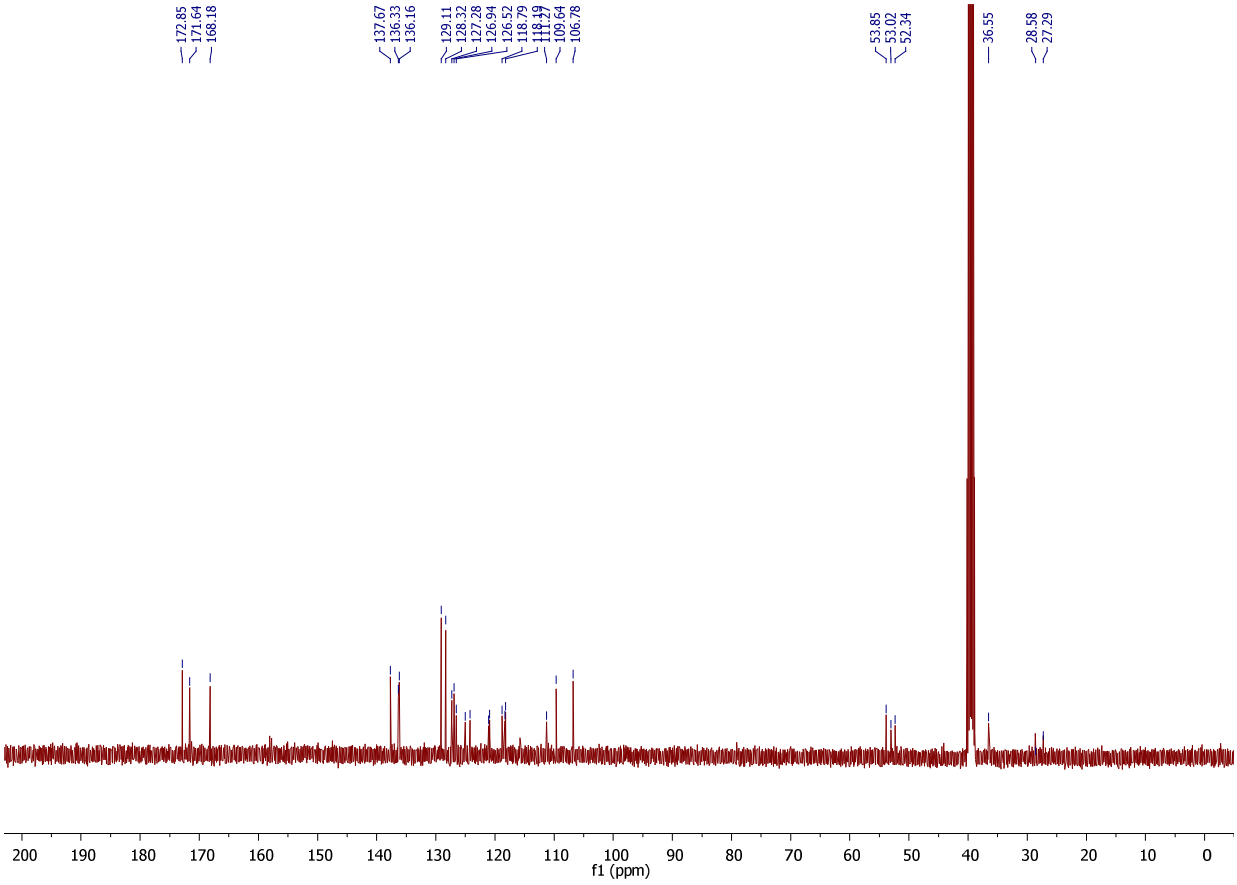

wWF, MS Spectra (Positive and Negative, top and bottom respectively).

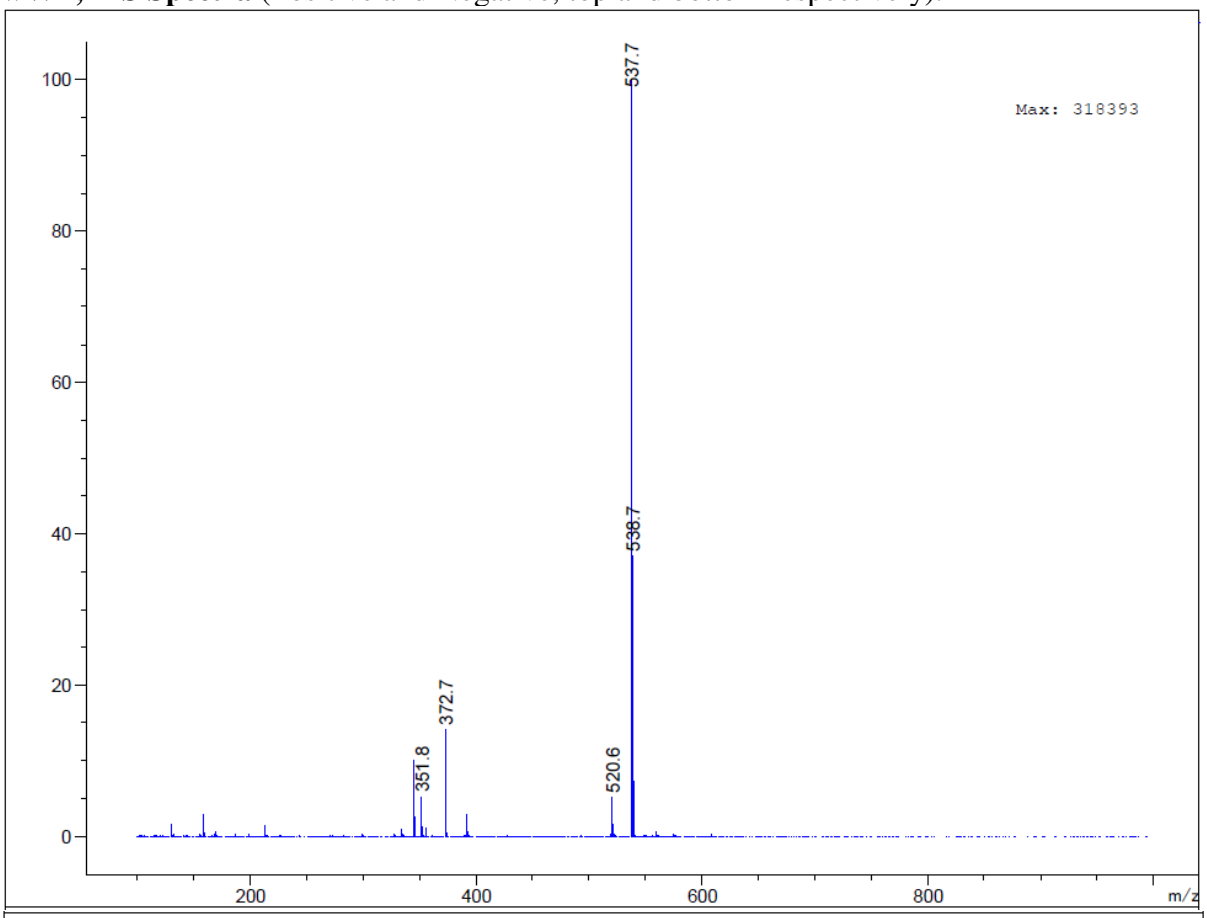

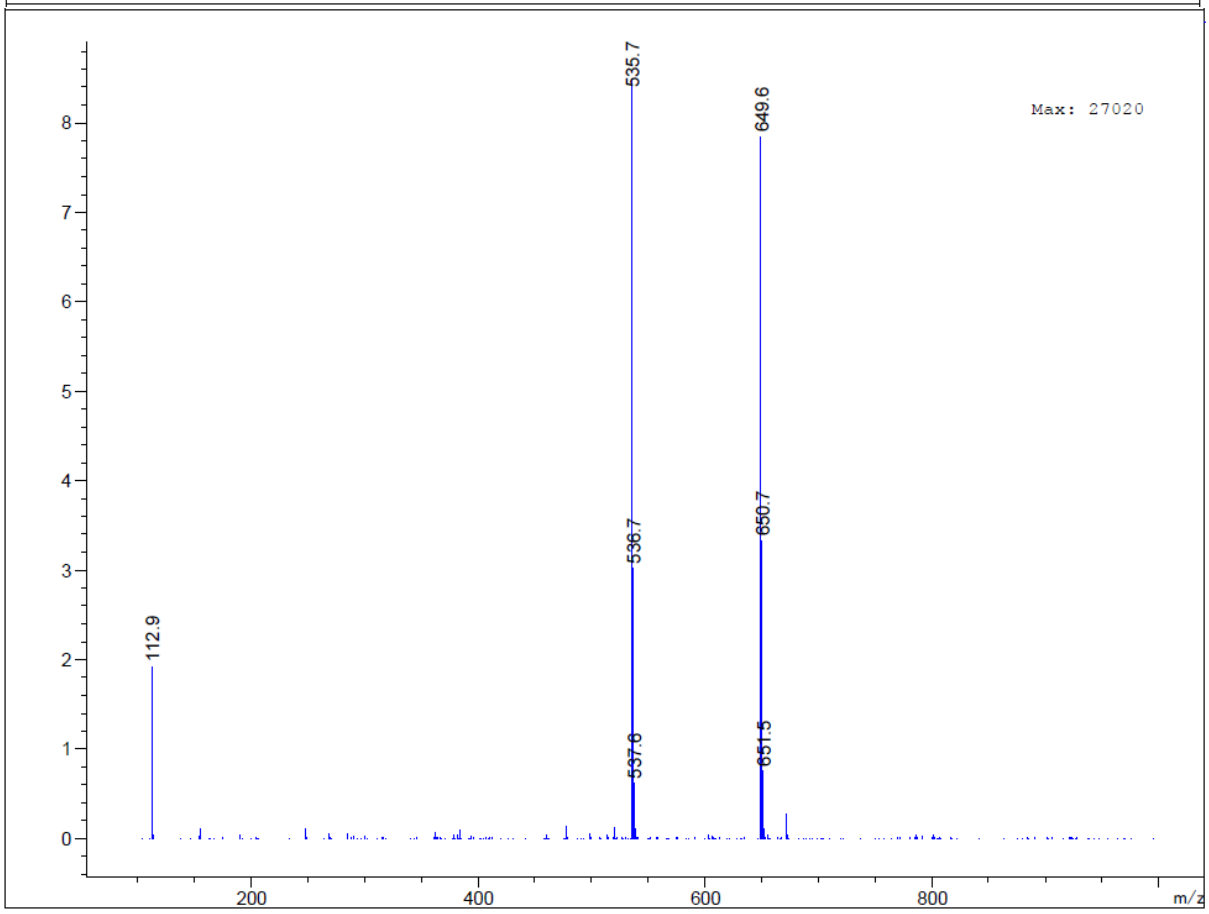

Spectroscopic Data for wFF

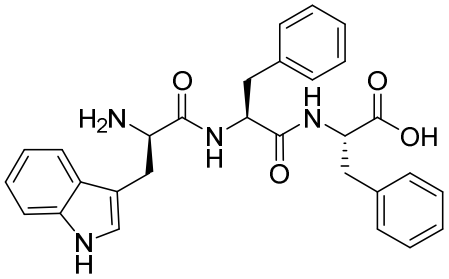

Chemical Formula: $C_{29}H_{30}N_4O_4$
Exact Mass: 498.23
Molecular Weight: 498.58

^{1}H-NMR (400 MHz, DMSO-*d_6*, TMS)

^{1}H-NMR (400 MHz, DMSO, TMS), δ (ppm): 10.94 (d, *J* = 1.8 Hz, 1H, NH), 8.97 (d, *J* = 8.9 Hz, 1H, NH), 8.66 (d, *J* = 7.8 Hz, 1H, NH), 7.82 (d, *J* = 3.8 Hz, 2H, NH_2), 7.64 (d, *J* = 7.9 Hz, 1H, Ar), 7.37 – 6.92 (m, 14H, Ar), 4.80 – 4.74 (m, 1H, αCH), 4.52 – 4.41 (m, 1H, αCH), 3.92 – 3.90 (m, 1H, αCH), 3.16 – 3.06 (m, 2H, βCH_2), 2.98-2.91 (m, *J* = 14.0, 9.3 Hz, 1H, βCH_2), 2.87-2.81 (m, *J* = 14.8, 3.9 Hz, 1H, βCH_2), 2.75-2.67 (m, *J* = 13.6, 10.8 Hz, 1H, βCH_2), 2.55-2.52 (d, *J* = 9.9 Hz, 1H, βCH_2).

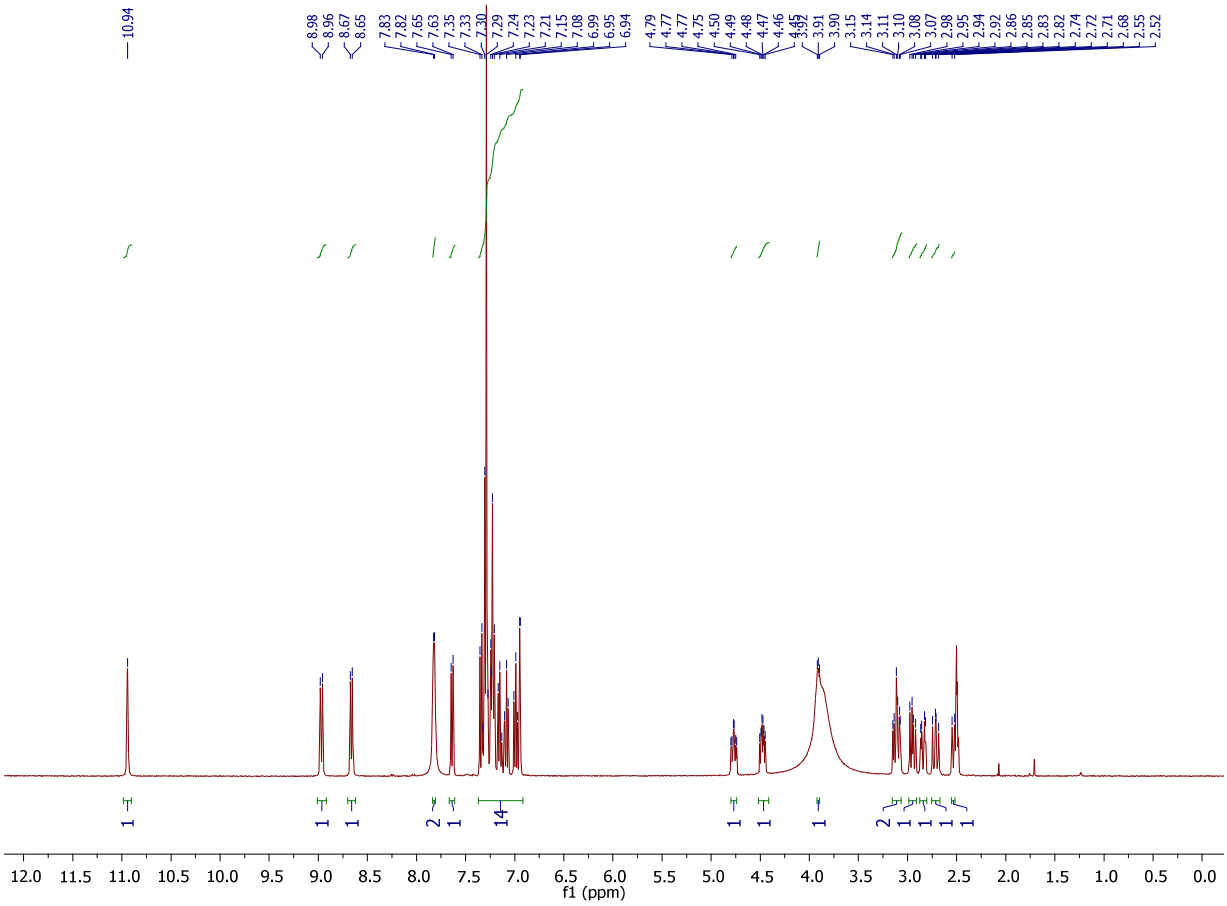

^{13}C-NMR (100MHz, DMSO-*d6*, TMS)

^{13}C-NMR (100 MHz, DMSO, TMS), δ (ppm): 172.8, 171.1, 168.2 (3 x CO); 137.6, 137.4, 136.4, 129.5, 129.1, 128.3, 128.0, 126.9, 126.6, 126.5, 125.0, 121.2, 118.7, 118.4, 111.4, 106.7 (Ar); 53.8, 53.5, 52.4 (3 x αC); 38.4, 36.6, 27.5 (3 x βCH_2).

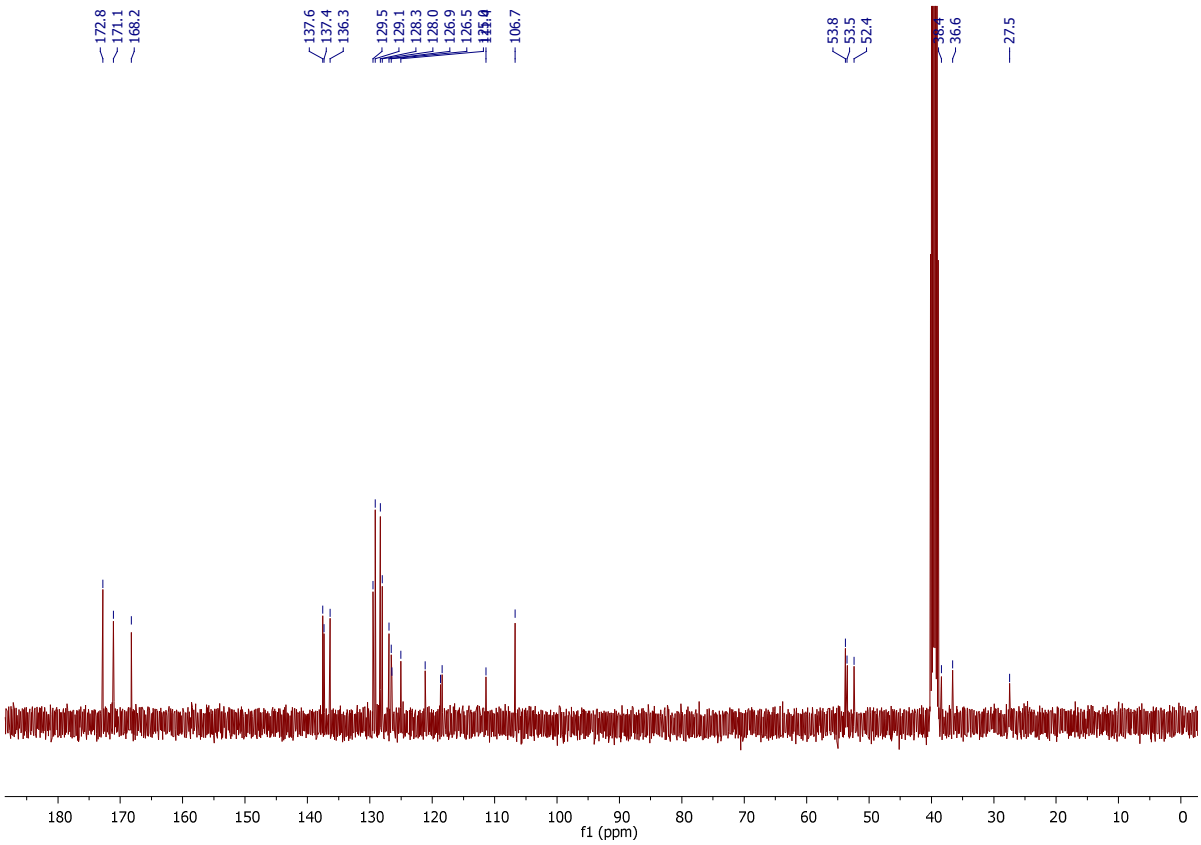

wFF, MS Spectra (Positive and Negative, top and bottom respectively).

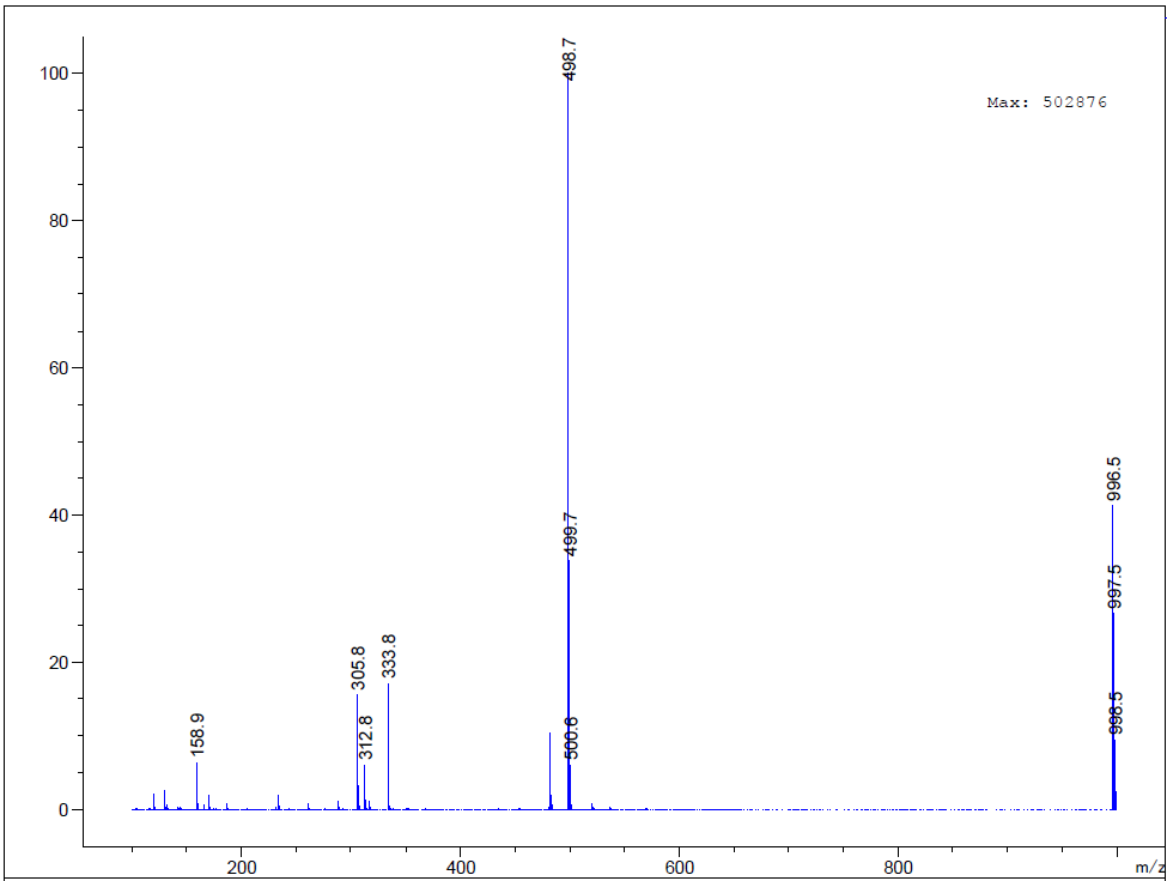

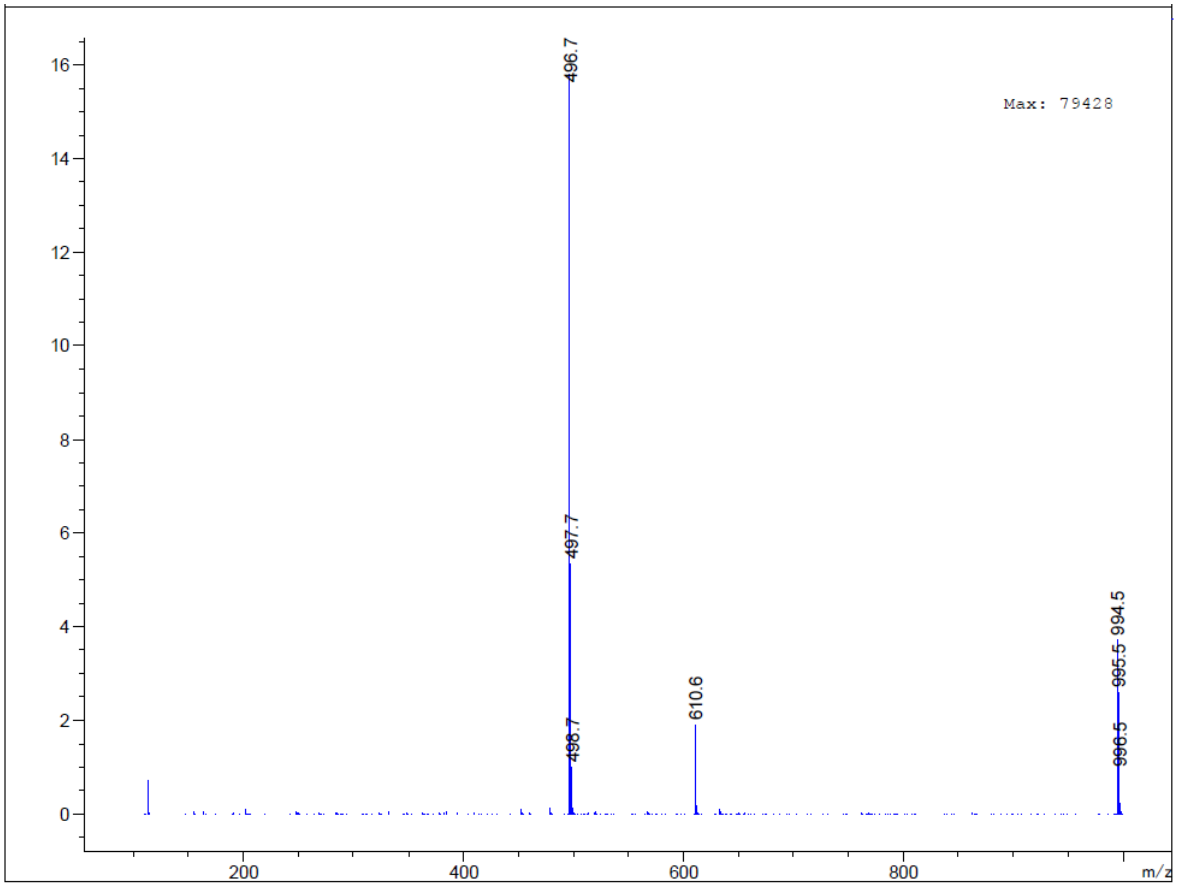

Peptide HPLC trace

Analytical HPLC trace for heterochiral tripeptides. HPLC (1260 Agilent Infinity system) equipped with a preparative gradient pump (G1311B), analytic C-18 column (Luna, 5 µm, 100 Å, 150 x 2 mm, Phenomenex) and Photodiode Array detector (G1315C) and Quadrupole LC/MS (6120). The gradient used consisted of acetonitrile (MeCN)/ H_2O with 0.1% formic acid with the following program: t = 0, 95% water (+0.1% formic acid) and 5% MeCN (+0.1% formic acid); t = 20 min, 5% water (+0.1% formic acid) and 95 % MeCN (+0.1 % formic acid).

1. xFF group

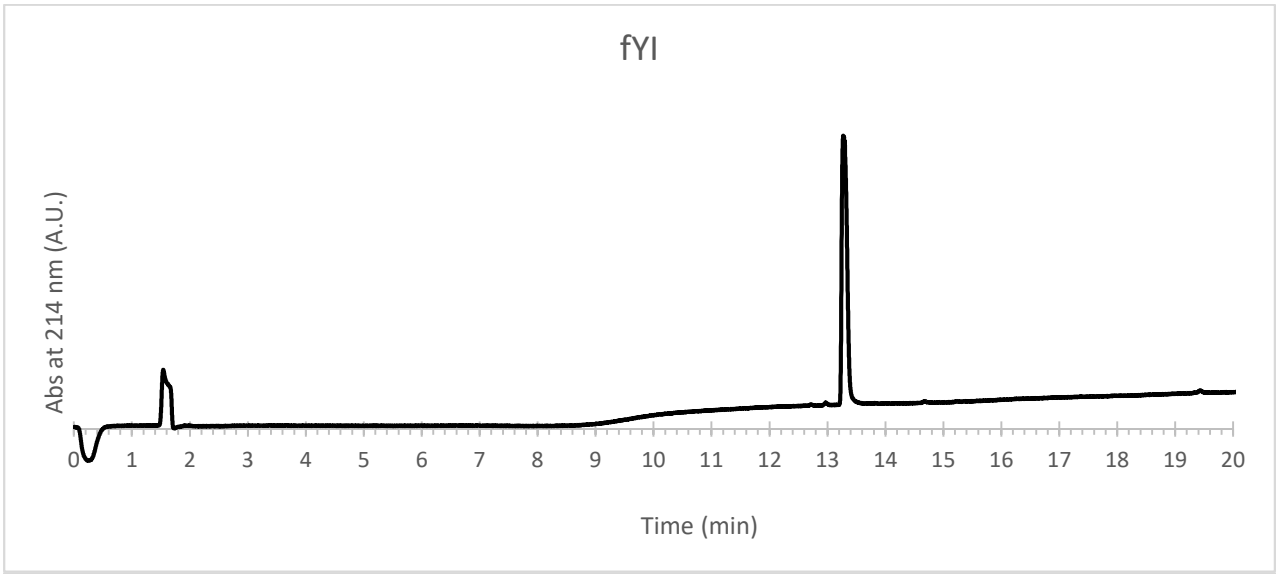

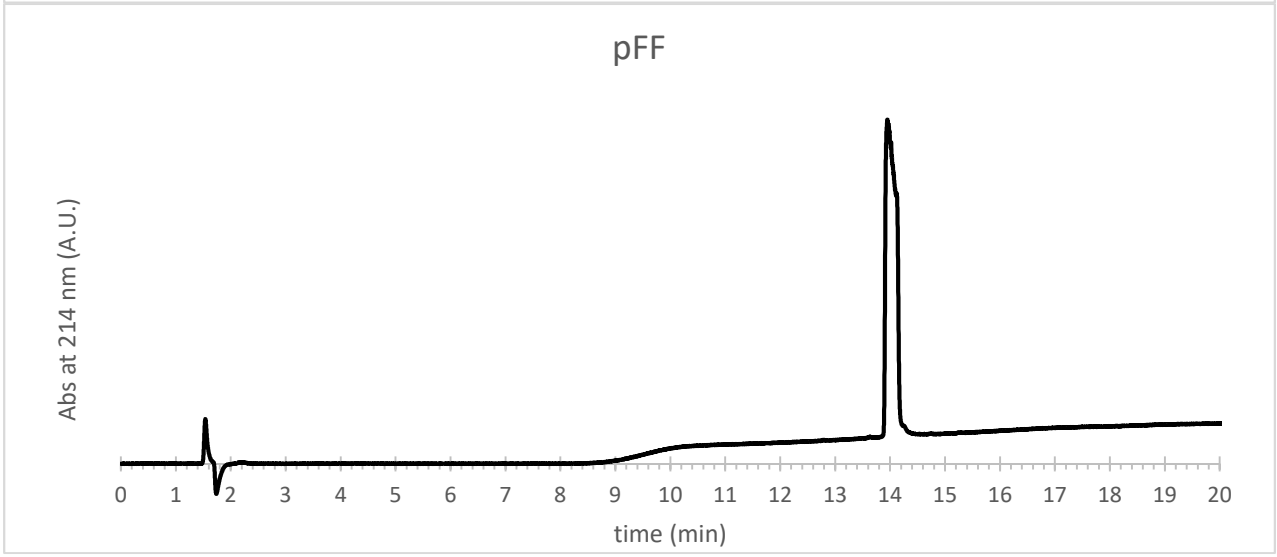

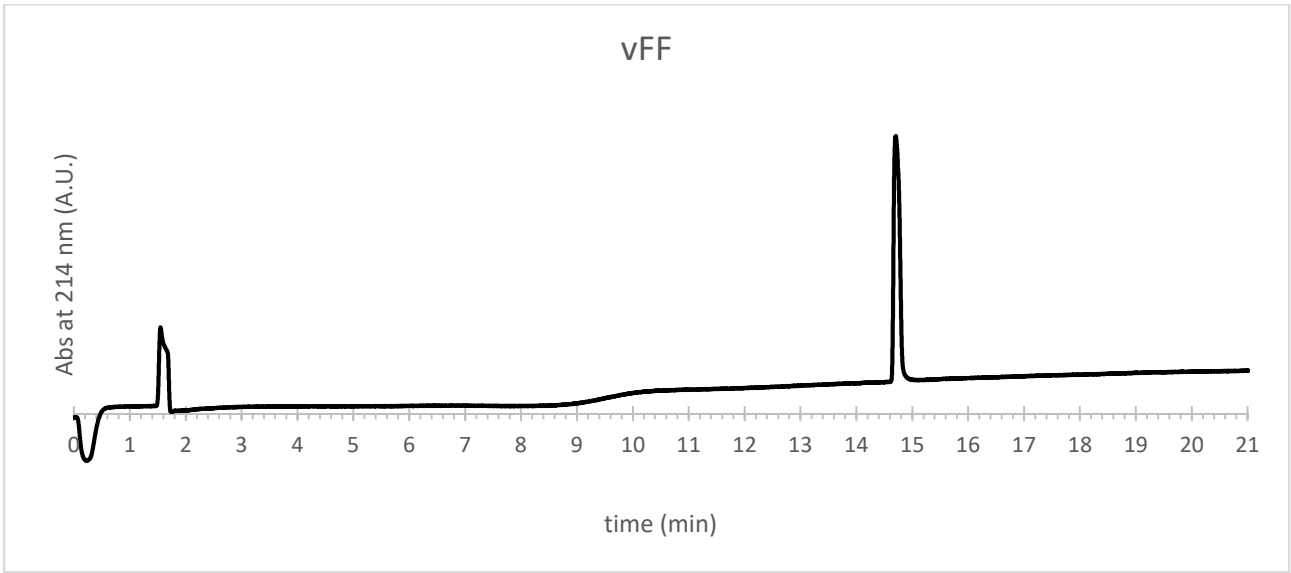
vFF
Abs at 214 nm (A.U.)
0 1 2 3 4 5 6 7 8 9 10 11 12 13 14 15 16 17 18 19 20 21
time (min)

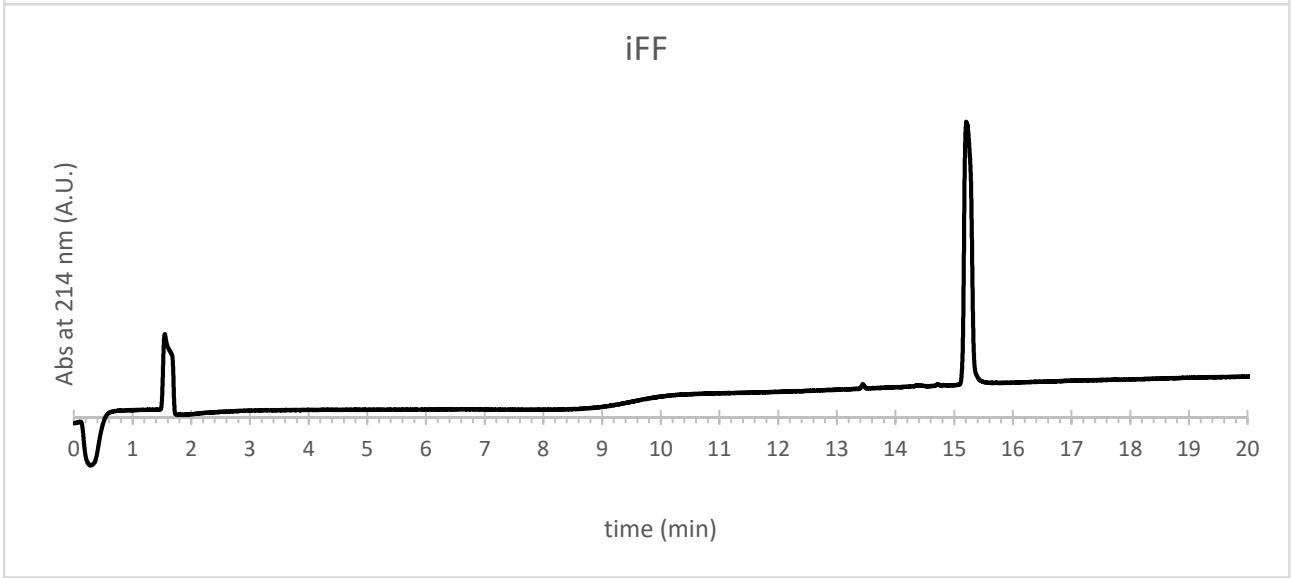
iFF
Abs at 214 nm (A.U.)
0 1 2 3 4 5 6 7 8 9 10 11 12 13 14 15 16 17 18 19 20
time (min)

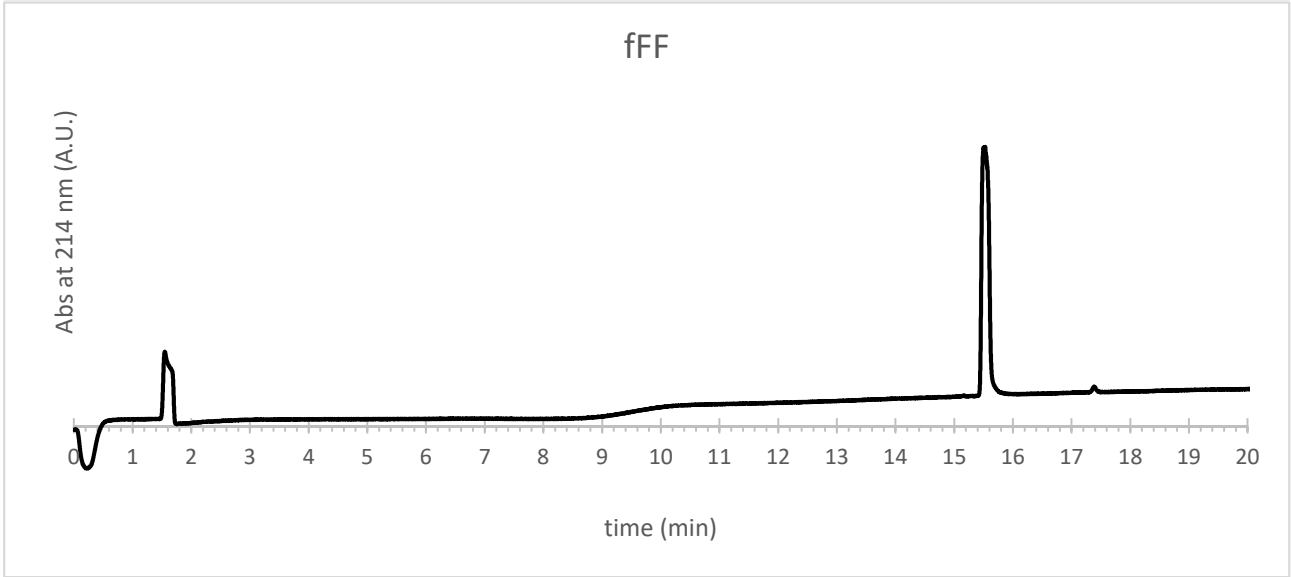
fFF
Abs at 214 nm (A.U.)
0 1 2 3 4 5 6 7 8 9 10 11 12 13 14 15 16 17 18 19 20
time (min)

2. xFW group

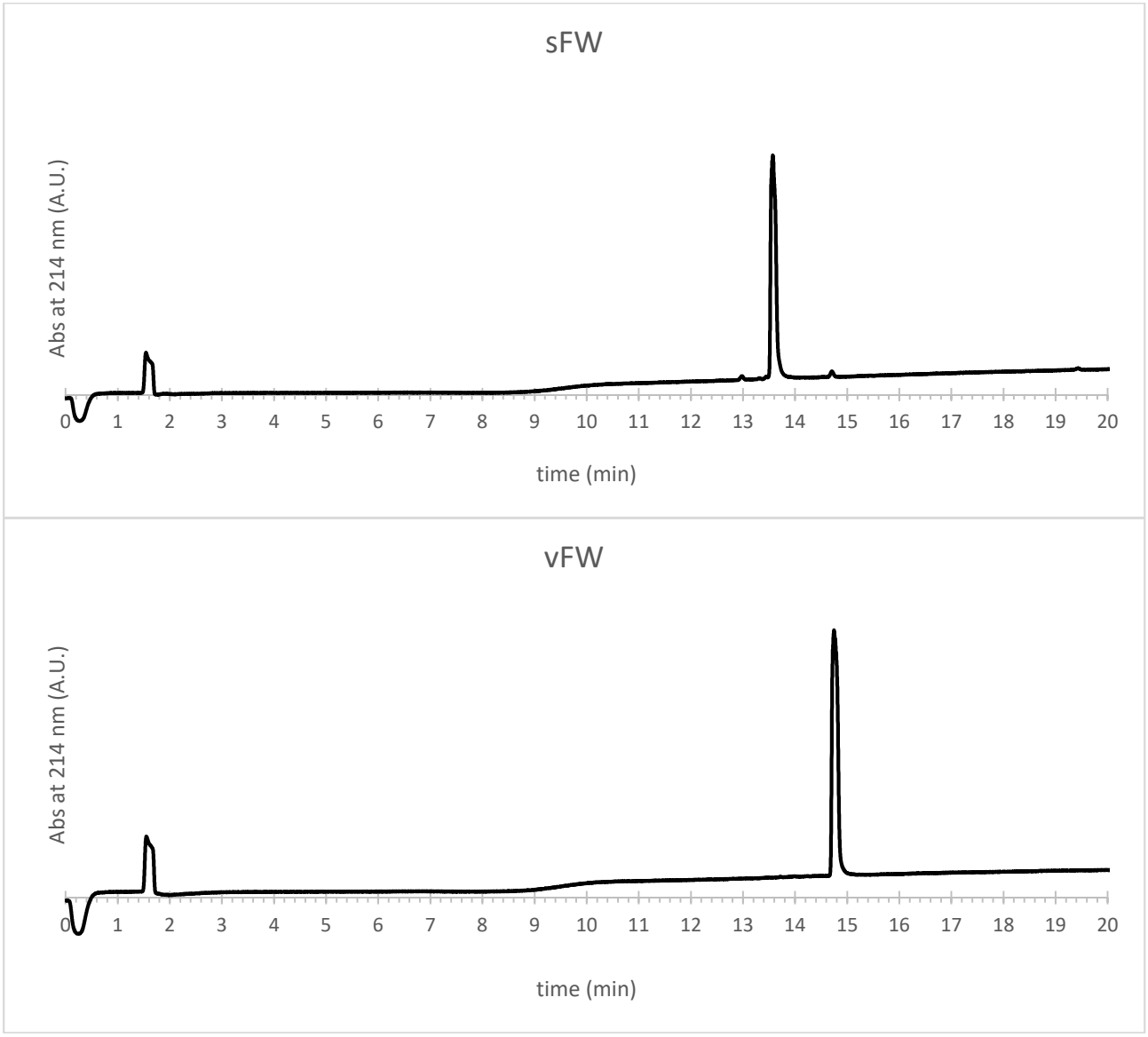
sFW
Abs at 214 nm (A.U.)
0 1 2 3 4 5 6 7 8 9 10 11 12 13 14 15 16 17 18 19 20
time (min)
vFW
Abs at 214 nm (A.U.)
0 1 2 3 4 5 6 7 8 9 10 11 12 13 14 15 16 17 18 19 20
time (min)

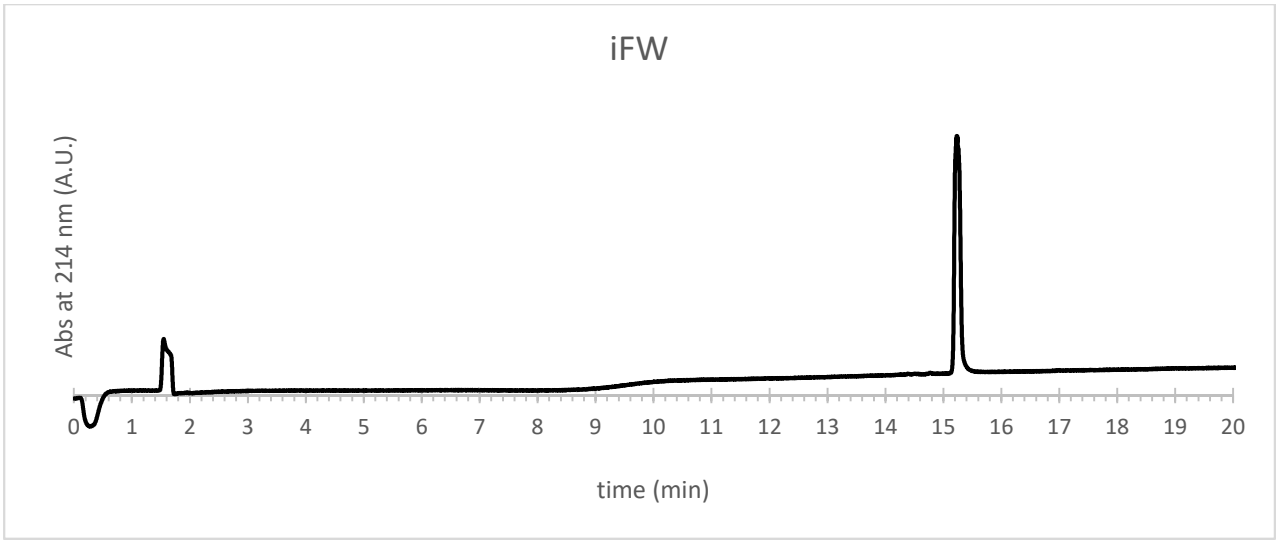
iFW
Abs at 214 nm (A.U.)
0 1 2 3 4 5 6 7 8 9 10 11 12 13 14 15 16 17 18 19 20
time (min)

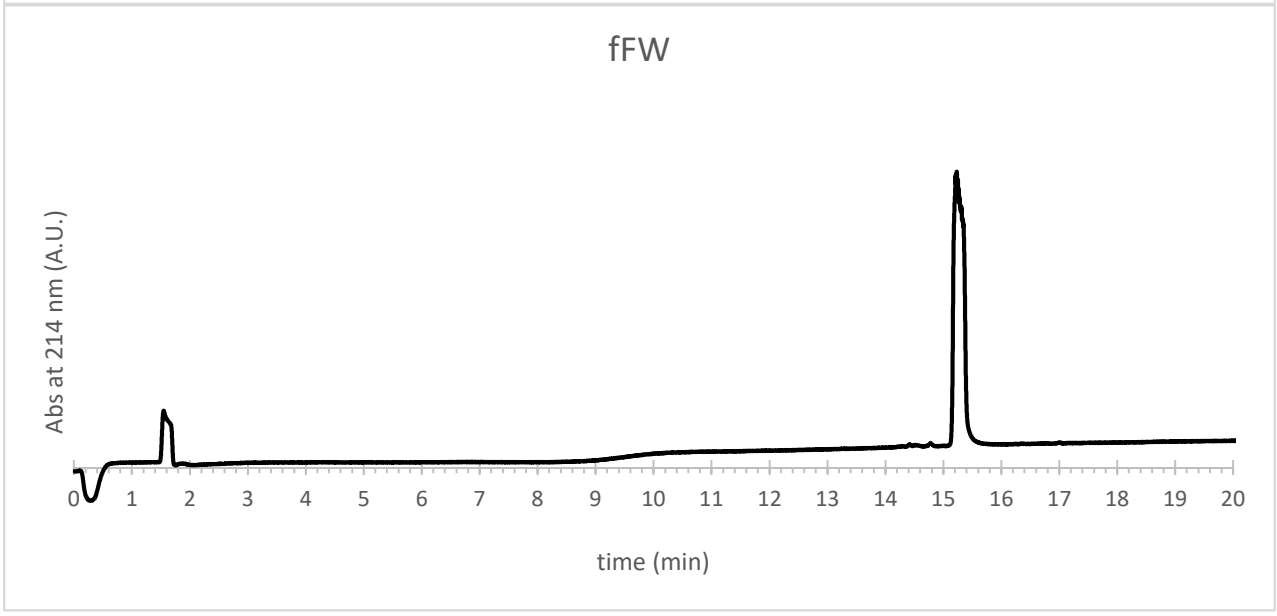
fFW
Abs at 214 nm (A.U.)
0 1 2 3 4 5 6 7 8 9 10 11 12 13 14 15 16 17 18 19 20
time (min)

3. xXX group

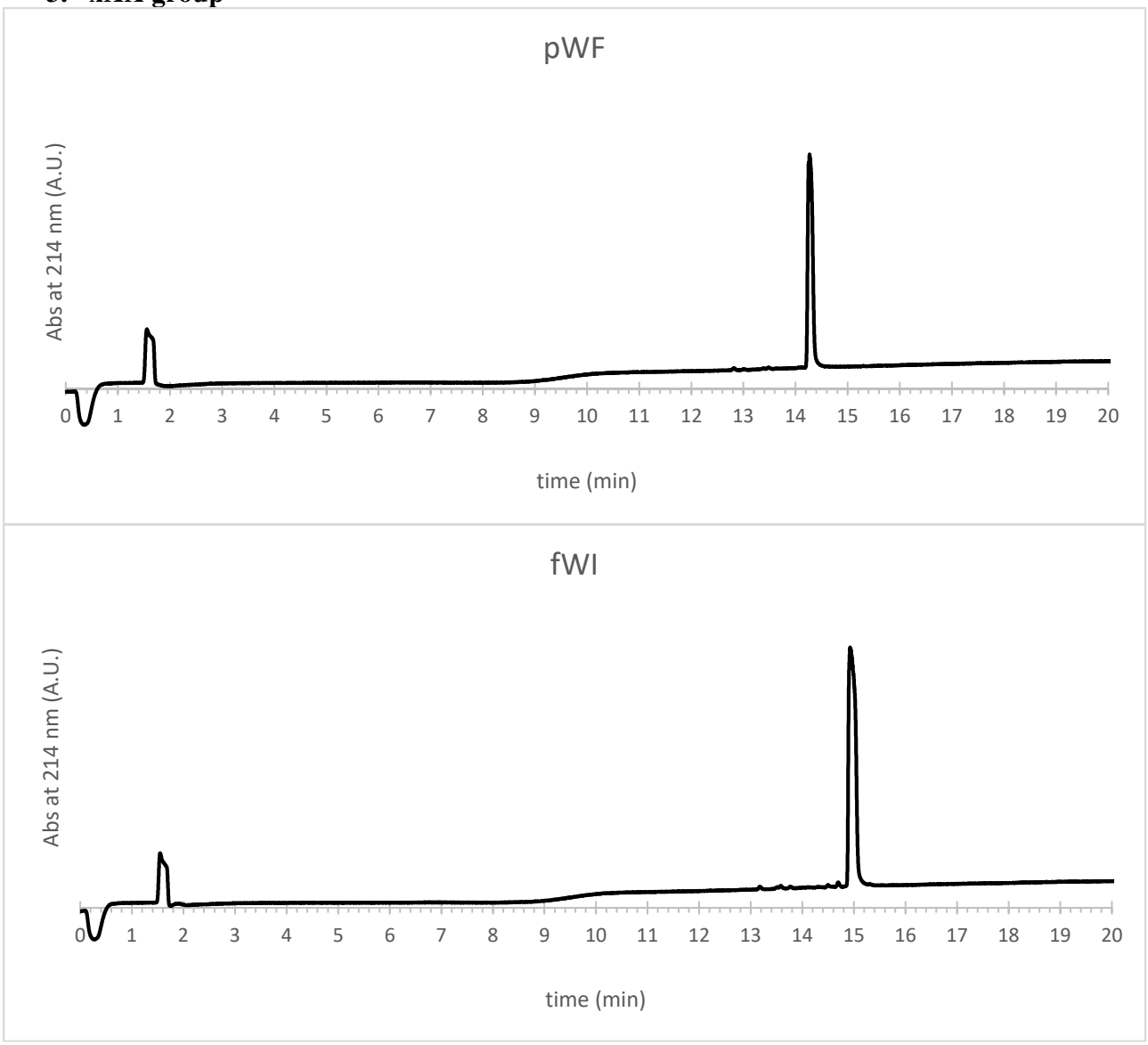
pWF
Abs at 214 nm (A.U.)
0 1 2 3 4 5 6 7 8 9 10 11 12 13 14 15 16 17 18 19 20
time (min)
fWI
Abs at 214 nm (A.U.)
0 1 2 3 4 5 6 7 8 9 10 11 12 13 14 15 16 17 18 19 20
time (min)

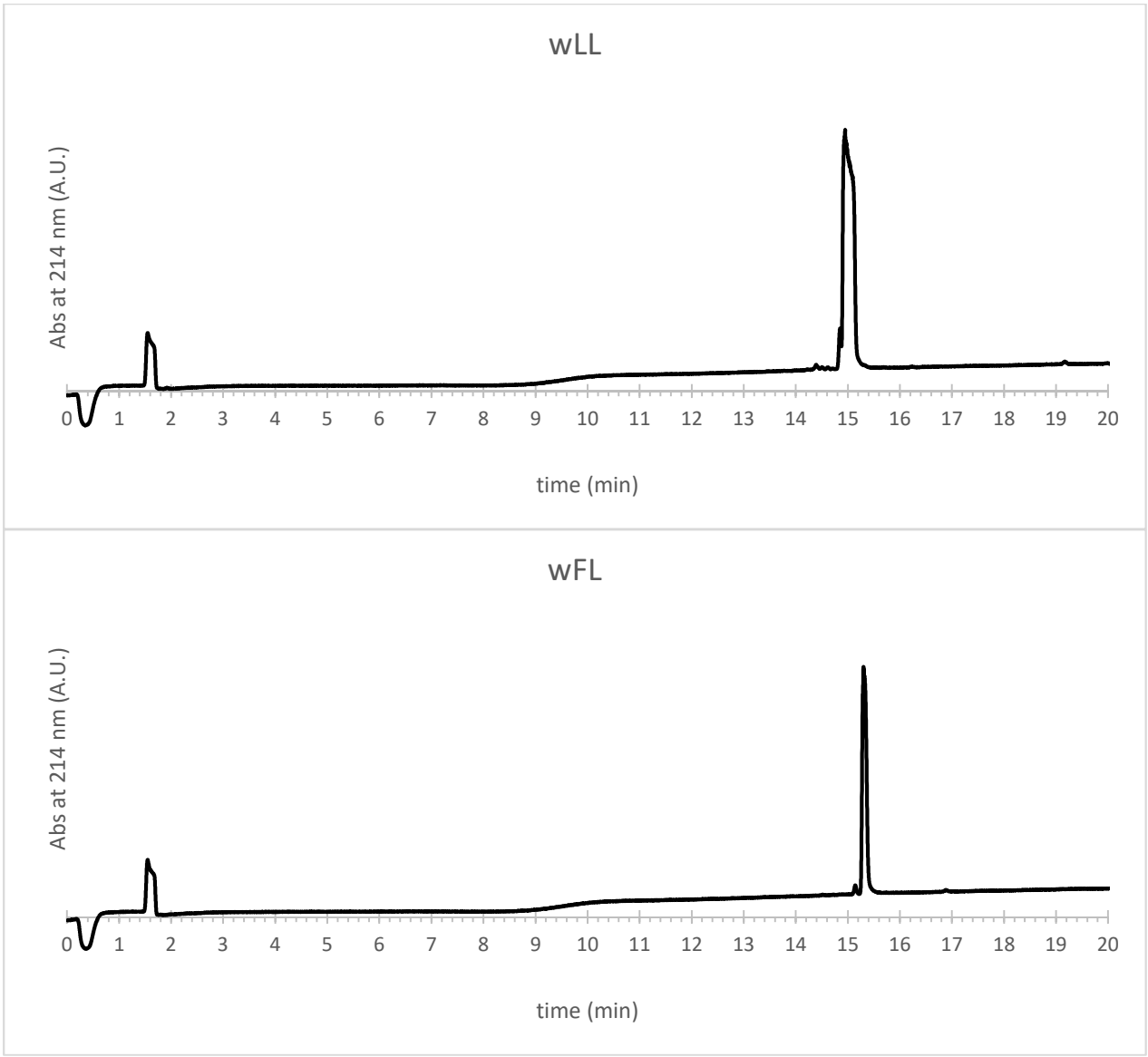
wLL
Abs at 214 nm (A.U.)
0 1 2 3 4 5 6 7 8 9 10 11 12 13 14 15 16 17 18 19 20
time (min)
wFL
Abs at 214 nm (A.U.)
0 1 2 3 4 5 6 7 8 9 10 11 12 13 14 15 16 17 18 19 20
time (min)

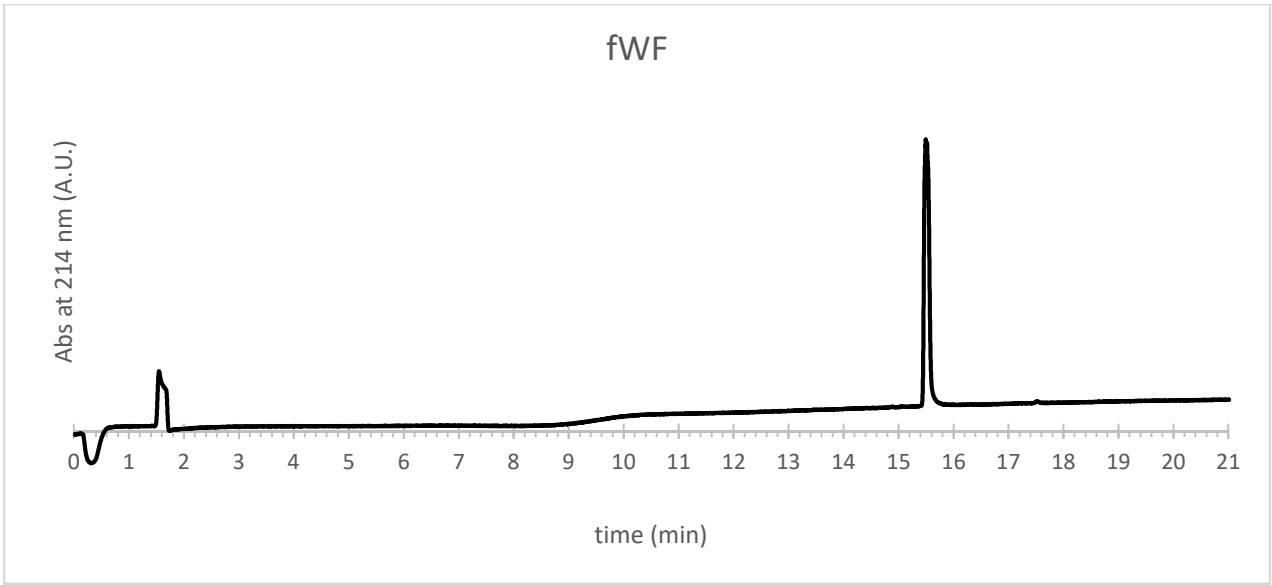
fWF
Abs at 214 nm (A.U.)
0 1 2 3 4 5 6 7 8 9 10 11 12 13 14 15 16 17 18 19 20 21
time (min)

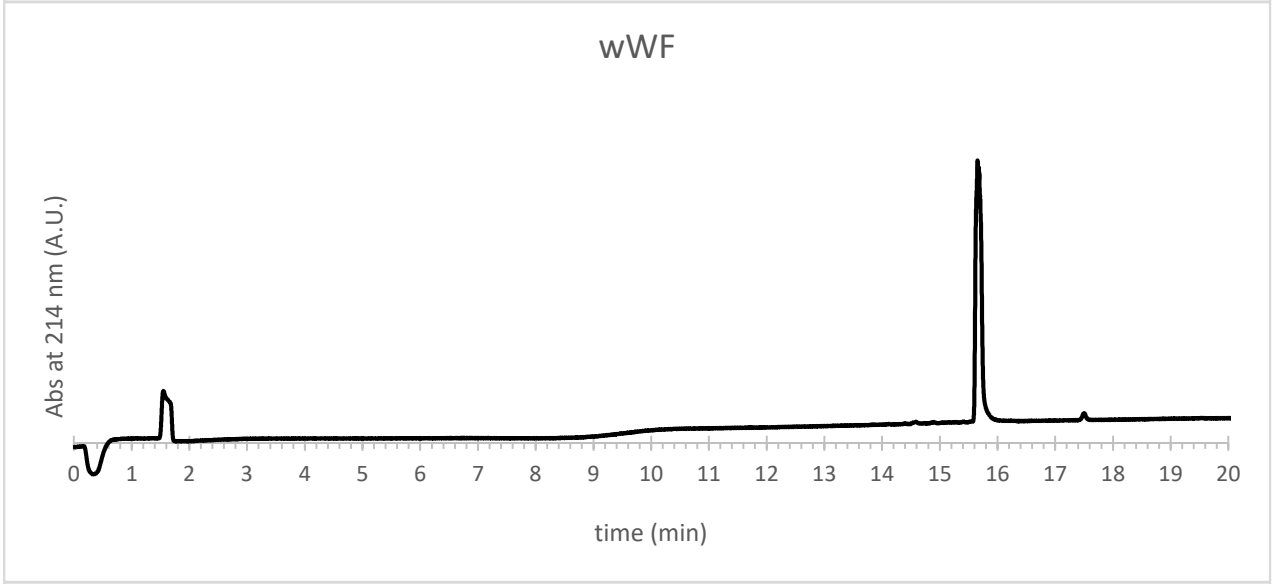
wWF
Abs at 214 nm (A.U.)
0 1 2 3 4 5 6 7 8 9 10 11 12 13 14 15 16 17 18 19 20
time (min)

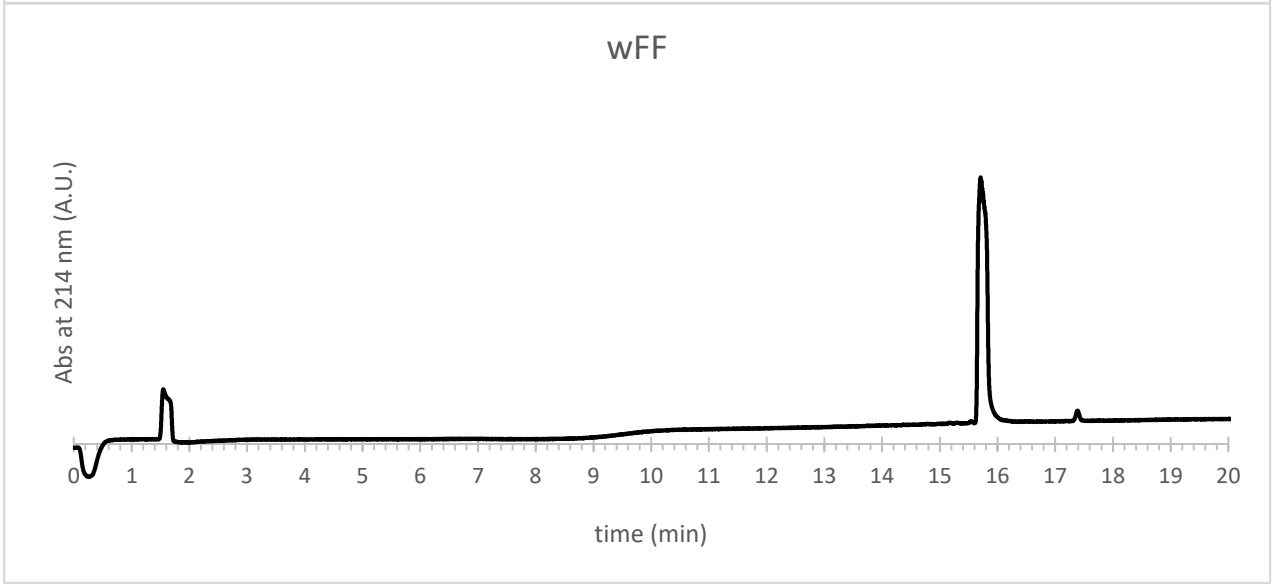
wFF
Abs at 214 nm (A.U.)
0 1 2 3 4 5 6 7 8 9 10 11 12 13 14 15 16 17 18 19 20
time (min)

Oscillator Rheometry

Time sweep analysis

Tests performed at: 1.00 Pa (pFF, fFF, iFW, fFW, fWI, wWF, wFL), 2.00 Pa (vFW, wLL), 5.00 Pa (vFF, iFF, fWF) are reported below.

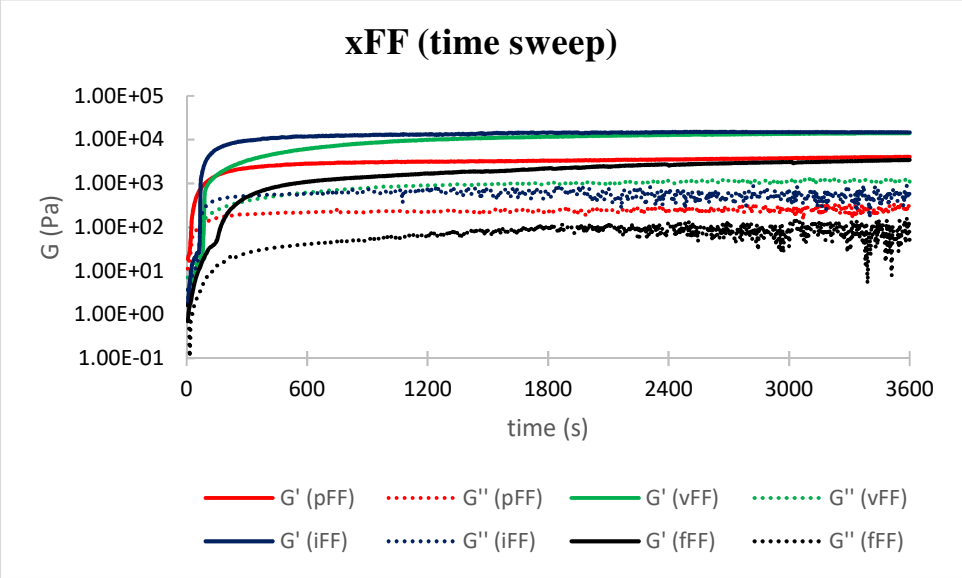

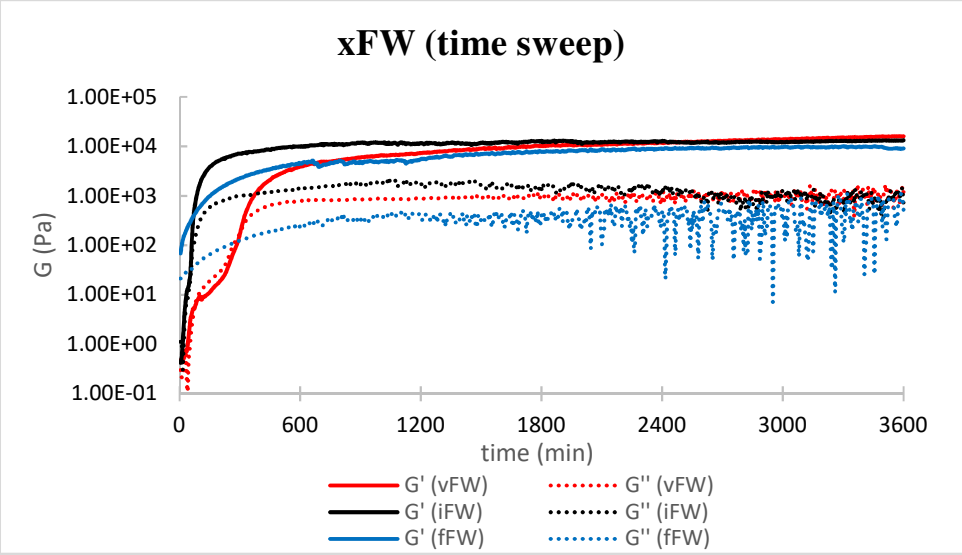

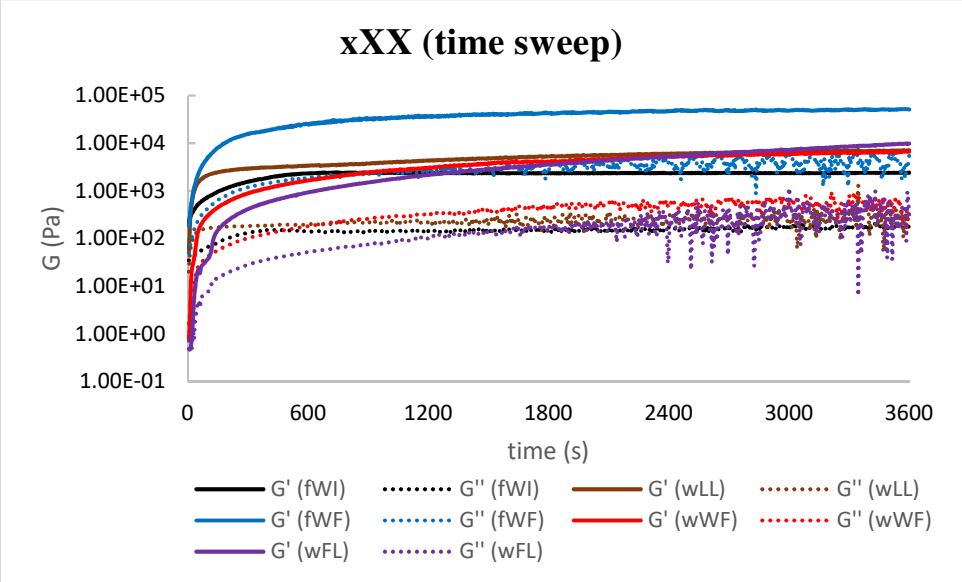

FT-IR Spectra

1. xFF group

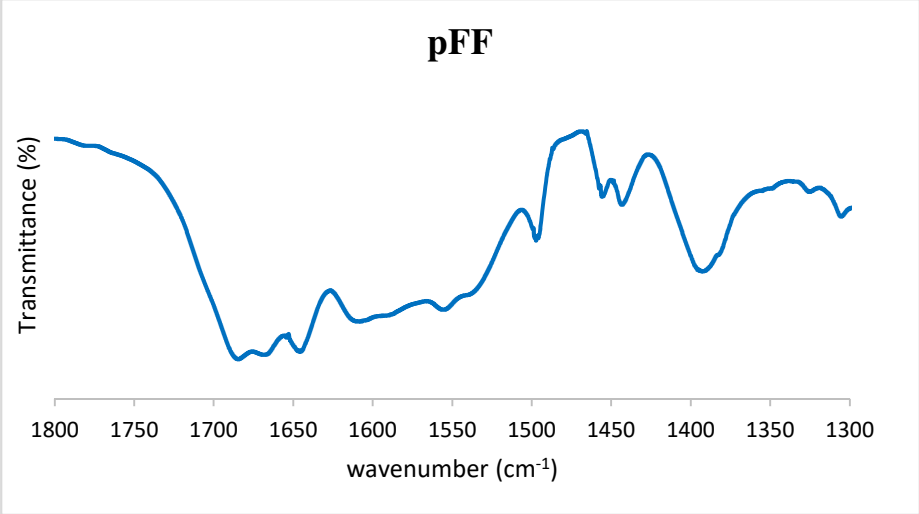

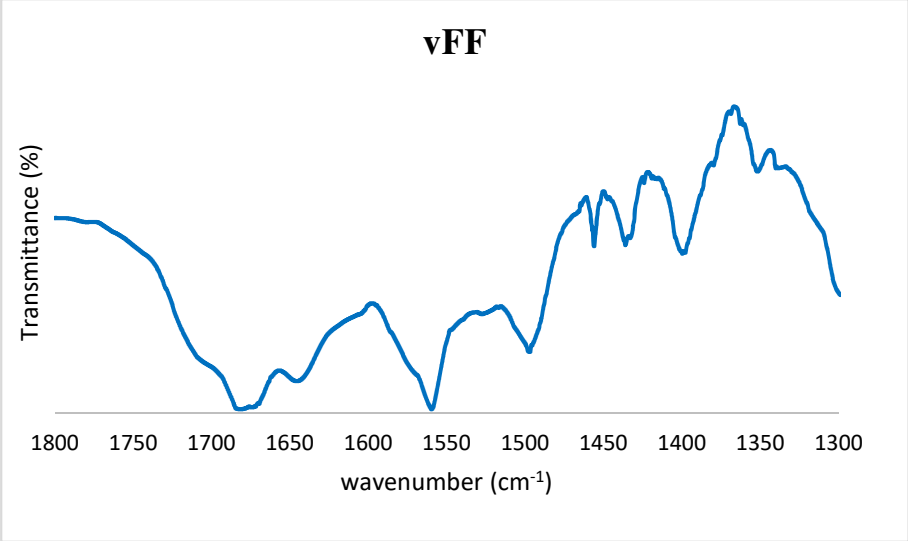
vFF
Transmittance (%)
1800 1750 1700 1650 1600 1550 1500 1450 1400 1350 1300
wavenumber (cm-1)

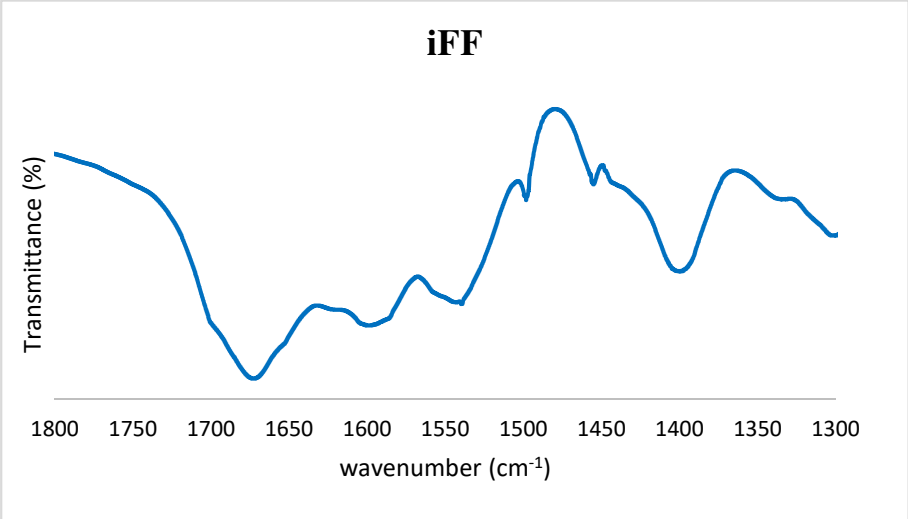
iFF
Transmittance (%)
1800 1750 1700 1650 1600 1550 1500 1450 1400 1350 1300
wavenumber (cm-1)

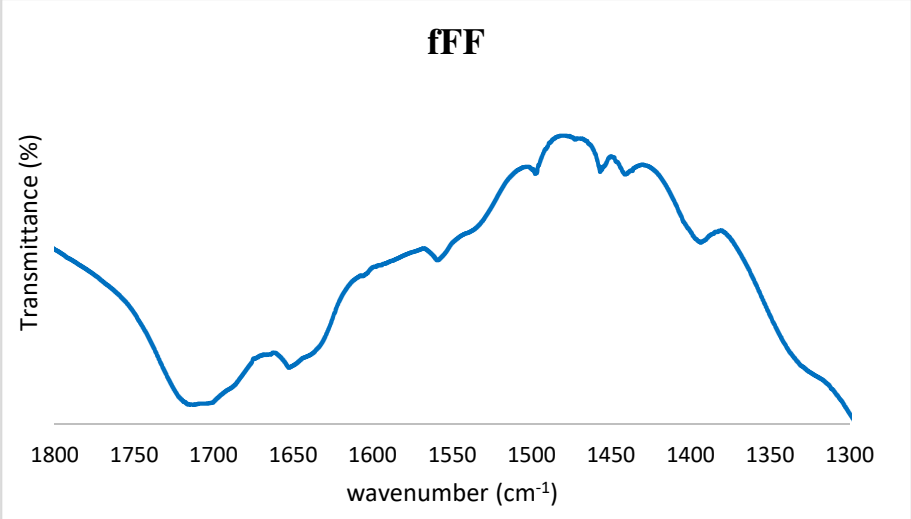
fFF
Transmittance (%)
1800 1750 1700 1650 1600 1550 1500 1450 1400 1350 1300
wavenumber (cm-1)

2. xFW group

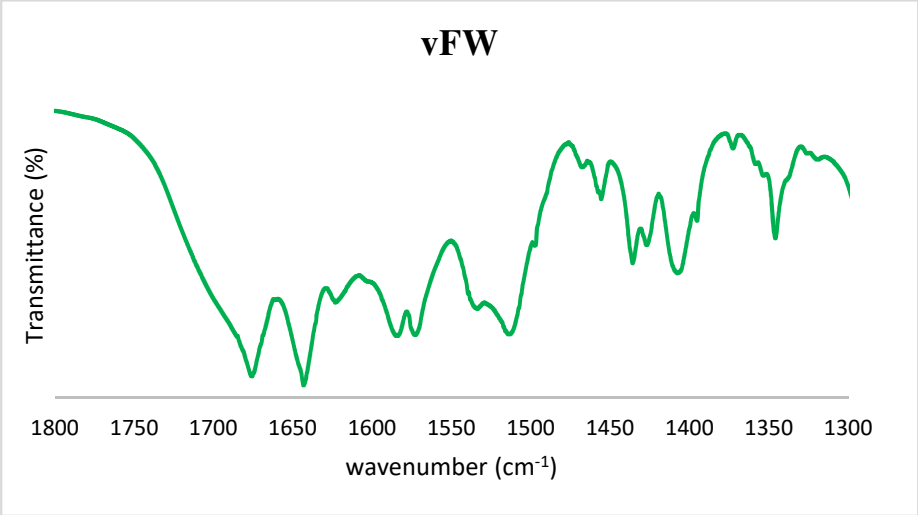
vFW
Transmittance (%)
1800 1750 1700 1650 1600 1550 1500 1450 1400 1350 1300
wavenumber (cm-1)

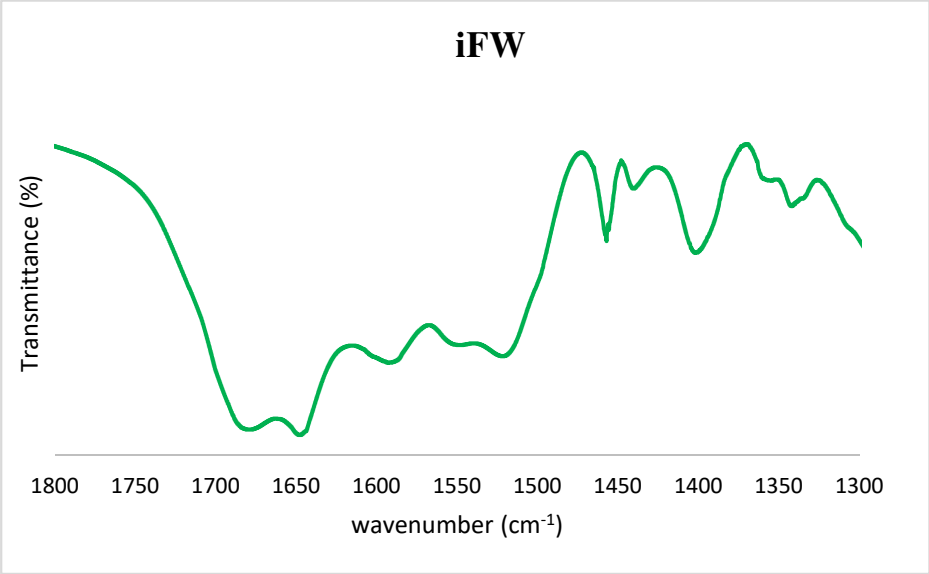
iFW
Transmittance (%)
1800 1750 1700 1650 1600 1550 1500 1450 1400 1350 1300
wavenumber (cm-1)

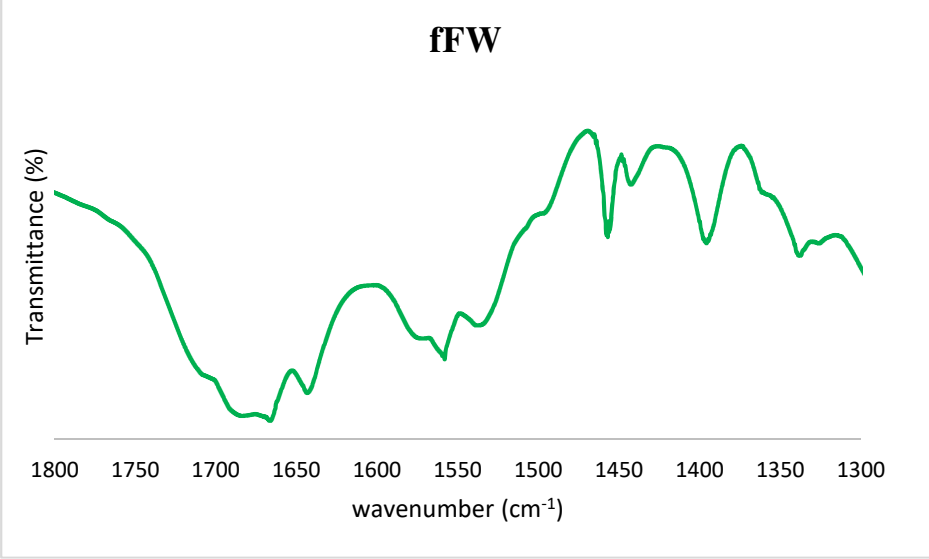
fFW
Transmittance (%)
1800 1750 1700 1650 1600 1550 1500 1450 1400 1350 1300
wavenumber (cm-1)

3. xXX group

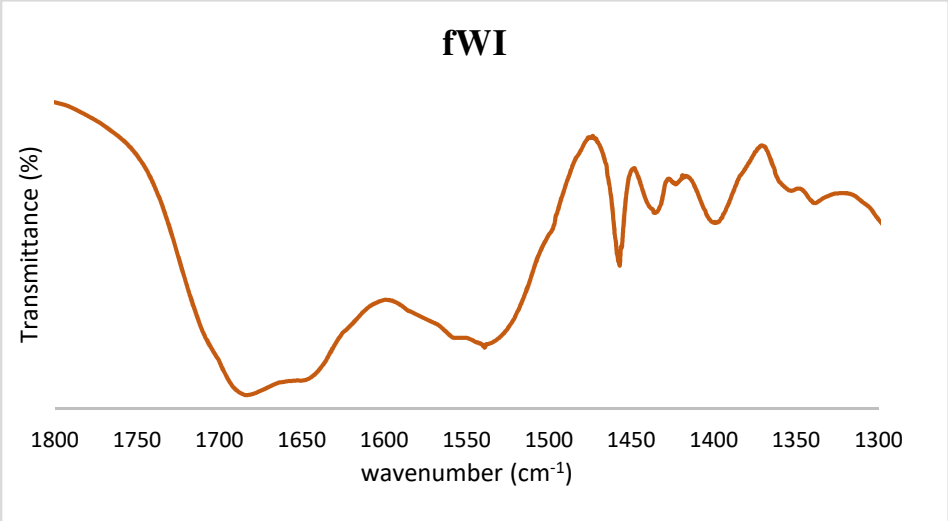
fWI
Transmittance (%)
1800 1750 1700 1650 1600 1550 1500 1450 1400 1350 1300
wavenumber (cm-1)

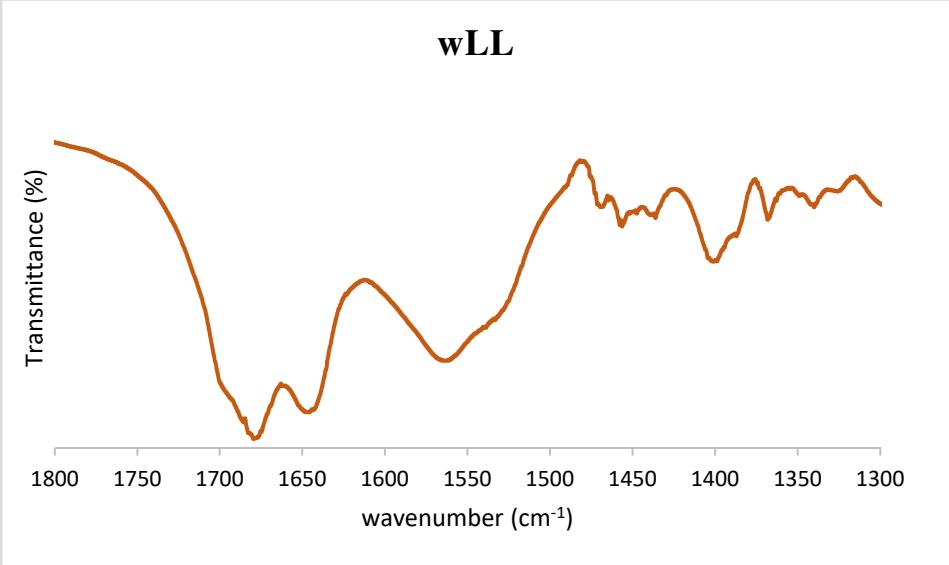
wLL
Transmittance (%)
1800 1750 1700 1650 1600 1550 1500 1450 1400 1350 1300
wavenumber (cm-1)

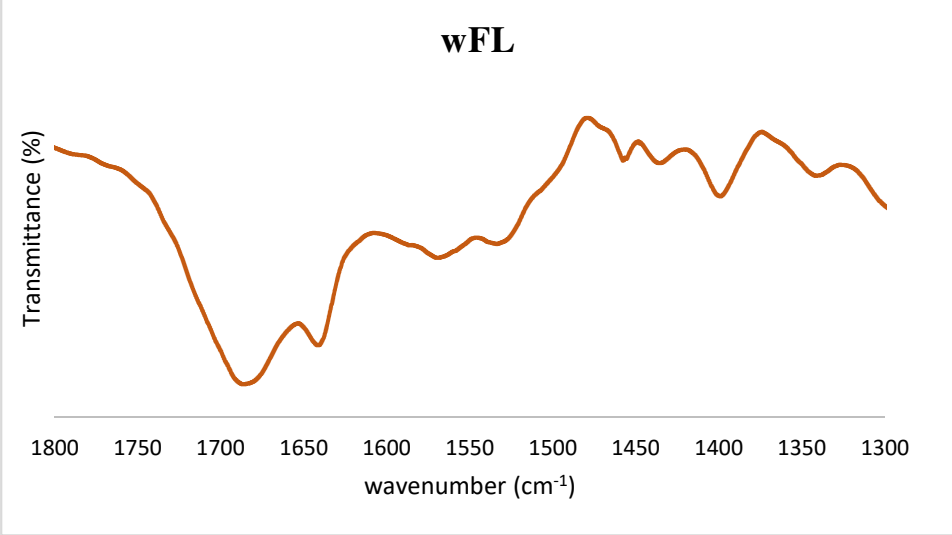
wFL
Transmittance (%)
1800 1750 1700 1650 1600 1550 1500 1450 1400 1350 1300
wavenumber (cm-1)

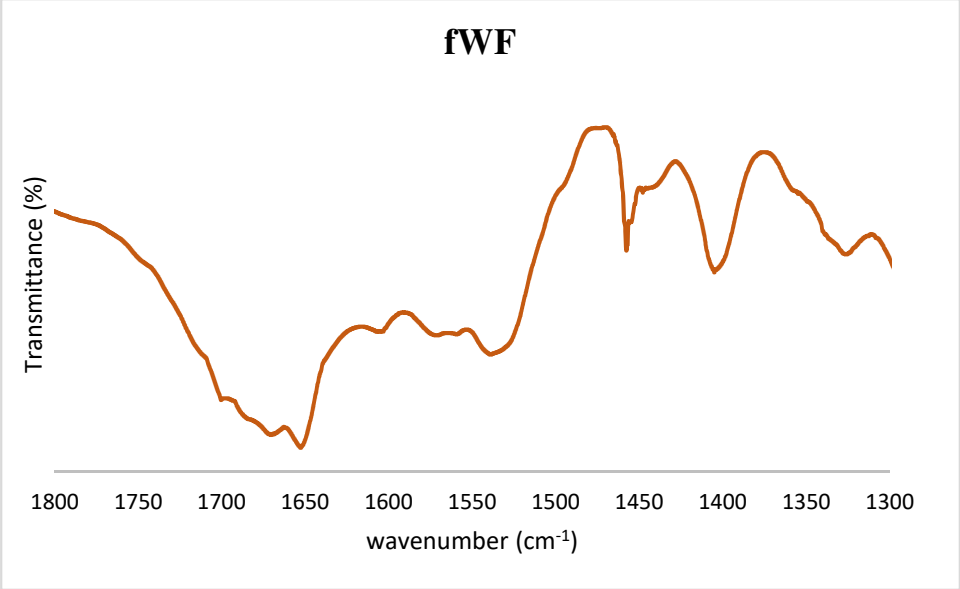
fWF
Transmittance (%)
1800
1750
1700
1650
1600
1550
1500
1450
1400
1350
1300
wavenumber (cm-1)

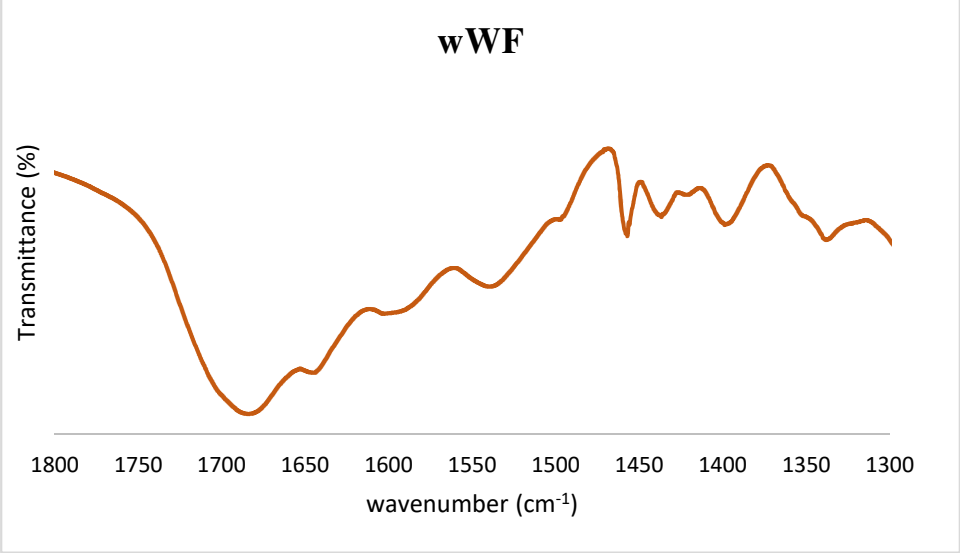
wWF
Transmittance (%)
1800
1750
1700
1650
1600
1550
1500
1450
1400
1350
1300
wavenumber (cm-1)

XRD Crystallographic data

***Table S1**: Crystallographic data for fYI in methanol:water and fYI in phosphate buffer.*

	fYI in methanol:water	fYI in phosphate buffer
Formula	$C_{24}H_{31}N_3O_5 \cdot 3H_2O$	$C_{24}H_{31}N_3O_5 \cdot 3H_2O$
Temperature (K)	100	100
Wavelength (Å)	0.7	0.7
Crystal system	Monoclinic	Monoclinic
Space group	*P 2₁*	*P 2₁*
a (Å)	5.935(1)	5.936(1)
b (Å)	15.615(3)	15.618(3)
c (Å)	26.376(5)	26.342(5)
α (°)	90	90
β (°)	93.37(3)	93.33(3)
γ (°)	90	90
V (Å^3)	2440.2(9)	2438.0(9)
Z, ρcalc (g/cm^3)	2, 1.275	2, 1.277
μ (mm^{-1})	0.058	0.093
F (000)	1004	1004
Data collection θ range	0.762 – 25.929	0.763 – 29.995
Refl. Collected / unique	16308/ 7925	14540 / 11651
Rint	0.026	0.084
Completeness (%)	95.5	98.1
Data/Restraints/Parameters	7925 / 1 / 612	11651 / 1 / 612
GooF	1.109	1.055
R1, wR2 [I>2σ(I)]	0.0789 / 0.2336	0.1043 / 0.2996
R1, wR2 all data	0.0807 / 0.2346	0.1267 / 0.3170
CCDC code		

***Table S2**: Crystallographic data for Vff, Iff and fFF.*

	Vff	Iff	fFF
Formula	$C_{23}H_{29}N_3O_4 \cdot CH_4O$	$3C_{24}H_{31}N_3O_4 \cdot CH_4O \cdot 6H_2O$	$C_{27}H_{29}O_4N_3 \cdot C_3H_8O \cdot 2H_2O$
Temperature (K)	100	100	100
Wavelength (Å)	0.7	0.7	0.7
Crystal system	Orthorhombic	Triclinic	Monoclinic
Space group	*P 2₁ 2₁ 2₁*	*P 1*	*P 2₁*
a (Å)	5.290(1)	5.820(1)	12.308(3)
b (Å)	14.870(3)	18.780(4)	5.946(1)
c (Å)	30.010(6)	19.030(4)	19.728(4)
α (°)	90	117.10(3)	90
β (°)	90	91.60(3)	100.08(3)
γ (°)	90	90.57(3)	90
V (Å^3)	2360.7(8)	1850.3(8)	1421.5(5)
Z, ρcalc (g/cm^3)	4, 1.248	1, 1.257	2, 1.298
μ (mm^{-1})	0.079	0.103	0.072
F (000)	948	764	596
Data collection θ range	1.337 - 28.625	1.185 – 28.646	1.032 - 28.214
Refl. Collected / unique	20757 / 6172	32837 / 18022	17943 / 5980
Rint	0.039	0.035	0.069
Completeness (%)	98.3	94.6	96.7
Data/Restraints/Parameters	6172 / 7 / 293	18022 / 99 / 999	5980 / 7 / 381
GooF	1.031	1.08	1.044
R1, wR2 [I>2σ(I)]	0.0777 / 0.2188	0.0454 / 0.1116	0.0589 / 0.1629
R1, wR2 all data	0.0822 / 0.2259	0.0535 / 0.1169	0.0765 / 0.1772
CCDC code	-	-	-

***Table S3**: Crystallographic data for VFF, IFF and FFF.*

	VFF	IFF	FFF
Formula	$C_{23}H_{29}N_3O_4 \cdot 2CH_4O$	$C_{24}H_{31}N_3O_4 \cdot 2CH_4O$	$C_{27}H_{29}N_3O_4 \cdot 2CH_4O$
Temperature (K)	100	100	100
Wavelength (Å)	0.7	0.7	0.7
Crystal system	Monoclinic	Monoclinic	Monoclinic
Space group	*C 2*	*C 2*	*C 2*
a (Å)	23.980(5)	23.950(5)	24.247(5)
b (Å)	4.910(1)	4.983(1)	4.954(1)
c (Å)	23.210(5)	24.278(5)	23.805(5)
α (°)	90	90	90
β (°)	111.56(3)	113.32(3)	104.60(3)
γ (°)	90	90	90
V (Å^3)	2541(1)	2661(1)	2767(1)
Z, ρcalc (g/cm^3)	4, 1.243	4, 1.222	4, 1.257
μ (mm^{-1})	0.056	0.07	0.072
F (000)	1024	912	1120
Data collection θ range	0.929 - 28.301	0.899–28.312	1.712 - 22.706
Refl. Collected / unique	10546 / 6109	10901 / 6128	4163 / 3188
Rint	0.056	0.035	0.048
Completeness (%)	97.9	96.1	87.7
Data/Restraints/Parameters	6109 / 1 / 315	6128 / 1 / 323	3188 / 1 / 349
GooF	1.013	1.038	0.955
R1, wR2 [I>2σ(I)]	0.0611 / 0.1767	0.0493 / 0.127	0.0538 / 0.1237
R1, wR2 all data	0.0897 / 0.1558	0.059 / 0.1342	0.0883 / 0.1429
CCDC code	-	-	-

***Table S4**: Crystallographic data for iFW, vFW.*

	iFW	vFW
Formula	$C_{26}H_{32}N_4O_4 \cdot 3H_2O$ [+disordered solvent]	$C_{25}H_{30}N_4O_4 \cdot 3H_2O$ [+disordered solvent]
Temperature (K)	100	100
Wavelength (Å)	0.7	0.7
Crystal system	Hexagonal	Hexagonal
Space group	*P 6$_5$*	*P 6$_5$*
a (Å)	31.620(5)	31.639(5)
b (Å)	31.620(5)	31.639(5)
c (Å)	5.680(1)	5.611(1)
α (°)	90	90
β (°)	90	90
γ (°)	120	120
V (Å^3)	4918(2)	4864(2)
Z, ρcalc (g/cm^3)	6, 1.051	6, 1.034
μ (mm^{-1})	0.076	0.076
F (000)	1668	1620
Data collection θ range	1.47 – 28.62	1.268 – 28.279
Refl. Collected / unique	20194 / 6502	41430 / 7955
Rint	0.121	0.073
Completeness (%)	94.7	97.2
Data/Restraints/Parameters	6502 / 49 / 362	7955 / 49 / 353
GooF	0.974	0.999
R1, wR2 [I>2σ(I)]	0.0646 / 0.161	0.0434 / 0.107
R1, wR2 all data	0.0789 / 0.176	0.067 / 0.1219
CCDC code	-	-

***Table S5**: Crystallographic data for pWF and wFF.*

	pWF	wFF
Formula	$C_{25}H_{28}N_4O_4$	$C_{29}H_{30}N_4O_4 \cdot H_2O$
Temperature (K)	100	100
Wavelength (Å)	0.7	0.7
Crystal system	Monoclinic	Monoclinic
Space group	*P 2₁*	*P 2₁*
a (Å)	5.368(1)	13.65(1)
b (Å)	13.549(3)	5.0421(8)
c (Å)	15.290(3)	18.999(6)
α (°)	90	90
β (°)	96.12(3)	101.98(5)
γ (°)	90	90
V (Å^3)	1105.7(4)	1279(1)
Z, ρcalc (g/cm^3)	2, 1.347	2, 1.341
μ (mm^{-1})	0.089	0.084
F (000)	476	548
Data collection θ range	1.98 – 33.04	1.079 – 28.364
Refl. Collected / unique	23542 / 7546	13262 / 5962
Rint	0.015	0.069
Completeness (%)	98.9	91.9
Data/Restraints/Parameters	7546 / 1 / 298	5962 / 66 / 371
GooF	1.078	1.002
R1, wR2 [I>2σ(I)]	0.0262 / 0.0702	0.0567 / 0.1424
R1, wR2 all data	0.0266 / 0.0706	0.0802 / 0.1587
CCDC code		

References

1. Bordi, F.; Paradossi, G.; Rinaldi, C.; Ruzicka, B. Chemical and physical hydrogels: Two casesystems studied by quasi elastic light scattering. In *Physica A: Statistical Mechanics and its Applications*; **2002**, *304*, 119–128.
2. Caló, E.; Khutoryanskiy, V. V. Biomedical applications of hydrogels: A review of patents and commercial products. *Eur. Polym. J.* **2015**, *65*, 252–267.
3. Liang, G.; Yang, Z.; Zhang, R.; Li, L.; Fan, Y.; Kuang, Y.; Gao, Y.; Wang, T.; Lu, W. W.; Xu, B. Supramolecular hydrogel of a D-amino acid dipeptide for controlled drug release in vivo. *Langmuir* **2009**, *25*, 8419–8422.
4. Du, X.; Zhou, J.; Shi, J.; Xu, B. Supramolecular Hydrogelators and Hydrogels: From Soft Matter to Molecular Biomaterials. *Chem. Rev.* **2015**, *115*, 13165–13307.
5. Jin, Q.; Zhang, L.; Cao, H.; Wang, T.; Zhu, X.; Jiang, J.; Liu, M. Self-assembly of copper(II) ion-mediated nanotube and its supramolecular chiral catalytic behavior. *Langmuir* **2011**, *27*, 13847–13853.
6. Draper, E. R.; Adams, D. J. Low-Molecular-Weight Gels: The State of the Art. *Chem* **2017**, *3*, 390–410.
7. Frederix, P. W. J. M.; Scott, G. G.; Abul-Haija, Y. M.; Kalafatovic, D.; Pappas, C. G.; Javid, N.; Hunt, N. T.; Ulijn, R. V.; Tuttle, T. Exploring the sequence space for (tri-) peptide self-assembly to design and discover new hydrogels. *Nat. Chem.* **2015**, *7*, 30-37.
8. Hovmöller, S.; Zhou, T.; Ohlson, T. Conformations of amino acids in proteins. *Acta Crystallogr. Sect. D Biol. Crystallogr.* **2002**, *58*, 768–776.
9. Pelley, J. W. Protein Structure and Function. *Elsevier's Integr. Biochem.* **2007**, 19-28.
10. Fletcher, J. M.; Harniman, R. L.; Barnes, F. R. H.; Boyle, A. L.; Collins, A.; Mantell, J.; Sharp, T. H.; Antognozzi, M.; Booth, P. J.; Linden, N.; Miles, M. J.; Sessions, R. B.; Verkade, P.; Woolfson, D. N. Self-assembling cages from coiled-coil peptide modules. *Science (80-.).* **2013**, *340*, 595–599.
11. Gradišar, H.; Božič, S.; Doles, T.; Vengust, D.; Hafner-Bratkovič, I.; Mertelj, A.; Webb, B.; Šali, A.; Klavžar, S.; Jerala, R. Design of a single-chain polypeptide tetrahedron assembled from coiled-coil segments. *Nat. Chem. Biol.* **2013**, *9*, 362–366.
12. Mondal, S.; Adler-Abramovich, L.; Lampel, A.; Bram, Y.; Lipstman, S.; Gazit, E. Formation of functional super-helical assemblies by constrained single heptad repeat. *Nat. Commun.* **2015**, *6*, 8615.

13. Ljubetič, A.; Lapenta, F.; Gradišar, H.; Drobnak, I.; Aupič, J.; Strmšek, Ž.; Lainšček, D.; Hafner-Bratkovič, I.; Majerle, A.; Krivec, N.; Benčina, M.; Pisanski, T.; Veličković, T. Ć.; Round, A.; Carazo, J. M.; Melero, R.; Jerala, R. Design of coiled-coil protein-origami cages that self-assemble in vitro and in vivo. *Nat. Biotechnol.* **2017**, *35*, 1094–1101.
14. Noguchi, H.; Mylemans, B.; De Zitter, E.; Van Meervelt, L.; Tame, J. R. H.; Voet, A. Design of tryptophan-containing mutants of the symmetrical Pizza protein for biophysical studies. *Biochem. Biophys. Res. Commun.* **2018**, *497*, 1038–1042.
15. Voet, A. R. D.; Noguchi, H.; Addy, C.; Simoncini, D.; Terada, D.; Unzai, S.; Park, S.-Y.; Zhang, K. Y. J.; Tame, J. R. H. Computational design of a self-assembling symmetrical β-propeller protein. *Proc. Natl. Acad. Sci.* **2014**, *111*, 15102–15107.
16. Ulijn, R. V.; Smith, A. M. Designing peptide based nanomaterials. *Chem. Soc. Rev.* **2008**, *37*, 664–675.
17. Hartgerink, J. D. Covalent capture: A natural complement to self-assembly. *Curr. Opin. Chem. Biol.* **2004**, *8*, 604–609.
18. Fichman, G.; Gazit, E. Self-assembly of short peptides to form hydrogels: Design of building blocks, physical properties and technological applications. *Acta Biomater.* **2014**, *10*, 1671–1682.
19. Hunter, C. A.; Sanders, J. K. M. Nature of pi-pi-Interactions. *J. Am. Chem. Soc.* **1990**, *112*, 5525–5534.
20. Bertolani, A.; Pirrie, L.; Stefan, L.; Houbenov, N.; Haataja, J. S.; Catalano, L.; Terraneo, G.; Giancane, G.; Valli, L.; Milani, R.; Ikkala, O.; Resnati, G.; Metrangolo, P. Supramolecular amplification of amyloid self-assembly by iodination. *Nat. Commun.* **2015**, *6*, 7574.
21. Zhang, S. Emerging biological materials through molecular self-assembly. *Biotechnol. Adv.* **2002**, *20*, 321–339.
22. Zhang, S.; Altman, M. Peptide self-assembly in functional polymer science and engineering. *React. Funct. Polym.* **1999**, *41*, 91–102.
23. Zhang, S.; Rich, A. Direct conversion of an oligopeptide from a b-sheet to an a-helix: a model for amyloid formation. *Proc Natl Acad Sci USA* **1997**, *94*, 23–28.
24. Smith, A. M.; Banwell, E. F.; Edwards, W. R.; Pandya, M. J.; Woolfson, D. N. Engineering increased stability into self-assembled protein fibers. *Adv. Funct. Mater.* **2006**, *16*, 1022–1030.
25. Aggeli, A.; Nyrkova, I. A.; Bell, M.; Harding, R.; Carrick, L.; McLeish, T. C. B.;

Semenov, A. N.; Boden, N. Hierarchical self-assembly of chiral rod-like molecules as a model for peptide -sheet tapes, ribbons, fibrils, and fibers. *Proc. Natl. Acad. Sci.* **2001**, *98*, 11857–11862.

26. Schneider, J. P.; Pochan, D. J.; Ozbas, B.; Rajagopal, K.; Pakstis, L.; Kretsinger, J. Responsive hydrogels from the intramolecular folding and self-assembly of a designed peptide. *J. Am. Chem. Soc.* **2002**, *124*, 15030–15037.
27. Larsen, T. H.; Branco, M. C.; Rajagopal, K.; Schneider, J. P.; Furst, E. M. Sequence-dependent gelation kinetics of β-hairpin peptide hydrogels. *Macromolecules* **2009**, *42*, 8443–8450.
28. Stendahl, J. C.; Rao, M. S.; Guler, M. O.; Stupp, S. I. Intermolecular forces in the self-assembly of peptide amphiphile nanofibers. *Adv. Funct. Mater.* **2006**, *16*, 499–508.
29. Santoso, S.; Hwang, W.; Hartman, H.; Zhang, S. Self-assembly of Surfactant-like Peptides with Variable Glycine Tails to Form Nanotubes and Nanovesicles. *Nano Lett.* **2002**, *2*, 687–691.
30. Reches, M.; Gazit, E. Casting metal nanowires within discrete self-assembled peptide nanotubes. *Science (80-.).* **2003**, *300*, 625–627.
31. Tang, C.; Smith, A. M.; Collins, R. F.; Ulijn, R. V.; Saiani, A. Fmoc-Diphenylalanine Self-ASsembly Mechanism Induces Apparent pKaShifts. *Langmuir* **2009**, *25*, 9447–9453.
32. Smith, A. M.; Williams, R. J.; Tang, C.; Coppo, P.; Collins, R. F.; Turner, M. L.; Saiani, A.; Ulijn, R. V. Fmoc-diphenylalanine self assembles to a hydrogel via a novel architecture based on π-π interlocked β-sheets. *Adv. Mater.* **2008**, *20*, 37–41.
33. Reches, M.; Gazit, E. Formation of closed-cage nanostructures by self-assembly of aromatic dipeptides. *Nano Lett.* **2004**, *4*, 581–585.
34. Jayawarna, V.; Smith, A.; Gough, J. E.; Ulijn, R. V Three-dimensional cell culture of chondrocytes on modified di-phenylalanine scaffolds. *Biochem. Soc. Trans.* **2007**, *35*, 535–7.
35. Toledano, S.; Williams, R. J.; Jayawarna, V.; Ulijn, R. V. Enzyme-triggered self-assembly of peptide hydrogels via reversed hydrolysis. *J. Am. Chem. Soc.* **2006**, *128*, 1070–1071.
36. Jayawarna, V.; Richardson, S. M.; Hirst, A. R.; Hodson, N. W.; Saiani, A.; Gough, J. E.; Ulijn, R. V. Introducing chemical functionality in Fmoc-peptide gels for cell culture. *Acta Biomater.* **2009**, *5*, 934–943.
37. Sutton, S.; Campbell, N. L.; Cooper, A. I.; Kirkland, M.; Frith, W. J.; Adams, D. J.

Controlled release from modified amino acid hydrogels governed by molecular size or network dynamics. *Langmuir* **2009**, *25*, 10285–10291.

38. Hong, Y.; Legge, R. L.; Zhang, S.; Chen, P. Effect of amino acid sequence and pH on nanofiber formation of self-assembling peptides EAK16-II and EAK16-IV. *Biomacromolecules* **2003**, *4*, 1433–1442.
39. Lopez de la Paz, M.; Goldie, K.; Zurdo, J.; Lacroix, E.; Dobson, C. M.; Hoenger, A.; Serrano, L. De novo designed peptide-based amyloid fibrils. *Proc. Natl. Acad. Sci.* **2002**, *99*, 16052–16057.
40. Fung, S. Y.; Keyes, C.; Duhamel, J.; Chen, P. Concentration effect on the aggregation of a self-assembling oligopeptide. *Biophys. J.* **2003**, *85*, 537–548.
41. Aggeli, A.; Bell, M.; Carrick, L. M.; Fishwick, C. W. G.; Harding, R.; Mawer, P. J.; Radford, S. E.; Strong, A. E.; Boden, N. pH as a trigger of peptide β-sheet self-assembly and reversible switching between nematic and isotropic phases. *J. Am. Chem. Soc.* **2003**, *125*, 9619–9628.
42. Derjaguin, B.; Landau, L. Theory of the stability of strongly charged lyophobic sols and of the adhesion of strongly charged particles in solutions of electrolytes. *Prog. Surf. Sci.* **1993**, *43*, 30–59.
43. Verwey, E. J. W.; Overbeek, J. T. G. Theory of the stability of lyophobic colloids. *J. Colloid Sci.* **1955**, *10*, 224–225.
44. Hong, Y.; Lau, L. S.; Legge, R. L.; Chen, P. Critical self-assembly concentration of an ionic-complementary peptide EAK16-I. *J. Adhes.* **2004**, *80*, 913–931
45. Zhang, S.; Holmes, T.; Lockshin, C.; Rich, A. Spontaneous assembly of a self-complementary oligopeptide to form a stable macroscopic membrane. *Proc. Natl. Acad. Sci.* **1993**, *90*, 3334–3338.
46. Carrick, L. M.; Aggeli, A.; Boden, N.; Fisher, J.; Ingham, E.; Waigh, T. A. Effect of ionic strength on the self-assembly, morphology and gelation of pH responsive β-sheet tape-forming peptides. *Tetrahedron* **2007**, *63*, 7457–7467.
47. Guilbaud, J. B.; Vey, E.; Boothroyd, S.; Smith, A. M.; Ulijn, R. V.; Saiani, A.; Miller, A. F. Enzymatic catalyzed synthesis and triggered gelation of ionic peptides. *Langmuir* **2010**, *26*, 11297–11303.
48. Laromaine, A.; Koh, L.; Murugesan, M.; Ulijn, R. V.; Stevens, M. M. Protease-triggered dispersion of nanoparticle assemblies. *J. Am. Chem. Soc.* **2007**, *129*, 4156–4157.
49. Langer, R.; Vacanti, J. P. Tissue engineering. *Science (80-.).* **1993**, *260*, 920–926.
50. Cui, H.; Webber, M. J.; Stupp, S. I. Self-assembly of peptide amphiphiles: from

molecules to nanostructures to biomaterials. *Biopolymers* **2010**, *94*, 1–18.

51. Matson, J. B.; Zha, R. H.; Stupp, S. I. Peptide self-assembly for crafting functional biological materials. *Curr. Opin. Solid State Mater. Sci.* **2011**, *15*, 225–235.
52. Griffith, L. G. Polymeric biomaterials. *Acta Mater.* **2000**, *48*, 263–277.
53. Ellis-Behnke, R. G.; Liang, Y.-X.; You, S.-W.; Tay, D. K. C.; Zhang, S.; So, K.-F.; Schneider, G. E. Nano neuro knitting: Peptide nanofiber scaffold for brain repair and axon regeneration with functional return of vision. *Proc. Natl. Acad. Sci.* **2006**, *103*, 5054–5059.
54. Narmoneva, D. A.; Oni, O.; Sieminski, A. L.; Zhang, S.; Gertler, J. P.; Kamm, R. D.; Lee, R. T. Self-assembling short oligopeptides and the promotion of angiogenesis. *Biomaterials* **2005**, *26*, 4837–4846.
55. Zhang, S.; Holmes, T. C.; DiPersio, C. M.; Hynes, R. O.; Su, X.; Rich, A. Self-complementary oligopeptide matrices support mammalian cell attachment. *Biomaterials* **1995**, *16*, 1385–1393.
56. Horii, A.; Wang, X.; Gelain, F.; Zhang, S. Biological designer self-assembling peptide nanofiber scaffolds significantly enhance osteoblast proliferation, differentiation and 3-D migration. *PLoS One* **2007**, *2*, e190.
57. Zhang, F.; Shi, G. S.; Ren, L. F.; Hu, F. Q.; Li, S. L.; Xie, Z. J. Designer self-assembling peptide scaffold stimulates pre-osteoblast attachment, spreading and proliferation. *J. Mater. Sci. Mater. Med.* **2009**, *20*, 1475–1481.
58. Humphries, M. J. The molecular basis and specificity of integrin-ligand interactions. *J. Cell Sci.* **1990**, *97 (Pt 4)*, 585–592.
59. Garcia, A. M.; Iglesias, D.; Parisi, E.; Styan, K. E.; Waddington, L. J.; Deganutti, C.; De Zorzi, R.; Grassi, M.; Melchionna, M.; Vargiu, A. V.; Marchesan, S. Chirality Effects on Peptide Self-Assembly Unraveled from Molecules to Materials. *Chem* **2018**, *4*, 8, 1862-1876.
60. Branco, M. C.; Pochan, D. J.; Wagner, N. J.; Schneider, J. P. Macromolecular diffusion and release from self-assembled β-hairpin peptide hydrogels. *Biomaterials* **2009**, *30*, 1339–1347.
61. Marchesan, S.; Qu, Y.; Waddington, L. J.; Easton, C. D.; Glattauer, V.; Lithgow, T. J.; McLean, K. M.; Forsythe, J. S.; Hartley, P. G. Self-assembly of ciprofloxacin and a tripeptide into an antimicrobial nanostructured hydrogel. *Biomaterials* **2013**, *34*, 14, 3678-3687.
62. Kurbasic, M.; Romano, C.; Garcia, A.; Kralj, S.; Marchesan, S. Assembly of a

Tripeptide and Anti-Inflammatory Drugs into Supramolecular Hydrogels for Sustained Release. *Gels* **2017**, *3*, 29.

63. Edwards-Gayle, C. J. C.; Hamley, I. W. Self-assembly of bioactive peptides, peptide conjugates, and peptide mimetic materials. *Org. Biomol. Chem.* **2017**, *15*, 5867–5876.
64. Zurcher, D. M.; Mcneil, A. J. Tools for identifying gelator scaffolds and solvents. *J. Org. Chem.* **2015**, *80*, 2473–2478.
65. Amit, M.; Yuran, S.; Gazit, E.; Reches, M.; Ashkenasy, N. Tailor-Made Functional Peptide Self-Assembling Nanostructures. *Adv. Mater.* **2018**, *30*, 1707083.
66. Zhang, Y.; Gu, H.; Yang, Z.; Xu, B. Supramolecular Hydrogels Respond to Ligand-Receptor Interaction. *J. Am. Chem. Soc.* **2003**, *125*, 13680–13681.
67. Görbitz, C. H. The structure of nanotubes formed by diphenylalanine, the core recognition motif of Alzheimer's β-amyloid polypeptide. *Chem. Commun.* **2006**, 2332–2334.
68. Jayawarna, V.; Ali, M.; Jowitt, T. A.; Miller, A. F.; Saiani, A.; Gough, J. E.; Ulijn, R. V. Nanostructured hydrogels for three-dimensional cell culture through self-assembly of fluorenylmethoxycarbonyl-dipeptides. *Adv. Mater.* **2006**, *18*, 611–614.
69. Fan, Z.; Sun, L.; Huang, Y.; Wang, Y.; Zhang, M. Bioinspired fluorescent dipeptide nanoparticles for targeted cancer cell imaging and real-time monitoring of drug release. *Nat. Nanotechnol.* **2016**, *11*, 388–394.
70. Tuttle, T. Computational Approaches to Understanding the Self-assembly of Peptide-based Nanostructures. *Isr. J. Chem.* **2015**, *55*, 724–734.
71. Iscen, A.; Schatz, G. C. Peptide amphiphile self-assembly. *EPL (Europhysics Lett.* **2017**, *119*, 38002.
72. Frederix, P. W. J. M.; Scott, G. G.; Abul-Haija, Y. M.; Kalafatovic, D.; Pappas, C. G.; Javid, N.; Hunt, N. T.; Ulijn, R. V.; Tuttle, T. Exploring the sequence space for (tri-) peptide self-assembly to design and discover new hydrogels. *Nat. Chem.* **2015**, *7*, 30–37.
73. Marchesan, S.; Waddington, L.; Easton, C. D.; Winkler, D. A.; Goodall, L.; Forsythe, J.; Hartley, P. G. Unzipping the role of chirality in nanoscale self-assembly of tripeptide hydrogels. *Nanoscale* **2012**, *4*, 6752–6760.
74. Barnes, H. A.; Hutton, J. F.; Walters, K. An Introduction to Rheology. *J. Nonnewton. Fluid Mech.* **1989**, ISBN 0444871403.
75. Goodwin, J.; Hughes, R. *Rheology for Chemists. An introduction*; **2008**, ISBN 9788578110796.

76. Naé, H. N. Introduction to rheology. In *Rheological Properties of Cosmetics and Toiletries*; **2017,** ISBN 9781351418553.
77. Wyss, H. M. Rheology of soft materials. In *Fluids, Colloids and Soft Materials: An Introduction to Soft Matter Physics*; **2018,** ISBN 9781118065624.
78. Marchesan, S.; Styan, K. E.; Easton, C. D.; Waddington, L.; Vargiu, A. V. Higher and lower supramolecular orders for the design of self-assembled heterochiral tripeptide hydrogel biomaterials. *J. Mater. Chem. B* **2015**, *3*, 8123–8132.
79. Chen, Z.; Krause, G.; Reif, B. Structure and orientation of peptide inhibitors bound to beta-amyloid fibrils. *J. Mol. Biol.* **2005**, *354*, 760–776.
80. Greenfield, N. J. Using circular dichroism spectra to estimate protein secondary structure. *Nat. Protoc.* **2007**, *1*, 2876–2890.
81. Bulheller, B. M.; Rodger, A.; Hirst, J. D. Circular and linear dichroism of proteins. *Phys. Chem. Chem. Phys.* **2007**, *9*, 2020–2035.
82. Toniolo, C. The circular dichroism of some aliphatic amino acid derivatives. A reexamination. *J. Phys. Chem.* **1970**, *74*, 1390–1392.
83. Matsuo, K.; Gekko, K. Construction of a synchrotron-radiation vacuum-ultraviolet circular-dichroism spectrophotometer and its application to the structural analysis of biomolecules. *Bull. Chem. Soc. Jpn.* **2013**, *86*, 675–689.
84. Amdursky, N.; Stevens, M. M. Circular Dichroism of Amino Acids: Following the Structural Formation of Phenylalanine. *ChemPhysChem* **2015**, *16*, 2768–2774.
85. Basu, K.; Baral, A.; Basak, S.; Dehsorkhi, A.; Nanda, J.; Bhunia, D.; Ghosh, S.; Castelletto, V.; Hamley, I. W.; Banerjee, A. Peptide based hydrogels for cancer drug release: Modulation of stiffness, drug release and proteolytic stability of hydrogels by incorporating d-amino acid residue(s). *Chem. Commun.* **2016**, *52*, 5045–5048.
86. Marchesan, S.; Easton, C. D.; Kushkaki, F.; Waddington, L.; Hartley, P. G. Tripeptide self-assembled hydrogels: Unexpected twists of chirality. *Chem. Commun.* **2012**, *48*, 2195–2197.
87. Kelly, S. M.; Jess, T. J.; Price, N. C. How to study proteins by circular dichroism. *Biochim. Biophys. Acta - Proteins Proteomics* **2005**, *1751*, 119–139.
88. Krittanai, C.; Johnson, W. C. Correcting the circular dichroism spectra of peptides for contributions of absorbing side chains. *Anal. Biochem.* **1997**, *253*, 57–64.
89. Chakrabartty, A.; Kortemme, T.; Padmanabhan, S.; Baldwin, R. L. Aromatic Side-Chain Contribution to Far-Ultraviolet Circular Dichroism of Helical Peptides and Its Effect on Measurement of Helix Propensities. *Biochemistry* **1993**, *32*, 5560–5565.

90. Kong, J.; Yu, S. Fourier transform infrared spectroscopic analysis of protein secondary structures. *Acta Biochim. Biophys. Sin. (Shanghai).* **2007**, *39*, 549–559.
91. Adochitei, A.; Drochioiu, G. Rapid characterization of peptide secondary structure by FT-IR spectroscopy. *Rev. Roum. Chim.* **2011**, *56*, 783–791.
92. Haris, P. I.; Chapman, D. The conformational analysis of peptides using fourier transform IR spectroscopy. *Biopolymers* **1995**, *37*, 251–263.
93. Pelton, J. T.; McLean, L. R. Spectroscopic methods for analysis of protein secondary structure. *Anal. Biochem.* **2000**, *277*, 167–176.
94. Kurbasic, M.; Romano, C.; Garcia, A.; Kralj, S.; Marchesan, S. Assembly of a Tripeptide and Anti-Inflammatory Drugs into Supramolecular Hydrogels for Sustained Release. *Gels* **2017**, *3*, 29.
95. Papadopoulos, N. G.; Dedoussis, G. V. Z.; Spanakos, G.; Gritzapis, A. D.; Baxevanis, C. N.; Papamichail, M. An improved fluorescence assay for the determination of lymphocyte-mediated cytotoxicity using flow cytometry. *J. Immunol. Methods* **1994**, *177*, 101–111.
96. Supino, R. MTT assays. *Methods Mol. Biol.* **1995**, *43*, 137–149.
97. Kabsch, W.; IUCr; K., D.; A., K. P.; K., D.; S., M.; G., R. R. B.; P., E.; S., F.; K., W.; W., K.; W., K.; W., K.; W., K.; P., K.; S., W. M. XDS. *Acta Crystallogr. D. Biol. Crystallogr.* **2010**, *66*, 125–32.
98. Evans, P. Scaling and assessment of data quality. In *Acta Crystallographica Section D: Biological Crystallography*; **2006**, *62*, 72–82.
99. Evans, P. R.; Murshudov, G. N. How good are my data and what is the resolution? *Acta Crystallogr. Sect. D Biol. Crystallogr.* **2013**, *69*, 1204–1214.
100. Sheldrick, G. M. A short history of SHELX. *Acta Crystallogr. Sect. A Found. Crystallogr.* **2008**, *64*, 112–122.
101. Sheldrick, G. M. Crystal structure refinement with SHELXL. *Acta Crystallogr. Sect. C Struct. Chem.* **2015**, *71*, 3–8.
102. Farrugia, L. J. WinGX and ORTEP for Windows: An update. *J. Appl. Crystallogr.* **2012**, *45*, 849–854.
103. Parkin, S.; Moezzi, B.; Hope, H. 2: an Empirical Absorption Correction Program. *J. Appl. Crystallogr.* **1995**, *28*, 53–56.
104. Spek, A. L. PLATON SQUEEZE: A tool for the calculation of the disordered solvent contribution to the calculated structure factors. *Acta Crystallogr. Sect. C Struct. Chem.* **2015**, *71*, 9–18.

A passage from "Twenty thousand leagues under the sea" by Jules Verne

[…]
"Eh? What happened to master?" Conseil asked, very startled. "Did master get bitten?"

"No, my boy, but I'd gladly have sacrificed a finger for such a find!"

"What find?"

"This shell," I said, displaying the subject of my triumph.

"But that's simply an olive shell of the 'tent olive' species, genus Oliva, order Pectinibranchia, class Gastropoda, branch Mollusca."

"Yes, yes, Conseil! But instead of coiling from right to left, this olive shell rolls from left to right!"

"It can't be!" Conseil exclaimed.

"Yes, my boy, it's a left-handed shell!"

"A left-handed shell!" Conseil repeated, his heart pounding.

"Look at its spiral!"

"Oh, master can trust me on this," Conseil said, taking the valuable shell in trembling hands, "but never have I felt such excitement!"

And there was good reason to be excited! In fact, as naturalists have ventured to observe, "dextrality" is a well-known law of nature. In their rotational and orbital movements, stars and their satellites go from right to left. Man uses his right hand more often than his left, and consequently his various instruments and equipment (staircases, locks, watch springs, etc.) are designed to be used in a right-to-left manner. Now then, nature has generally obeyed this law in coiling her shells. They're right-handed with only rare exceptions, and when by chance a shell's spiral is left-handed, collectors will pay its weight in gold for it.
[…]

Neptunea Constricta (Doll, 1907)

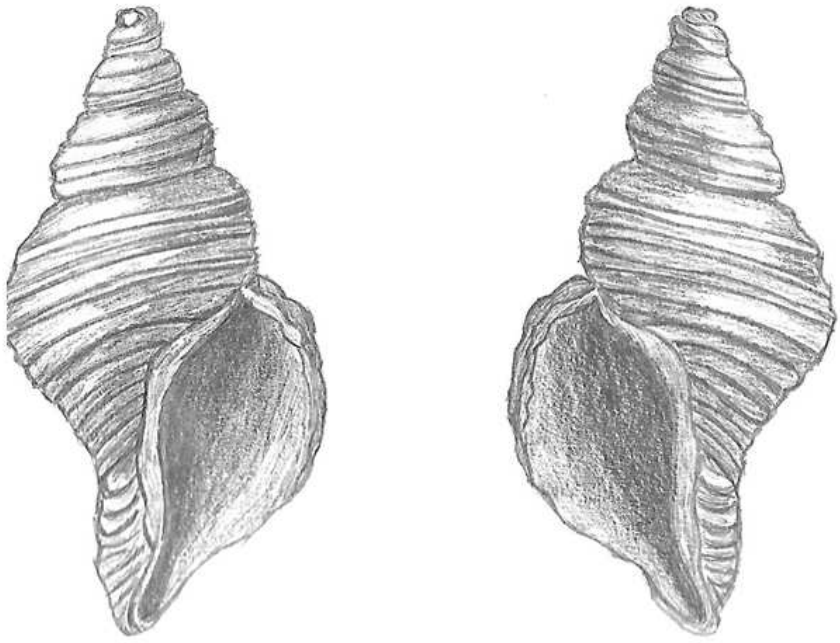

Neptunea Constricta (Doll, 1907)

Examples of chiral shells. Special thanks for the hand drawings to my mother, Maria Grazia Rovito (MGR,2018).